UNIVERSITY OF SOUTHAMPTON

Modelling the signal propagation through structural connections in the brain: A circuit theory approach

by

Sarbani Das

Thesis for the degree of Doctor of Philosophy

in the

Faculty of Engineering, Science and Mathematics
School of Electronics and Computer Science

September 2021

UNIVERSITY OF SOUTHAMPTON

ABSTRACT

FACULTY OF ENGINEERING, SCIENCE AND MATHEMATICS
SCHOOL OF ELECTRONICS AND COMPUTER SCIENCE

Doctor of Philosophy

Modelling the signal propagation through structural connections in the brain: A circuit theory approach

by Sarbani Das

The neural function of the brain is characterized by activated brain regions and the connectivities among them. It is still unknown, how a static structural connectivity network affects the occurrence of task-dependent dynamic functional connectivity or why two structurally connected brain regions, are not functionally connected and vice-versa. Studies have shown, the underlying cause for many neurodegenerative diseases is the functional disruptions in neural connections. So understanding the relationship between structural and functional connectivity is important for understanding the impairment characteristics in the brain networks which is in essence depends upon the nature of signal flow through the structural connections in the brain. The purpose of this work is to characterize the signal propagation characteristics through structural connectivity and its influence on functional connectivity of the brain by applying a circuit theory-based modelling approach. Modelling structural connections using circuit theory will allow the analysis of signal propagation in both time and frequency domains. So far the studies on the correlation between structural and functional connectivity were done from the time domain perspective of signal propagation. However, the very definition of functional connectivity indicates that the underlying structural connectivity networks has filter like properties and holds the frequency-phase characteristics. In this work, we explore this phenomenon following a step-by-step approach: (1) we develop an automated tool for extracting structural connectivity network from structural MRI image by considering a more general (compared to standard cortical mapping) non-anatomical equal-area parcellation process of the Regions of Interest (ROI) of the brain and extracting the geometrical properties of the white matter tracts between the ROIs, (2) developing circuit-based model for characterising signal propagation through a single myelinated axon fibre and representing it as a simplified transfer function encompassing its time and frequency properties, (3) extending this model for coupled axon fibres and characterising the time and frequency properties of the signal propagation through them under the influence of ephaptic coupling between them and finally;(4) applying

the models developed in (2) and (3) for creating an automated tool that is capable to characterising signal propagation through a bundle of axons - the typical scenario of a white matter tract. Our work results in an end-to-end tool taking inputs as the structural and diffusional MRI data and outputting the phase and frequency characteristics of the signal through the axon bundle with a defined geometrical property - the underlying phenomenon for deriving the relationship between structural and functional brain connectivity.

Contents

List of Figures

List of Tables

Nomenclature

ACT	Anatomical Constrained Tractography
AFD	Apparent Fibre Density
AP	Action potential
BOLD	Blood-oxygen-level-dependent
CNS	Central Nervous System
CSD	Constraint Spherical Deconvolution
CV	Conduction velocity
DTI	Diffusion Tensor Imaging
DWI	Diffusion-weighted magnetic resonance imaging
EEG	Electroencephalogram
EQSP	Equal Area Sphere Partitioning
FA	Fractional Anisotropy
FC	Fibre-bundle cross section
FD	Fibre density
FDC	Fibre density and cross-section
FMN	Frog Motor Nerve
FMRI	Functional magnetic resonance imaging
FOD	Fibre Orientation Distribution
GBCL	Globular Bushy Cell Medial
GBCM	Globular Bushy Cell Lateral
HH	Hodgkin-Huxley
ICC	Intraclass correlation coefficient
IN	Internode
LF	Limiting Frequency
MML	Maximum myelin length
MRI	Magnetic resonance imaging
NR	Nodes of Ranvier
ODF	Orientation Distribution Function
PNS	Peripheral Nervous System
SIFT	Spherical-Deconvolution Informed Filtering Tractograms
SBC	Spherical Bushy Cell
ROI	Region of Interest

Declaration of Authorship

I, Sarbani Das declare that this thesis entitled *Modelling the signal propagation through structural connections in the brain: A circuit theory approach* and the work presented in it is my own and has been generated by me as the result of my own original research.

I confirm that:

1. This work was done wholly or mainly while in candidature for a research degree at this University;
2. Where any part of this thesis has previously been submitted for a degree or any other qualification at this University or any other institution, this has been clearly stated;
3. Where I have consulted the published work of others, this is always clearly attributed;
4. Where I have quoted from the work of others, the source is always given. With the exception of such quotations, this thesis is entirely my own work;
5. I have acknowledged all main sources of help;
6. Where the thesis is based on work done by myself jointly with others, I have made clear exactly what was done by others and what I have contributed myself;
7. None of this work has been published before submission

Signed:..... Date:.....

Acknowledgements

It has been a gratifying experience so far to carry out my Ph.D. research work along with my family life with two little kids. It won't have been possible without the continuous support and guidance of my supervisor Prof. Koushik Maharatna. His timely inputs have given a thrust to come over various obstacles in making progress. I would also like to thank my co-supervisor, Dr Brigitte Vollmer, for her time to time support and encouragement during my Ph.D. I want to thank Dr. Saptarshi Das for the kind helps he has extended toward me throughout my Ph.D. journey. A big thank you must go to my husband, for his continuous support and encouragement to achieve my goals, and to my two kids, who are my inspiration to achieve any greatness. Lastly, I would like to thank my parents specially my mother who has been always the pillar of strength for me.

Chapter 1

Introduction

Neurodegenerative diseases are a serious concern in the modern world as the prediction made by the World Health Organization (WHO) that by 2040, as many developed countries' populations get older, neurodegenerative diseases such as Alzheimer's and other causes of dementia, as well as conditions that affect mainly motor functions, such as Parkinson's disease and Amyotrophic Lateral Sclerosis, will outstrip other diseases to become the second leading cause of mortality after cardiovascular disease (Gammon, 2014). Recent research shows that neural functions not only depend upon the brain region activated but the topography of communication network both structural and functional amongst them (Sporns et al., 2005; Honey et al., 2007; Hagmann et al., 2008; Deco et al., 2008; Honey et al., 2009; Rubinov et al., 2009; Rubinov and Sporns, 2010; Honey et al., 2010; Mišić et al., 2016). Several studies also pointed out that impairment in such a network is the fundamental reason behind different neurodegenerative conditions (Sporns et al., 2005; Rubinov and Sporns, 2010; Braun et al., 2015; Fleischer et al., 2017). Over the past decade, techniques have been developed to characterise structural brain networks and to couple this with functional brain networks (Honey et al., 2007; Hagmann et al., 2008; Honey et al., 2009; Rubinov et al., 2009). Application of these techniques to characterise the brain networks of a neurodegenerative disorder patient appears to be a promising technique to understand the impairment characteristics of the network. This can lead to improving the early prediction of neurodegenerative outcomes, and importantly this can help in exploring the manipulation of these networks by applying neuro-modulation which will be the new means to treat neurodegenerative patients.

1.1 Motivation

However, the problem is, the present understanding of the relationships between anatomical and functional connectivity networks are at a nascent stage. By nature, the functional connectivity is temporally dynamic and its topography varies from one frequency

band to the other. On the other hand, structural brain connectivity does not change rapidly over time and thus is static in nature in the scale of temporal variation of functional connectivity. But how such a static structural connectivity network impacts and enables the occurrence of task-dependent dynamic functional connectivity is still an unsolved problem in neuroscience. The other problem is that how the signal actually propagates through a bundle of axons from one ROI to another ROI is not clear. Given a bundle of axons, there is no definite evidence that all the axons will fire at the same time. Moreover, there could be the random firing of axons which may influence the signal propagation throughout the axon bundle. So, the correspondence between structural connectivity and functional connectivity is hinged upon the fact of how the signal actually propagates through the structural brain connectivity network. We hypothesised that signal propagation disruptions leading to disruptions of functional connectivity might happen not only because of the time-domain property of signal but also because of the frequency domain property of the transmission medium i.e. myelinated axon. We also hypothesise that it behaves as a filter that only passes a certain frequency range while dampens the other frequency range depending upon its geometry. This has motivated us to explore this phenomenon and put it in the perspective of functional and structural brain connectivity. Recent research shows that an axon can be modelled as a Hodgkin-Huxley (mHH) circuit arrangement combined with passive cable theory (Huxley and Stämpeli, 1949; Hodgkin and Huxley, 1952; Fitzhugh, 1962). This research work will design a circuit theory-based computational model which characterizes the frequency-phase characteristics of signal propagation through a bundle of axons. This will then be extended to develop a framework of an automated toolchain that takes input from MRI data and output the phase and frequency characteristics of the signal.

1.2 Aims and objectives

Following our motivation, the aims of this thesis are (1) modelling the signal propagation through a bundle of myelinated axon fibre by applying a circuit theory-based computational modelling approach and (2) creating a framework of an end-to-end automated toolchain that processes raw MRI data and extract phase-frequency relationship of the signal of the nerve bundle at the output.

So the objectives are:

- (1) Developing an automated tool-chain for extracting geometry of white matter tracts from MRI.
- (2) Modelling frequency characteristics of a single myelinated axon.
- (3) Modelling the effect of ephaptic coupling between two myelinated axons and find the influence on signal propagation.

- (4) Translating these models into a framework of an automated toolchain that characterizes signal propagation through a bundle of axons.

Figure 1.1 shows a flow-chart representation of the thesis work.

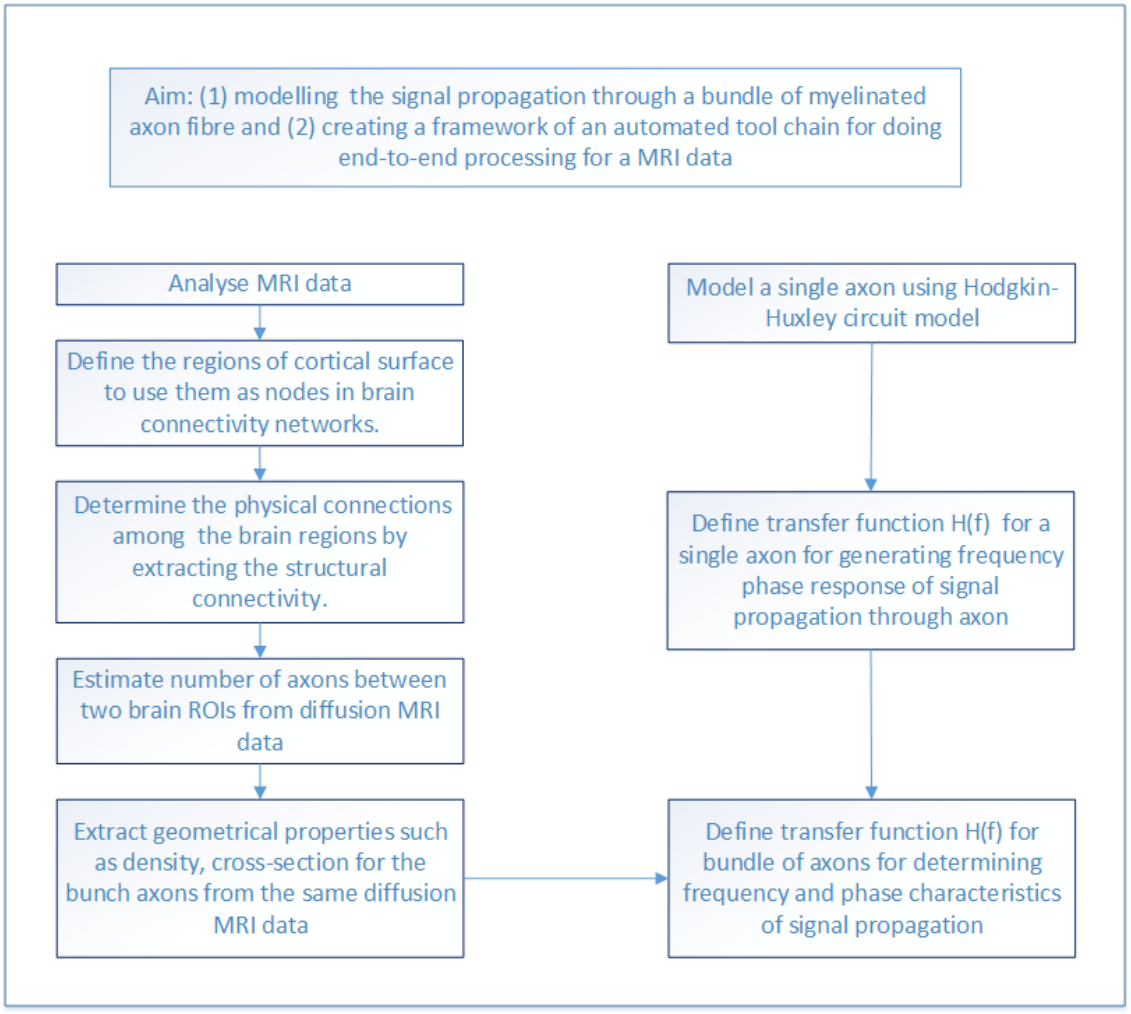

FIGURE 1.1: A Flowchart representation of the thesis work

1.3 Contribution

The contributions of this research include:

1. The existing method of cortical parcellation from MRI data is mainly based on fixed Brodmann atlas; which does not support neonate's brain or adult's brain with neuro-plasticity anomalies. We have designed and developed an algorithm

to parcellate the cortical surface in non-anatomical equal size areas from structural MRI data and extracted geometrical properties of white matter tracts from diffusional MRI data using equal area cortical parcellation.

2. We have created mathematical models of the transfer function of a single myelinated axon and signal propagation characteristics of two myelinated axons coupled by ephaptic coupling.

3. We have designed a computational circuit model for a bunch of axons; derived the mathematical relation between conduction velocity of axons in a bundle with its fibre density; determined limiting the frequency of signal transmission through axon in a bundle and explore temporal and phase-frequency characteristics of signal propagation through a bundle of myelinated axons.

Papers: The list of papers accepted and in preparations:

Conference paper:

1. Das, S. and Maharatna, K., 2020, July. An automated tool-chain for quantitative characterisation of structural connectome from MRI based on non-anatomical cortical parcellation. In 2020 42nd Annual International Conference of the IEEE Engineering in Medicine & Biology Society (EMBC) (pp. 5653-5656). IEEE.

Journal paper:

1. Sarbani Das, Koushik Maharatna. *Filtering property of myelin sheathe and its effect on neural signal propagation in single and ephaphtically coupled axons* (In preparation for Scientific Reports).

2. Sarbani Das, Koushik Maharatna. *Signal propagation dynamics in myelinated axon bundle* (In preparation for a journal).

1.4 Thesis organization

The thesis is organized as below: Chapter 2 presents a literature review covering brain connectivity, MRI Image processing, neuronal dynamics and axon physiology. Chapter 3 presents an automated tool development for parcellation and extraction of the structural connectome and its geometry from Structural and dMRI data. Chapter 4 presents the circuit model for analysing signal propagation through a single myelinated axon in time and frequency domains. Chapter 5 presents the circuit model for modelling the effects of ephaptic coupling in two myelinated axons. Chapter 6 presents the circuit model for analysing signal propagation dynamics in a bundle of myelinated axons and define a system definition for determining phase-frequency characteristics of signal propagation through the bundle.

Chapter 2

Background and Literature Review

2.1 Brain connectivity

The most fundamental characteristic of the neural network is brain connectivity. Brain connectivity analysis is a way to study the information processing in neural networks. The neural networks are build of spatially segregated but functionally integrated brain regions which continuously communicate through neural pathways. There exist three kinds of connectivity patterns among neuronal populations or anatomically segregated brain regions: anatomical links which are the axonal pathways (axon bundles), statistical dependencies of brain regions - the functional connectivity and causal interactions between them - the effective connectivity (Rubinov and Sporns, 2010). The three kinds of brain connectivity are depicted in Figure 2.1.

2.1.1 Structural connectivity

Structural connectivity is the anatomical links of the brain that are made of synaptic and axonal (white matter) pathways. It is static and does not change rapidly over time in the scale of temporal variation of functional connectivity. It is the backbone for functional connectivity as brain function gets affected if axonal pathways are disrupted. So structural connectivity provides the base for couplings of a set of neurally activated macroscopic cortical columns (Honey et al., 2009). The aim of structural connectivity analysis is to determine the geometric properties of the white matter connectivity of the brain which is obtained from Diffusion MRI imaging data. There is a new strategy developed by Sporns et al. (2005) to describe the structural connectivity; the 'Connectome' matrix which is a unified and readily available neuro-informatics resource to be used in all areas of experimental and theoretical neuroscience. Though Sporns et al. (2005) coined

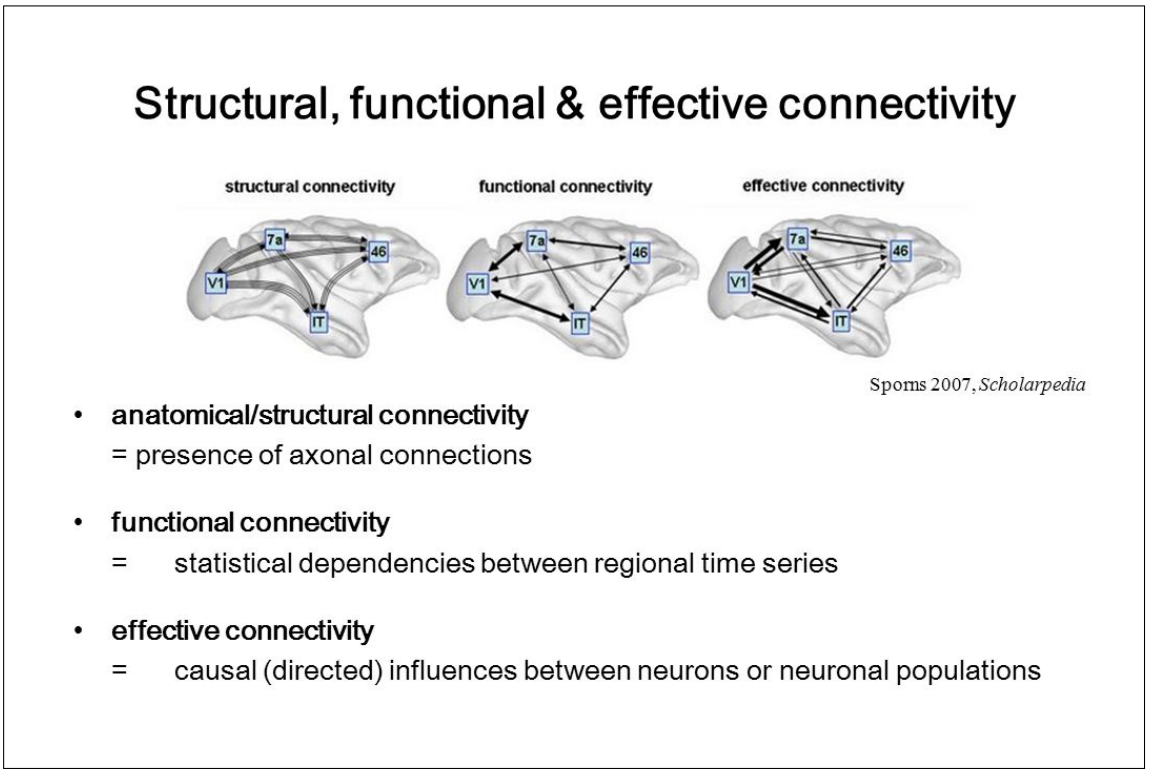

FIGURE 2.1: Structural, Functional and Effective Connectivity. [Source: SPM Course, London 2017]

the term connectome but the representation of brain connectivity as a matrix has been around for a long time; such as Felleman and Van Essen (1991) presented distributed hierarchical connectivity of cerebral cortex for rhesus monkey and around same time Yamamoto and Achacoso (1992) presented connectivity in the nematode Caenorhabditis elegans.

2.1.2 Functional connectivity

Functional connectivity is a way to characterize the integration among activated brain areas by measuring the correlations of neural activities (Friston, 2011). It is dynamic and varies in temporal scale. There are two brain imaging techniques commonly used to obtain functional connectivity of the brain - EEG and functional MRI (fMRI). EEG measures the electrical activity of the brain via electrodes that are placed on the scalp. It tells from the surface measurements how active the brain is. When a particular task or job is performed, a certain area of the brain gets activated and receives slightly more oxygen-rich blood. fMRI measures the blood oxygenation level dependent (BOLD) signals from the active parts of the brain. Because of the imaging methodology, EEG signal has high time resolution but low spatial resolution whereas fMRI BOLD signal has low time resolution but high spatial resolution. According to Segall et al. (2012), functional connectivity measured by using resting-state functional magnetic resonance

imaging (rs-fMRI) is an indirect measure of neuronal activity of neuronal cells mainly form the gray matter (GM) and the majority of connectome research excluded GM measures. In his work, Segall et al. (2012) explored the gray matter area to understand both structural and functional connectivity. A functional correlation matrix is obtained by analysing the functional connectivity among brain areas.

2.1.3 Effective connectivity

Effective connectivity describes the causal relationships among brain regions. According to Aertsen (1991) effective connectivity is the time-dependent, simplest possible circuit diagram that replicates the observed timing relationships between the recorded neurons. According to Friston (2011) integration within a distributed system is usually better understood regarding effective connectivity because effective connectivity refers explicitly to the influence that one neural system exerts over another, either at a synaptic or population level. Effective connectivity corresponds to the parameter of a model that tries to explain observed dependencies (functional connectivity). Friston et al. (2003) has developed an approach for the analysis of effective connectivity using experimentally designed inputs and fMRI responses, which is called Dynamic Causal Modelling. Dynamic Causal Modelling infers the value of causal connectivity strength that one neural system exerts over another which is physically not measurable. Granger causality is a way to investigate causality between two variables in a time series. The method is a probabilistic account of causality; it uses empirical data sets to find patterns of correlation.

2.1.4 Graph theory measures to analyse brain connectivity

As described by (Rubinov and Sporns, 2010), brain connectivities are analysed by characterizing them using graph-theoretic measures. Some graph theory parameters characterize the whole graph (network), while others are node-specific. There are different graph theory measures that detect functional integration and segregation, quantify centrality of individual brain regions or pathways, characterize the pattern of local anatomical circuitry and test the resilience of the network to insult.

2.1.4.1 Measures of functional segregation

The measure of segregation quantifies the presence of densely interconnected groups of brain regions responsible for specialized processing (Rubinov and Sporns, 2010).

Clustering Coefficient : Clustering coefficient is a measure of the degree to which nodes in a graph tend to cluster together. Measures of segregation are based on the number of triangles in the network, with a high number of triangles implying

segregation (Rubinov and Sporns (2010)). Clustering coefficient quantifies the fraction of triangles around an individual node, which is equivalent to the fraction of the node's neighbours that are also neighbours of each other. The high value of clustering coefficient implies densely interconnected groups of brain ROIs that are functionally segregated.

Modularity : The measures of segregation not only describe the presence of densely interconnected groups of regions but also find the exact size and composition of these individual groups. The network's modular structure (community structure), is described by subdividing the network into groups of nodes, with a maximally possible number of within-group links, and a minimally possible number of between-group links. The degree to which the network may be subdivided into such clearly delineated and non-overlapping groups is quantified by the modularity (Rubinov and Sporns (2010)). A high value of modularity indicates that the node within a module has a dense connection and that there are minimum possible connections outside of the modules.

2.1.4.2 Measures of functional integration

Measures of integration estimate the ease with which brain regions communicate and are commonly based on the concept of a path (Rubinov and Sporns, 2010).

Characteristic Path Length : Characteristic path length measures the average shortest paths between all node pairs in the graph. To calculate this, we constructed a table with all of the shortest paths between all pairs of a node and then calculated the average.

Global Efficiency : Global efficiency is a related measure that quantifies the average inverse shortest path length in a network.

2.1.4.3 Measures of centrality

Measures of node centrality variously assess the importance of individual nodes on interacting with many other regions, facilitating functional integration, and playing a key role in network resilience to insults (Rubinov and Sporns, 2010).

Degree : The degree of a node is equal to the number of nodes it is connected to. It reflects the importance of the nodes in the network.

Betweenness Centrality : Betweenness centrality measures the importance or influence of the node in the network. It estimates this by determining the shortest paths that cross the node.

2.1.4.4 Measures of network resilience

Measures of resilience quantify anatomical features that reflect network vulnerability to insults (Rubinov and Sporns, 2010).

Degree Distribution : The degree of all nodes in the network comprises degree distribution.

Assortativity : Assortativity coefficient measures the trend of each node regarding how it connects with nodes of the same degree. A positive value means that the node is connected to nodes that have the same degree.

2.1.5 Relationship between structural and functional connectivity: studies done so far

In this section, we have explored the existing works which have been previously done on establishing the relationship between structural and functional connectivity. Batista-García-Ramó and Fernández-Verdecia (2018) in their study of structural and functional relation, mentioned that neuro-image processing, network theory and computational modelling have played essential roles in the study of structure-function interactions. Available literature in this area can be broadly categorized into two categories. The first category of work has used computational modelling while the second category of work has been carried out using the data analysis method. The work done by (Honey et al., 2007; Hagmann et al., 2008; Honey et al., 2009; Rubinov et al., 2009) falls into the former category where the computational modelling has been used to derive functional connectivity from structural connectivity. On the other hand, the work done by (Honey et al., 2010) and (Hütt et al., 2014) is based on statistical analysis of diffusional MRI data and fMRI data for finding the correlation between the two connectivity. There are other sets of research works that have been carried out recently such as the works done by (Mišić et al., 2016; Messé et al., 2015; Díaz-Parra et al., 2017; Zamora-López et al., 2016) pertain to the study of connectivity patterns to both functional and anatomical in humans and animals, and the study of the relationship of brain connectivity with neurodegenerative conditions such as Alzheimers and Parkinsons diseases were done by (Son et al., 2017; Manza et al., 2016; Fleischer et al., 2017). Reviewing the research works done by (Honey et al., 2007; Hagmann et al., 2008; Honey et al., 2009; Rubinov et al., 2009), we found an important aspect of the relationship between the two forms of connectivity. These research works show that in some cases the functional connectivity can be derived from the structural connectivity, but not always, which means if there is structural connectivity between two brain ROIs they may not become functional connected. On the contrary, their research works also show that there are instances where even if there was no structural connectivity, there was functional connectivity (Honey

et al., 2009). In his research work, Rubinov et al. (2009) simulated spontaneous brain dynamics on structural connectivity networks, using coupled non-linear maps. Using computational modelling, Honey et al. (2009) investigated if systems-level properties of functional networks as well as their spatial statistics and persistence across time can be explained by properties of the underlying anatomical network. They measured resting-state functional connectivity (using fMRI) and structural connectivity (using diffusion spectrum imaging tractography) in the same individuals at high resolution and built a model. Their research reveals that resting-state functional connectivity is variable and is often present between regions which do not have any direct structural linkage. However, the strength, persistence, and spatial statistics of the functional connectivity is limited by the large-scale anatomical structure of the human cerebral cortex. Hagmann et al. (2008) constructed connection maps of the entire cortical surface and did computational analyses of the same to figure out the regions of the cortex that are connected. Honey et al. (2007) used a computational approach in order to relate the features of spontaneous cortical dynamics to the underlying anatomical connectivity. Simulating non-linear neuronal dynamics on a network that captures the large-scale interregional connections of macaque neocortex, and applying information-theoretic measures to identify functional networks, they found the relationship between structural and functional connectivity at multiple temporal scales. The studies that were done on connectivity patterns, both functional and anatomical, in humans and animals in recent years are (Sethi et al., 2017; Mišić et al., 2016; Messé et al., 2015; Díaz-Parra et al., 2017; Zamora-López et al., 2016) and their relationship with neurodegenerative conditions are (Son et al., 2017; Manza et al., 2016; Fleischer et al., 2017). According to Honey et al. (2010), the degree of correspondence between structural and functional connectivity depends on spatial resolution and time scales.

As mentioned by Batista-García-Ramó and Fernández-Verdecia (2018) there are some limitations on existing studies. For example (1) the images acquisition and processing offer inherent limitations of the methodology. For instance, when structural connectivity is based on DTI, it can ignore long-distance and fibre-cross connections and does not provide information about the directionality of the connections. In the case of fMRI, it is important to note some aspects: neuronal activity is not directly a measure of the blood oxygenation level dependence (BOLD) signal; it is an integration of a variety of neuronal activities and the increase of excitatory or inhibitory synaptic activity can cause an increase of metabolic activity. Logothetis et al. (2001) mentioned in his work that the haemodynamic response seems to be better correlated with the LFPs, implying that activation in an area is often likely to reflect the incoming input and the local processing in a given area rather than the spiking activity. Such limitations, properties of neuroimaging techniques, may lead to imprecise brain network representations, affecting the analysis of network properties such as the study of the structure-function relationship. (2) Next, in the case of using methodologies and procedures such as connectivity measure and graph construction to produce the correlation there is no established guidelines

to follow. (3) In the case of computational modelling, parameter estimation becomes complex when high numbers of variables being used for modelling.

While reviewing the relevant literatures, we have observed that there is a gap in the studies of finding the correlation between functional and structural connectivity. The functional connectivity of the brain is obtained by measuring the phase correlation of time series signals between two activated brain regions. This signifies that the signal propagated through a bundle of axons has frequency characteristics which determine the propagation criteria as well along with other factors. But in the studies done so far on brain connectivity, the frequency domain analysis has not been considered. In our approach, we will represent the bundle of axons using a circuit theory-based model and perform the phase and frequency response analysis of the signal in the frequency domain. Analysing signal propagation through axon in frequency domain will surely lead to finding the correlation between functional and structural brain connectivity.

2.2 Neuro-image processing of Structural MRI data for cortical surface parcellation

Brain connectivity is about the integration of spatially segregated brain regions. So delineating and defining the spatially segregated brain regions as nodes of the network is the first step of brain connectivity analysis. Cortical parcellation serves the purpose of parcellating the cortical and subcortical layers of the cortex in terms of some reference atlas and assigning to them a neuroanatomical label either automatically or manually resulting in a complete labelling of cortical sulci and gyri (Fischl et al., 2004). It is performed on structural MRI images because structural magnetic resonance imaging (MRI) provides extensive detail about the anatomical structure of the brain. First, a brief description of structural T1 and T2 weighted MRIs are given followed by the process of surface reconstruction and then cortical parcellation.

2.2.1 Structural MRI(T1 and T2 weighted MRI)

Structural MRI imaging provides anatomical information of the brain. Pathological processes are described in terms of T1 and T2 signal behaviours, in addition to contrast enhancement, anatomical location, and morphological characteristics (Symms et al., 2004).

T1 Weighted scan as shown in Figure 2.2 gives the good contrast between gray and white matter. It produces a very high resolution (1mm) image. It is very useful in identifying brain structure and is used for parcellation of the cortical surface.

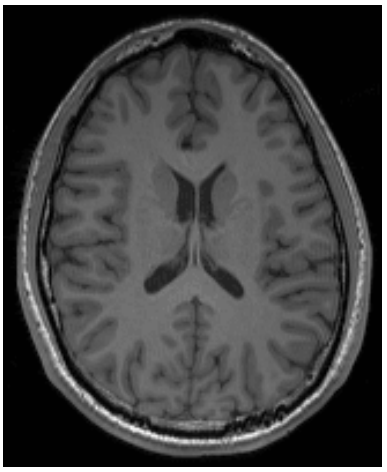

FIGURE 2.2: T1 Weighted Image

T2 Weighted spin echo (TSE) scan as shown in Figure 2.3 produces very high-resolution T2-weighted images within a reasonable scan time. In T2-TSE images, both fat and water are hyper-intense and appear bright.

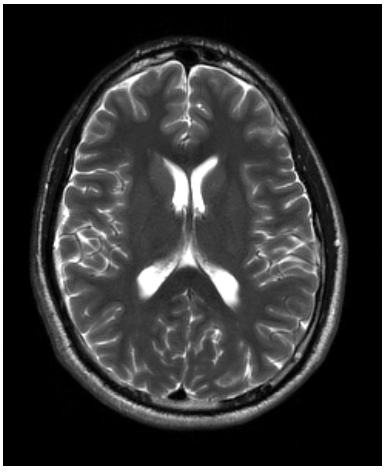

FIGURE 2.3: T2 Weighted Image

2.2.2 Cortical surface reconstruction and parcellation

To study cortical properties in humans, it is necessary to obtain an accurate and explicit representation of the cortical surface from 3D structural MRI image (Dale et al., 1999). Cortical reconstruction is basically the derivation of a computerized representation of the cerebral cortical layer based on three-dimensional (3D) magnetic resonance (MR) images of the brain for quantitative analysis of the human brain structure. The reconstructed surface is used for serving as a reference basis for all further analysis, and must be geometrically accurate and topologically correct in order to provide valid and accurate quantitative measures of brain structure (Han et al., 2004).

I. Segmentation: Segmentation is a process to reconstruct gray/white and pial surfaces of the cerebral cortex from a high-resolution T1-weighted MRI scan. It is essential for the analysis of features of the cortical surface, including structural properties such as cortical thickness, as well as functional characteristics such as topographic structure. The whole procedure is a complex task that involves some subtasks such as intensity normalization, skull-stripping, filtering, segmentation and surface deformation. Dale et al. (1999) defined an automated process that performs these whole sets of procedures on raw T1 weighted brain image, and returns reconstructed segmented cortical surface.

II. Inflation, Flattening, and a Surface-Based Coordinate System: The most common process of analysing functional MRI data is to project the functional data from a sequence of slices onto a standardized anatomical 3D substrate. But this process has a major drawback. As the cortex is a 2D sheet with 60-to-70% folded and curved geometry, it gives difficulty in visualization and error in computation. To overcome these problems a set of procedures was designed by (Fischl et al., 1999) for modifying the representation of the cortical surface to (1) inflate the surface so that activity buried inside sulci may be visualized, (2) cut and flatten an entire hemisphere, and (3) transform each hemisphere into a simple parametrizable surface such as a sphere for establishing a surface-based coordinate system.

III. Parcellation: Techniques for labelling geometric features of the cerebral cortex are useful for analysing a variety of functional and structural neuroimaging data. Identification of every point in the entire cortex, rather than the labelling of a discrete set of cortical features is known as a parcellation (Fischl et al., 2004). One of the main aims in neuroscience is defining the brain regions based on neuronal activation related to specific tasks.

2.2.3 Brain parcellation

To study cortical properties, it is necessary to obtain a representation of the cortical surface from MRI image (Dale et al., 1999). Cortical parcellation serves the purpose by parcellation of the cortical and sub-cortical layers of the cortex in terms of some reference atlas and assigning to them a neuroanatomical label either automatically or manually resulting in complete labelling of cortical sulci and gyri (Fischl et al., 2004). It is performed on structural MRI images because structural MRI provides extensive detail about the anatomical structure of the brain.

There are some important key points to consider while defining brain regions in the cortical parcellation process. First, a parcellation scheme should completely cover the surface of the cortex, or of the entire brain, and individual nodes should not spatially overlap (Rubinov and Sporns, 2010). Second, structural and functional networks should

share the same parcellation scheme because networks constructed using distinct parcellation schemes may significantly differ in their properties and cannot, in general, be quantitatively or meaningfully compared (Wang et al., 2009; Honey et al., 2009) and might not as a whole have a homogeneous and corresponding functional and structural connectivity architecture (Horn et al., 2014). Third, if applied parcellation is based on preselected regions of interest (ROI) then it might lead to selection bias, do not account for inter-individual anatomical differences.

Two approaches are mainly followed for performing cortical parcellation of structural MRI images; anatomically based cortical parcellation and non-anatomically based cortical parcellation.

2.2.3.1 Cortical parcellation based on anatomical nomenclature

This is a technique for automatically assigning a neuro-anatomical label from an atlas to each location on a cortical surface. It is done based on probabilistic information estimated from a manually labelled training set. This procedure incorporates both geometric information derived from the cortical model, and neuroanatomical convention, as found in the training set. This procedure performs complete labelling of cortical sulci and gyri and it uses manually labelled data as the basis for an automated parcellation procedure (Fischl et al., 2004). An anatomical parcellation on the spherical surface is shown in Figure 2.4.

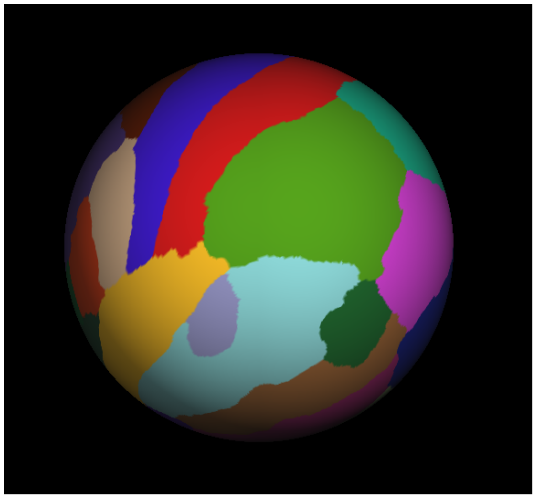

FIGURE 2.4: Anatomical Parcellation on spherical surface

2.2.3.2 Cortical parcellation based on non-anatomical Recursive Zonal Equal Area Partitioning

Parcellation following a standardized anatomical atlas is not appropriate in some cases (Tymofiyeva et al., 2012), such as (1) developing brain of neonates, who have immature sulcation, (2) cases of cerebral reorganization after brain damage (neuroplasticity), (3) cases where young children undergoing treatment of intractable epilepsy, cortical plasticity and change of connectivity allow the contralateral hemisphere to assume the functions of the lost hemisphere without significant neurologic deficits, and (4) in the case of normal anatomy of the adult brain, where different subjects have, different dominant hemispheres. In these cases, a non-anatomical equal-area cortical parcellation is more appropriate than anatomical parcellation. The non-anatomical equal-area parcellation process divides the cortical surface into some equal size areas, which is a template free and atlas free approach and not constrained by anatomy. A non-anatomical equal-area cortical parcellation on a spherical surface is shown in Figure 2.5. It is performed by dividing the cortical surface into nodes based on Recursive Zonal Equal Area Sphere Partitioning (Leopardi, 2006).

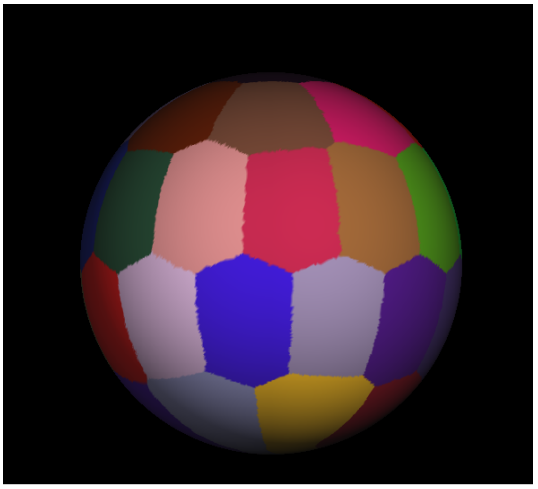

FIGURE 2.5: Non-anatomical Equal Area Parcellation on spherical surface

In this work, the Freesurfer tool (Fischl, 2012) has been extended to perform the non-anatomic equal partition cortical parcellation because Freesurfer is the most commonly utilized tool to perform automated labelling. It utilizes surface registration to align the subject surface and atlas to provide the anatomical labelling of the surface (Fischl et al., 2004). FreeSurfer (Fischl, 2012) has been shown to have good reliability. It utilized the intraclass correlation coefficients (ICCs) to compare volumes of manually and automatically labelled regions of interest. The only limitation of this software was that in the past it did not work on neonates. But now it has developed an automated segmentation and surface extraction pipeline that is designed to accommodate paediatric brain MRI images from a population of 0-2 year-olds relying on clinical T1-weighted MR images.

2.3 Neuroimaging processing of Diffusional MRI data for Structural Connectome

A connectome is a structural description of the human brain in the form of a connection matrix which is as defined by a unified, time-invariant, and readily available neuroinformatics resource for use in all areas of experimental and theoretical neuroscience (Sporns et al., 2005). Connectome is a square adjacency matrix where the nodes represent the brain regions and values represent the anatomical links among the brain regions. The connectome representation of structural connectivity significantly increases the understanding of how functional brain states derive from their underlying structural base and gives a clear perception into how brain function is affected if the brain structure is disrupted (Sporns et al., 2005). The diffusion-weighted MRI imaging technique is an effective way to extract white matter connectivity of whole-brain (Hagmann et al., 2007).

2.3.1 Diffusion of water in white matter: the basis of Diffusional MRI

Diffusion-weighted magnetic resonance imaging (DWI) uses the diffusive motion of water to perform macroscopic in vivo investigations of white matter tissue microstructure. The interaction of diffusing water and coherently ordered cellular structures, such as axon membranes, results in an anisotropic profile of diffusion which forms the basis of many aspects of DWI (Raffelt et al., 2012).

2.3.1.1 Structure of white matter tracts

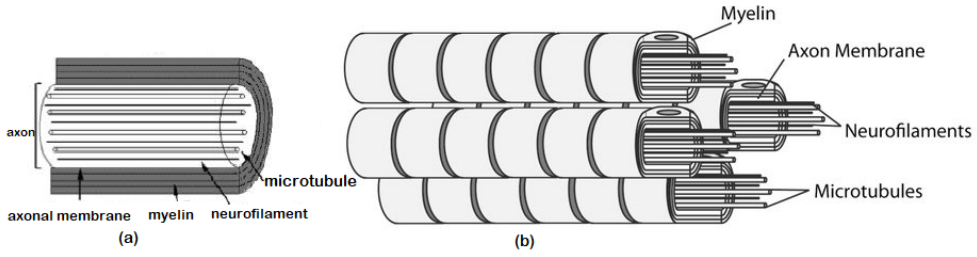

FIGURE 2.6: (a) Axon Beaulieu (2014) (b) White matter microstructure Ellingson et al. (2015)

The microstructure of white matter consists of submillimetre-scale tubular fascicles filled with thousands of small neuronal fibres (axons) wrapped by multiple lamellae of the membrane (myelin) and ordered filaments of proteins (microtubulin) that build the axonal skeleton within these fibres as shown in Figure 2.6. In addition, neuroglial cells surround and support this fibre arrangement. The extent to which these structures affect water displacement is not clear, but it is reasonable to speculate that water passage

through the cellular components of white matter is not unrestricted. Cell membranes are permeable to water molecules to a variable extent depending on the number of proteins that are spread on the membrane and the existence and functionality of water channels (such as extracellular water, myelin water, intra-axonal water, glial intracellular water) (Jones, 2010).

2.3.1.2 Fractional anisotrophy (FA)

Measurement of the degree and directionality (i.e., anisotropy) of water diffusion at the micron level within a tissue provides an indirect measure of the underlying microstructure. The diffusing water molecule samples and interacts with the local environment, and thus, by measuring the degree and direction of water motion, the structure can be inferred. For example, if the water encounters highly ordered barriers such that the distance travelled in one direction is greater than that in another direction in the same amount of time, the diffusion is said to be anisotropic. This fundamental property of anisotropic water diffusion is the physical basis behind the utility of diffusion tensor imaging (DTI) and tractography of white matter tracts in the brain. Diffusion in the isotropic and anisotropic sample have explained in Figure 2.7. Figure 2.8 shows a simplistic schematic longitudinal view of a myelinated axon. Myelin, the axonal membrane, microtubules, and neurofilaments are all longitudinally oriented structures that could hinder water diffusion perpendicular to the length of the axon (Beaulieu, 2002).

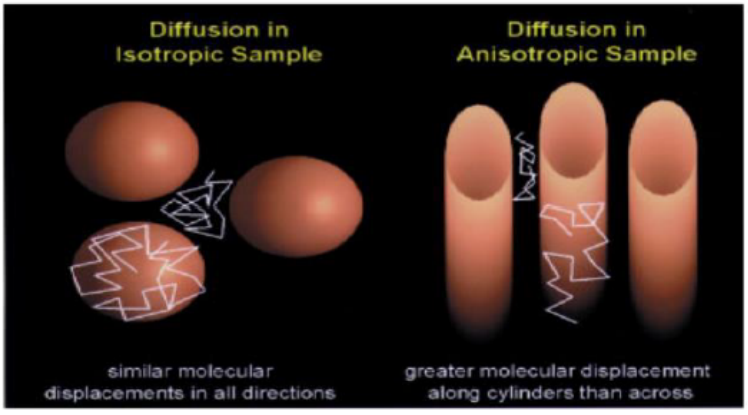

FIGURE 2.7: Isotropic and Anisotropic diffusion

2.3.2 Diffusional Weighted MRI

The DWI-MRI works on the physical principles of water diffusion in the brain and imaging techniques. The DWI-MRI technique is sensitive to water molecular movement in a specific direction. By acquiring many DWI images sensitive to different directions, a 3D picture of the diffusion at a particular point in tissue can be created. DWI-MRI

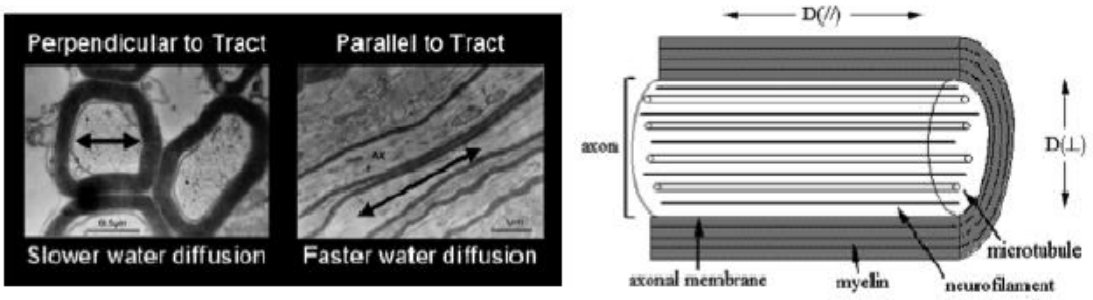

FIGURE 2.8: Diffusion of water molecules through white matter structure

is used to assess or diagnose acute stroke and to image white matter fibre tracts in the brain. An image of diffusional MRI data is shown in figure 2.9.

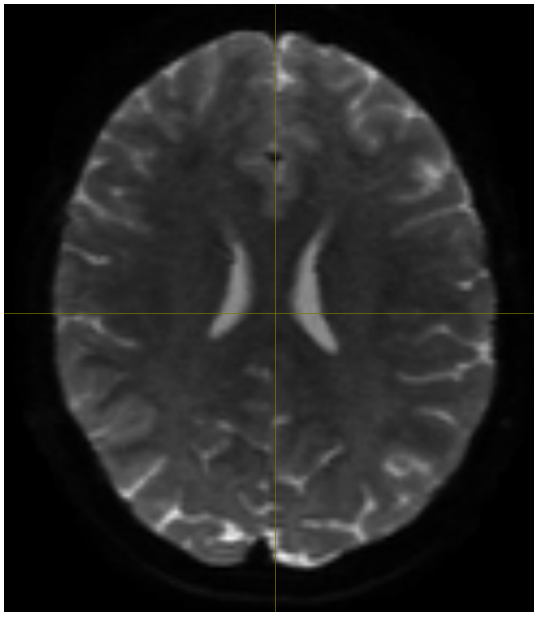

FIGURE 2.9: Diffusional Weighted MRI image

2.3.3 Pre-processing Diffusional MRI data

The MRI image data gets induced with various artefacts and noise during decoding time. The pre-processing of MRI image data is important to retrieve the correct information about the brain.

2.3.3.1 Denoising

The first step in DWI-MRI image processing is image denoising. The type of noise present in DWI-MRI data is thermal noise. It is very important to remove thermal

noise at the very beginning so that other processing steps such as motion and distortion correction in their smoothing and interpolation steps can not alter noise characteristics. The denoising process follows the method defined by Veraart et al. (2016), to remove noise-only principal components, thereby enabling signal-to-noise ratio enhancements. This yields parameter maps of improved quality for visual, quantitative, and statistical interpretation.

2.3.3.2 Distortion correction

In this step, the DWI-MRI image is processed to correct the three types of distortion captured during MRI image acquisition time: the motion distortion (occur due to motion of the patient), the eddy-current distortion (electrical currents induced by a changing magnetic field) and susceptibility induced distortion (A magnetic susceptibility artifact is caused by the presence of an object in the FOV with a higher or lower magnetic susceptibility).

2.3.4 Constrained Spherical Deconvolution (CSD)

Spherical deconvolution (Tournier et al., 2004) is a technique that presents information about the distributions of brain white matter fibres in regions containing multiple fibre orientations. All white matter bundles in the brain share the same diffusion characteristics. Thus, any difference in diffusion anisotropy is mainly for partial volume effects. The fibre orientation density function (ODF) gives the distribution of fibre orientations within the voxel and the response function is the diffusion-weighted attenuation profile for a typical fibre bundle in a single voxel. The attenuation of the diffusion-weighted signal measured over the surface of a sphere is described as the convolution over the sphere of a response function with the fibre orientation density function (ODF). Thus the spherical deconvolution method is used to obtain the fibre ODF in a voxel (Tournier et al., 2004). The spherical deconvolution method is performed by the simple matrix inversion method. If low pass filtering is not done on the DWI-MRI signal to remove the noise in the signal, then it will generate a spurious negative lobe in reconstructed FODs. This is physically not possible. This phenomenon is used by adding a constraint on the presence of these negative values in the FOD to remove the noise artifacts without filtering out the high angular frequencies. This process is referred to as constrained spherical deconvolution (CSD) (Tournier et al., 2007).

2.3.5 Anatomical Constrained Tractography (ACT)

Anatomical Constrained tractography is about defining an accurate delineation for diffusion MRI streamlines for determining the propagation and termination of the streamlines. This is implemented by segmenting the anatomical image into a five tissue type image (5TT). In that image, the volumes of tissue types appear in the order of, Cortical gray matter, sub-cortical gray matter, white matter, CSF, Pathological tissue. The pathological tissue type is used optionally where the architecture of the tissue present is not defined. Thus information available from anatomical image segmentation, and the known properties of the neuronal axons being reconstructed, biologically realistic priors are applied to the streamlines generation and known as Anatomical Constrained tractography (Smith et al., 2012).

2.3.6 Spherical-deconvolution Informed Filtering of Tractograms (SIFT)

SIFT is an algorithm for filtering more biologically accurate streamlines from whole-brain fibre-tracking data sets. It follows the approach to find a subset of streamlines that best matches the diffusion signal. This method uses the results of spherical deconvolution of the diffusion signal to determine which streamlines to remove from the data set, hence the acronym SIFT: spherical-deconvolution informed filtering of tractograms. The algorithm first assigns some white matter axon volume per unit length to each streamline in the reconstruction, construct the fibre orientation distributions and compare them. Streamlines that are detrimental are removed and more plausible streamlines are generated (Smith et al., 2013).

2.3.7 Structural Connectome

In this step, the filtered streamlines are mapped to the nodes of the parcellated structural image to construct the structural connectome matrix. The method either uses a simple voxel lookup value at each streamline endpoint, or performs a radial search from each streamline endpoint to locate the nearest node, or traverses from each streamline endpoint inwards along the streamline, in search of the last node traversed by the streamline or project the streamline forwards from the endpoint in search of a parcellation node voxel or assign the streamline to all nodes it intersects along its length.

2.3.8 White Matter tracts and its geometrical properties

The white matter is basically the myelinated axons tracts of the central nervous system (CNS). The main job of the tracts is to carry nerve impulses between neurons. The

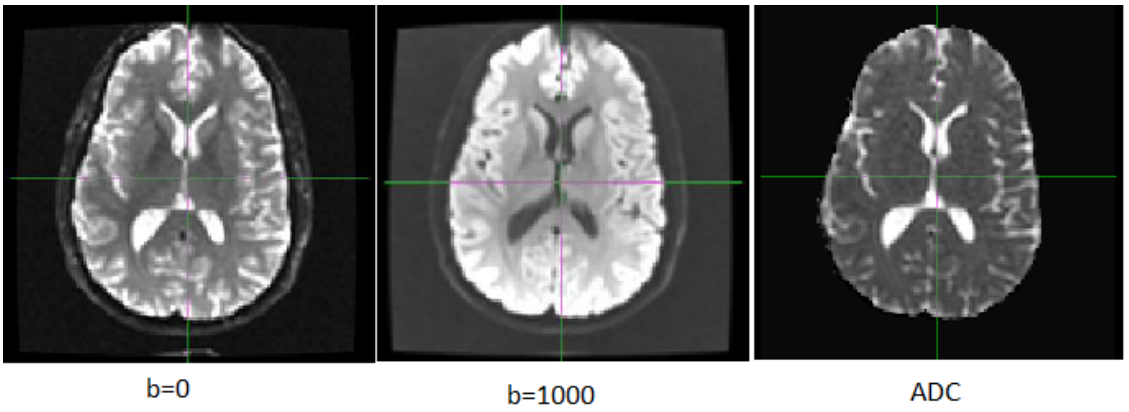

FIGURE 2.10: ADC- Apparent Diffusion Coefficient from diffusion MRI image

white matter is white because of the fatty substance that covers the nerve bundles (axons). This fatty substance surrounding the long nerve fibres acts as electrical insulation and stops neurotransmitters from dissipating while carrying the signal. So the myelin is an important factor for transferring the message from one place to another. Figure 2.11 shows the white matter structure of the human brain taken by diffusional MRI (dMRI). The voxels within tracts are colour coded according to their FA values (i.e., blue, low anisotropy; and red, high anisotropy. Fractional anisotropy (FA) is a scalar value between zero and one that describes the degree of anisotropy of a diffusion process. A value of zero means the diffusion is isotropic. Advanced neuroimaging techniques such as diffusion tensor imaging (DTI), diffusion MRI Tractography are used to study brain white matter by using magnetic resonance imaging (MRI) brain images (Hagmann et al., 2007; Tournier et al., 2011).

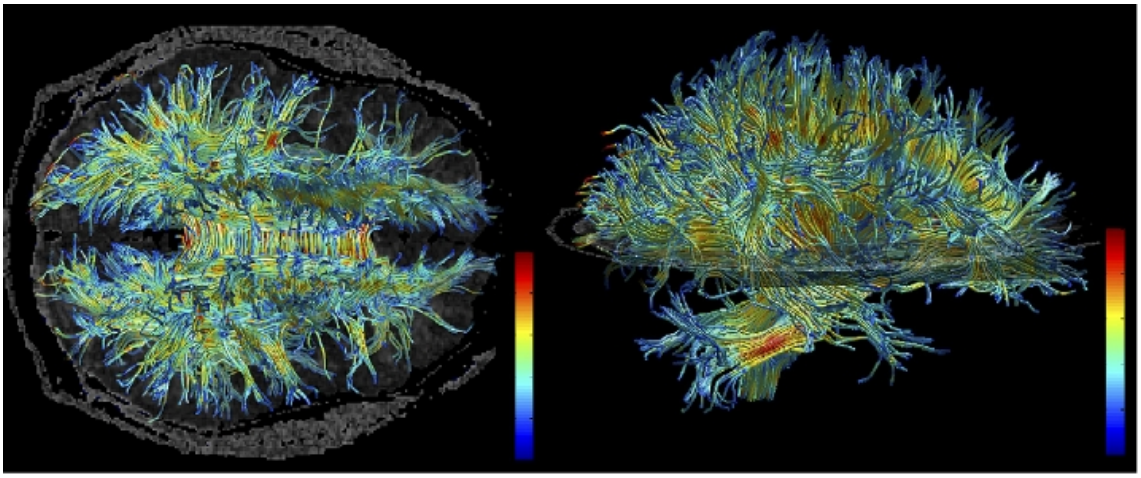

FIGURE 2.11: White matter structure of human brain (from MRI)

2.3.8.1 Apparent Fibre density (AFD) of white matter tracks

The spherical deconvolution is a method that provides an estimate of the distribution of fibres within imaging voxel of diffusion-weighted magnetic resonance images (Tournier et al., 2007). The method as shown in Figure 2.12 is based on the assumption that the

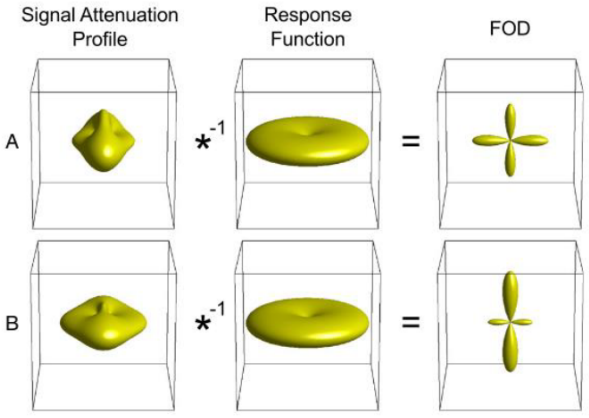

FIGURE 2.12: Calculating FOD

measured high angular resolution diffusion signal can be expressed as the convolution over spherical coordinates of a single canonical fibre response function with the fibre orientation distribution (FOD). The response function is assumed to correspond to the DWI signal (as a function of orientation) that would be measured for a voxel with a single fibre population oriented along the z-axis (Tournier et al., 2004). The FOD can then be estimated by performing the reverse spherical deconvolution operation using spherical and rotational harmonics. FOD is a continuous distribution representing the partial volume of the underlying fibres as a function of orientation (Tournier et al., 2004). AFD is a relative measure of the intra-axonal volume occupied by fibres aligned with a direction. It is based on the assumption that intra-axonal water is restricted in the radial direction and the radial DW signal emanating from the intra-axonal compartment is independent of axonal diameter and hence proportional to the intra-axonal water content. Figure 2.13 shows (A) Coherently ordered axons within a single imaging voxel. (B) The perpendicular plane of fibres in A, illustrating the intra-cellular (restricted diffusion) and extra-cellular compartments. (C) Expected attenuated dMRI signal profile at high b-values ($>$ 3000s/mm2). The magnitude of the radial dMRI signal is approximately proportional to the volume of the intracellular compartment (green in B). (D) The amplitude of the FOD (Apparent Fibre Density) along a given orientation is proportional to the magnitude of the dMRI signal in the perpendicular (radial) plane (as shown in C), and hence to the intra-axonal volume along with the corresponding orientation.

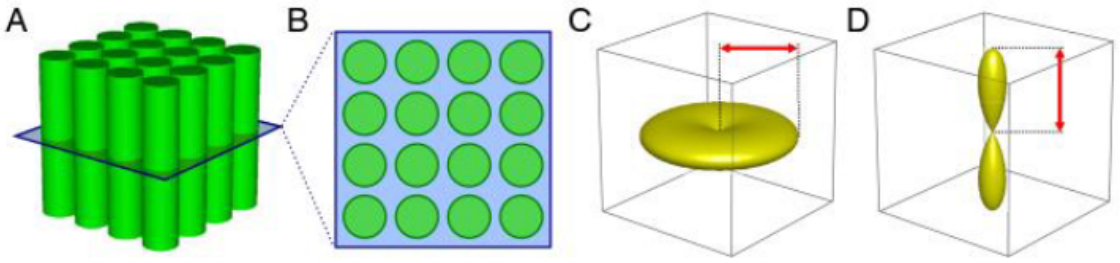

FIGURE 2.13: Apparent Fibre Density overview (Raffelt et al., 2012)

2.3.8.2 Fibre-bundle cross section (FC) and Fibre density and cross-section (FDC) of white matter tracks

While fibre density gives the number of fibre per bundle per voxel, to obtain a more complete measure related to the total number of white matter axons, information from both within-voxel microscopic fibre density and macroscopic morphology must be combined (Raffelt et al., 2017). Fibre-bundle cross-section (FC) gives the calibre of a fibre bundle. It is another property that factors into the bundles total intra-axonal space across its full cross-sectional extent and hence influence its total capacity to carry information. To obtain a more comprehensive measure related to the total intra-axonal volume within a pathway, both Fibre bundle (FD), Fibre cross-section (FC) values need to be taken into account and ideally be combined. Therefore, FDC= FD X FC.

2.4 Neuronal dynamics

Neurons are the fundamental unit of communication in the nervous system. Neurons communicate with each other in the neural network using pulse frequency modulation of spikes or action potentials (Weiss, 1996). The flow of ions in the cell is controlled by gated ion channels present in neuron cell membrane (Izhikevich, 2007). The main components of a Neuron are dendrites, soma or nucleus and axon as shown in figure 2.14. The central processing unit of the neuron is the soma. It produces enzymes, proteins,

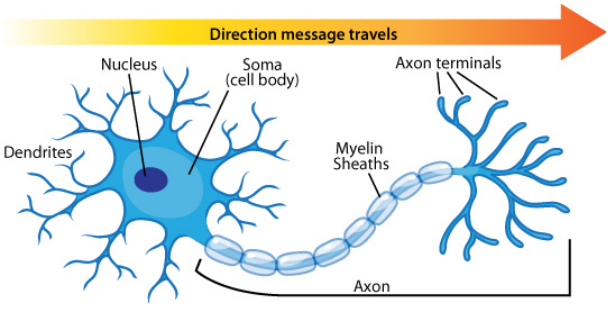

FIGURE 2.14: Anatomy of a Neuron

and other essential cell chemicals. The receiving unit of a neuron are dendrites that receive both excitatory and inhibitory synaptic inputs from presynaptic terminals. An excitatory synaptic input helps to increase the membrane potential and brings it closer to the threshold membrane potential where an inhibitory synaptic input decreases it. When the potential across the neuron membrane reaches the threshold potential, an action potential or spike is generated (Andrew, 2003). The Figure 2.15 shows the description of an action potential wave: (1) stimulus starts the rapid change in membrane potential, (2) depolarization: influx of sodium ions, (3) repolarization: sodium channel inactivation, outflux of potassium ions, (4) hyperpolarization: lowered membrane potential caused by the efflux of potassium ions, closing of the potassium channels, (5) resting state: membrane potential at resting state and no ions exchange. A single presynaptic cell does not possess enough electrical strength to produce an action potential in a postsynaptic neuron. The integration of many excitatory postsynaptic potentials (EPSPs) both spatially or temporally, generate an action potential. The axon hillock which connects the neuron to the axon; has the largest concentration of voltage-gated ion channels and therefore has the lowest membrane threshold potential (Kandel et al., 2000). Temporal and spatial inputs are integrated at the axon hillock to generate action

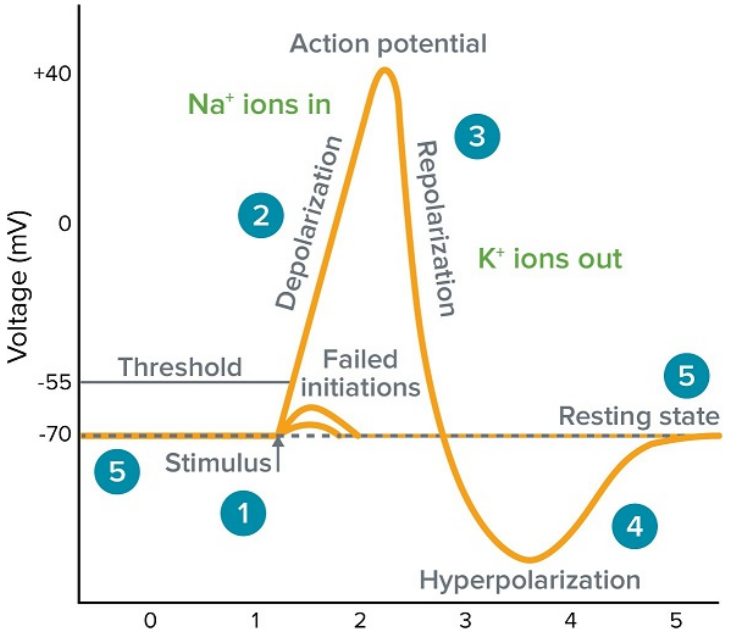

FIGURE 2.15: An action potential curve

potentials that propagate down the axon to the terminal buttons (Hill and Blagburn, 2001). The myelin sheath in the axon isolates the inside of the neuron from the excitatory extracellular fluid. It has a high electrical resistance, which decreases conduction efficiency and velocity. The action potential generated at the axon hillock passively decays. The action potential would attenuate to 50% of its peak value in about 20mm of axonal length if it were not for the Nodes of Ranvier (Weiss, 1996). The Nodes of

Ranvier exposes the axon directly to the extracellular fluid, which contains ions necessary to regenerate an action potential. They are uniformly spaced in an axon. The Nodes of Ranvier have a large concentration of sodium channels that can be excited once the action potential reaches them. The myelin sheath and the Nodes of Ranvier work together to propagate the action potential in a myelinated neuron. It looks as though the electrical signal is leaping from node to node (Stephanova and Bostock, 1995). This kind of leaping propagation of the action potential from one node to another is called saltatory conduction.

2.4.1 Ion channels

The plasma membrane of neuron cells is built up with lipid fat and protein structures. The complex structure of proteins creates the ion channels across the membrane which regulates the flow of ions. The main ion channels across the membrane are sodium and potassium channels. Hodgkin and Huxley in their electric circuit described the conductance of ion channels to changes in membrane potential using Ohm's law (V=IR; V=I/G; V=Voltage measured across the conductor, I=Current through the conductor, R=Resistance of the conductor, G=Conductance). The conductance across the cell membrane is the summation of all ion channel conductance. The calculation of the conductance is accomplished by using an equivalent circuit model using Ohm's law. The current I_x where x is the conducting ion is a function of membrane conductance g_x, the voltage V_m, being applied to the membrane and the battery potential E_x.

$$I_k = g_k(V_M - E_k) \tag{2.1}$$

$$g_k = I_k/(V_k - E_k) \tag{2.2}$$

$$I_{Na} = g_{Na}(V_M - E_{Na}) \tag{2.3}$$

$$g_{Na} = I_{Na}/(V_M - E_{Na}) \tag{2.4}$$

Membrane conductance for sodium(Na) and potassium(K) was calculated as a function of membrane potential, where both the voltage and current are known.

Conductance of potassium depended on the maximum potassium conductance $\overline{G_k}$, and a gating variable n.

$$G_k = \overline{G_k}n^4 \tag{2.5}$$

where $\overline{G_k}$ is known constant. The gating variable's dependence on voltage and time can be put into two forms. One such form is dependent on the rate constants α_n and β_n.

$$\frac{dn}{dt} = \alpha_n(1-n) - \beta_n n \tag{2.6}$$

The other form is written in terms of a time constant τ_n and the final value n_∞.

$$\tau_n \frac{dn}{dt} + n = n_\infty \tag{2.7}$$

$$n_\infty = \frac{\alpha_n}{(\alpha_n + \beta_n)} \tag{2.8}$$

The time and rate constants for the potassium channel n gate, τ_n, α_n and β_n are all functions of the membrane potential. Hodgkin and Huxley characterize the rate and time constants empirically using data collected from voltage clamp experiments.

$$\alpha_n = \frac{-0.01(V_M + 50)}{e^{-0.1(V_M+50)} - 1} \tag{2.9}$$

$$\beta_n = 0.125e^{-0.0125(V_M+60)} \tag{2.10}$$

$$\tau_n = \frac{1}{\alpha_n + \beta_n} \tag{2.11}$$

The membrane potential V_M , is expressed in mV, and the α and β quantities are expressed in ms^{-1}. Sodium channel conductance is dependent on the maximum sodium conductance $\overline{G_{Na}}$ as well as the activation and inactivation gate, m and h respectively [34].

$$G_N a = \overline{G_{Na}} m^3 h \tag{2.12}$$

The conductance equation for sodium is more complicated and requires two gating variables. $\overline{G_{Na}}$ is a measured constant, and the m and h gating variables are both described using a first-order differential equation. The combined action of m and h variables controls the sodium channels.

$$\frac{dm}{dt} = \alpha_m(1-m) - \beta_m m \tag{2.13}$$

$$\frac{dh}{dt} = \alpha_h(1-h) - \beta_h h \tag{2.14}$$

Using a time constant τ_m, τ_h and the final values m_∞ and h_∞

$$\tau_m \frac{dm}{dt} + m = m_\infty \tag{2.15}$$

$$\tau_h \frac{dh}{dt} + h = h_\infty \tag{2.16}$$

with

$$m_\infty = \frac{\alpha_m}{\alpha_m + \beta_m} \tag{2.17}$$

$$h_\infty = \frac{\alpha_h}{\alpha_h + \beta_h} \tag{2.18}$$

All above are functions of membrane potential.

$$\alpha_m = \frac{-0.1(V_m + 35)}{e^{-0.1(V_m+35)} - 1} \tag{2.19}$$

$$\beta_m = 4e^{-\frac{0.0125(V_m+60)}{18}} \tag{2.20}$$

$$\tau_m = \frac{1}{\alpha_m + \beta_m} \tag{2.21}$$

$$\alpha_h = 0.07e^{-0.05(V_m+60)} \tag{2.22}$$

$$\beta_h = \frac{1}{1 + e^{-0.1(V_m+30)}} \tag{2.23}$$

$$\tau_h = \frac{1}{\alpha_h + \beta_h} \tag{2.24}$$

The m gate increases conduction, and the h gate decreases conduction with the increase in membrane activation (Weiss, 1996). The leakage channel in a neuron model represents other conducting ions not represented by the potassium or sodium channels.

2.4.2 Nernst potential or equilibrium potential

The two forces that drive each ion species through the membrane channel are concentration and electric potential gradients. First, the ion diffuses down the concentration gradient creating positive and negative charges accumulating on the opposite sides of the membrane surface. This generates an electric potential gradient across the membrane-called membrane voltage. This membrane voltage slows the diffusion of ions as ions are attracted to the opposite side and repelled from the same side. This leads to an equilibrium state where concentration gradient and electric potential gradient exert equal and opposite forces that counterbalance each other. The value of such an equilibrium potential depends on the ionic species and is given by the Nernst equation (Izhikevich, 2007):

$$E_x = \frac{RT}{zF} \log \frac{c_X^o}{c_X^i} \tag{2.25}$$

Where c_X is the concentration of the ions inside and outside of the cell, T is the temperature of the environment in kelvin (K°=273.16+C°), and z is the valence of the ion (z=1 for Na^+ and K^+; z = -1 for Cl^- ; and z=2 for Ca^{2+}), R is the gas constant in joules per kelvin per mole (8,315 mJ/K°.Mol) and F is the Faraday's constant coulombs per mole (96,480 coulombs/Mol). Nernst equilibrium potentials in a typical mammalian neuron are summarized in table 2.1.

Equilibrium Potentials	
Na^+	61mV
K^+	-90mV
Cl^-	-89mV
Ca^{2+}	136mV

Table 2.1: Nernst equilibrium potentials in a typical mammalian neuron

2.4.3 Resting potentials

Most membranes contain a diversity of channels. The value of the membrane potentials at which all inward and outward currents balance each other so that net membrane current is zero corresponds to the resting membrane potential (Izhikevich, 2007). So the resting membrane potential is the stable state with regards to diffusion and electrical gradients. The Goldman equation can be used to calculate the resting membrane potential. To write the Goldman equation for a neuron membrane permeable to only potassium and sodium, the intracellular and extracellular concentrations of the ions are required, as well the relative permeability of sodium to potassium.

2.4.4 Hodgkin-Huxley neuron model

In 1950, Hodgkin-Huxley performed an experiment on giant squid and derived the equations for the action potential. The schematic diagram of Hodgkin-huxley model is shown in Figure 2.16. It is the lipid fat and protein structures that built up the plasma membrane of neuron cell. According to Hodgkin Huxley Model, the semipermeable cell membrane acts as a capacitor and divides the interior of the cell from the extracellular liquid. The complex structure of proteins creates the ion channels across the membrane which regulates the flow of ions inside to outside or vice versa. When an input current $I(t)$ is given into the cell, it may add the further charge on the capacitor, or pass through the channels in the cell membrane. Because of active ion transport through the cell membrane, the ion concentration in the extracellular liquid is different from that inside the cell. The Nernst potential generated by these ion concentration differences is represented by a dc voltage source. Putting the above considerations in a mathematical equation, equation 2.26 is derived.

$$I(t) = I_C(t) + \sum kI_k(t) \tag{2.26}$$

where the sum runs over all ion channels. From the definition of a capacity C, if Q is a charge and u the voltage then $C = Q/u$, then $dQ/dt = Cdu/dt$, so the charging current $IC = Cdu/dt$. Hence from above equation

$$C\frac{du}{dt} = -\sum kI_k(t) + I(t) \tag{2.27}$$

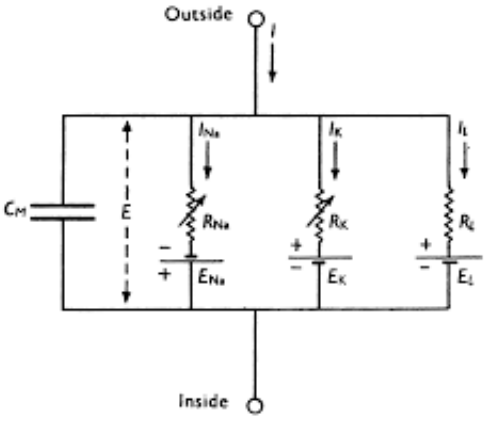

FIGURE 2.16: Hodgkin Huxley cell equivalent

So u is the voltage across the membrane and $\sum_k I_k$ is the sum of the ionic currents which pass through the cell membrane (Gerstner et al., 2014). By replacing the ionic currents in the equation, the total current I_M flowing through the membrane is:

$$I_M = C_M\frac{dV}{dt}+I_k+I_{Na}+I_L = C_M\frac{dV}{dt}+\overline{G_{Na}}m^3h(V-V_Na)+\overline{G_K}n^4(V-V_K)+\overline{G_L}(V-V_L) \tag{2.28}$$

where V is the membrane potential and C_M is the membrane capacitance; I_K and I_Na are the currents generated by the flow of the sodium and potassium ions through the channels and I_L is a leakage current with V_{Na}, V_K and V_L the corresponding equilibrium potentials. $\overline{G_{Na}}$, $\overline{G_K}$, $\overline{G_L}$ are the sodium, potassium and leakage maximum conductance through the membrane, respectively. The activation and inactivation parameters of the sodium channels m and h and the activation parameter of the potassium channel is n; which signified the fractions of open and closed channels:

$$\frac{dm}{dt} = \alpha_m(1-m) - \beta_m m \tag{2.29}$$

$$\frac{dh}{dt} = \alpha_h(1-h) - \beta_h h \tag{2.30}$$

$$\frac{dn}{dt} = \alpha_n(1-n) - \beta_n n \tag{2.31}$$

where α_m, β_m, α_h, β_h, α_n and β_n are the exponentially voltage dependent rate constants α_m, α_h and α_n determine the rate of ion transfer from outside to inside while β_m, β_h and β_n determine the transfer in the opposite direction as described by (Hodgkin and Huxley, 1952). The m gate increases conduction, and the h gate decreases conduction with the increase in membrane activation (Weiss, 1996). The leakage channel in a neuron model represents other conducting ions not represented by the potassium or sodium channels. The Table 2.2 describes the values for the maximum ionic conductance, for the leakage conductance and the corresponding equilibrium (reversal) potentials, as fetched from

literature (Hodgkin and Huxley, 1952).

Membrane Characteristics Parameters	
g_{Na}	120mS/cm2
g_K	36mS/cm2
g_L	0.3mS/cm2
V_{Na}	-115mV
V_K	12mV
V_L	-10.6mV

Table 2.2: Values of maximum ionic conductance, leakage conductance and the equilibrium (reversal) potentials

2.4.5 Core conductor theory and cable equation

The physical concept that provides the basis for a cable theory treatment of current and potential in neuronal core conductors is that: for nerve axons or dendrites, the resistance to electric current flow across the membrane is much greater than the core resistance and because of those relative resistances, electric current inside the core conductor tends to flow parallel to the cylinder axis for a considerable distance before significant fraction can leak out across the membrane (Rall, 2011). Cable theory in computational neuroscience was introduced by Professor William Thomson (later known as Lord Kelvin) in 1850 but the importance of cable theory in modelling the behaviour of axons began surfacing in the 1930s from work done by Cole, Curtis, Hodgkin, Sir Bernard Katz, Rushton, Tasaki and others. The aim behind cable theory is to provide a mathematical model to calculate electric current and voltage along passive neurites such as dendrites, axons. The core conductor model is built upon some assumptions as mentioned here. (1) The cell membrane is a cylindrical boundary that separates two conductors of electrical current, the intracellular and extracellular solutions. These conductors are assumed to be homogenous and ohmic. (2) All electrical variables have cylindrical symmetry. (3) Ohms law of voltage and current is sufficient to describe the system therefore electromagnetic effects are considered negligible. (4) Current in the inner and outer conductors flow in the longitudinal directions only and current through the membrane is through the radial direction only. (5) At a given longitudinal position the inner and outer conductors are equipotential. Therefore, the only change in membrane potential is in the longitudinal direction.

Figure 2.18 shows a neuron's dendritic membrane where A. shows a sketch of the neuron, B. shows a cylindrical representation of the dendrite, C. shows an electrical cable model for this length of the cylinder. Each of the sub-cylinders labelled 1, 2, and 3 is assumed to be an isopotential patch of membrane. The membrane of each sub-cylinder is represented by a parallel combination of membrane capacitance $cm\Delta x$ and an unspecified circuit for

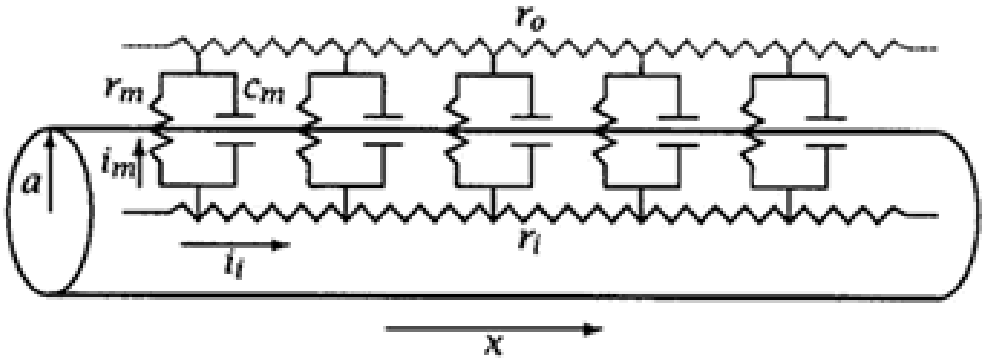

FIGURE 2.17: Cable model of axon (Johnston and Wu, 1994)

the ionic conductance in the membrane, represented by a box. The total current through a membrane patch is $Im(x)\Delta x$. Note that the membrane current varies with distance x down the cylinder. Im and cm are membrane current and capacitance per unit length of the cylinder so that multiplying by Δx gives the total current and capacitance in a sub-cylinder. The membrane of each sub-cylinder is represented by a parallel combination of membrane capacitance $cm\Delta x$ and an unspecified circuit for the ionic conductance in the membrane, represented by a box. The total current through a membrane patch is $I_m(x)x$.
The membrane current is denoted by I_m.
The capacitance per unit length of cylinder is C_m.
The membrane potentials inside the cell $V_i(x)$ and outside the cell $V_e(x)$.
The potentials vary with distance down the cylinder. The membrane potential is $V_i(x) - V_e(x)$
The total current flowing down the interior of the cylinder is $I_i(x)$
The total current flowing parallel to the cylinder in the extracellular space $I_e x$
The resistance of the solutions inside the cylinder between the center of one sub-cylinder and the center of the next is $r_i\Delta x$ The resistance in the extracellular space between the center of two sub-cylinders is $r_e\Delta x$ The resistances per unit length of cylinder are r_i and r_e.
Ohms law for current flow in the intracellular and extracellular spaces gives:

$$V_i(x) - V_i(x + \Delta x) = I_i(x)r_i\Delta x V_e(x) - V_e(x + \Delta x) = I_e(x)r_e\Delta x \tag{2.32}$$

By rearranging and taking the limit as Δx goes to 0,

$$\lim \frac{V_i(x + \Delta x) - V_i(x)}{\Delta x} = \frac{\delta V_i}{\delta x} = -r_i I_i(x) \tag{2.33}$$

$$\frac{\delta V_e}{\delta x} = -r_e I_e(x) \tag{2.34}$$

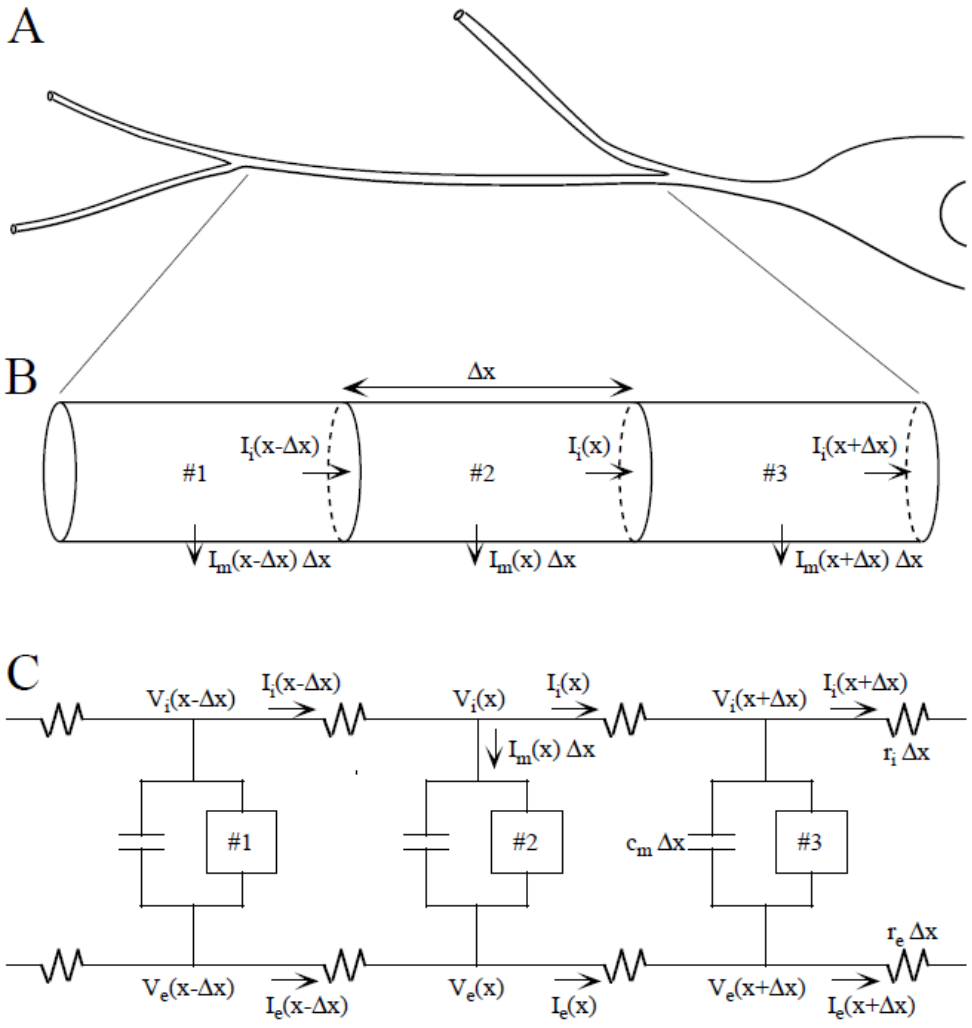

FIGURE 2.18: A Sketch of a portion of the dendritic tree of a neuron emerging from the soma at right. B Portion of a secondary dendrite divided into three sub-cylinders. The axial current Ii and the membrane current Im are shown next to the arrows. C Discrete electrical model for the three sub-cylinders.

By the law of conservation, current at the intracellular and extracellular nodes gives:

$$I_i(x-\Delta x)-I_i(x) = I_m(x)\Delta x or \frac{\delta l_i}{\delta x} = -I_m(x)I_e(x-\Delta x)-I_e(x) = -I_m(x)\Delta x or \frac{\delta l_e}{\delta x} = I_m(x) \tag{2.35}$$

Defining the membrane potential as $V = V_i - V_e$

It allows the membrane current I_m to be written as the sum of the ionic current $I_ion(x, V, t)$ through the box and the current through the membrane capacitance:

$$I_m(x)\Delta x = I_{ion}(x, V, t)\Delta x + C_m(x)\Delta x \frac{\delta V}{\delta t} \tag{2.36}$$

I_m, I_{ion} are the ionic current per unit length of membrane cylinder.

Differentiating and subtracting 2.33 and substituting 2.34 allows the following relationship between membrane potential and membrane current to be written:

$$\frac{\delta^2 V}{\delta x^2} = \frac{\delta^2 (V_i - V_e)}{\delta x^2} = -r_i \frac{\delta l_i}{\delta x} + r_e \frac{\delta l_e}{\delta x} = (r_i + r_e) I_m \tag{2.37}$$

Substituting 2.36 gives the nonlinear cable equation:

$$\frac{1}{r_i + r_e} \frac{\delta^2 V}{\delta x^2} = C_m \frac{\delta V}{\delta x} + I_i on \tag{2.38}$$

2.38 models the distribution of membrane potential in a membrane cylinder.

2.4.6 Axonal functions

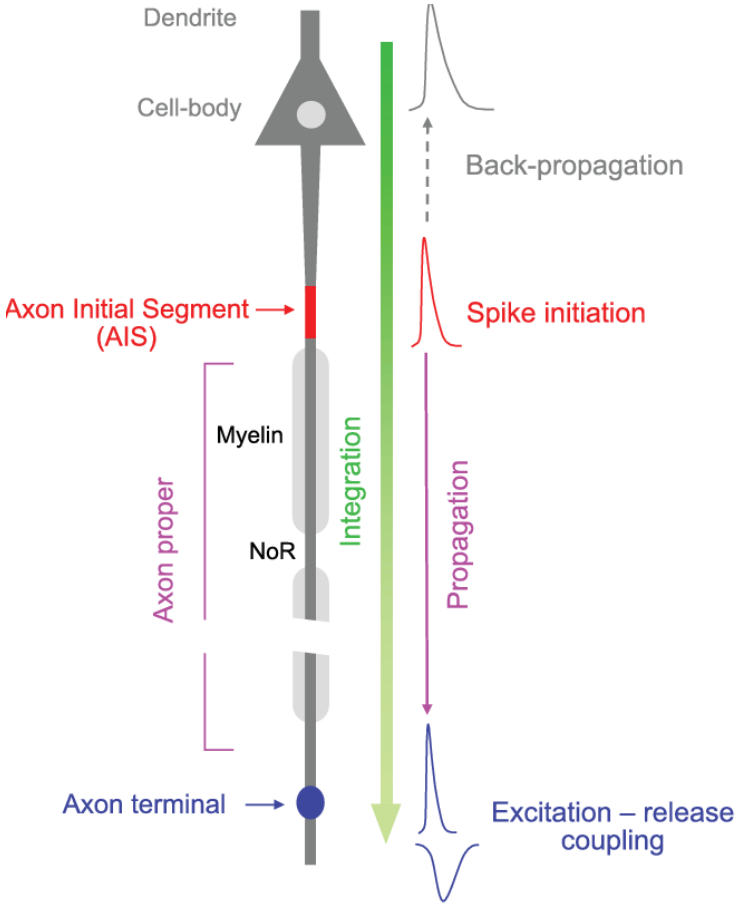

FIGURE 2.19: Summary of axonal functions (Debanne et al., 2011)

Figure 2.19 depicts the summary of axonal functions (Debanne et al., 2011). A pyramidal neuron is schematized with its different compartments. Four major functions of the axon are illustrated (i.e., spike initiation, spike propagation, excitation release coupling, and integration). A spike initiates in the axon initial segment (AIS) and propagates towards

the terminal where the neurotransmitter is released. In addition, electrical signals generated in the somatodendritic compartment are integrated along the axon to influence spike duration and neurotransmitter release (green arrow). The other important part of the axon is myelin which makes the information transmission faster through the axon. It is a concentrically laminated membrane structure surrounding an axon around which lamellae (or cellular protrusions) repeat radially at a period of about 12 nm (Waxman, 1995). Different glial cell types make myelin in a different manner, depending on the location. In PNS nerves Schwann cells make myelin, and in CNS oligodendrocytes. Where in the PNS, one Schwann cell forms a single myelin sheath, in the CNS, the oligodendrocyte sends cell processes to myelinate multiple segments on many axons. The basic myelin sheath arrangement and the electrophysiological characteristics are essentially the same, though there are several molecular or morphological differences between nerve fibres in the PNS and CNS (Susuki, 2010). It has been identified that axonal signalling regulates myelination in the PNS axon, but it was unclear how myelination is regulated in the CNS (Susuki, 2010). But, now there are more kinds of literature available on how the activity is related to myelination. Kaiser (2020) in his book has described that concerning the role of neural activity, optogenetic stimulation of projection neurons of the mouse motor cortex increases proliferation of oligodendrocyte progenitor cells and differentiation of oligodendrocytes in both cortex and subcortical white matter. As a result, the thickness of the myelin sheath is increased along the whole length of axons of stimulated neurons, not just near the stimulation site (Gibson et al., 2014). Such an interplay between activation and myelination also seems to occur in humans in both adults and children. Diffusion imaging studies showed changed fractional anisotropy of language-related fibre tracts in bilingual compared to monolingual children (Mohades et al., 2012). Similar changes were observed for adults who learned Chinese as a second language (Schlegel et al., 2012; Hosoda et al., 2013), suggesting that activity-related changes in myelination can occur throughout the life span right into adulthood. Fibre tract changes were also observed after learning new motor skills such as piano playing or juggling (Bengtsson et al., 2005; Scholz et al., 2009).

About myelination, it is not that all axons are myelinated but in the CNS, almost all axons with diameters greater than 0.2 m are myelinated. The ratio between axon diameter and that of the total nerve fibre (axon and myelin) is 0.6-0.7, a ratio that is well maintained regardless of the axon calibre. Between two adjacent myelin segments, there are approximately $1\mu m$ long gaps called nodes of Ranvier where the axon is exposed to the extracellular space. Suminaite et al. (2019) illustrated emerging evidence that the myelin sheath itself has rich physiology capable of influencing axonal physiology and local adaptive mechanisms might influence sheath length and in turn conduction. In past, in-vivo voltage-clamp experiments reported filter like characteristics FMN axon (Schumann et al., 1983; Nonner et al., 1978).

2.5 Saltatory conduction in a myelinated axon

Since an axon can be myelinated or unmyelinated, there are two ways the action potential propagates through the axon: saltatory conduction where nerve signal leaps through the myelinated axon, and continuous conduction for unmyelinated axon. Saltatory conduction of the action potential in the myelin fibre is well studied. This process is outlined as the charge passively spreading to the next node of Ranvier to depolarize it to a threshold which will then trigger an action potential in this region which will then passively spread to the next node and so on.

Saltatory conduction provides one advantage over conduction that occurs along an axon without myelin sheaths. This is that the increased speed afforded by this mode of conduction assures faster interaction between neurons. On the other hand, depending on the average firing rate of the neuron, calculations show that the energetic cost of maintaining the resting potential of oligodendrocytes can outweigh the energy savings of action potentials. So, axon myelination does not necessarily save energy (Harris and Attwell (2012)).

2.6 Ephaptic coupling between myelinated axons

Ephaptic coupling is a form of communication within the nervous system different from direct communications such as electrical synapses and chemical synapses. Ephaptic coupling refers to the coupling of adjacent (touching) nerve fibres either caused by the exchange of ions between the cells, or as a result of local electric fields. Ephaptic coupling between the two adjacent nerves is not sufficient to stimulate an action potential in the resting nerve but it can influence the synchronization and timing of action potential firing in neurons. Myelination is thought to inhibit ephaptic interactions.

2.6.1 Effect of coupling on excitation/inhibition of action potential in neighbouring neurons

Arvanitaki (1942) first introduce the term 'ephapse' to describe the coupling and to distinguish it from synaptic communications in the neuron(s). According to Katz and Schmitt (1940) ephaptic coupling between the two adjacent nerves is insufficient to stimulate an action potential in the resting nerve. Katz and Schmitt (1940) in their experiment, demonstrated that maximum depolarization in neighbouring nerve was approximately 20% of the threshold potential. Ramon and Moore (1978) in their experiment demonstrated that by modulating conditions such as increasing extracellular resistance by changing the medium or by lowering threshold voltage by increasing calcium concentration in the cellular fluid, action potential was possible to generate in

the neighbouring nerve. According to some study ephaptic coupling can inhibit action potential propagation in the neighbouring neuron.

2.6.2 Effect of coupling on the propagation of action potential in synchronized neurons

Research has shown that ephaptic coupling has an effect on synchronization and timing of action potentials in neurons (Binczak et al., 2001; Scott, 1975). In the adjacent fibres if simultaneous stimulation is performed the impulse slows down while propagating to the next node. This happens because both fibres are limited to exchange ions solely with the interstitial fluid (increasing the resistance of the nerve). Slightly offset impulses (conduction velocities differing by less than 10%) are able to exchange ions constructively and the action potentials propagate slightly out of phase at the same velocity.

Shneider and Pekker (2015) in their work, have shown a mechanism similar to saltatory conduction for modelling coupling effect. They calculated the dynamics of current and voltage near to the vicinity of the node and scaled, up to what distance coupling can be possible. More recent research, however, has focused on the more general case of electric fields that affect a variety of neurons. It has been observed that local field potentials in cortical neurons can serve to synchronize neuronal activity (Anastassiou et al., 2011)

2.7 Axon bundle physiology

Axons are the slender, electrically excitable, cable-like extensions of nerve cells that form the nerves and tracts that relay information between neurons within the nervous system and between neurons and peripheral target tissues in highly regulated manners. In the central and peripheral nervous systems, most axons over a critical diameter are enwrapped by myelin, which reduces internodal membrane capacitance and facilitates rapid conduction of electrical impulses. Myelin which covers the vast majority of the axonal surface, influencing the axon's physical shape, the localisation of molecules on its membrane and the composition of the extracellular fluid (in the periaxonal space) that immerses it, is produced by oligodendrocytes and Schwann cells. In the CNS, myelinated axons are densely packed within white matter and the myelin sheaths of neighbouring fibres often directly touch as shown in top-left in Figure. 2.20. In PNS, the axons are bundled together into groups called fascicles, and each fascicle is wrapped in a layer of connective tissue called the perineurium as shown in bottom-left in Figure. 2.20. Top-right of Figure. 2.20 shows one cell in the CNS bundle and bottom-right of Figure. 2.20 shows one cell in the PNS bundle. In PNS, each axon is surrounded by a delicate endoneurium layer. A tough fibrous sheath called epineurium encloses all the fascicles to form the nerve. Here, we have used a number of different axon types both

from PNS and CNS axons to run the study as shown in Table 2.3. In Table 2.3, we also have shown the different parameter values such as inner diameter (D_{NR}), outer diameter (D_{IN}) and myelin length (L_{IN}), of the different axon types that we have used in this study. A schematic representation of different parameters of an axon is shown in Figure 2.21. Among PNS axons, here we have used data of Group A nerve fibre, which are found in both motor and sensory pathways. The Group A nerve fibres are again classified into four groups (I, II, III, IV) based on their physical features and signal conduction properties. We have used data of myelinated Group A nerve fibre I, II, III in our experiments. Then, in CNS axons we have used data of auditory nerve fibres SBC, GBCMed and GBCLat axons. The PNS axons data were taken from Tsubo and Kurokawa (2018). The CNS axons data were taken from Ford et al. (2015). The FMN data were taken from Binczak et al. (2001).

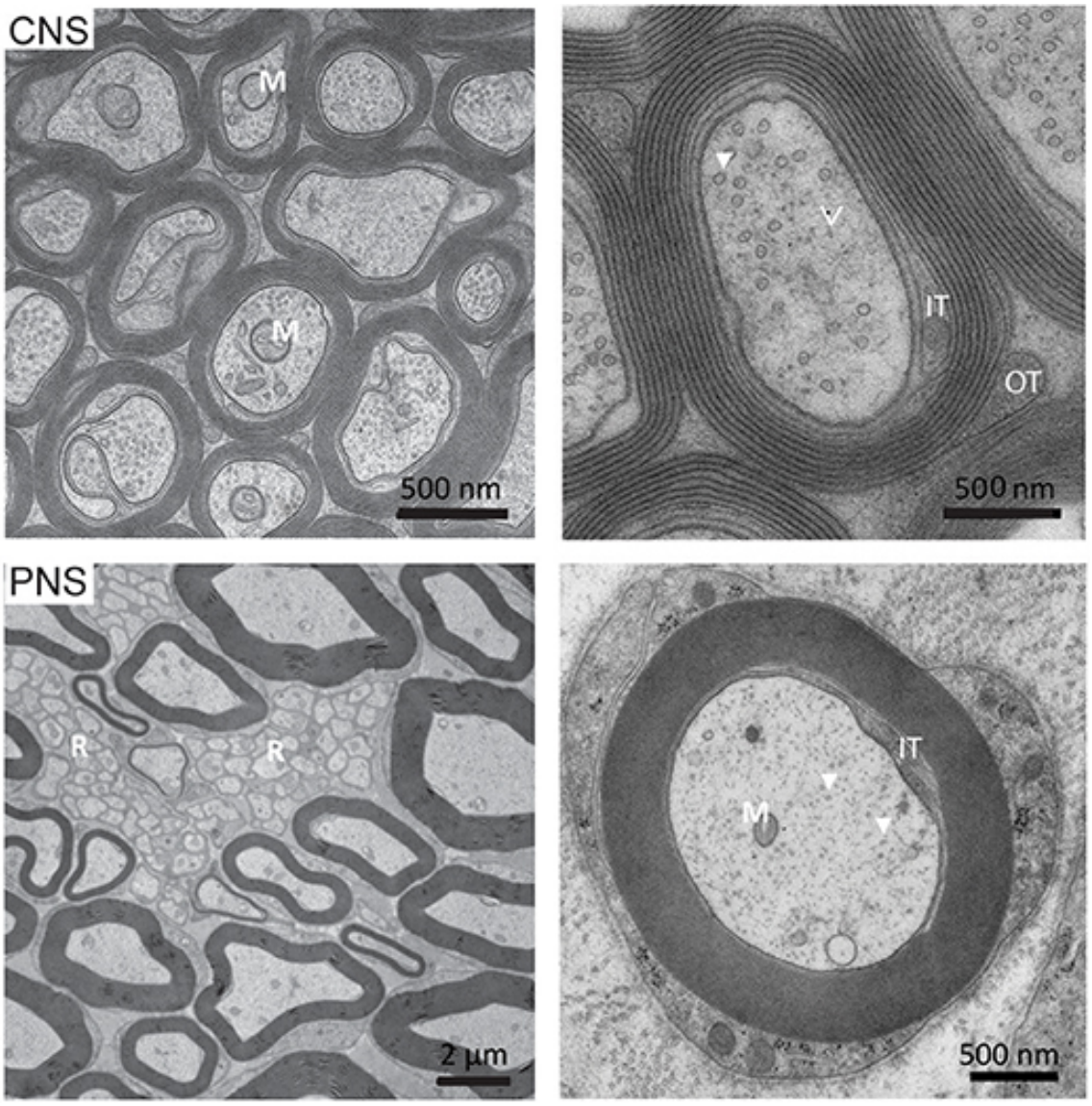

FIGURE 2.20: Ultrastructure of myelinated axons in the CNS and PNS

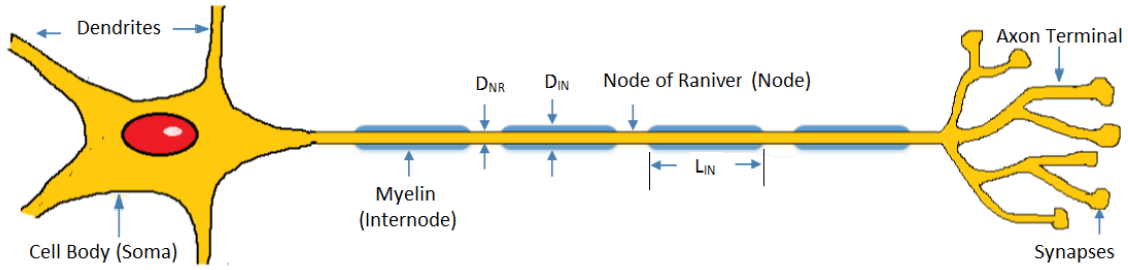

FIGURE 2.21: Schematic figure of an axon

2.8 Conclusions

The study of literature on myelinated axon shows that signal propagation through myelinated axon were studied mainly in time scale. Functional connectivity of the brain is defined by the phase correlation of neural signal in different frequency band. Our hypothesis is that studying the filter like properties of passing signal of certain frequency range while dampens the other frequency range depending upon its geometry, can correlates the disruptions of functional connectivity to underneath structural connectivity. Hence, we will be modelling phase-frequency characteristic of signal prorogation through single myelinated axon and then bundle of axons in our work.

Type	Name	Description	Inner diameter $D_{NR}(\mu m)$	Outer diameter $D_{IN}(\mu m)$	Myelin length $L_{IN}(mm)$
Frog Motor Nerve	FMN	FMN	10	14	2
I	$A\alpha$	PNS	20	28	2
I	$A\alpha$	PNS	13	18.2	2.3
II	$A\beta$	PNS	12	16.8	1.2
II	$A\beta$	PNS	6	8.4	0.6
III	$A\delta$	PNS	5	7	0.5
III	$A\delta$	PNS	1	1.4	0.1
Auditory nerve fibre	SBC	CNS	0.85	1.77	163.8
Auditory nerve fibre	GBCMed	CNS	1.50	3.20	238.6
Auditory nerve fibre	GBCLat	CNS	1.68	4.01	197.7

Table 2.3: Different axon types and their parameter values; Inner diameter is the internode axon diameter; Outer diameter is the internodal myelin diameter; Myelin length is the length of myelinated area between two consecutive nodes as shown in Figure 2.21

Chapter 3

Automated Tool development for Parcellation and Extraction of Structural Connectome and its Geometry

Brain connectivity is pivotal for neural function. Studies on brain connectivity have revealed that even if two brain areas are structurally connected they may not be functionally connected and vice versa (Honey et al., 2007; Hagmann et al., 2008; Honey et al., 2009; Rubinov et al., 2009). This signifies that there is selective propagation of the signal through the underlying physical connection of the brain. The functional connectivity of the brain is measured by phase correlation in time series signals between two areas of the brain. So characterizing the phase and frequency response of structural connectivity of the brain will lead to understanding the dynamics of signal propagation through a physical connection. To characterize the physical connection of the brain, we are analysing the MRI data. MRI is a medical imaging technique to generate images of the anatomy and the physiological process of the brain. In this chapter, we will be developing a toolchain for

- parcellating cortical surface into non-anatomical equal sized areas,
- constructing structural connectome, the structural connectivity,
- extracting geometrical properties of the axon bundle between two ROIs.

3.1 Brain parcellation

Brain connectivity is about the integration of spatially segregated brain regions. So delineating and defining the spatially segregated brain regions as nodes of the network is the first step of brain connectivity analysis (Rubinov and Sporns, 2010). Cortical parcellation serves the purpose by parcellation of the cortical and subcortical layers of the cortex in terms of some reference atlas and assigning to them a neuroanatomical label either automatically or manually resulting in complete labelling of cortical sulci and gyri (Fischl et al., 2004). The most commonly used method of defining network nodes is to register the brain to a standardized anatomical atlas based on the Brodmann areas. But this process of parcellation has limitations in many cases such as (1) developing brain of neonates, who have immature sulcation, (2) cases of cerebral reorganization after brain damage (neuroplasticity), (3) cases where young children undergoing treatment of intractable epilepsy, cortical plasticity and change of connectivity allow the contralateral hemisphere to assume the functions of the lost hemisphere without significant neurologic deficits, and (4) in the case of normal anatomy of the adult brain, where different subjects have different dominant hemispheres. In these cases, a non-anatomical equal-area cortical parcellation is more appropriate than anatomical parcellation. Typically Freesurfer (Fischl, 2012) is used for parcellation and reconstruction of brain surface from MRI images. But Freesurfer does not support parcellation of the cortical surface into non-anatomical equal-sized areas. Here we have developed a new methodology to perform parcellation of the cortical surface into equal-sized areas using Freesurfer as a tool. The structural MRI data, obtained from the human connectome databank (db.humanconnectome.org) has been used here.

3.1.1 Performing cortical surface partitioning using EQSP: Recursive Equal Zone Sphere Partitioning

The recursive zonal equal-area sphere partitioning (EQSP) given by Leopardi (2006) divides a spherical surface into equal-sized areas. We have used the EQSP algorithm to partition each hemisphere into equal-sized areas and make new atlas for cortical parcellation. While reconstructing cortical surface from MRI image Freesurfer turns each hemisphere into an inflated spherical surface. The spherically inflated original surface was used to perform the partitioning. The details of generating this spherically inflated surface using Freesurfer (Fischl, 2012) surface reconstruction pipeline are described in section Section 3.1.2. Each hemisphere was inflated to a spherical surface and then was used for partitioning. Here the cortical surface was parcellated into 80 equal nodes where 80 is an arbitrary number. The algorithm was designed in such a way that users can choose the number of nodes for their parcellation process. The steps to perform the partitioning are described below:

- First the vertex coordinates of the entire surface points of the inflated spherical surface of the hemisphere were obtained from Freesurfer pipeline.
- Next an array in Cartesian coordinates representing the 'centre' points of an EQ partition of the sphere into 40 regions was created using the EQSP algorithm.
- Then the centre points were scaled to the original surface. The scaling factor was obtained manually by comparing the original surface coordinates with the uni sphere surface coordinates. Here the scaling factor obtained was 100. The centre point of each partitioned region is shown in Figure 3.1.

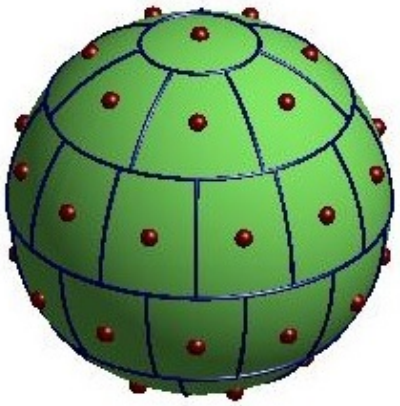

FIGURE 3.1: Centre point of each partitioned regions

- For each of the surface points the nearest centre point was found and was assigned to a label file that is defined for that centre point. Thus all the surface points of the cortical surface were assigned to the nearest centre point and listed in label files.
- Next, these label files were saved into a computer disk. Thus for each parcellated area, a label file was created. Two sets of label files were created as per parcellated areas for each hemisphere. A label is an integer value, or a name (depending on context) which can be associated with a vertex of a surface mesh, or with a voxel of an MRI volume, to indicate that it belongs to some region of interest.
- Next, all label files are put together to create the annotation file for each hemisphere following the steps of surface reconstruction in Freesurfer. The generated annotation files for left and right hemisphere is shown in Figure 3.2.
- Next cortical parcellation atlas file was generated using a probabilistic information algorithm given by Freesurfer by utilizing the annotated subjects.

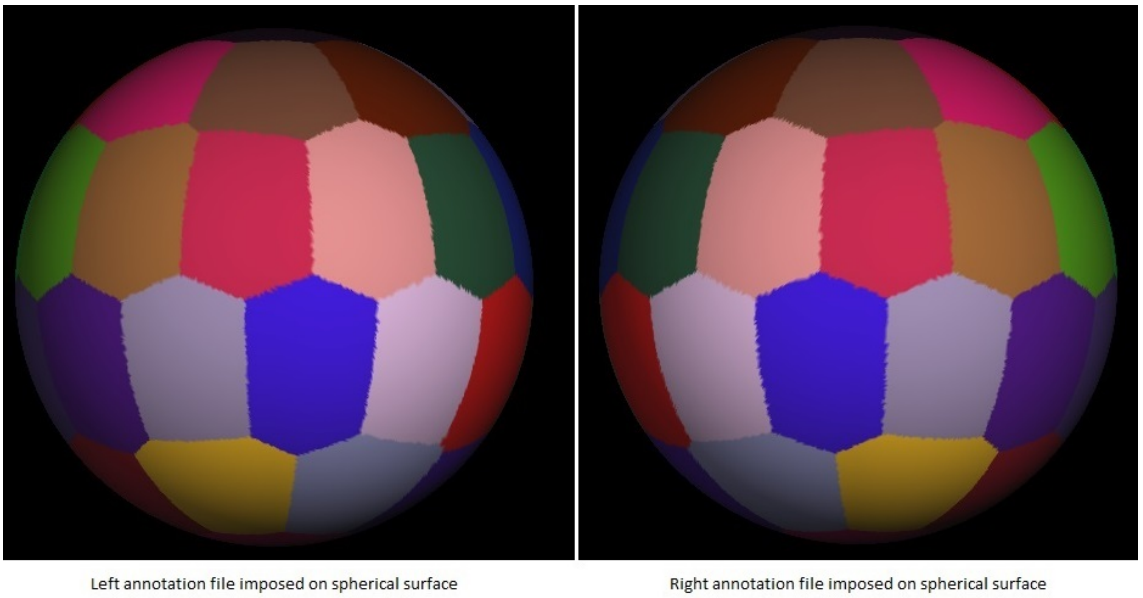

FIGURE 3.2: The Annotation files of Left Hemisphere and Right Hemisphere

Thus the two atlas files leftaparc.gcs and rightaparc.gcs were generated to be used in the surface reconstruction pipeline later for creating parcellated and segmented brain surface. The atlas file in Freesurfer is saved with .gcs extension.

3.1.2 Reconstructing the cortical surface using equal zone cortical surface partitioning atlas

FreeSurfer (Fischl, 2012) provides a full processing pipeline for structural MRI data, which involves: Skull stripping, B1 bias field correction (Bias field signal is a low-frequency and very smooth signal that corrupts MRI images), gray-white matter segmentation, reconstruction of gray-white boundary surface and pial surface, Labeling of regions on the cortical surface and sub-cortical brain structures, registration of the cortical surface of an individual with an atlas. But it can also be grouped into three steps by using appropriate options. Here the whole process was performed in three steps.

- First, the main T1 MRI image is processed to correct errors that occur in the image due to motion, intensity non-uniformity and intensity fluctuation. Then the image is processed to remove the skull.
- The major steps are done in next step are segmentation of cortical surface, separation of white matter surface, cutting of midbrain from the cerebrum, generation of left and right hemisphere generate the original surface, inflating the white surface,

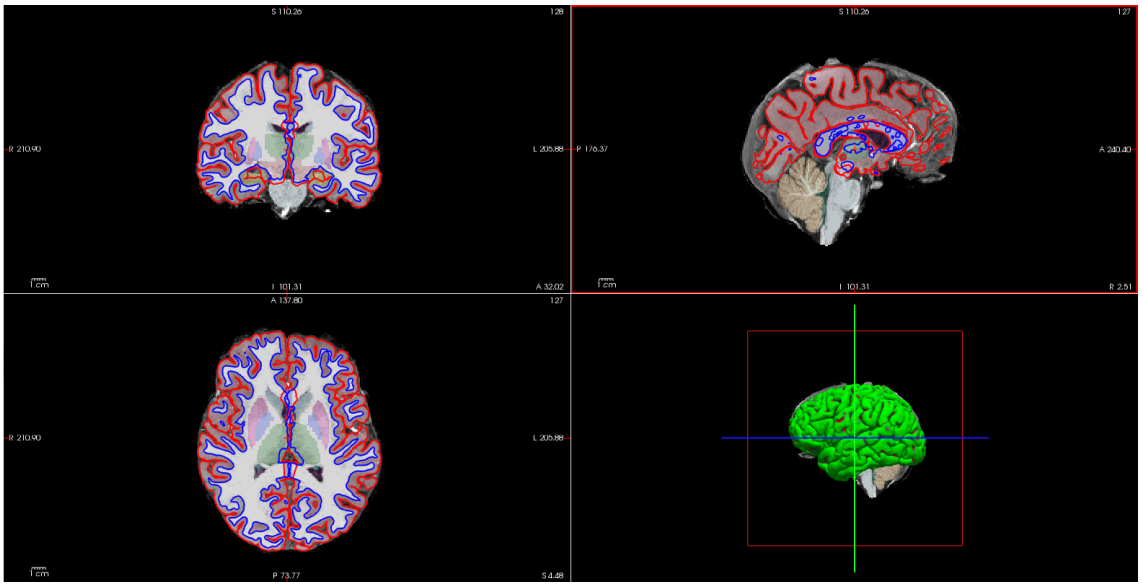

FIGURE 3.3: Segmented Brain Volume and White/Pial surfaces

transforming it to a spherical surface, generating pial surface (the surface representing the boundary between grey matter and cerebrospinal fluid) and white surface.

- In this step, inflate the Orig surface into a sphere. This sphere surface was used in the equal parcellation process to create an equal parcellation atlas as described in section 3.1.1. Generate parcellated cortical surface mapping the leftaparc.gcs and rightaparc.gcs atlas files created in equal parcellation steps. Maps the cortical labels from the cortical parcellation (aparc) to the segmentation volume (aseg). Generate the final parcellated and segmented image.

3.1.3 Results and validation of the model

3.1.3.1 Viewing volumes

View of the output volumes such as white matter; surfaces such as white and sub-cortical segmentation of is shown in Figure 3.3. These are the axial, coronal and sagittal views of the segmented volumes. The blue line is the boundary between white matter and gray matter and defines the white surface. It is used to calculate the total white matter volume. The red line is the boundary between the cortical gray matter volume and CSF and is defined as the pial surface. Figure 3.4(a) shows the complete segmentation of the subcortical structures. As shown in the image, the red area is the cerebral cortex, the gray area is the white matter, the green area is the thalamus, the yellow area is the hippocampus, and the pink area is the putamen. The complete list of segmented areas is given in the table 3.4(b).

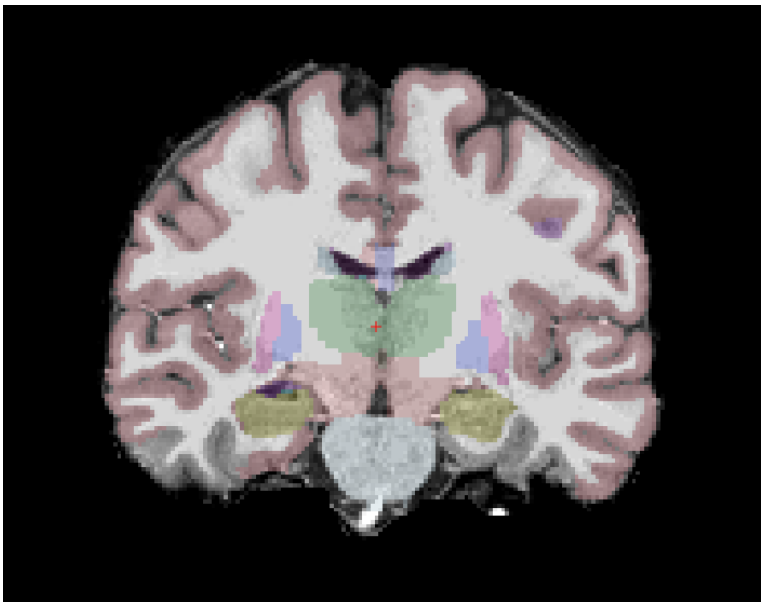

(a) Segmented areas.

Area Names	Color Code
Cerebral-White-Matter	
Cerebral-Cortex	
Lateral-Ventricle	
Inf-Lat-Vent	
Cerebellum-White-Matter	
Cerebellum-Cortex	
Thalamus-Proper	
Caudate	
Putamen	
Pallidum	
Hippocampus	
Amygdala	
Accumbens-area	
VentralDC	
vessel	
choroid-plexus	

(b) Segmented areas colour code.

FIGURE 3.4: Segmented cortical surface and their colour code

3.1.3.2 Viewing surfaces in 3D

Pial Surface: The volume shown in the image Figure 3.5, is the pial surface. The green regions are gyri and red regions are sulci. In this surface the sulci are mostly hidden.

White Surface: The surface shown in the image Figure 3.6, is the white surface. The white surface shows the boundary between white matter and gray matter. Here sulci is better visible.

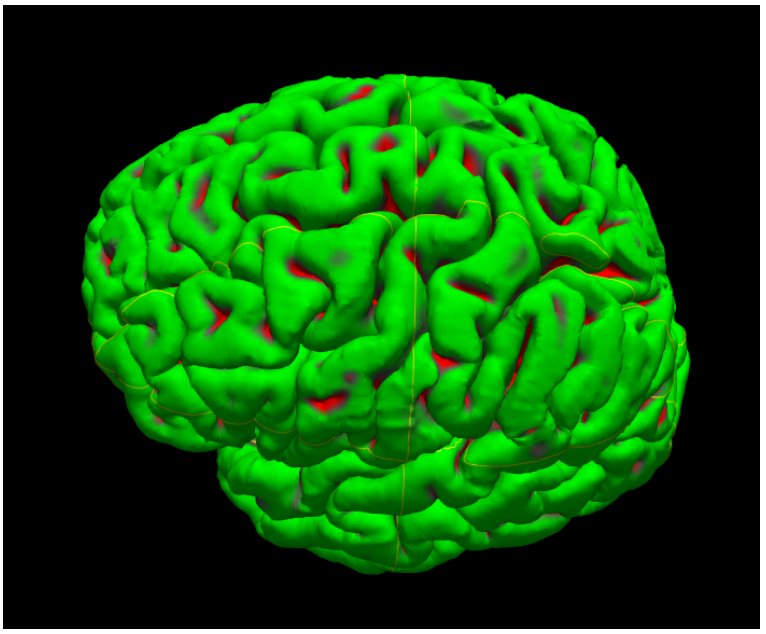

FIGURE 3.5: The pial surface

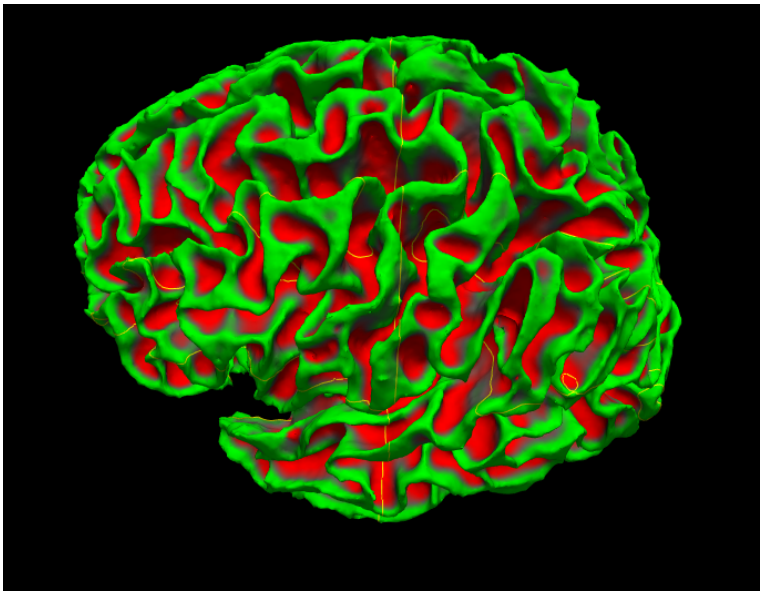

FIGURE 3.6: The white surface

Inflated Surface: The surface shown in the image Figure 3.7, is the curvature of the inflated surface. In the inflated surface the sulci is completely visible.

Cortical Parcellation: The surface shown in the image Figure 3.8, is the 3D view (sagittal view) of the parcellated cortical surface. The image shown in Figure 3.9 is the 2D (axial, sagittal and coronal) views of the parcellated and segmented image. Each parcellated node has been represented with a unique colour code as defined in the colorlookup table.

The table 3.10 displays the statistical values such as the number of vertexes and surface

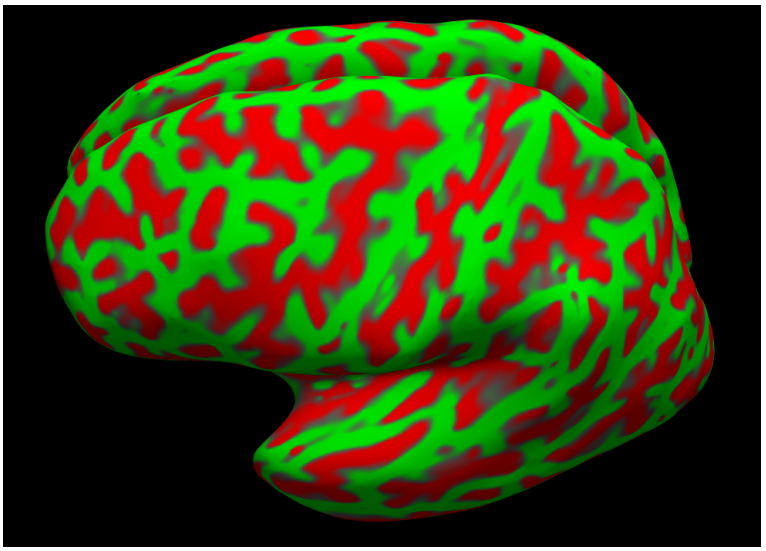

FIGURE 3.7: The inflated surface

area for each parcellated node. In the statistics table, the number of vertices is unitless and the surf area of parcellated nodes are in mm^2.

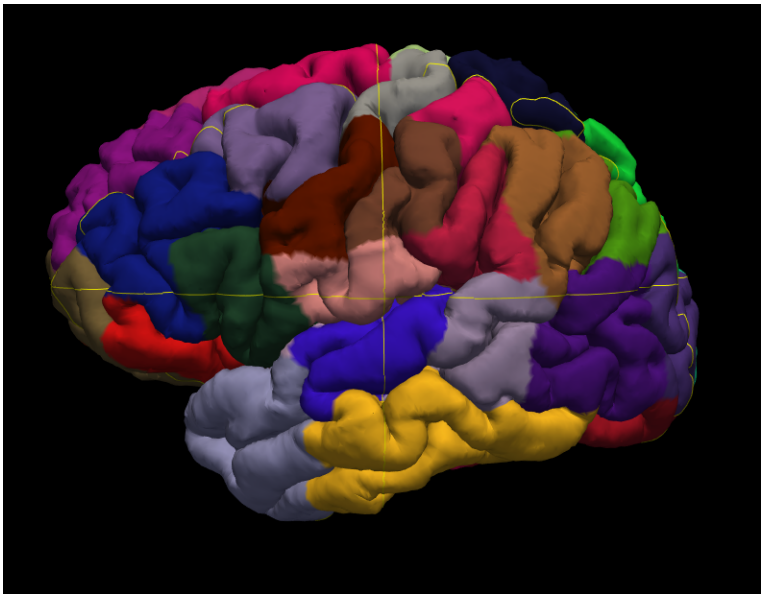

FIGURE 3.8: The parcellated cortical surface

So, in summary in this work, each surface point of an inflated spherical surface of each hemisphere has been assigned to an equally divided area of a sphere and saved as label files. Then the Label files were put together to generate annotation files for the surface. Then from the annotation files, the atlas files were created for left and right hemispheres. The output statistics of the parcellated segmented image shows that all parcellated areas from atlas files have been successfully mapped to the cortical surface. Thus a novel approach was designed to reconstruct a surface from an MRI image by parcellating the cortical surface into equal-sized areas using the Freesurfer tool.

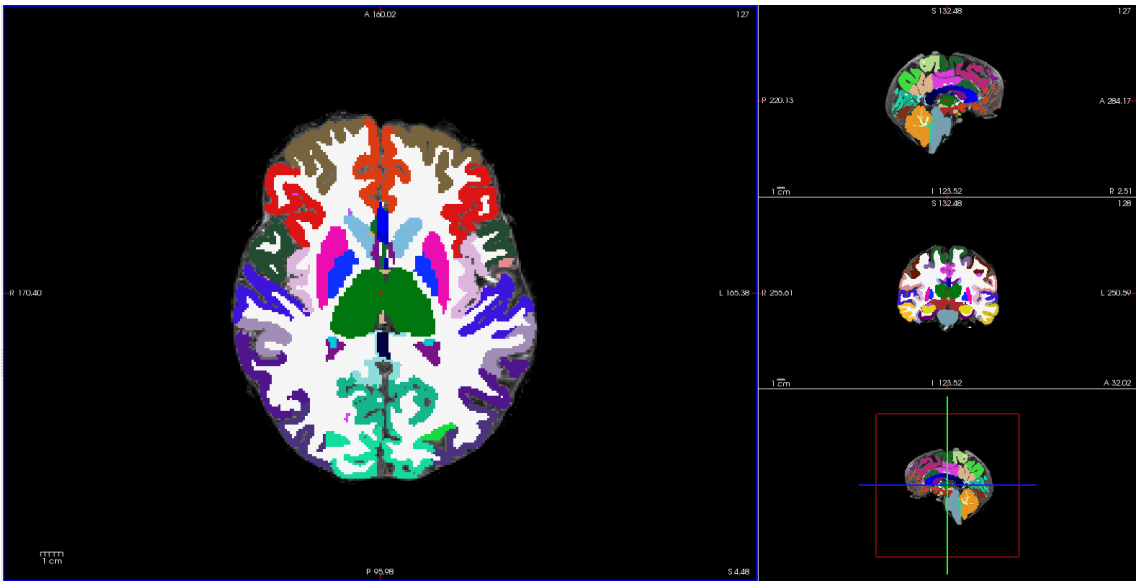

FIGURE 3.9: The parcellated segmented surface

Hemispher	StructName	NumVert	SurfArea	Hemispher	StructNam	NumVert	SurfArea
left	node1	3470	1958	right	node1	3043	1831
left	node2	2839	1875	right	node2	2984	2056
left	node3	4132	2768	right	node3	3596	2455
left	node4	3794	2247	right	node4	3392	2322
left	node5	2877	1728	right	node5	3441	2134
left	node6	2284	1473	right	node6	2389	1459
left	node7	2486	1479	right	node7	2503	1452
left	node8	2826	1695	right	node8	2539	1626
left	node9	2340	1667	right	node9	1998	1485
left	node10	3751	2570	right	node10	2826	2006
left	node11	5223	3428	right	node11	4207	2799
left	node12	4184	2756	right	node12	5313	3518
left	node13	3116	2061	right	node13	4013	2716
left	node14	2666	1774	right	node14	2891	1920
left	node15	2567	1788	right	node15	2630	1700
left	node16	3135	1970	right	node16	2850	1794
left	node17	3789	2420	right	node17	2813	1726
left	node18	3027	1822	right	node18	3028	1797
left	node19	2656	1794	right	node19	3137	1857
left	node20	2508	1742	right	node20	2326	1602
left	node21	2599	2197	right	node21	2309	2024
left	node22	3503	2436	right	node22	2993	2053
left	node23	4340	3028	right	node23	3784	2566
left	node24	3001	2003	right	node24	3444	2227
left	node25	2451	1637	right	node25	2616	1734
left	node26	3388	2285	right	node26	2801	1795
left	node27	2807	1858	right	node27	2808	1854
left	node28	4546	3006	right	node28	3321	2212
left	node29	4711	2958	right	node29	4901	3132
left	node30	4451	2817	right	node30	5190	3116
left	node31	2981	1979	right	node31	4287	2762
left	node32	1846	1474	right	node32	1927	1354
left	node33	2959	2160	right	node33	2568	1805
left	node34	2387	1583	right	node34	2554	1745
left	node35	4543	3037	right	node35	3498	2319
left	node36	4618	3022	right	node36	3637	2516
left	node37	4807	3227	right	node37	5709	3826
left	node38	3857	2529	right	node38	4319	2728
left	node39	2173	1422	right	node39	2755	1822
left	node40	3484	2353	right	node40	4755	3276

FIGURE 3.10: Left and right hemisphere parcellation statistics

3.2 Structural connectome construction

The neuroimaging data of diffusional-weighted MRI reveals the white matter connectivity of the human brain. The structural MRI and diffusional MRI data both are necessary for structural connectome construction and were obtained here from Human Connectome Project (HCP) databank. The main two steps of DW_MRI image processing are denoising and distortion correction. The image denoising is performed first because motion and distortion correction during their smoothing and interpolation steps can not alter the noise characteristics and produce a low quality visual and statistical result. Then the image is corrected for distortion such as eddy current, motion and susceptibility induced distortion. The diffusional MRI data obtained from the human connectome databank is already preprocessed hence didn't need to perform the denoising and distortion correction here.

3.2.1 Structural Image processing

The parcellated structural image is used here to construct the nodes of the connectome matrix.

- First the values of the parcellated node in the image were modified so that numbers in the image correspond to rows and columns of the connectome. The parcellated structural MRI image is shown in Figure 3.11.
- Then tissues of the structural image file were segmented into five tissue types (cortical gray matter, sub-cortical gray matter, white matter, CSF, pathological tissue) for applying the tractography process. The five tissue types act as anatomical prior and define the propagation and termination conditions for white matter tracts.

3.2.2 Diffusional Image processing

- In diffusion image processing, first the response function was estimated. This is the signal value of a voxel containing a single, coherently-oriented fibre bundle and it is used as the kernel for the deconvolution step.
- Then constrained spherical deconvolution was performed to generate an image with three volumes, corresponding to the tissue densities of CSF, gray matter and white matter. This is displayed in mrview as an RGB image with CSF as red, GM as green and WM as blue as shown in Figure 3.12.
- Then anatomically constrained tractography was performed to generate the initial tracts as shown in Figure 3.13.

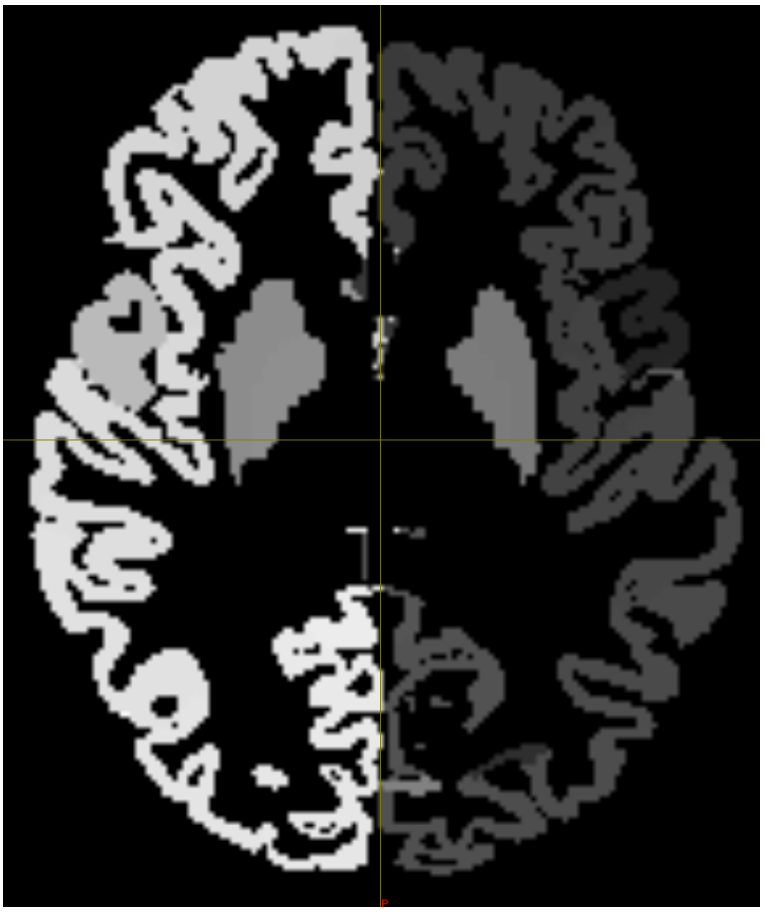

FIGURE 3.11: Parcellated Image

- Then the tracts were filtered using the Spherical-deconvolution Informed Filtering of Tractograms (SIFT) algorithm which was applied to reduce the overall tracts count and get more biologically meaningful estimates of structural connection density.

3.2.3 Structural Connectome construction

The connectome matrix was built using the generated white matter tracks and the parcellated nodes. Here we are using a novel approach to use the equal-sized parcellated nodes constructed in 3.1.2. The nodes of the connectome matrix are the parcellated ROIs and the values of the matrix are the white matter connectivity strengths among the ROIs. A toolchain has been developed in python that can take a set of subjects in a group as input and generate the set of connectome matrix as output. The flowgram of the whole process of structural connectome construction is shown in Figure 3.14.

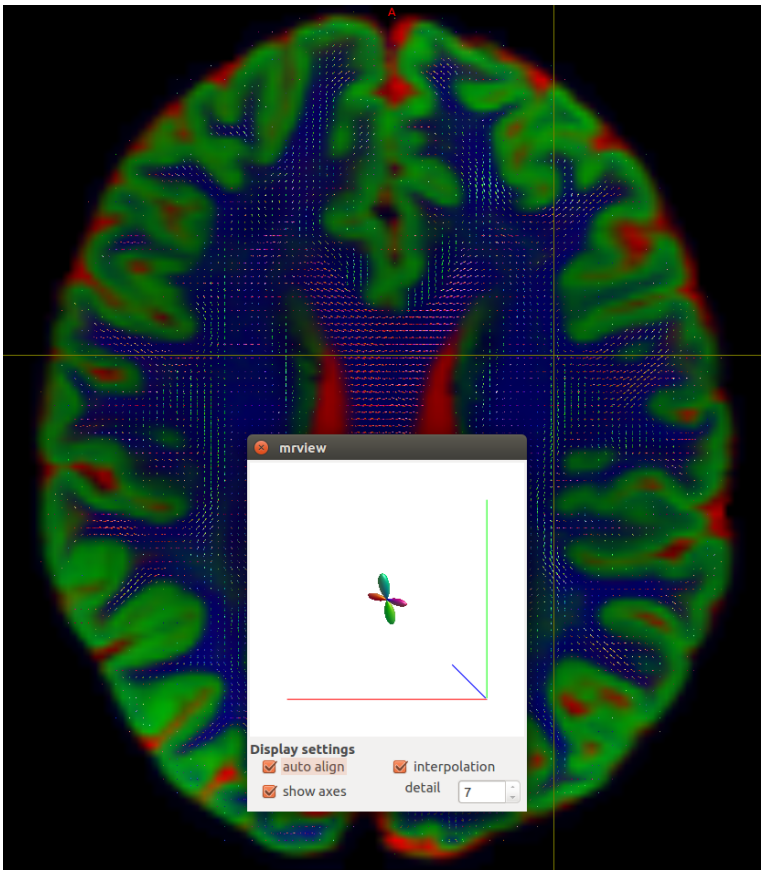

FIGURE 3.12: Fibre Oriented Distribution in voxels

3.2.4 Graph Theory analysis:

The graph theory measures are calculated on the constructed structural connectome matrix to quantify the properties of the structural network. To calculate the network measures, we integrate Matlab based Brain connectivity toolbox (brain-connectivity-toolbox.net) into our toolchain as the final steps of processing.

3.2.5 Results and validation of tool

Data Acquisition: A single-subject MRI data is obtained from WU-Minn the Human Connectome Project (HCP) database at http://db.humanconnectome.org. The characteristics of the subject are as follows: Subject ID: 100307; Gender: Female; aged 26-30; Female, Accession ID: ConnectomeDB S00230.

Cortical Parcellation: We parcellate the cortical surface into $N = 80$ equal-sized areas where each of the hemispheres are parcellated into 40 equal regions. We arrange the parcellated areas of each hemisphere in such a way that the symmetry of the left and right hemispheres is maintained. In Figure 3.9, we show the axial view of generated parcellated segmented brain image used as nodes in graph theory analysis.

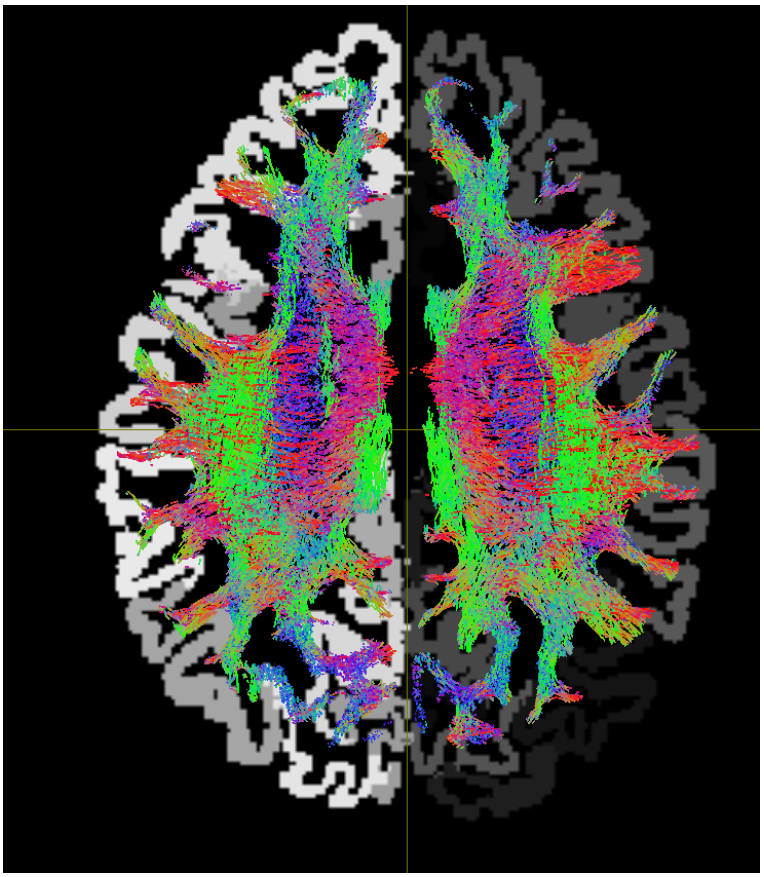

FIGURE 3.13: The Generated Tracks

Structural Connectome Extraction: From diffusional MRI data for each voxel of white matter fibre oriented distribution (FOD) values are calculated. Then following an iterative algorithm for each voxel, the convoluted fibre oriented distribution is traced to generate the tracks. Thus, 1 million tracks are generated. Then the tracks are filtered to select 0.8 million more biologically plausible tracks. The constructed structural connectome is shown in Figure 3.15, where nodes are the parcellated ROIs and edges are the streamline count of white matter tracts extracted. In Figure 3.16, we show the matrix of the structural connectome developed from white matter tracks and parcellated brain image. The light blue, green and yellow regions are where connectivity strength is high.

Graph Theory Measures : Table 3.1 shows the values of density, characteristic path length (CPL), small world index (SWI), transitivity, assortativity of the structural connectivity network; which is of the form of a weighted undirected graph; constructed from extracted white matter tracts and parcellated ROIs. The streamline count is used as the connectivity metric in the network, hence the weight of the network is the streamline count. Fig. 3.17 shows the graphical representations of the degree distribution, community structure indices, betweenness centrality and clustering coefficients of the structural brain connectivity. The optimal community structure subdivides the network into non-overlapping groups of nodes that maximises the number of within-group edges

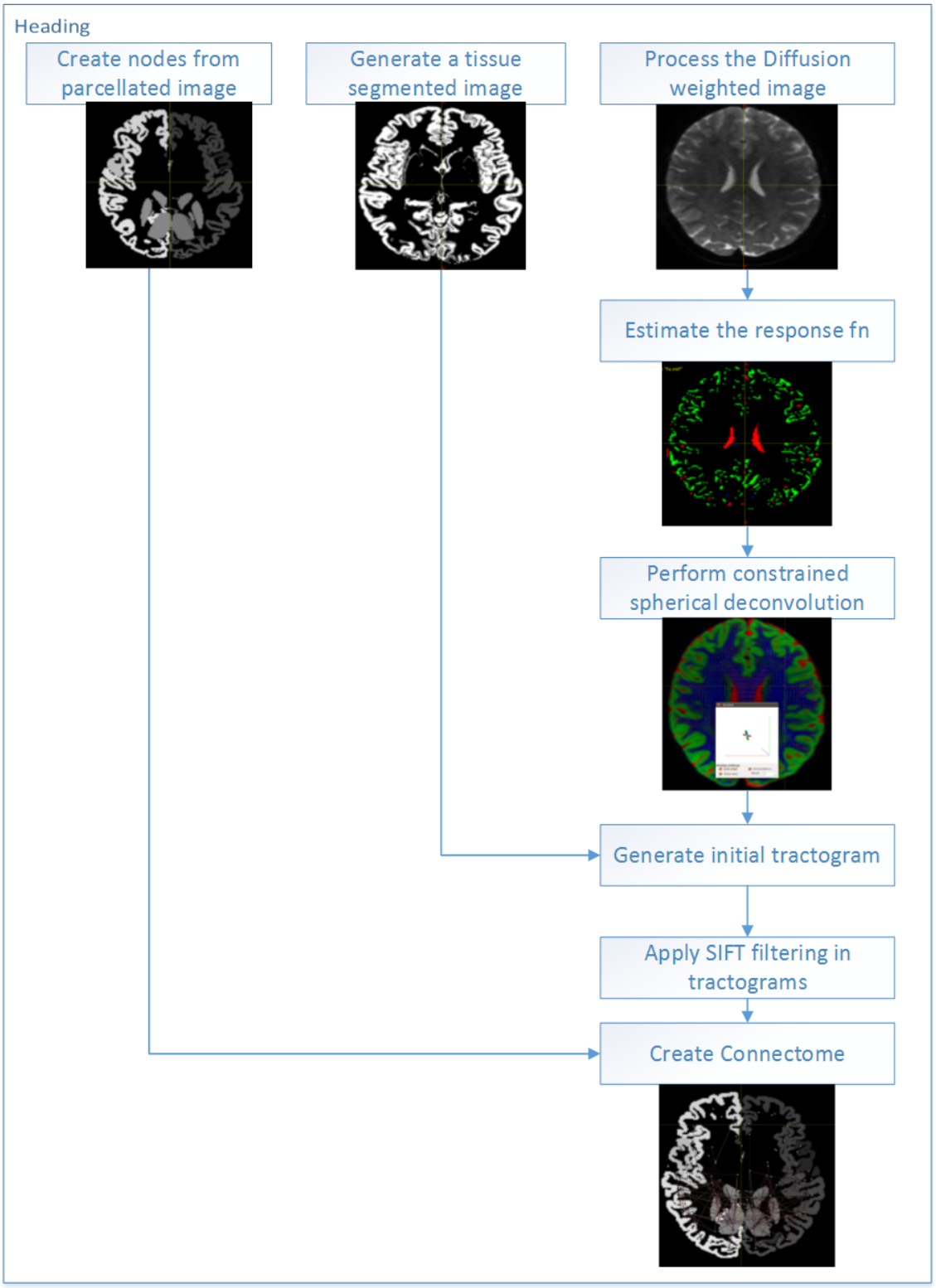

FIGURE 3.14: Connectome generation steps

and minimizes the number of between-group edges. The modularity is the degree to which the network may be subdivided into such clearly delineated groups, and here

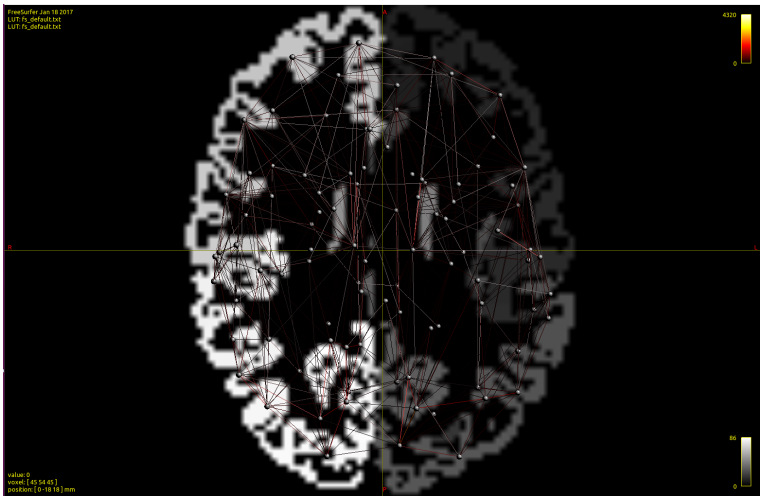

FIGURE 3.15: The Structural Connectome constructed using the equal sized parcellated nodes and white matter streamlines.

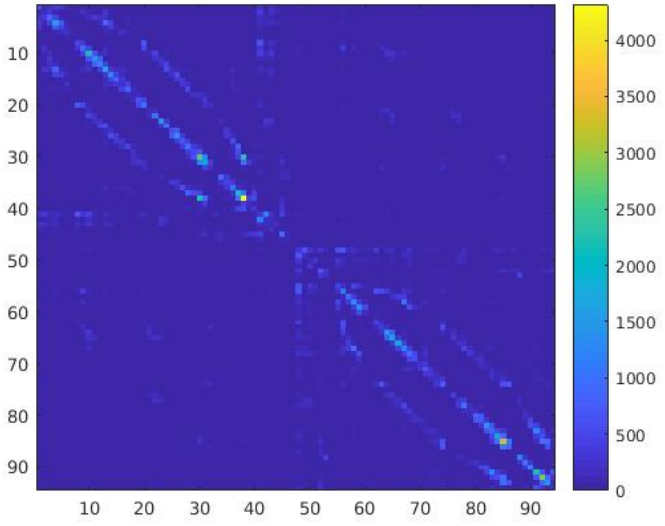

FIGURE 3.16: The structural connectivity strength among the equal sized ROI-to-ROI.

Metrics	Density	CPL	SWI	Transitivity	Assortivity	Modularity
Values	0.5117	1.1297	10.69	0.7783	-0.1191	0.553

Table 3.1: Graph theory measures

the value is 0.553 as shown in Table 3.1. These measures are useful for comparing or studying brain connectivity networks.

3.2.6 Conclusion

In this section, the diffusion MRI data were processed to extract white matter tracts. By using the equal-sized brain ROIs generated in the previous section and extracted

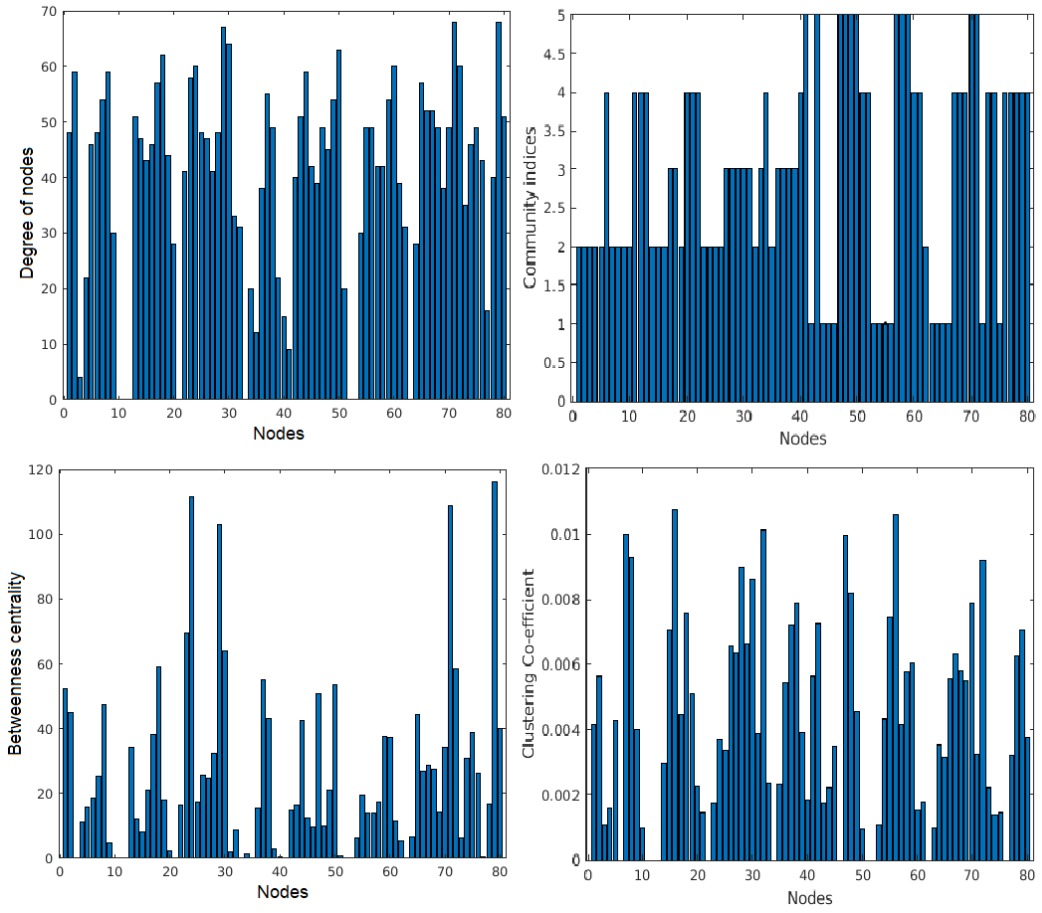

FIGURE 3.17: The graphical representations of structural network measures

white matter tracts the structural connectivity of the brain was obtained in form of a 'Connectome' matrix.

3.3 Geometrical properties estimation of axon bundles

Diffusion MRI (dMRI) is the most popular method for characterizing the white matter microstructure. The displacement of water molecules during diffusion encoding helps to characterize and quantify the underlying cellular structure (Hagmann et al., 2007; Jelescu and Budde, 2017).

Based on the kinds of literature (Raffelt et al., 2017, 2012; Assaf et al., 2008); measuring fibre density (FD) is the most popular method for quantifying white matter tracts. Since the intracellular volume of axons within a tract is influenced by a number of axons, the measure of fibre density (FD) is basically the measure of intracellular volume. So in this section, we are extracting measures such as FD of white matter track by processing diffusion-weighted MRI (DWI) data to use it for modelling our circuit. It has been observed that a measure of FD alone cannot fully quantify the white matter track,

because not only the number of axons but a change of axon diameter can also influence the intra-axonal volume (Raffelt et al., 2017). So measuring the fibre bundle cross-section (FC) is also an integral part to quantify white matter tracks. Here, we are processing diffusion MRI data and extracting quantifying measures such as FD, FC and FDC=FD*FC of white matter tracks which can be called geometrical properties of the bunch of axons. The diffusion MRI data from the databank of Human Connectome Project (HCP) https://db.humanconnectome.org has been downloaded and used here. The open source software Mrtrix3 https://github.com/MRtrix3/) has been used to process the diffusion data to extract the measures of white matter tracks.

3.3.1 Computing Fibre Density (FD) and Fibre Cross-section (FC) and Fibre Density Cross-ection(FDC) of white matter tracts between two ROIs

We have performed the following steps to compute Fibre Desnsity (FD), Fibre Cross-section (FC) and Fibre Density Cross-section (FDC) values from white matter tracts:

First, the diffusion MRI data were processed to remove noise and artefacts such as eddy current distortion, motion distortion and susceptibility-induced distortion to extract clean data. The DWI volumes often have a non-negligible bias field, mostly due to high-density receiver coils. If it is left uncorrected, it can be incorrectly interpreted as a spatially varying fibre density. Therefore bias field correction is highly required. The low-frequency intensity inhomogeneities were eliminated by applying a bias field correction algorithm. A Group average response function can be used as the unit of the final apparent fibre density metric. So this was calculated by first estimating a response function per subject, then averaging them. To increase anatomical contrast and improve downstream template building, registration, tractography and statistics, the diffusion data was upsampled. Fibre orientation distribution (FOD) estimation (Tournier et al., 2007) basically determining orientations of fibre bundles in a single voxel. It was computed by performing Constrained Spherical Deconvolution (CSD) (Tournier et al., 2007) method using the group average response function. Then each FOD lobe in the FOD images was segmented to identify the number and orientation of fixels in each voxel. The output also contains the apparent fibre density (AFD) (Raffelt et al., 2012) value per fixel (estimated as the FOD lobe integral): (Smith et al., 2013) to estimate fixels and their AFD. Next fixel orientations were reoriented, subject fixels were assigned to template fixels and fibre cross-section (FC) metric and fibre density (FD) and cross-section (FDC) were computed on the fixel. Then whole-brain fibre tractography was performed to extract white matter tracts from the FOD template and tractography biases were reduced by performing SIFT (Smith et al., 2013) algorithm. Tracts were then mapped to the parcellated image to generate the connectome matrix for the entire brain. Next, streamlines are extracted based on their node assignment to parcellated

nodes. Next, the list of streamlines connecting two brain nodes was extracted from the connectome. The extracted streamlines are then mapped to the fixel data image files to link the measured metrics (FD/FC/FDC) to the tracts. Earlier, the FD, FC and FDC values were computed on the fixel images. Next, track scalar files (tsf files) are generated by mapping fixel values to streamline points, saving them in a tsf file. Finally, the track scalar files were visualised using the tractography tool in MRview. The fibre tracts are the one that connect two brain regions and streamlines are the estimates of the underlying white matter tracts which are reconstructed by Diffusion Tensor Imaging (DTI). All these output files are accessible from Matlab and values can be used for computation.

The different steps and the intermediate outputs of computing fibre density (FD) values from diffusion MRI data have been shown in a flowchart form in Figure 3.18.

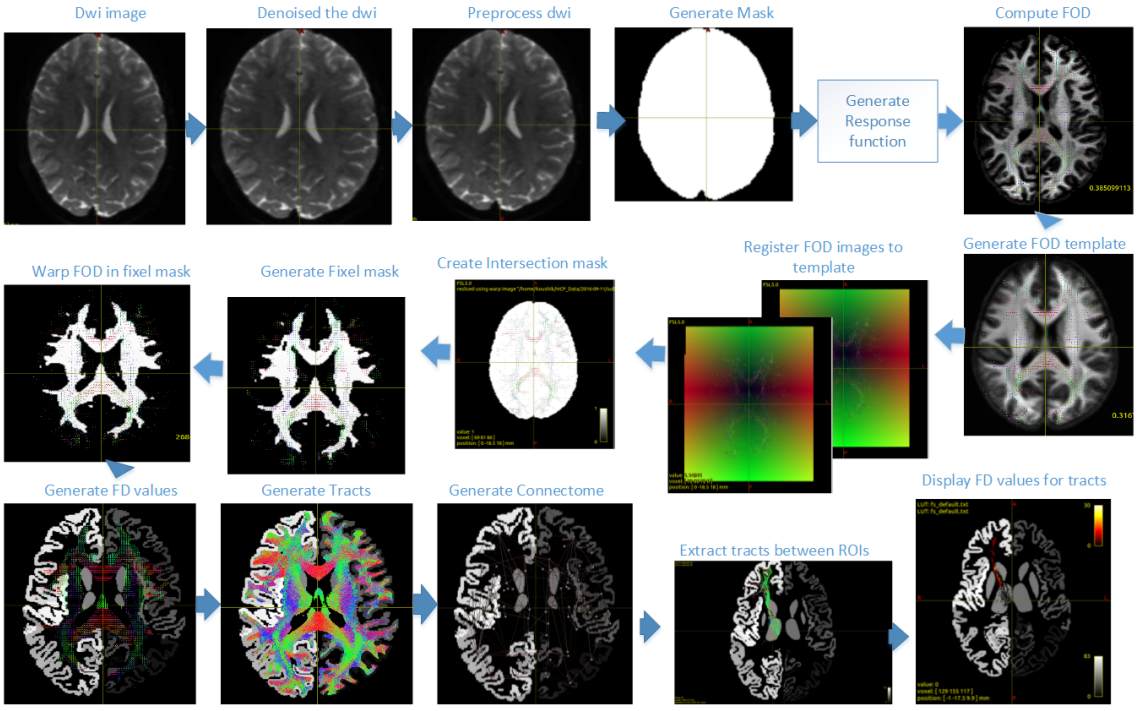

FIGURE 3.18: Flow chart for computing FD values

3.3.2 Results and validation of tool

Here we are showing step by step the various outputs that were obtained during the geometry extraction process

- The first output is the total number of white matter tracks in the brain from diffusional MRI data. Figure 3.19(a) shows the white matter tracts for the whole brain that was obtained in our experiment. Also a text file was generated where

there is one row for each streamline, and each row contains a list of numbers corresponding to the parcels to which that streamline was assigned.

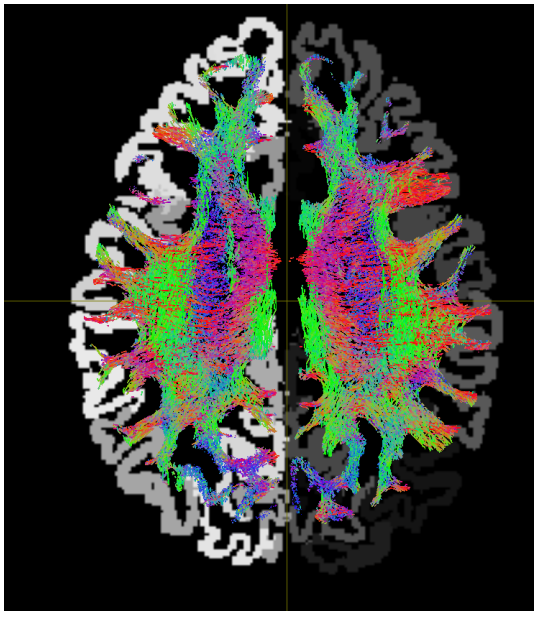

(a) 2 million white matter tracks were generated

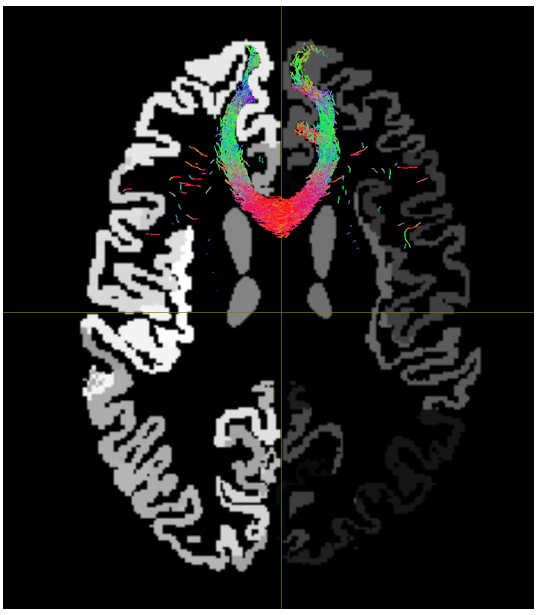

(b) Tracts between left and right superiorfrontal

- Next, the streamlines are extracted from the tractogram based on their assignment to parcellated nodes. The text file that was generated earlier containing streamlines and their assigned nodes is used here to extract the streamlines from tractograms. The streamlines between brain regions cortex left superior frontal and cortex right superior frontal, have been extracted from whole-brain tractography and shown in Figure 3.19(b). The number of streamlines connecting these two brain regions is 4175. The total number of streamlines connected between these two regions may be higher as there may be loss of streamlines during the reconstruction process. But these are the estimated streamlines that are solely connecting these two brain regions.

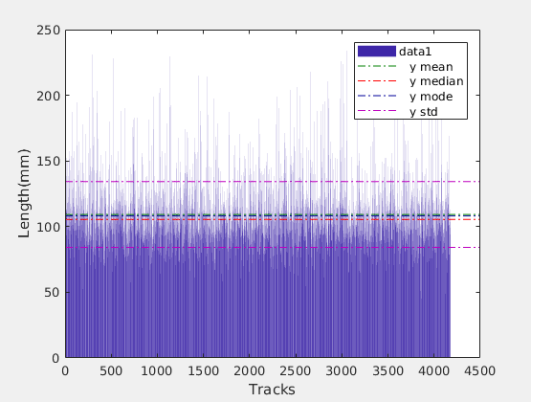

(c) Length of the tracts between left and right superior-frontal

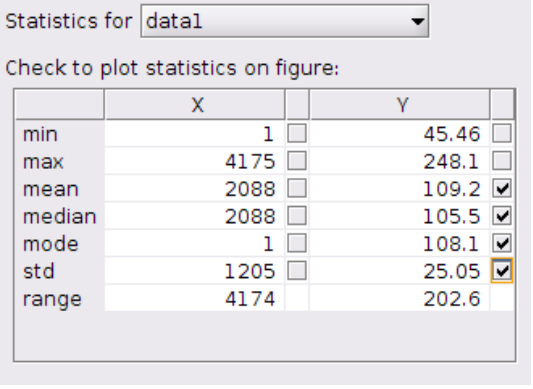

(d) Statistics values tract length

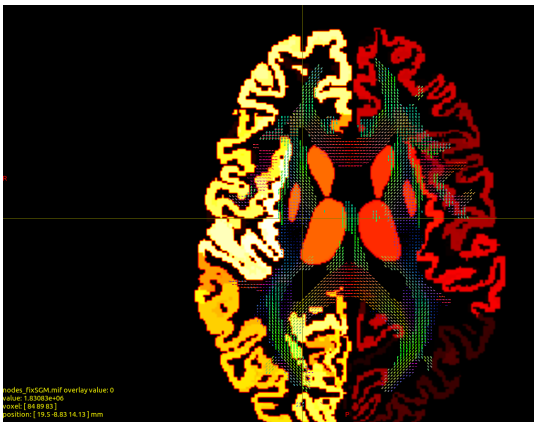

(e) FD values

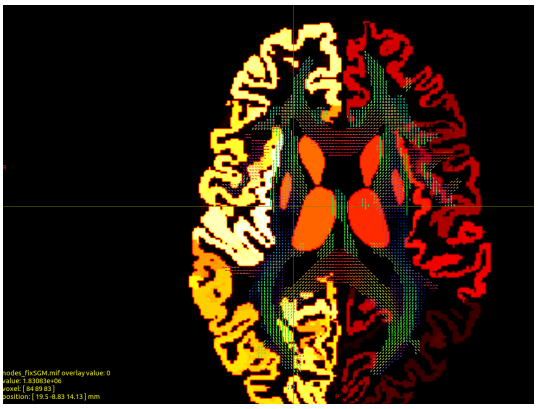

(f) FC values

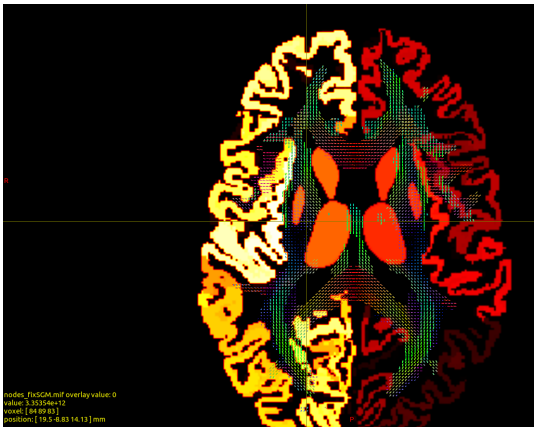

(g) FDC values in voxels

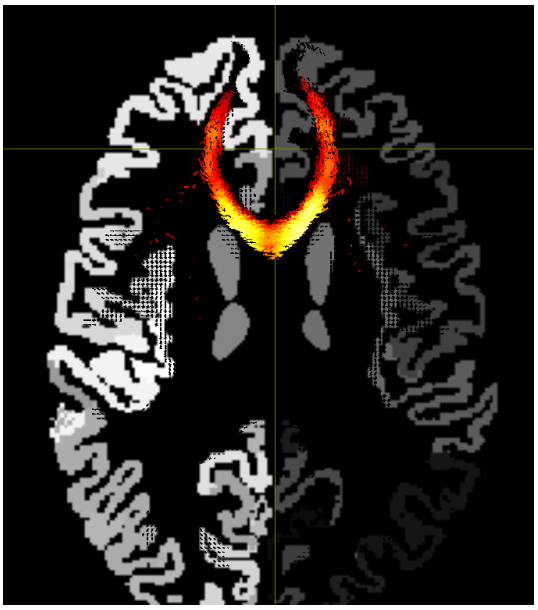

(h) FD and FC values in the tracts

FIGURE 3.19: Step by step generation of fixel based analysis results while extracting geometrical metrices of fibre tracts

- Next we calculate the fibre length (FL) value of all the streamlines between two brain ROIs as shown in Figure 3.19(c). We also calculated the statistic values such as mean,mode,std on the length of streamlines as shown in the Figure 3.19(d).

- Next, we mapped the streamlines to the fixel data image files to link the measured metrics (FD/FC/FDC) to the tracts. Then we extracted the FD in a fibre bundle by following the steps of fixel based analysis as mentioned before. Figure 3.19(e) shows the value of fibre density of a fibre bundle in a voxel. As shown in the figure the value of fibre density(FD) at position 19.5, -8.83, 14.13 in voxel [84 89 83] is 1.83e+06.

- Next, we extracted the fibre bundle calibre, internal diameter of fibre tract of white matter from fixel images obtained from tracks. Figure 3.19(f) shows the value of cross section of a fibre bundle in position at position 19.5, -8.83, 14.13 in voxel [84 89 83] is 1.83e+06.
- Also we obtained the value of fibre density cross-section by multiplying FD and FC for the tracks. Figure 3.19(g) shows the value of fibre density(FDC) at position 19.5, -8.83, 14.13 in voxel [84 89 83] is 3.35e+12 which is basically FD*FC.
- We are also able to view the FD/FC/FDC values of a particular tract. The Figure 3.19(h) shows the fibre density (FD) and fibre crosssection (FC) values over the extracted tract.

3.4 Discussion

In this chapter, first, we processed the structural MRI image and generated parcellated segmented cortical surface consists of equal-sized brain areas. Typically Freesurfer is used for parcellation of cortical surface anatomical areas based on Brodmann atlas. Using our methodology, we are now able to perform non-anatomical equal-area parcellation of the cortical surface using Freesurfer, which helps to process the subjects with neuroplasticity anomalies or adults brains with different dominant areas. Next, we processed the DWI-MRI data and extracted white matter tracts of the whole brain. By using the extracted white matter tracts and defined equal-sized brain ROIs we have defined the structural connectivity of the brain in form of a structural connectome matrix. The nodes of the matrix are equal-sized non-anatomical brain ROIs and the edges between the nodes are white matter counts between them. We performed graph theory analysis on the connectome matrix and extracted different network matrices to determine the functional segregation and integration of the brain. Next, we processed the streamlines data generated from the tractogram to calculate FD, FC and FDC values fibre bundle connecting the equal-sized areas from the cortical surface. Thus we extracted geometrical metrices of white matter tracts of the brain where the cortical surface is parcellated into equal-sized non-anatomical areas.

3.5 Conclusion

In this work, we present a toolchain that process structural and diffusional MRI data and calculate graph theory measures for quantifying the structural connectivity based on equal area parcellation to dene brain ROIs. Our tool is fully automated and does not need separate intervention at its different processing stages. Being based on equal parcellation, the construction of structural connectomes can be customized based on

user need making it available for structural connection analysis for neonates as well as brain injury cases. The entire toolchain has been validated with HCP data which showed correct working and its ease of use. Then, we also perform fixel based analysis and extracted geometrical features such as FD, FC and FDC of the white matter tracts connecting non-anatomical equal-sized areas of the brain. The main goal of the thesis is to define the phase-frequency characteristics of the structural connectivity of the brain so that a correlation between functional and structural connectivity can be established. A circuit based computational approach has been taken to model the structural connection between two ROIs. Here in this chapter, we have extracted the value of the parameters from MRI data that will be used to model the structural connections between two brain ROIs.

Chapter 4

Circuit Model for analysing Signal Propagation Dynamics in Single Myelinated Axon

4.1 Introduction

Functional brain connectivity is fundamentally computed from frequency-dependent phase relationships between two activated brain ROIs (Whitfield-Gabrieli and Nieto-Castanon, 2012), connected via structural connectivity. Analysing signal propagation dynamics of an equivalent circuit model of a bunch of axons in the frequency domain is paramount in understanding the implicit correlation between the structural and functional brain connectivity. The main objective of the thesis is to develop a computational circuit model that simulates the signal propagation characteristics of a bunch of axons and analyses its signal propagation disruptions behaviours both in temporal and frequency domains, which can provide an insight into possible functional connectivity disruptions in the presence of structural connections between two brain areas. Previously in Chapter 3, we have processed and extracted parameters of white matter tracts from diffusion-MRI data. Our objective here is to design an equivalent circuit of a single myelinated axon, which will be a building block for an equivalent circuit of a bunch of axons.

In this chapter, we have designed a computational circuit model of a single myelinated axon. We have used the circuit simulation tool Personal Simulation Program with Integrated Circuit Emphasis (PSpice) for our circuit design and modelling. The advantages of using the PSpice tool are: it provides an in-depth analysis of circuits and circuit designs with advanced simulation functions, processes Netlist circuit design, and operates from MATLAB/Simulink. First, we have simulated the signal propagation through

a single axon in the time domain by perturbing the model with an independent current source. Then we have calculated signal propagation matrices such as Conduction Velocity (CV), Maximum Myelin Length (ML) and compared them with published experimental data to validate our computational model. Finally, we have determined the frequency response of the cable circuit and generated a system definition for signal propagation through a single myelinated axon. Previously, many works were done on signal propagation through axon where exploration of signal propagation was done mainly in time scale (Fitzhugh, 1962; Goldman and Albus, 1968; Brill et al., 1977; Moore et al., 1978; Carpio and Peral, 2011; Seidl, 2014; Cohen et al., 2020). Here we have taken a novel approach to model the frequency and phase characteristics of axons through circuit theory modelling.

4.2 Impulse initiation and saltatory conduction modelling in a myelinated nerve fibre

A myelinated axon is made up of Nodes of Ranvier's (NR) and myelinated Internode (IN). The Action Potential (AP) generated at soma passively spreads out through the myelinated segment to the next NR to depolarize it to the threshold and trigger AP at the next NR. In this section, we designed an electric circuit model of a single myelinated axon using PSpice to simulate the activity of excitable membrane for NR and saltatory signal conduction (see Chapter 2, Section 2.5) for IN. Fitzhugh (1962) has provided a mathematical model for the electrical properties of a myelinated axon fibre. The model is consisted of the Hodgkin-Huxley ordinary differential equations (Chapter 2 Equation: 2.28) (Hodgkin and Huxley, 1952) to represent the membrane at the nodes of Ranvier, and a partial differential cable equation (Chapter 2 Equation: 2.38) to represent the internodes surrounded by myelin sheath. That mathematical model has been implemented in this circuit model. The details of parameters values for nodes and internodes of the circuit have been taken from literature (Hodgkin and Huxley, 1952; Tasaki and Frank, 1955; Binczak et al., 2001; Tsubo and Kurokawa, 2018; Ford et al., 2015) and presented in tabular forms later in the chapter. In the designing process, first, the models for NR and IN areas of axon were designed as nodes and internodes and then these two were connected for designing the whole model of a single myelinated axon. The resultant circuit model was perturbed by independent current sources, and the responses calculated by PSpice were compared with published experimental data Huxley and Stämpeli (1949); Tasaki and Fujita (1948); Binczak et al. (2001); Tsubo and Kurokawa (2018); Ford et al. (2015) for validation of the developed model.

4.2.1 Circuit modelling of Nodes of Ranvier as Hodgkin Huxley cell

As mentioned above, the circuit model for NR was designed based on the current equations given by Hodgkin and Huxley (1952). We adapted the SPICE-based neuron model from the works of Masanotti et al. (2006); Szlavik et al. (2006). The total membrane current during an action potential is given by the sum of a capacitive current and three ionic currents, carried by sodium, potassium, and other ions (Hodgkin and Huxley, 1952). A detail description of current and voltage dynamics of Hodgkin-Huxley circuit was given in literature review (Chapter 2 Section 2.4.4). The same dynamics have been formulated in the netlist code of PSpice to model the circuit. The Figure 4.1 shows a schematic representation of the netlist code of the Hodgkin Huxley model. As shown in

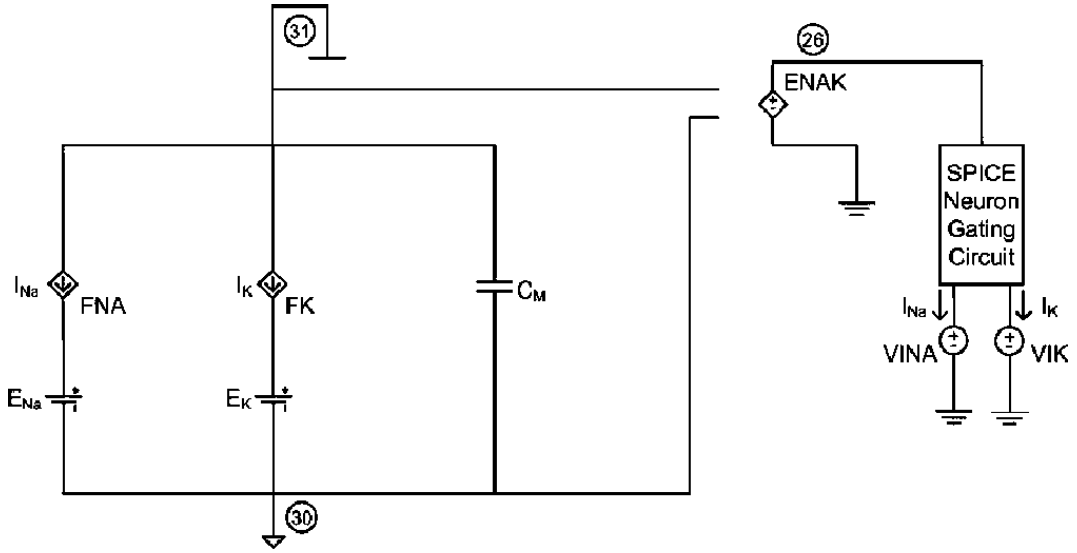

FIGURE 4.1: Hodgkin Huxley Cell and neuron gating circuit Szlavik et al. (2006)

the Figure 4.1 the Nernst potential (the potential at which there is no net flow of that particular ion from one side to another) of Sodium(Na) and Potassium(K) ion channels are scripted by E_{Na} and E_K variables. The capacitance of the membrane is scripted by C_M. The FNA and FK are two current-controlled control sources used to model the propagation of Na and K currents I_{Na} and I_K respectively. The magnitudes of Na and K currents are determined by the dynamics of gating variables represented in a gating circuit model as shown in Figure 4.2. A voltage-controlled voltage source ENAK with a unitary gain is modelled to detect potential change across the inner (node 31) and the outer surface (node 30) of the cell and generate an equivalent potential across the gating circuit. The current is generated in the gating circuit and passed to the Na and K channel by VINA and VK, the zero potential generators. Ionic currents from the current-controlled current source FNA and FK generates the membrane potential across inner and outer membranes. The activity of the m, h and n gates are modelled in the neuron gating circuit as shown in Figure 4.2. The rate constants α_n and β_n (description of rate constants are given in Chapter 2 Section 2.4.4) associated with gate n are defined by

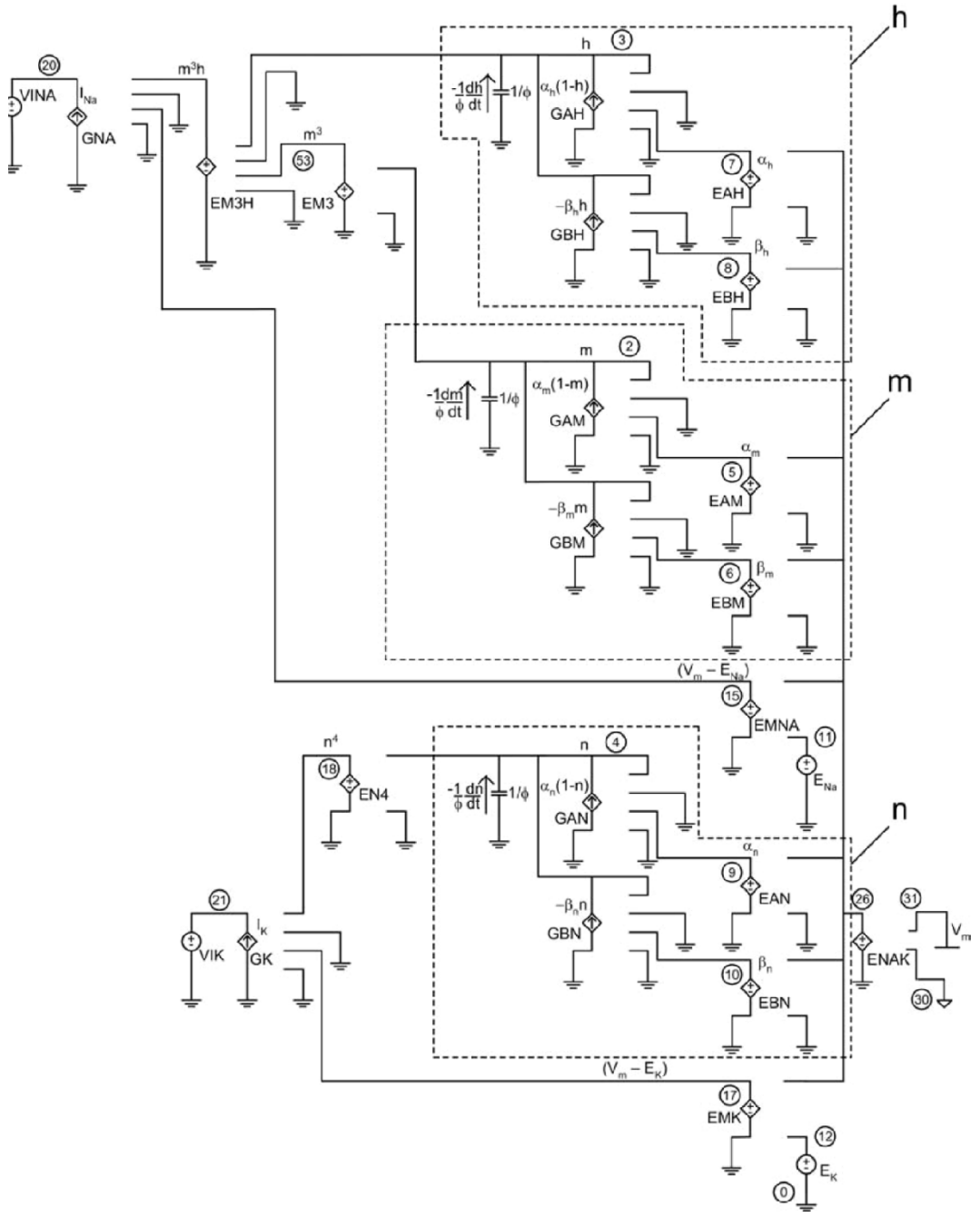

FIGURE 4.2: Circuit Design for gating variables Szlavik et al. (2006)

the voltage-controlled voltage sources EAN and EBN. These controlled voltage sources generate an output based on the membrane potential control voltage. The rate constant equations used in our PSpice model, are shown in Equation 4.1 and Equation 4.2 where V_m in these equations is the membrane potential in millivolts. Both of these equations contain terms associated with the membrane potential which is implemented in the voltage-controlled voltage source.

$$\alpha_n = \frac{-0.01(V_m + 50)}{e^{[-0.1(V_m+50)]} - 1} \tag{4.1}$$

$$\beta_n = 0.125e^{[-0.0125(V_m+60)]} \tag{4.2}$$

The rate constants associated with the m and h gates are shown in Equation 4.3 to Equation 4.6.

$$\alpha_m = \frac{-0.1(V_m+35)}{e^{[-0.1(V_m+35)]}-1} \tag{4.3}$$

$$\beta_m = 4e^{(\frac{(-V_m+60}{18})} \tag{4.4}$$

$$\alpha_h = 0.07e^{[-0.05(V_m+60)]} \tag{4.5}$$

$$\beta_h = \frac{1}{1+e^{[-0.1(V_m+30]}} \tag{4.6}$$

The voltage-controlled current sources GAN and GBN along with the capacitor, implement the rate equation associated with the n gate as shown in Equation 4.7. The capacitor provides the differential operation associated with the potential, which is the gating variable. The other terms in the equation are formed using the polynomial feature available in SPICE.

$$\frac{dn}{dt} = T.\alpha_n(1-n) - T.\beta_n n \tag{4.7}$$

Temperature dependence of the HH- model is included using the scaling constant T. The rate equations associated with the other two gating variables m and h are shown in Equation 4.8 and Equation 4.9, respectively

$$\frac{dm}{dt} = T.\alpha_m(1-m) - T.\beta_m m \tag{4.8}$$

$$\frac{dh}{dt} = T.\alpha_h(1-h) - T.\beta_h h \tag{4.9}$$

The gating variable n is used as the control voltage for the voltage-controlled voltage source EN4. This controlled source is used to generate a potential that is equivalent to the fourth power of the gating variable. The voltage-controlled current source GK takes, as control inputs, n^4 , as well as the difference between the transmembrane potential V_m and the Nernst equilibrium potential for potassium E_K . A voltage-controlled voltage source EMK is used to generate a potential equivalent to $(V_m - E_K)$. The voltage-controlled current source GK is used to generate a current equivalent to the total potassium ionic current using the SPICE polynomial feature. A current is generated by this controlled source that is equivalent to $\overline{G_k}n^4(V_m - E_K)$, where $\overline{G_k}$, computed for the cell surface area as per Table 4.1, is the maximum potassium conductance. The m gate increases conduction, and the h gate decreases conduction with the increase in membrane activation. Thus the circuit model of NR was destined as a node of the circuit considering the parameter values as given in Table 4.1. The quantities in the circuit that needed defining were the initial conditions to the gating variables, the concentration of potassium inside and outside the cell, the temperature, the cell capacitance, as well as the conductance of the potassium and sodium channels. All of these parameters have

Parameter	Value
m_0	0.0393
h_0	0.6798
n_0	0.2803
c^o_{Na}	491.0 mM/L
c^i_{Na}	50.0 mM/L
c^o_K	20.11 mM/L
c^i_K	400.0 mM/L
G_{Na}	120.0 mS
G_K	36.0 mS
C_E	1.0 pF

Table 4.1: Parameters for node of Ranvier

been previously published (Hodgkin and Huxley (1952); Stephanova and Bostock (1996); Szlavik et al. (2006); Weiss (1994)) and are presented in Table 4.1. The expressions for the α and β are appropriate of temperature of 6.3^oC as per Hodgkin and Huxley (1952). But, in our model, we scaled them with temperature scaling factor T to adapt to any other temperatures as well. For validating our model results with published data, we kept the temperature factor, T, of $0.26E-3$ at 18.5^oC (Bunow et al., 1985). The Figure 4.3.(a) shows the schematic view of the circuit model of a node designed using resistors, capacitors and conductors.

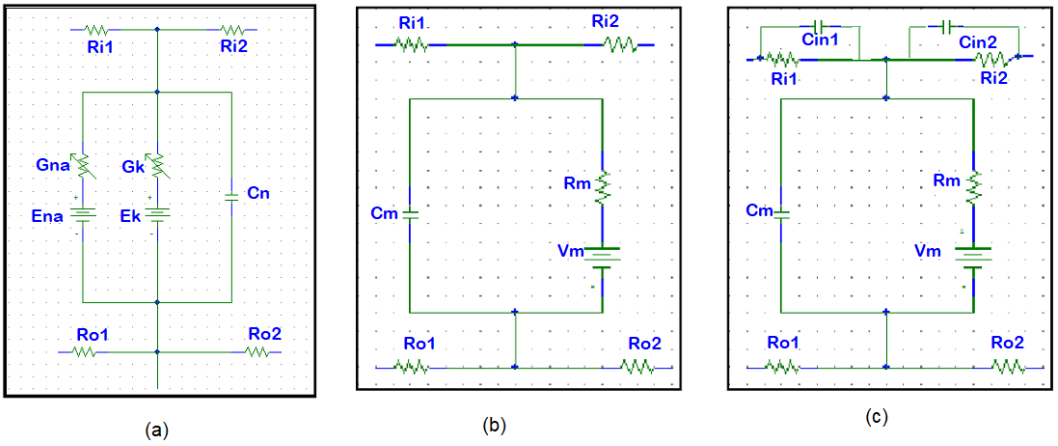

FIGURE 4.3: (a)The schematic diagram of NR, (b) The schematic diagram of IN of Pure resistive circuit, (c) The schematic diagram of IN of resistive-capacitive circuit used for modelling intracellular fluid

4.2.2 Circuit modelling of myelin sheath as a passive cable model

The myelinated node or the internode has been designed as a resistance-capacitance (RC) circuit to represent the membrane potential of the core conductor model (see Chapter 2.4.5) of distributed leaky cable Fitzhugh (1962). A dc voltage source V_m is used in the circuit to create the resting membrane potential. The voltage source V_m is

put in series with the resistance R_m of the myelin sheath. The resistor R_m and voltage source V_m in series models the conductance of ions across the myelin. The myelin sheath has the ability to store the charge represented by a capacitor. The battery and resistor series network is put in parallel with the capacitor C_m to model the properties of the myelin sheaths permeability. There are two different types of modelling approaches available in the literature for modelling axonal fluid in an axon: (1) pure resistive, (2) resistive-capacitive Tsubo and Kurokawa (2018). Here, we are incorporating both of these approaches in our model design. The Figure 4.3.(b) shows the circuit model of an internode of pure resistive circuits and Figure 4.3.(c) shows the circuit model of an internode of a resistive-capacitive circuit. The parameter values for the RC circuit has been used from FMN, PNS ($A\alpha - 20\mu m$, $A\alpha - 13\mu m$, $A\beta - 12\mu m$, $A\beta - 6\mu m$, $A\delta - 5\mu m$,$A\delta - 1\mu m$) and CNS (SBC, GBCMed, GBCLAt) axons as shown in Table 4.2. The SBC, GBCMed, GBCLat axons have different internode axon diameters than the diameter of the node. The internode axon diameters of SBC, GBCMed, GBCLat axons are $1.35\mu m$, $2.41\mu m$ and $3.06\mu m$ respectively. These internode axon diameters are used for their parameters value calculation in Table 4.2. The values of PNS axons are obtained from Tsubo and Kurokawa (2018) and parameter values of CNS axons are obtained from Ford et al. (2015) and parameter values of FMN are sourced from Hodgkin and Huxley (1952).

4.2.3 Circuit arrangements of nodes and internodes

The circuit designs of NR and IN were saved as sub-circuit library files. PSpice supports the creation of subcircuit library files. Each subcircuit design has input and output ports specified, through which it can interact with the overall circuit design. The design of a subcircuit is useful when a specific circuit design is being used many times in the overall circuit design. Another added advantage of the subcircuit file is, it quickly allows any modification of the parameters of the model. The subcircuit library files allow for the modelling of any size neuron with ease. An axon length can be modified by adding more nodes connected by internode segments. For example, we wanted to model an IN of length 2mm. So two IN subcircuits were connected to the model the 2mm internode segment. The whole circuit of a single myelinated axon was designed by interconnecting the subcircuit for node and internodes through their input and output ports as shown in Figure 4.4. The output ports of the subcircuit of the node were connected to input ports of the subcircuit of 2mm IN and then output ports 2mm IN were connected to input ports of the subcircuit node. The NR and IN both have input and output ports in the inner conductor and outer conductor. The inner conductor models the inside of the axon and the outer conductor models the extracellular fluid. The outer conductor resistances as shown in Figure 4.3 were set to 1 to model it as connecting wires with very low resistance compared to axoplasm resistance (1Ω much less than $14M\Omega$ mm axoplasm resistance Fitzhugh (1962)). The inner conductor resistances were set as $7M\Omega$, half of $14M\Omega$

Name	$D_{NR}(\mu m)$	$D_{IN}(\mu m)$	$R_L(M\Omega/mm)$	$C_L(pFmm)$	$R_{MY}(M\Omega mm)$	$C_{MY}(pF/mm)$	$L_{IN}(mm)$
FMN	10	14	14	–	$250-400$	$1-1.6$	2
$A\alpha$	20	28	3.5	74	320	1.3	2
$A\alpha$	13	18.2	8.28	31	320	1.3	1.3
$A\beta$	12	16.8	9.72	27	320	1.3	1.2
$A\beta$	6	8.4	38.89	6.7	320	1.3	0.6
$A\delta$	5	7	55.6	4.7	320	1.3	0.5
$A\delta$	1	1.4	1,400	0.19	320	1.3	0.1
SBC	0.85	1.8	768.17	0.34	320	1.3	0.164
GMCM	1.5	3.2	241.04	1.08	320	1.3	0.239
GBCL	1.68	4.0	149.52	1.73	320	1.3	0.198

Table 4.2: Parameters for internode for different types of axons (The parameter values of PNS axons are obtained from Tsubo and Kurokawa (2018) and dimensions of CNS axons are obtained from Ford et al. (2015) and parameter values of FMN are sourced from Hodgkin and Huxley (1952). These data were obtained by applying the conversion formulas to axons of various diameters as it is mentioned in Tsubo and Kurokawa (2018))

mm longitudinal axoplasm resistance. The inner conductor resistance is set to half the required resistance because when two resistors are connected in series the resistances are additive. The terminal resistance of the circuit was set to a high resistance value,

$10^{20} M\Omega$ to model the boundary condition. Here, we described the circuit arrangement with the values of FMN. Similarly, we developed the model for all other axon types we have used in our experiment. The Figure 4.4 shows a schematic of the connections of subcircuits.

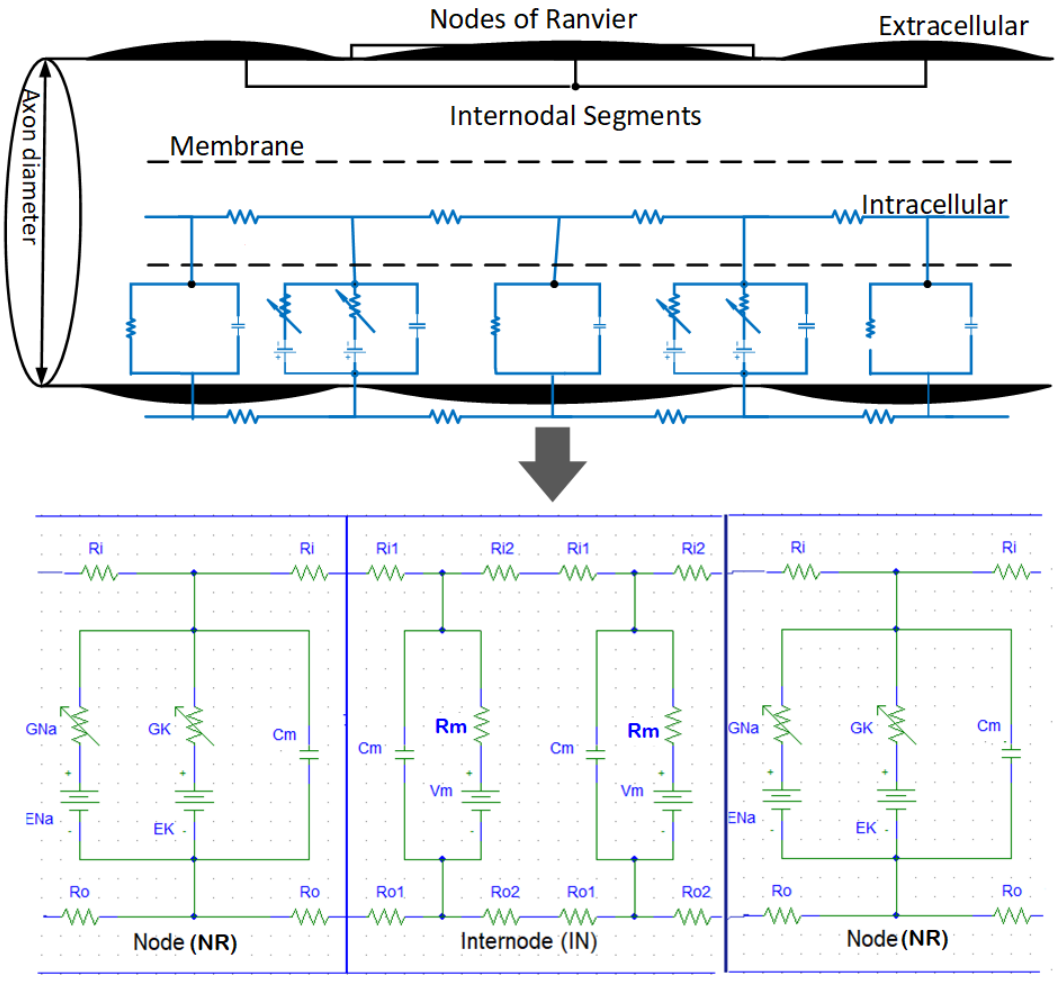

FIGURE 4.4: The schematic diagram of connections between NR and IN

4.2.4 Circuit simulation

To stimulate the circuit, a current pulse of 6nA was applied to the inner conductor. The applied current was sufficient to increase the membrane potential above the threshold and generate an action potential to propagate down the axon fibre.

4.2.5 Result and validation of the model with respect to published experimental data

Here are the lists of results that we have observed by perturbing the circuit with input stimulus current:

- ***Generation of action potential***: The circuit required a minimum 6nA stimulus current to generate an action potential. Input current less than 6nAmp was not sufficient to generate the action potential. The Figure 4.5 shows the generated action potential in the node with respect to the given stimulus current. The x-axis is showing time and the y-axis is showing the membrane voltage. As shown in the Figure 4.5 the resting potential of the membrane is -65mV, the peak voltage in depolarization is 53mV and the membrane voltage in repolarization is -70mV.

- ***Activation of m, h and n gates***: The Figure 4.6 shows the activation of m, h and n gating variables during action potential generation. The green line shows the m-gating variable, the red line shows the h-gate activation variable, and the blue line shows the activation of the n-gate.

- ***Dynamics of Na, K and capacitive currents***: The Figure 4.7 shows the Na,K,and capacitive currents across the membrane. These curves are showing different dynamics of HH cell that match with the experimental output of Hodgkin and Huxley (1952).

- ***Temporal distribution of action potential***:Figure 4.8 shows the temporal propagation of action potential through 5 nodes. The green curve is generated from 1st node V(xsub2.26); red is from 2nd node V(xsub4.26); purple is from 3rd node V(xsub6.26); yellow is from 4th node V(xsub8.26) and pink is from 5th node V(xsub10.26). The figure shows how the spikes are propagating in time scale.

- ***Conduction velocity***: CV is an important aspect of nerve conduction studies. It is the speed at which an impulse propagates down an axonal pathway. We computed the CV of impulse propagation from one node to another for FMN, PNS ($A\alpha - 20\mu m$, $A\alpha - 13\mu m$, $A\beta - 12\mu m$, $A\beta - 6\mu m$, $A\delta - 5\mu m$,$A\delta - 1\mu m$) and CNS (SBC, GBCMed, GBCLAt) axons. The description of these of axons are given in Table 2.3 in Chapter 2. The longitudinal propagation velocity CV is calculated from the measured propagation time PT and internodal myelin length L, using the following equation:

$$CV = \frac{L(mm)}{PT(ms)} \tag{4.10}$$

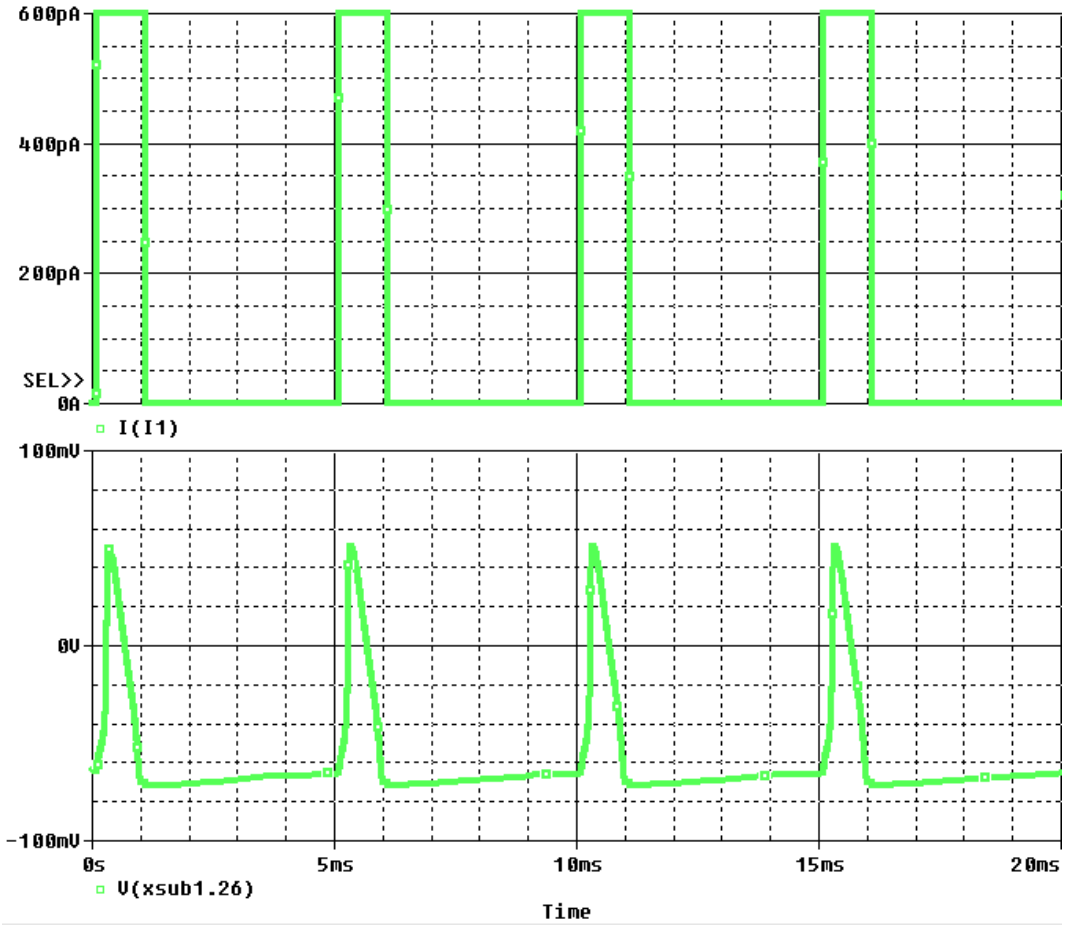

FIGURE 4.5: Action potetial generated at nodes of Ranvier; V(xsub1.26): Membrane potential; I(I1): Input current

Table 4.3 displays the conduction velocity of different axon types computed in both resistive and resistive-capacitive models along with published values available in the literature. We found that the computed value of CV of FMN axons obtained from resistive model matches with the value published in literature Binczak et al. (2001) and within range in experimental measurement by Tasaki and Fujita (1948). The computed value of CV of PNS and CNS axons obtained from resistive-capacitive model matches with the value published in literature Tsubo and Kurokawa (2018); Ford et al. (2015). We also plot the CV values of different axon types in a bar chart form in Figure 4.11. From the bar chart, we also observed that CV decreases with a decrease in axon diameter. As the results obtained from the resistive-capacitive model is giving more accurate values with published data for PNS and CNS axons and results obtained from the resistive model result is matching with FMN axon, we selected the resistive-capacitive model for PNS-CNS axons and resistive model for FMN axons for basic models for our experiments and explorations.

- ***Maximum myelin length***: Our simulation result shows that after 12 IN segments, the signal was failed to propagate to the next node. That means 11mm

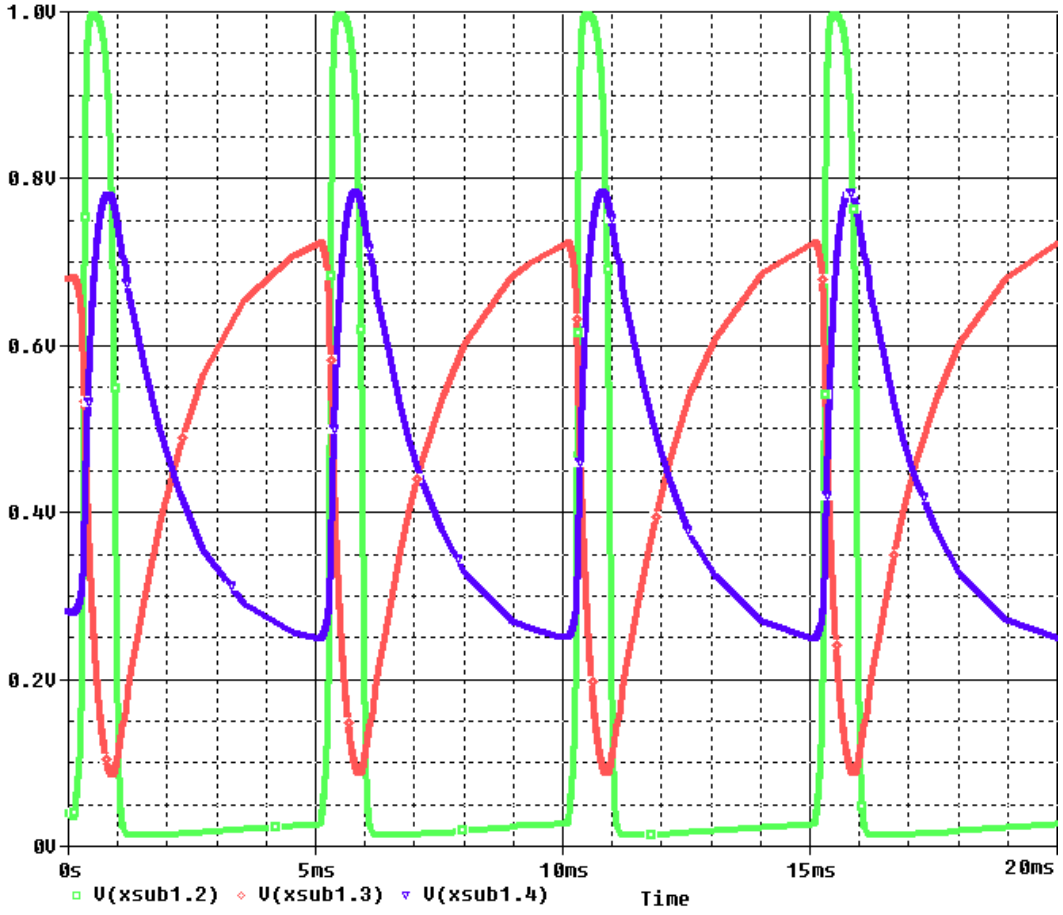

FIGURE 4.6: HH neuron node showing m,h, and n gate activation; V(xsub1.2): m variable, V(xsub1.3): h variable, V(xsub1.4): n variable

Axon Types	**IN length (mm)**	**CV (m/s) (Published data)**	**CV (m/s) (Resistive model)**	**CV(m/s) (Resistive-Capacitive model)**
FMN	2	28	28.62	-
$A\alpha - 20\mu m$	2	120	112.04	119.35
$A\alpha - 13\mu m$	1.3	80	31.96	80.41
$A\beta - 12\mu m$	1.2	75	27.25	72.62
$A\beta - 6\mu m$	0.6	33	12.92	33.05
$A\delta - 5\mu m$	0.5	30	8.53	29.52
$A\delta - 1\mu m$	0.1	3	0.69	3.14
$SBC - 1.35\mu m$	0.164	4.4	0.97	4.46
$GBMed - 2.41\mu m$	0.239	8.5	2.42	7.11
$GBCLat - 3.06\mu m$	0.198	11.3	4.11	11.22

Table 4.3: Conduction velocity for different axon diameters

of 12 internode segments is Maximum Myelin Length (MML) beyond which the signal fails to bring the adjacent node above its threshold voltage and causes failure of signal propagation to the next NR. This happens because as myelin length increases current flowing through axonal fluid gets decreased, and next NR does

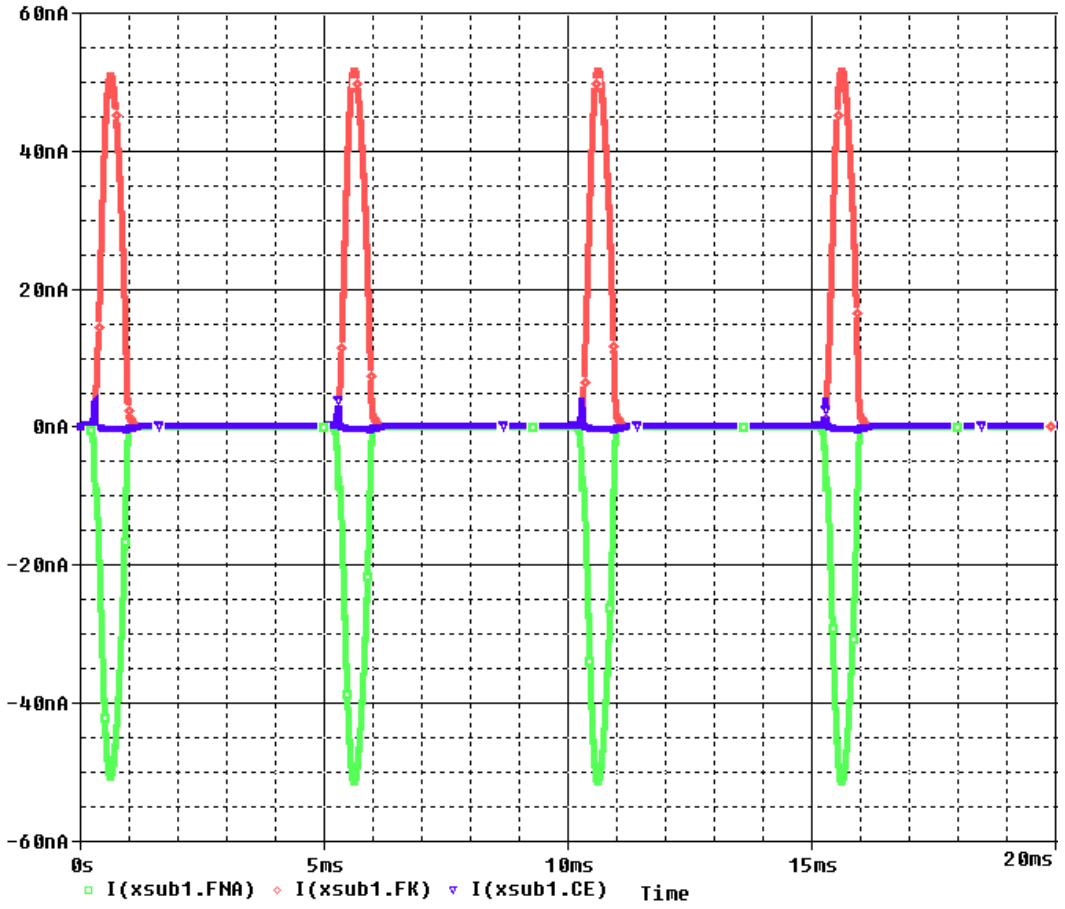

FIGURE 4.7: Na:I(xsub1.FNA), K:I(xsub1.FK) and capacitive: I(xsub1.CE) currents dynamics during generation of AP

not get enough current to bring its membrane voltage potential above threshold voltage to generate an impulse. Figure 4.9 shows the membrane potentials at two adjacent nodes where signal propagation fails to occur. Figure 4.10 shows dynamic of membrane potentials through internode when signal is successfully propagated to next node Figure 4.10.(a); when signal fails to spread to next node Figure 4.10.(b). The length of 12 internode segments is 12mm here. This dynamic of signal propagation failure correlates with the description given in Binczak et al. (2001). Similar to FMN, we determine the maximum myelin length of signal propagation for other 6 different types of PNS and 3 different types of CNS axons and show in Figure 4.2.5.

- ***Conduction velocity and myelin length***: Here we explored conduction velocity values for different myelin lengths of an axon up to MML. In Figure 4.13 we placed the conduction velocity values calculated from the resistive-capacitive circuit model at various myelin lengths for all axon types. We can see that initially up to a certain length of myelin, CV decreases with the increase of myelin length. Then it gets increased and then again starts decreasing. For example for PNS-Aα-20μm diameter axon, the values of CV decrease with increased myelin length up to 15mm.

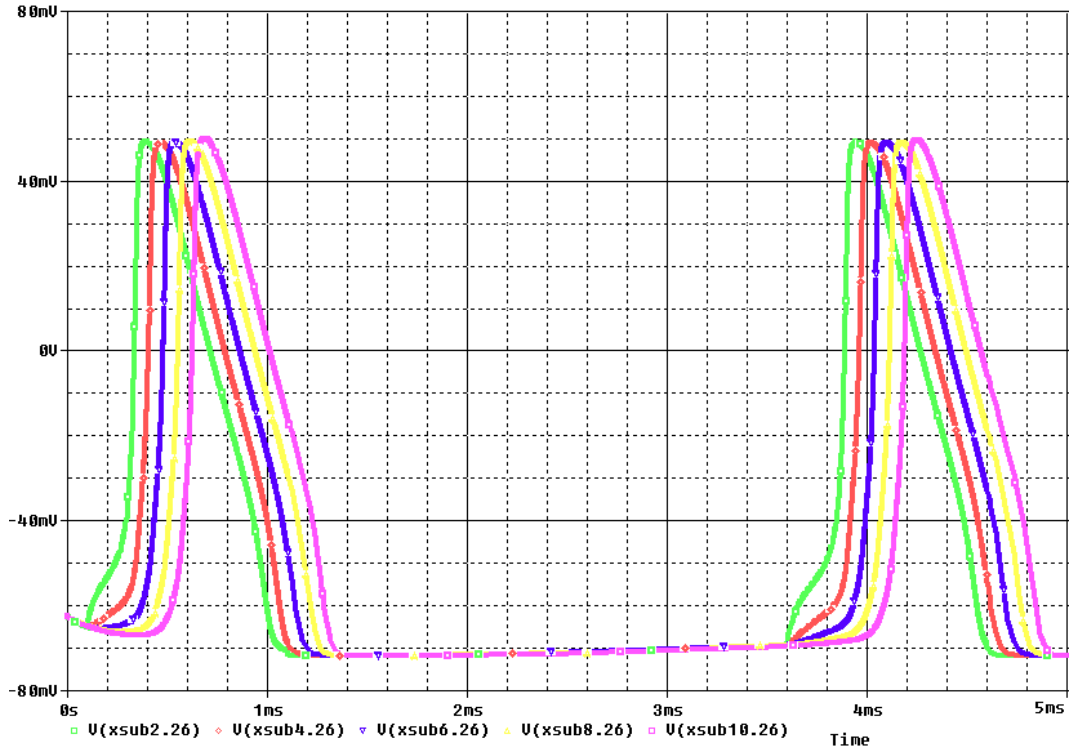

FIGURE 4.8: Temporal distribution of action potential

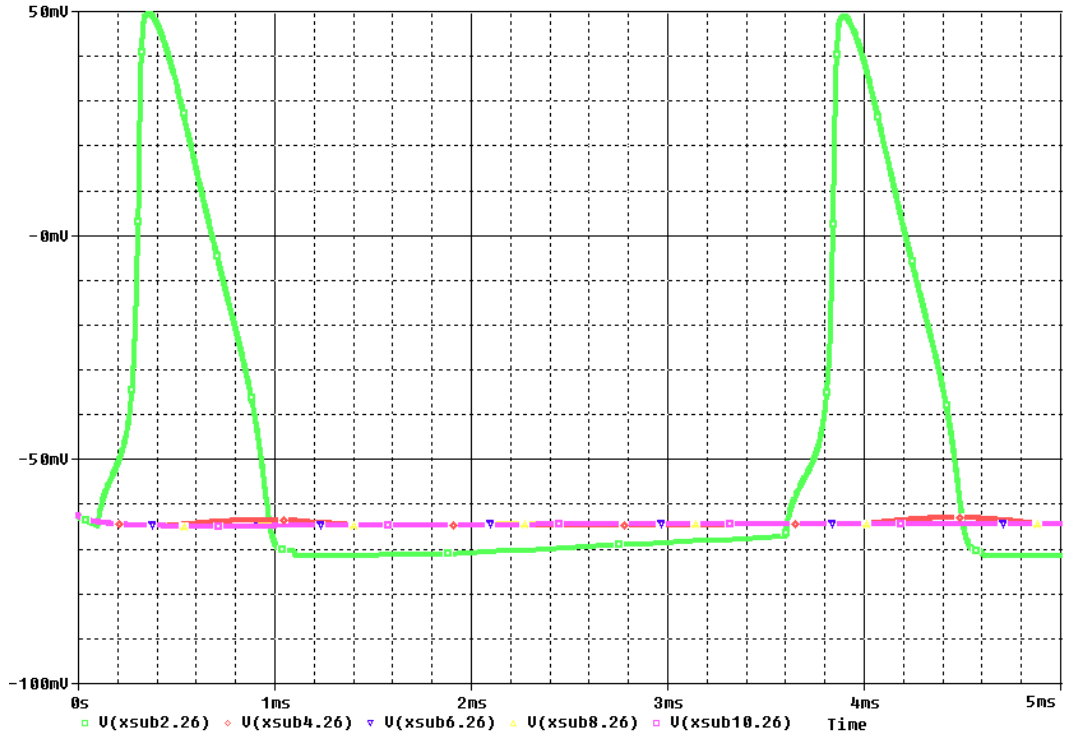

FIGURE 4.9: Action potential failed to reach threshold to the next node

After that for 16mm of myelin length CV value gets increased and then again it starts decreasing. This happens due to the loss of an impulse; which couldn't fire

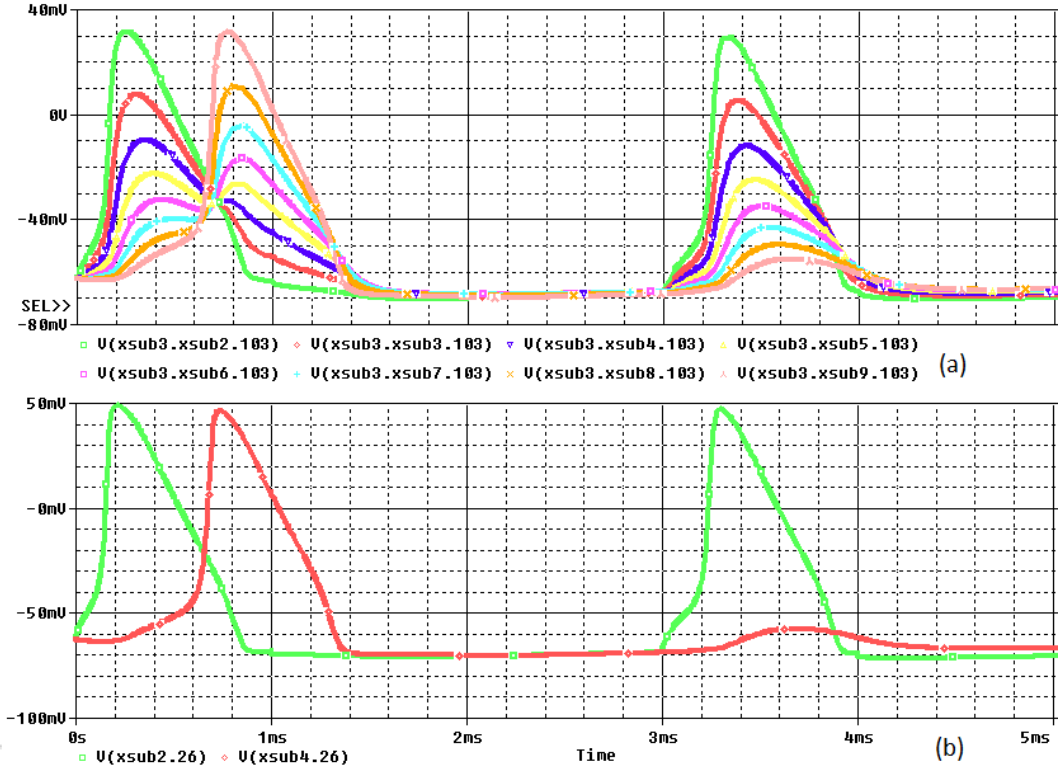

FIGURE 4.10: Dynamic of membrane voltage at various internode length when action potential (a) is successfully propagated to next node; (b) has failed to reach next node

an AP but resulted in some Na^+ ion channel activation at the NR node. For example; when myelin length is 16mm, some of the impulses from the AP pulse train couldn't get generated due to the low strength of the ionic current flowing through longer myelin length distance; but that stimulus current cause some Na^+ ions concentration inside the cell by opening their channel in NR. As a result, the membrane potential at NR reaches the threshold voltage quickly during the generation of the next AP. That in effect increased the CV of the axon. So, it shows that the Na^+ ions play an active part in CV and causes a non-linear behaviour in CV. As we can see from Figure 4.13, at 16mm for $A\alpha - 20\mu m$ axon, 9mm for $A\alpha - 13\mu m$ axon, 6mm for $A\alpha - 12\mu m$ axon, 0.4mm for $A\alpha - 1\mu m$ axon, 0.7mm for SBC axon, 2mm for GBCLat axon and 10mm for FMN axon, the increase of CV happens, but after that again CV starts decreasing. So, we can conclude that generally, CV decreases with the increase of myelin length if Na^+ concentration is constant, else it exhibits a non-linear behaviour.

4.3 Frequency response analysis of single myelinated axon

Literature shows, it is still an open question why two brain ROIs, which are structurally connected, are not sometimes functionally connected. In our work, we are trying to find an answer to this question by analyzing the signal propagation in the axon bundle in the

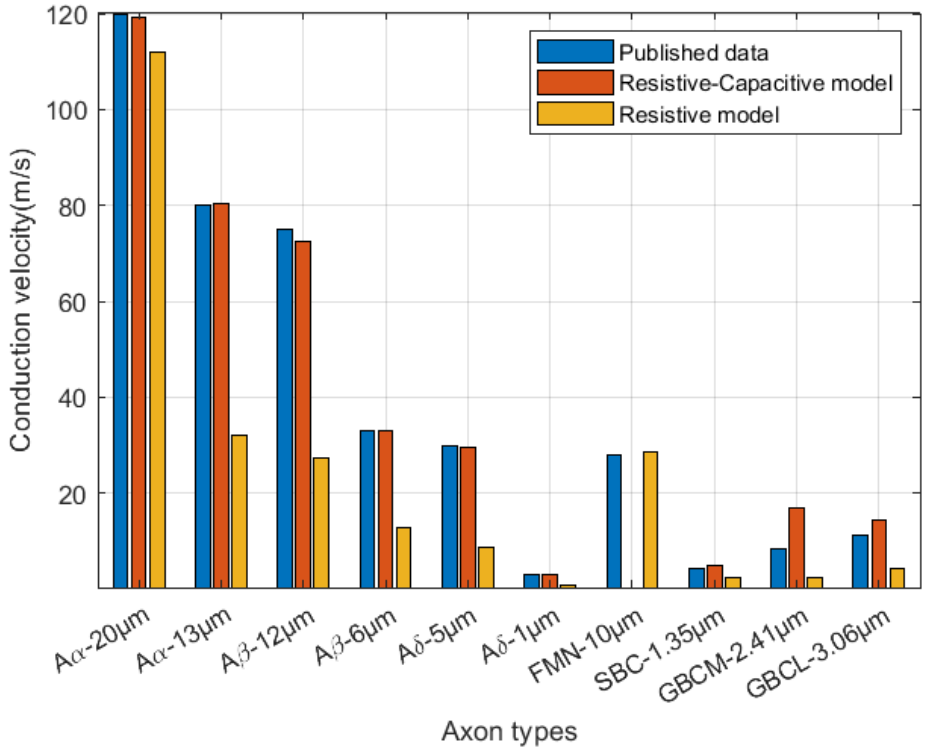

FIGURE 4.11: Conduction velocity of different axon types; conduction velocity decreases with reduction of axon diameter

frequency domain. Our hypothesis is that analyzing signal propagation in the frequency domain may exhibit filter like characteristics of passing selective signals through the system. So, we are trying to devise a model that can explain this phenomenon from the perspective of phase and the frequency characteristic of signal transmission. In the previous section, we have built a circuit model of the single axon and analyze its signal propagation dynamics in the time domain, and validate our model with published data. Here, our objective is to characterize that model with a system definition and analyze signal propagation characteristics through the axon in the frequency domain.

4.3.1 Modelling internode in simscape in MATLAB

Myelin is the fatty substance that surrounds axons to insulate them and increase the rate at which electrical impulses (called AP) are passed along the axon. Nodes of Ranvier are uninsulated parts of the axon that are highly enriched in ion channels, allowing them to participate in the exchange of ions required to regenerate the AP. In saltatory conduction along the myelinated axon, AP seems to "jump" from one node to the next along the axon, resulting in faster conduction of signal. That implies the responsible part of passing impulses through the axon is the myelin, as the job of the nodes is to regenerate the attenuated impulse passed by myelin. So, our focus here is on the myelin part of the axon to analyze the signal transmission properties in the frequency domain.

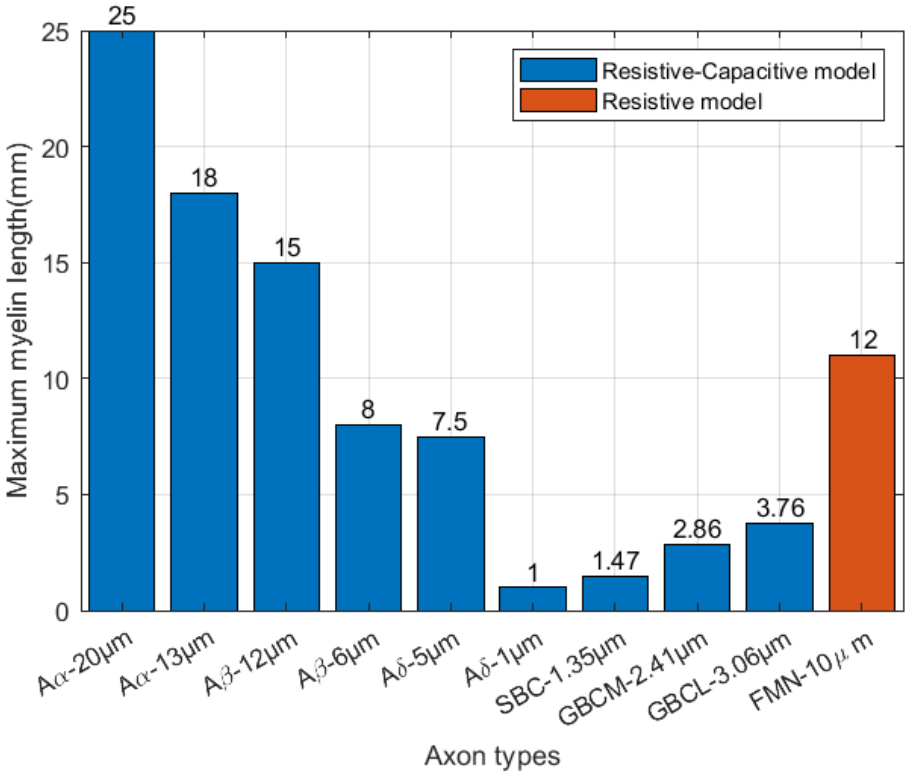

FIGURE 4.12: Maximum myelin length: The length of myelin internode till which the impulse signal propagate from one node to another node without failing, If the length of myelin is bigger then this then the impulse signal will not propagate to the next node; The value of maximum myelin length for different types of axons in both resistive and resistive-capacitive models

Simscape helps to create a model of a physical system within the Simulink environment. With Simscape, physical components models are built based on physical connections that directly integrate with block diagrams other modelling paradigms. The advantage of modelling in Simscape is, it provides more complex components and analysis capabilities. In this section, we have modelled the IN section of the axon using Simscape modelling. During circuit modelling, in the previous section, we have modelled the myelinated IN as a resistive capacitive (RC) circuit to represent it as a passive cable as described by Fitzhugh (1962) in his work. We have followed the same modelling here to design the Simscape circuit. Simscape has a repository of device elements. We have taken the resistor, capacitor and dc voltage from the repository and connected them as shown in Figure 4.14.(b) to model one segment of the internode. The dc voltage is used in the circuit to create the resting membrane potential. The dc voltage source is put in series with the myelin sheaths resistance. A resistor and dc voltage in series models the conductance of ions across the myelin. The myelin sheath has the ability to store charge represented by a capacitor. The battery and resistor series network is put in parallel with the capacitor to model the properties of the myelin sheaths permeability. The parameter values of the resistor, capacitor, battery and other parameters were obtained from Fitzhugh (1962); Tasaki and Frank (1955); Tsubo and Kurokawa (2018)

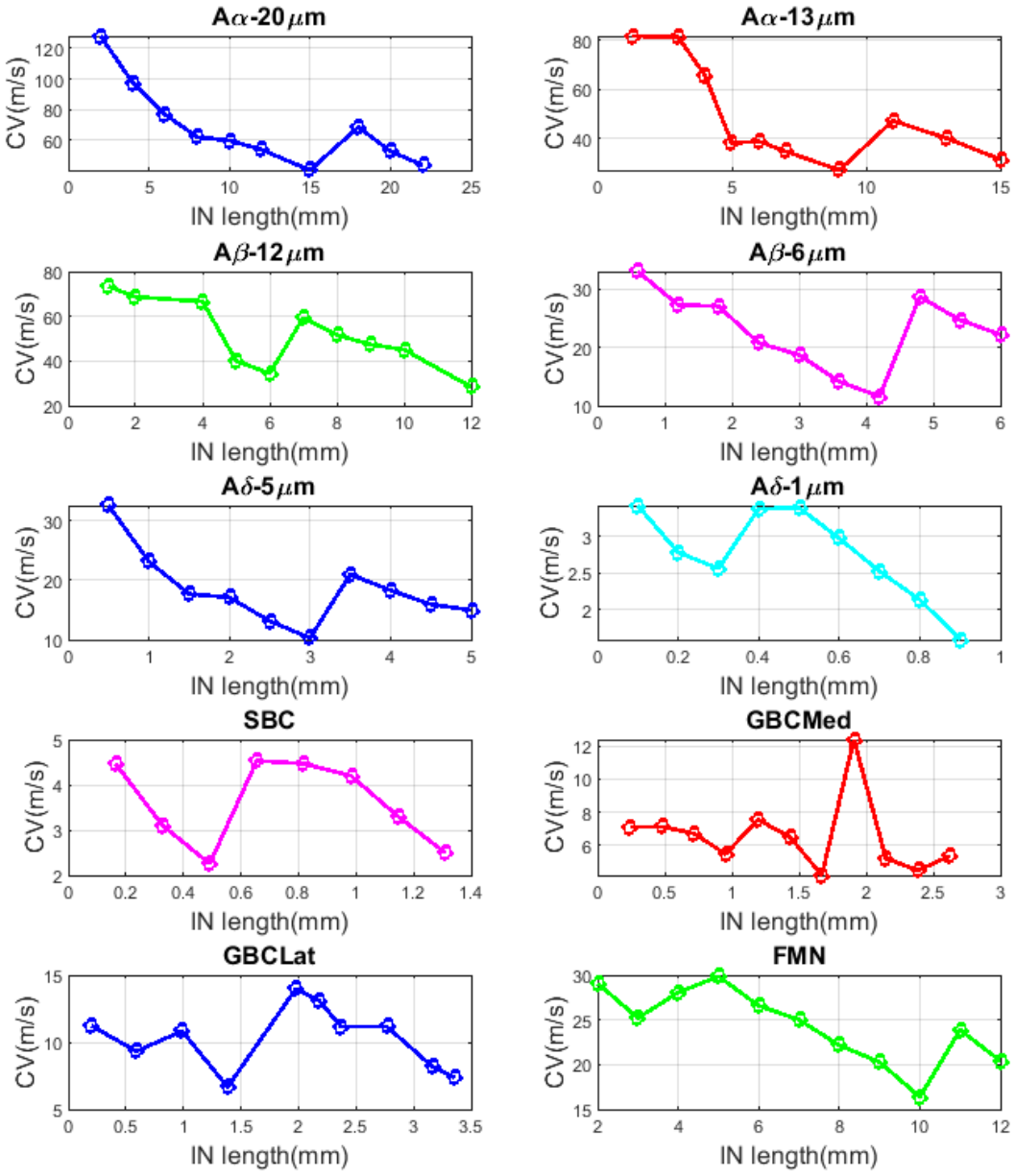

FIGURE 4.13: Conduction velocity at various internodal lengths

and provided in the Table 4.2. To model the 2mm of internode length these segments are connected with each other to form a chain-like structure as shown in Figure 4.14.(a). The circuit was simulated with impulse function and the response was used to determine the frequency characteristics of the system.

4.3.2 Model simulation and impulse response generation

The frequency response of a system can be measured by measuring its impulse response. Since the impulse function contains all frequencies, the impulse response defines the

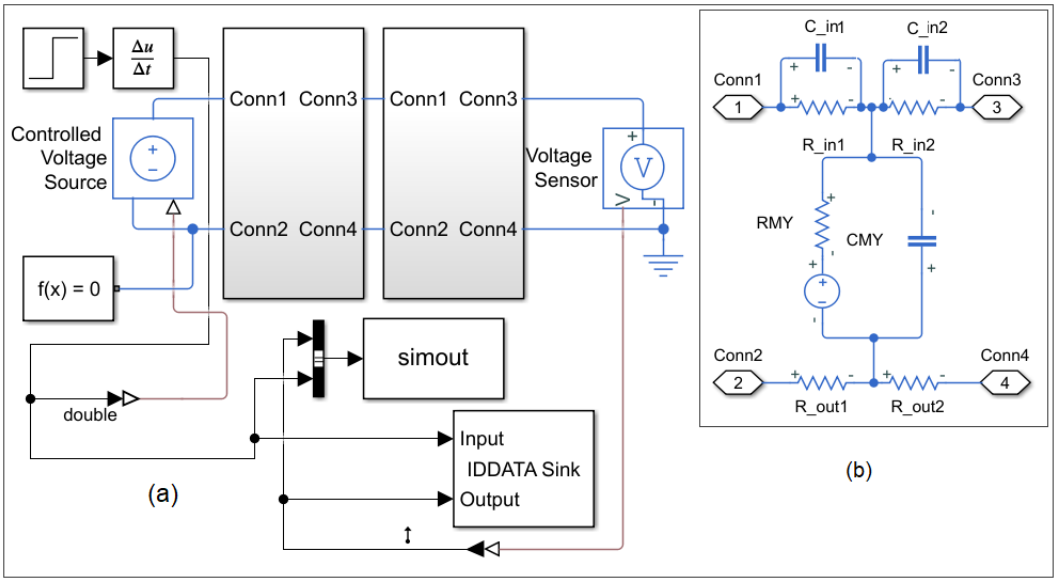

FIGURE 4.14: The Main Model of Internode in simscape

response of a system for all frequencies. To generate the impulse response for the internode, a derivative of a unit step function has been used, as shown in Figure 4.14. The initial and final values of the step function were as 0 and 1. The step time was set as 0.001 and the same as the sample time of the simulation. The input and output both were captured from the Simulink environment used later in the workspace to estimate the transfer function from them.

4.3.3 Estimation of the transfer function

A Transfer Function fully describes a control system by defining its 'Order', 'Type' and 'Frequency response'. If the impulse response of a system is given by h(t), then the transfer function of a system is given by H(s), where H(s) is the Laplace Transform of h(t). We simulated the system with impulse input and took the input and output of impulse function to MATLAB and estimated the transfer function by providing value for its Poles and Zeros. Poles and Zeros of a transfer function are the important frequencies for which the value of the denominator and numerator of transfer function becomes zero respectively. They are the roots of the characteristic equation of the system. By varying the values of the poles and the zeros, we checked the accuracy and stability of the transfer function. We checked the 'FitPercent' value to estimate the accuracy of our system model. The 'FitPercent' value is calculated by the normalised root mean squared error (NRMSE) as shown below:

$$fit = [1 - \frac{\|x - \hat{x}\|}{\|x - \bar{x}\|}] * 100\%$$

Coefficients	FMN	PNS Axon	SBC Axon	GBCLat Axon
C1	-897.4	1.927e13	-2.241e14	-6.668e12
C2	- 4.916e06	3.101e16	- 3.576e17	- 1.113e16
C3	5836	8.835e17	- 3.065e18	- 9.203e17
C4	6.113e06	1.239e10	1.463e11	4.189e09
C5	-	3.97e13	4.644e14	1.379e13
C6	-	3.236e16	3.706e17	1.191e16
C7	-	9.029e17	3.156e18	9.293e17

Table 4.4: Coefficients of transfer function

where $\hat{x}$ indicates the simulated output, $\bar{x}$ is the mean of the output and x is the measured output. To model the transfer function which can describe the myelin segment most accurately we calculated the prediction ability, the 'FitPercent' value of the transfer function of the system for poles value 1 to 10. The Figure 4.15(a) shows the 'FitPercent' value for FMN, PNS, SBC and GBCLat axons for their unit myelin lengths. The good prediction ability of a system is indicated by greater than 90% fit of the prediction results. So, we build an algorithm to select the smallest value for poles (other than pole 1) for which 'FitPercent' is more than 90% fit and for each poles we checked the system for zeros value 1 to pole minus one. We selected the value for zeros based on the best consistent results of frequency response for all myelin lengths. The higher value of poles gives a more accurate estimation of the system but increases the complexity of the system, so we tried to pick the lowest number of poles while the percentage of fit is more than 90. With that logic, we found out that the value of the poles for the system function for the FMN axon as 2, poles value for the PNS axon and the SBC axons as 4 and poles value for GBCLat axon as 5; are the lowest values which are giving 'FitPercent' value more than 90%, other than poles 1. But, when we observed the frequency response curve of all the axons for all myelin lengths we found out that for FMN axons poles value 2, zeros value 1 and for PNS, SBC and GBCLat axons poles value 4 and zeros value 2 are giving the most consistent frequency response characteristics as shown in Figure 4.16. Thus, for the internode segment of all the axons we generated the transfer functions of the form as shown below:

For FMN axons:

$$H(s) = \frac{C1 * s + C2}{s^2 + C3 * s + C4}$$

For PNS, SBC and GBCLat axons:

$$H(s) = \frac{C1 * s^2 + C2 * s + C3}{s^4 + C4 * s^3 + C5 * s^2 + C6 * s + C7}$$

The values coefficients of the transfer function for all axon types are given in Table 4.4.

4.3.4 Stability analysis

To analyse the stability of the system we used the root locus plot of the transfer function model. The root locus plots of system functions of FMN, PNS, SBC and GBCLat axons are shown in Fig. 4.15(b), where system poles are marked by x, and zeros are marked by o. The location of the poles is shown in s-plane confirms that the system is asymptotically stable and the response of the system is exponentially decaying in nature leading to a stable condition. Hence, we conclude that system design by transfer function model is a stable system.

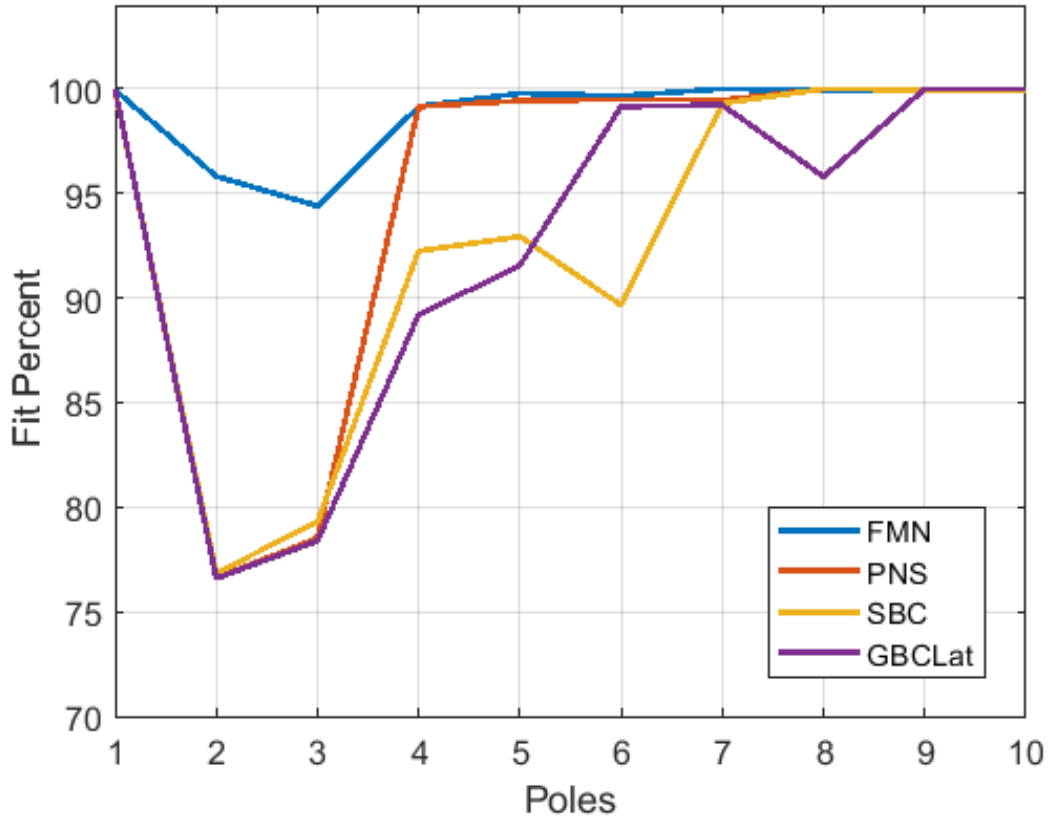

(a)

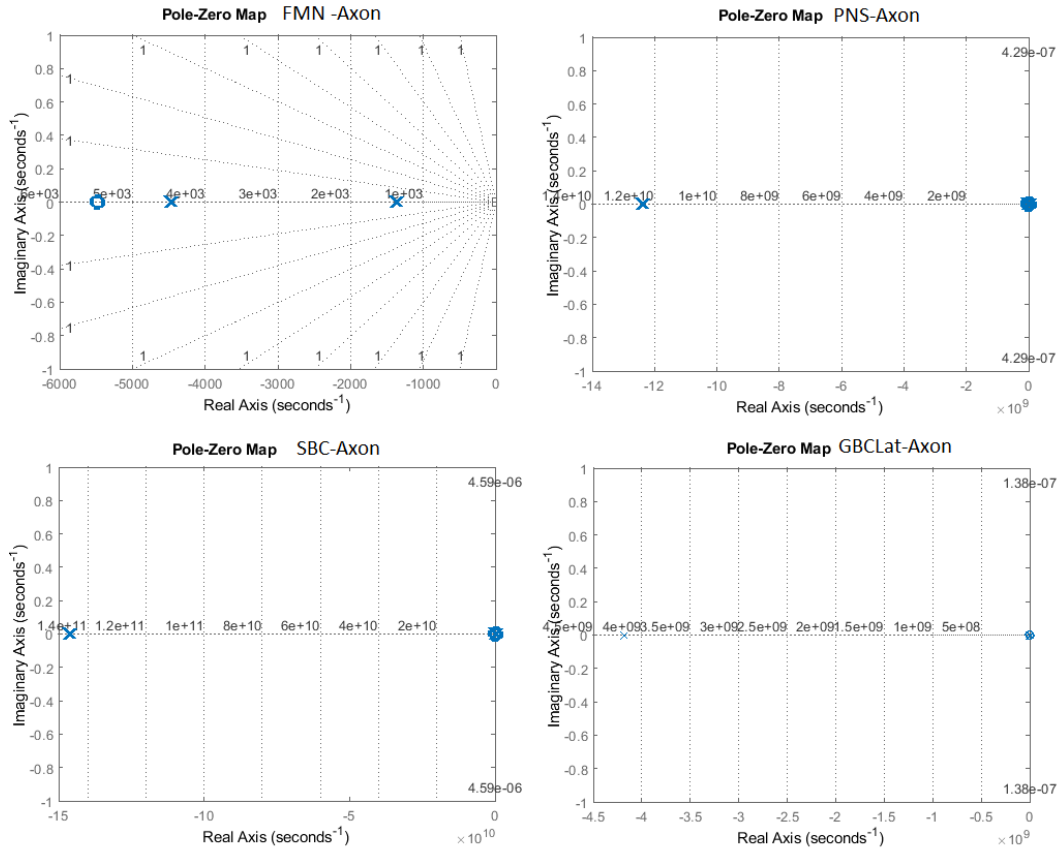

(b)

FIGURE 4.15: (a) The pole-zero plot of the transfer function for all axon types; (b)The pole-zero plot of the transfer function for all axon types

4.3.5 Frequency response analysis

The objective of determining the transfer function for the myelin segment is to obtain the phase-frequency characteristics of the system. In order to do so, we calculated the transfer function of the myelinated segments of a single axon for various lengths of the myelinated section. The frequency response of a system is characterized by the magnitude of the system's response, typically measured in decibels (dB) or as a decimal, and the phase, measured in radians or degrees, versus frequency in radians/sec or Hertz (Hz) as shown below:

$$Gain = 20 * log|\frac{V_{out}}{V_{in}}| \tag{4.11}$$

and

$$Phase = \arctan(\frac{V_{out}}{V_{in}}). \tag{4.12}$$

So here, we obtained gain and phase plots of the transfer functions for the different myelin segments for different axon types by plotting the magnitude and phase measurements on two rectangular plots as functions of frequency in radians/sec. Figure 4.16 shows the plotting of magnitude and phase as a function of frequency for different axon types. The shape of the curves conforms that the system exhibit the behaviour of a low pass filter, which implies that signal of higher frequency will be attenuated and will not be passed through the myelin segments.

4.3.6 Cut-off frequency determination

Next, we calculated the cut-off frequency of the unit myelin segments of each axon to determine up to which frequency the neural signal will be able to propagate through the segments. Ideally, the cut-off frequency is defined as being the frequency point where the capacitive reactance and resistance are equal. When this occurs the output signal is attenuated to 70.7% of the input signal value or -3dB (20 log (Vout/Vin)) of the input. In the case of neural signal, for an action potential to be fired the membrane voltage need to reach the threshold voltage V_{Th} which is the same as -30mV for HH cell, where the resting potential V_{rest} is -70mV and the Nernst or reversal potential V_{Nern} is 50mV. So the magnitude V_{mag} of an action potential is 120mV as per the below rule:

$$V_{mag} = V_{Nern} - V_{rest}. \tag{4.13}$$

Then, to reach the threshold membrane voltage of -30mV the magnitude of an action potential V_{out} needs to be 40mV as per ($V_{out} = V_{Th} - V_{rest}$). Using these values of V_{mag} and V_{out} we calculated the new cut-off frequency for the myelin segments following the Eq. 4.11 which gives us -9dB (20 log (Vout/Vmag) of the gain, which will determine the cut-off frequency of the myelin. Using this calculation, we obtained the value of cut-off frequency for all axon types. We found the value of cut-off frequency of FMN

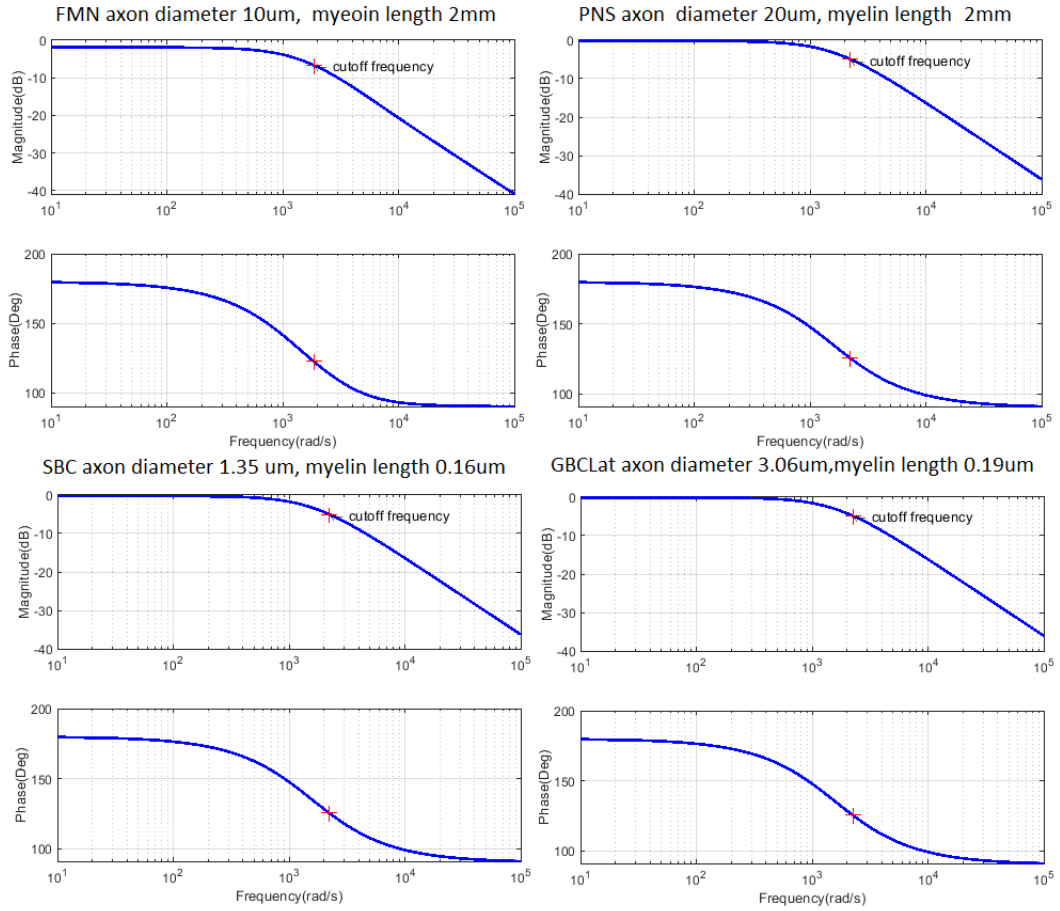

FIGURE 4.16: Gain and phase plots obtained from transfer functions of all axon types for their standard myelin length

axon for 2mm myelin segment as 600.64Hz. In Table 4.5, we put the cut-off frequency of different types of axons calculated from our circuit models. It is observed that the cut-off frequency values for all PNS A group axons are the same. This is because the ratio of inner diameter to myelin length is constant for all those PNS axons. In literature, Debanne et al. (2011) illustrated that depending on the axon type, conduction failures are encountered following moderate (10-50 Hz) or high-frequency (200-300 Hz) stimulation of the axon. The frequency value we obtained from our simulation results is of that scale of frequency values mentioned by Debanne et al. (2011).

4.3.7 Cut-off frequency Vs myelin diameter and length

Here, we investigated the relationship between cut-off frequency of the identified system function of an axon with its myelin length. We found out relation between cut-off frequency of myelin length and axon diameter. In Figure 4.17, the blue line is showing cut-off frequency for axon diameter $1\mu m$, $5\mu m$, $6\mu m$,$12\mu m$, $13\mu m$ and $20\mu m$ for IN length 1mm; and the red line is showing cut-off frequency for axon diameter $3.06\mu m$, $2.41\mu m$, $1.35\mu m$ and $1\mu m$ for IN length 0.1mm. We kept the myelin length 1mm constant

Axon Types	**IN length(mm)**	**Cut-off frequency (Hz)**
FMN	2	600.64
$A\alpha - 20\mu m$	2	758.68
$A\alpha - 13\mu m$	1.3	758.68
$A\beta - 12\mu m$	1.2	758.68
$A\beta - 6\mu m$	0.6	758.68
$A\delta - 5\mu m$	0.5	758.68
$A\delta - 1\mu m$	0.1	758.68
SBC	0.164	752.99
GBCLat	0.198	389.20

Table 4.5: Cut-off frequencies of myelin segment for different axon types

Coeffcients	**FMN**	**$A\alpha$ Axon**	**SBC Axon**	**GBCLat Axon**
a	455.4 (435.4, 475.3)	-1.371e+04 (-1.584e+06, 1.557e+06)	558.7 (431.6, 685.7)	84.23 (-1090, 1259)
b	-258.5 (-337.3, -179.7)	-1.449e+04 (-1.585e+06, 1.556e+06)	-224.9 (-334.2, -115.6)	-313.6 (-1474, 846.9)
c	0.3212 (0.169, 0.4733)	0.0006221 (-0.06733, 0.06858)	0.8125 (0.006366, 1.619)	0.1084 (-0.3788, 0.5956)

Table 4.6: Coefficients with (95% confidence bounds)

for larger diameter axons ,so that we can read the changes of cut-off frequency with diameter. The 1mm IN length is greater than the maximum IN length permitted for signal propagation in smaller diameter axons, so took 0.1mm for smaller diameter axons. Next, we determined the cut-off frequency for different length of IN segments for different axon types and plotted them in a graph. We observed from the results obtained from cut-off frequency calculation that axon types where inner diameter of axon to myelin length ratio is same their cut-off frequency is also same. So, we showed cut-off frequency vs myelin length plot only for axon types FMN, PNS $A\alpha 20\mu m$, CNS SBC and CNS GBCMed. Figure 4.18 shows the graphs cut-off frequency Vs. myelin length of PNS, SBC and GBCLat axons obtained from resistive-capacitive model, and of FMN axon obtained from resistive model. In the Figure 4.18 the blue dashed curves shows the change in cut-off frequency with myelin length and the red curve shows the fitted curve. We performed curve fitting on the cut-off frequency and myelin length data as shown in Figure 4.18 and obtained an mathematical exponential equation for cut-off frequency with myelin length:

$$f_c = a - b * exp(-c * L) \tag{4.14}$$

where f_c is the cut-off frequency and L is the myelin length and values of the coefficients as shown in Table 4.6. In the Section 4.2, we have learned that all axons have a myelin length limit, beyond which the signal fails to bring the adjacent node above its threshold, hence failed to propagate to the next node. That is why here we have calculated the frequency response of the system up to the maximum myelin length allowed for each axon. As it is observed from the graph of Figure 4.16, the myelin segment of myelinated

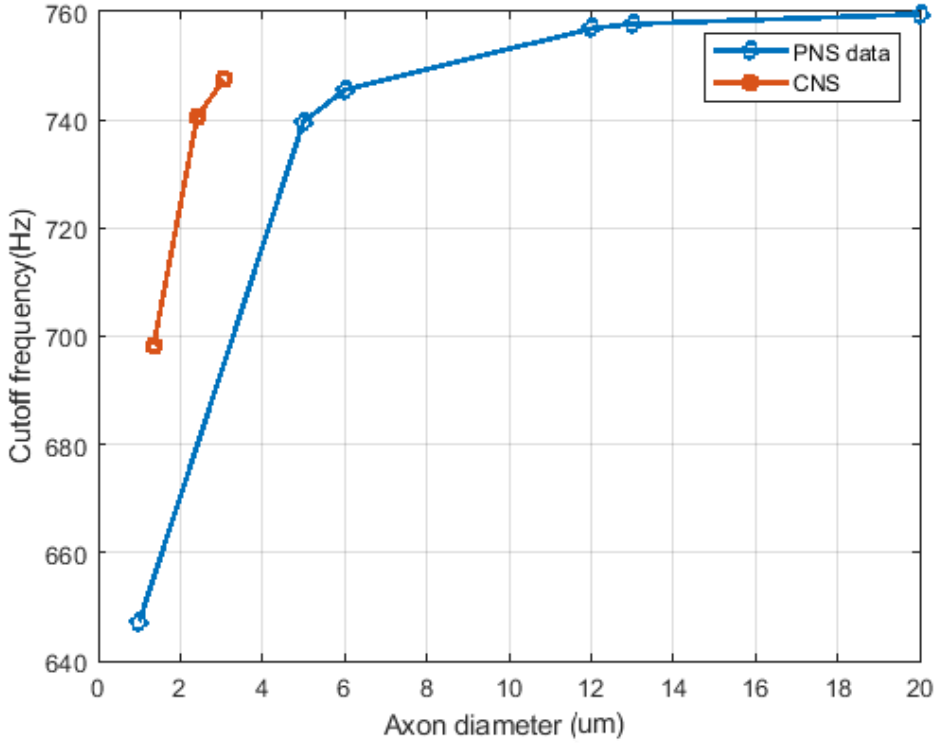

FIGURE 4.17: Axon Diameter Vs Cut-off frequency; Blue curve is showing cut-off frequency of PNS axons of diameters $1\mu m$,$5\mu m$,$6\mu m$, $12\mu m$, $13\mu m$ and $20\mu m$ for IN length 1mm; Red curve is showing cut-off frequency of CNS axons for diameters $3.06\mu m$, $2.41\mu m$, $1.35\mu m$ for IN length 0.1mm; 1mm IN length is greater than the maximum IN length permitted for signal propagation in CNS axons

axon behaves as a low pass filter and the value of its cut-off frequency is obtained from the calculation, it implies that the system will pass selective signals if the frequency of the signal is lower than the value of cut-off frequency.

4.4 Results and Discussion

In this work, we have designed and developed a computational circuit model of a single myelinated axon using circuit simulation software tool PSpice and analysed its signal propagation characteristics using computational analysis tool MATLAB. We have developed and validated our model with data of different axons such as Frog motor nerve, peripheral axons of group A, CNS axons SBC, GBSMed and GBCLat by simulating neuronal dynamics of AP and measuring their CV. After the validation of our model, we analysed its frequency characteristics of signal propagation and obtained a system function definition. Our objective here was to explore the signal propagation characteristics of a single myelinated axon in the frequency domain to understand if the axon has any characteristics of passing selective signals beyond which signal propagation will not happen. We have generated results that can conclude the possible reasons for signal

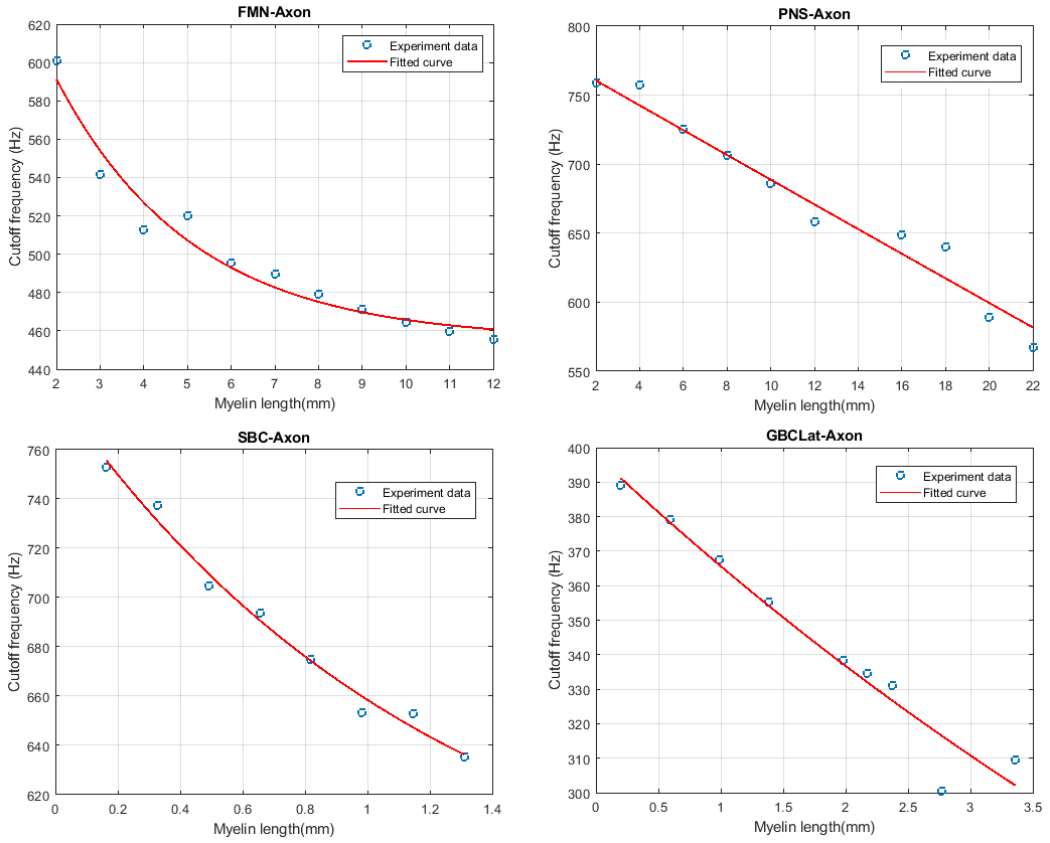

FIGURE 4.18: Myelin length vs cut-off frequency extracted for FMN, PNS and CNS axons

propagation failure in a myelinated single axon. The following points we conclude from our modelling and simulation results:

- CV determines how faster the information can transfer through the axon. Our simulation results show that CV varies inversely with the myelin length of an axon. It means that in elongated myelin sheath the CV will be reduced leading to slower propagation of a signal from one node to another. We presented this result in Figure 4.13 which is obtained from the resistive-capacitive model.

- Our simulation results predict that there is an upper limit of myelin length beyond which signal propagation failure occurs. So the myelin length of each axon should be within this limit for the successful propagation of a signal from one node to another. We presented this result in Figure 4.2.5. Stassart et al. (2018) mentioned that myelin length varies according to the need of a signal transmission.

- Our modelling of single axon exhibits that the myelin segments of axon exhibit the system behaviour of low pass filter. From there the simulation results predict, that while passing the signal from one node of Ranvier to another through myelin segment, the segment passes only selective signal below the cut-off frequency; above

the cut-off frequency the signal gets attenuated. We presented the cut-off frequency values of different axon types in Table 4.5.

- We also found from our simulation results that the cut-off frequency of myelin segment changes with the length and diameter of the myelin. The cut-off frequency decreases with an increase of myelin length shown in Figure 4.18 and a decrease of diameter. We derived a mathematical relation between cut-off frequency and myelin length from the generated results and presented it in Equation 4.14.

So, the myelin segment of a single axon is modelled with a system identification function. This system model of a single myelinated axon will be the basis of the modelling phase and frequency characteristics of a bunch of axons. Previously, many works were done on signal propagation through axon where exploration of signal propagation was done mainly in time scale. Here we have taken a novel approach to model the frequency and phase characteristics of a single axon. Next, our objective is to model signal disruption properties of a bunch of axons; which can help us to understand the absence of functional connectivity in structural connections.

4.5 Conclusions

In this paper, we explored the signal propagation disruption phenomenon in a myelinated axon using a cable theory PSPICE model. Our exploration shows that signal propagation disruption occurs at a higher myelin length and, the myelinated section of a single axon acts as a low pass filter where the cut-off frequency is dependent on myelin length. This implies that depending on the myelin geometry a rate coded nerve signal propagation through structural connection could be disrupted resulting in functional disconnection between two brain areas. In the next chapter, our aim is to explore this phenomenon in an ephaptically coupled bundle of axons to understand the relationship between structural and functional brain connectivity.

Chapter 5

Circuit Model for explaining Ephaptic Coupling effect in Two Myelinated Axons

5.1 Introduction

Non-synaptic interaction occurs due to one axon's electrodynamical effects on another within a bundle of parallel myelinated nerve fibres is known as ephaptic coupling. The word ephaptic originated from the Greek word "ephaps" meaning "to touch" (Arvanitaki, 1942). Ephaptic coupling plays a functional role in neural processing and signal propagation through a bundle of the axon by controlling features such as synchronization of impulses, Conduction Velocity (CV) and excitation/inhibition in axon bundle (Binczak et al., 2001; Anastassiou et al., 2011; Shneider and Pekker, 2015; Goldwyn and Rinzel, 2016; Capllonch-Juan and Sepulveda, 2017; Das et al., 2016). Modelling ephaptic interaction between impulses on myelinated nerve fibres is a significant part of future signal propagation modelling using a number of axons for finding frequency response. This chapter designs a circuit model of two myelinated parallel axons in PSPice to model the ephaptic interactions between parallel fibres impulses to be utilized in the next chapter when we model with multiple axons bundle. In the chapter, we first described the theory of ephaptic coupling in terms of the fundamentals of circuit theory. Then, we modelled ephaptic coupling between two parallel myelinated axons when they are aligned, and our simulation results conform to all the effects of ephaptic coupling. Finally, we modelled ephaptic coupling between myelinated axons when they are staggered and showed the simulation results. In the next chapter, we will design a circuit model of axon bundle by extending the model build in this chapter and analyze phase and frequency characteristics of signal propagation through axon bundle.

5.2 Theory of ephaptic coupling in terms of circuit theory

Ephaptic coupling is the mechanism by which one axon can influence AP generation in another axon in the bundle of parallel axons arrange in order. AP is generated in NR when membrane potential V_m reaches the threshold voltage V_{TH}. So eventually a time-dependent voltage gets generated due to axonal current. Now myelin sheath being an insulator the ephaptic coupling can only occur only at NRs between two parallel axons because that is where there is no myelin cover and membrane are in parallel suspended in extracellular fluid, which for the time being we assume NaCl solution. Such a scenario could be modelled in terms of capacitive resistive circuit elements as shown in Figure 5.1. Now we find out how to calculate $C(L)$ and $R(L)$ and which one of them dominates from

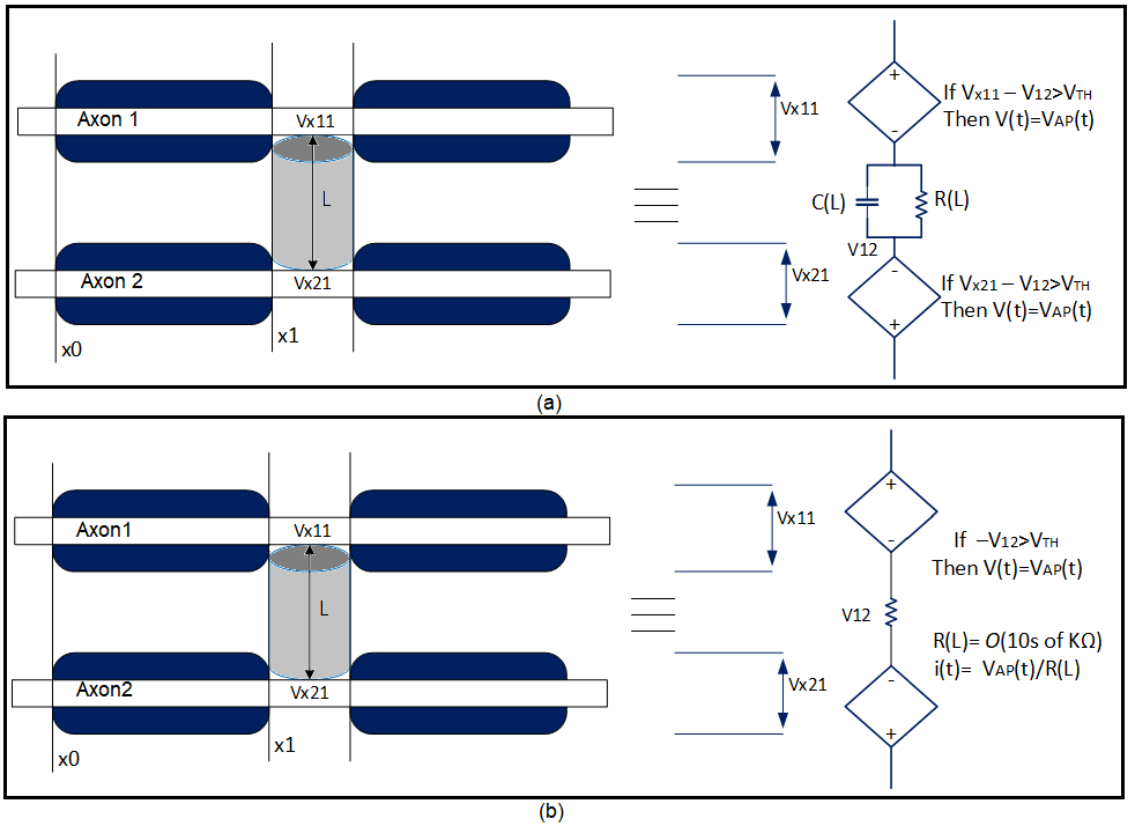

FIGURE 5.1: (a) Circuit model for ephaptic coupling between two parallel axons as both resistive and capacitive path; (b) Circuit model for ephaptic coupling between two parallel axons as resistive path as derived from calculation

coupling standpoint. Between the two expose NR it is the cylinder of NaCl which acts as the medium of coupling. Then

$$C(L) = \frac{\epsilon A}{L} \tag{5.1}$$

where $\epsilon_{NaCl} = 45$ for saturated NaCl at 20^oC. Therefore, $\epsilon = \epsilon_{NaCl} X \epsilon_0 = 45 * 8.85 * 10^{12}$ i.e., $O(10^{-10})$. Now area $A = \pi \frac{L_{NR}^2}{4}$; i.e., $C(L)$ is of $O(10^{12})$ considering Nodes of

Ranvier's (NR's) length L_{NR} of the $1 - 2\mu m$; and L is of $O(10^6)$. So $O(C(L)) = O(10^{-10} * 10^{-12}/10^{-6}) = O(10^{16})$; order of Impedance of C(L) $O(Z_{CL}) = \frac{1}{2\pi * f * C(L)}$; f = Frequency. Therefore $O(Z_{CL}) = O(10^{16})\Omega$. Of course this depends upon frequency, as the frequency increases this will come lower. But AP is of the Hz order and therefore $O(Z_{CL})$ will remain at $O(10^{16})\Omega$. Here we consider a parallel-plate capacitor since the dielectric medium between the two faces is not bounded by a cylindrical surface but actually extended throughout the extracellular fluid medium. Now,

$$R(L) = \rho \frac{L}{A} \tag{5.2}$$

where $\rho = 5\Omega - cm = 5 * 10^2\Omega - m$ for saturated NaCl; i.e. $O(10^2)$, $O(A) = O(10^-12)$ and $O(L) = O(10^-6)$. So, $O(R(L) = O(10^{-2} * 10^{-6})/10^{-12} = O(10^4)\Omega$; i.e., 10s of $K\Omega$. Therefore the resistance offered by the capacitive path is at least 12 orders higher than the resistive path; so if there is a coupling, it has to be resistive coupling. Now, if $i(t) = V_{12}/R(L)$ is enough to evoke an AP then the axon 2 will fire. As L increases $R(L)$ also increases; therefore polarisation current $i(t)$ decreases meaning that for distant axons there will not be any ephaptic coupling. The situation can be seen better with the Hodgkin-Huxley (HH) cell representation of the Axon 2 dependent voltage source. $i(t, L) = V_{AP}(t)/R(L) = O(= 10^{-3}/10^4) = O(10^{-7})$ amp (considering L is of m order). Typically an HH requires $O(nA)$ current to be activated and therefore this current should be sufficient to trigger AP in the 2nd axon. To carry out this experiment, we first build the circuit model of two parallel myelinated axon arrange in a bundle using the PSpice tool.

5.3 Circuit modelling of ephaptic coupling between two parallel myelinated axons

So far, in-vivo, in-vitro, numerical simulation studies were performed on ephaptic coupling (Binczak et al., 2001; Anastassiou et al., 2011; Shneider and Pekker, 2015; Goldwyn and Rinzel, 2016; Das et al., 2016; Capllonch-Juan and Sepulveda, 2017). In this work, we studied ephaptic coupling between parallel axons using the circuit theory approach and developed an electric circuit model using the circuit simulation tool PSpice. We created the circuit model of two parallel myelinated axons aligned in a bundle coupled with extracellular resistance. We studied this model to explore the effects of ephaptic coupling in signal propagation through a bundle of axons. The model of a single myelinated axon developed in Chapter 4, has been extended to model the two myelinated axons. We showed in Section 5.2 that the coupling between two NRs has to be resistive. As shown in Figure 5.1.(b), we connected the output port of two single axon model circuits in the outer conductor using a resistive path. We adapted the design concept from Barr and Plonsey (1992) but with modifications. The longitudinal extracellular resistance

R_{eL} value is calculated using cross-sectional area AE of two axon bundle and IN length L_{IN} and extracellular resistivity value R_e as $330\Omega cm$ (Goldwyn and Rinzel (2016)) using $(R_{eL} = R_e * L/AE)$. Thus based on the length of the axon the R_{eL} resistance is added up in series to model the extracellular resistance. We calculated one extracellular resis-

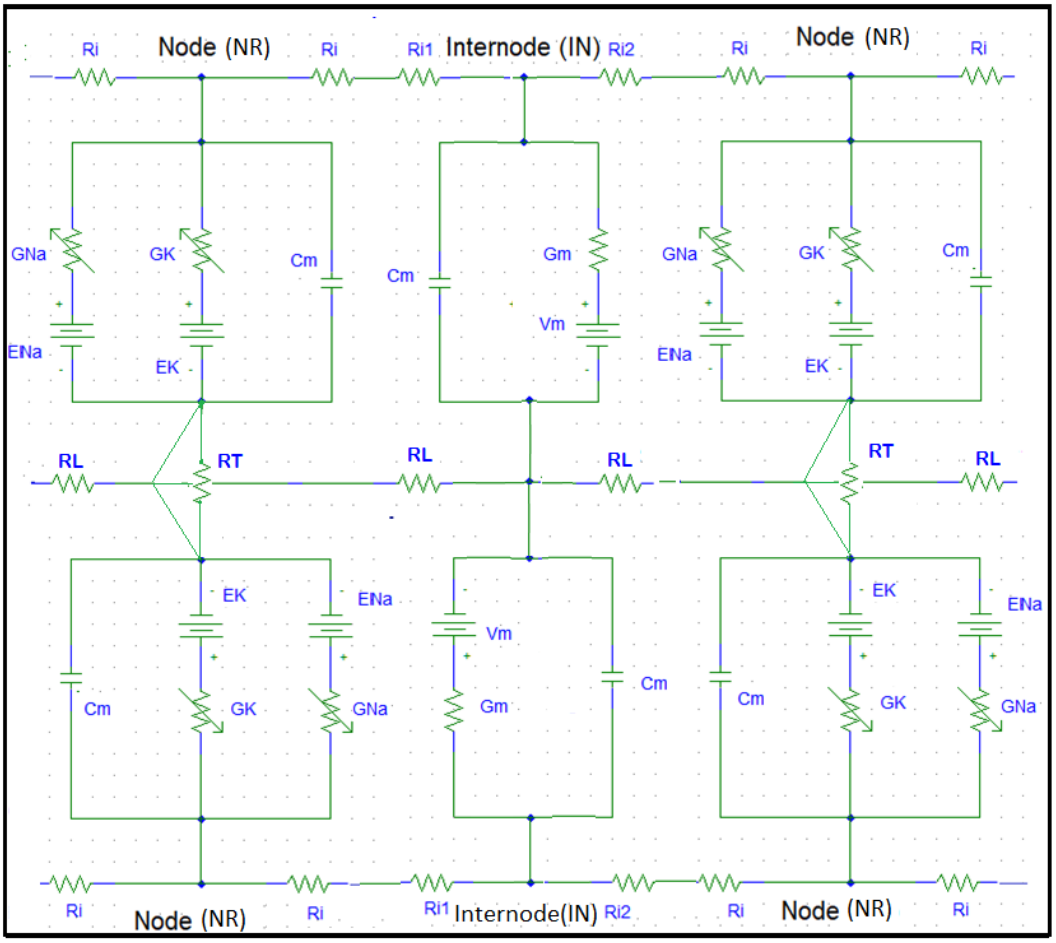

FIGURE 5.2: Circuit Modelling of two parallel axon aligned to each other connected by extracellular resistance

tance and connect the output port of NR of each axon to it. The transverse extracellular resistance R_T value between two NR is calculated by the formula of calculating $R(L)$. The resultant circuit model of two myelinated axons lying in parallel to each other in the extracellular fluid is shown in Figure 5.2. To simulate the circuit the rectangular input stimulus current pulses of 0.6nA (the same current that was applied to the single axon model) was applied intra-cellularly to the axon circuit. Voltage recordings were made from the NR cells 1, 3 of each axon in order to measure AP propagation through the coupled axon bundle. In our experiment, first, the stimulus current was applied at the first axon to see the coupling effect in the second. Then input currents were applied to the input of both the axons and results were recorded.

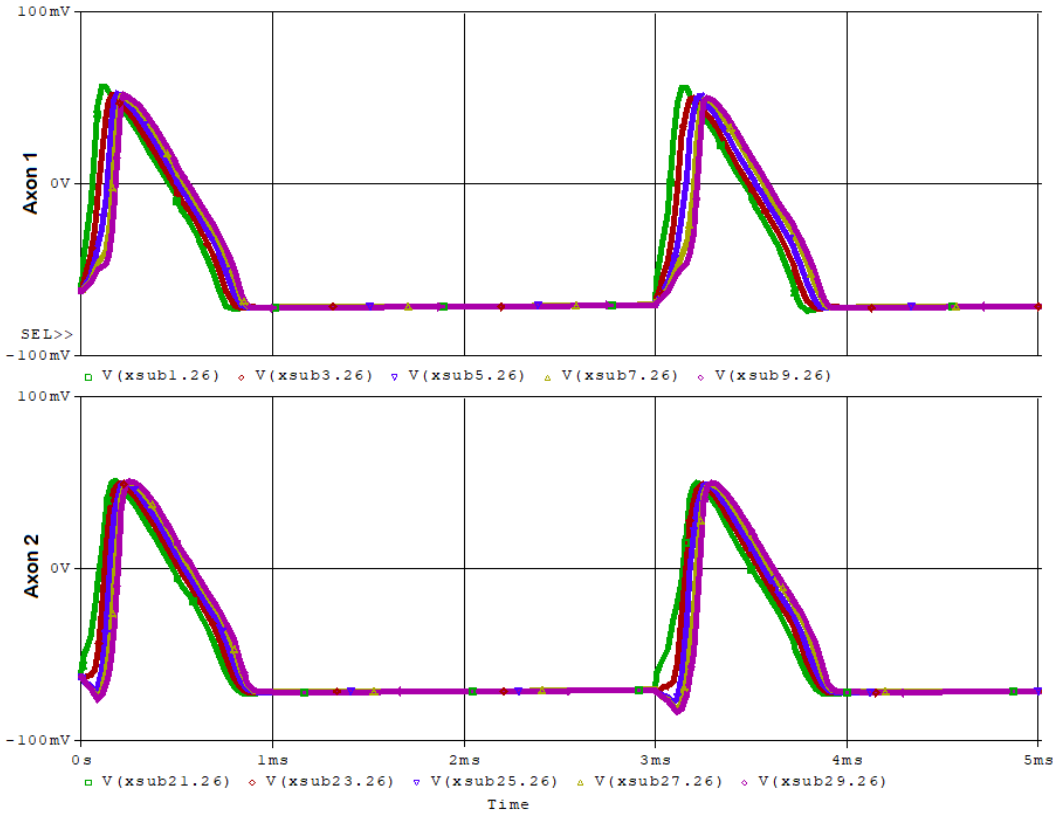

(a) Excitation of passive axon by ephatic coupling; Axon 1 is active and firing; Axon 2 was passive but got induced by Axon 2 and firing little later than Axon 1; The lines are representing the membrane voltages at five consecutive nodes in axons in a time span of 5ms; The green line : membrane voltage at node xsub1; the red line: membrane voltage at node xsub3; the blue line: membrane voltage at node xsub5; the yellow line: membrane voltage at node xsub7; the pink line: membrane voltage at node xsub9

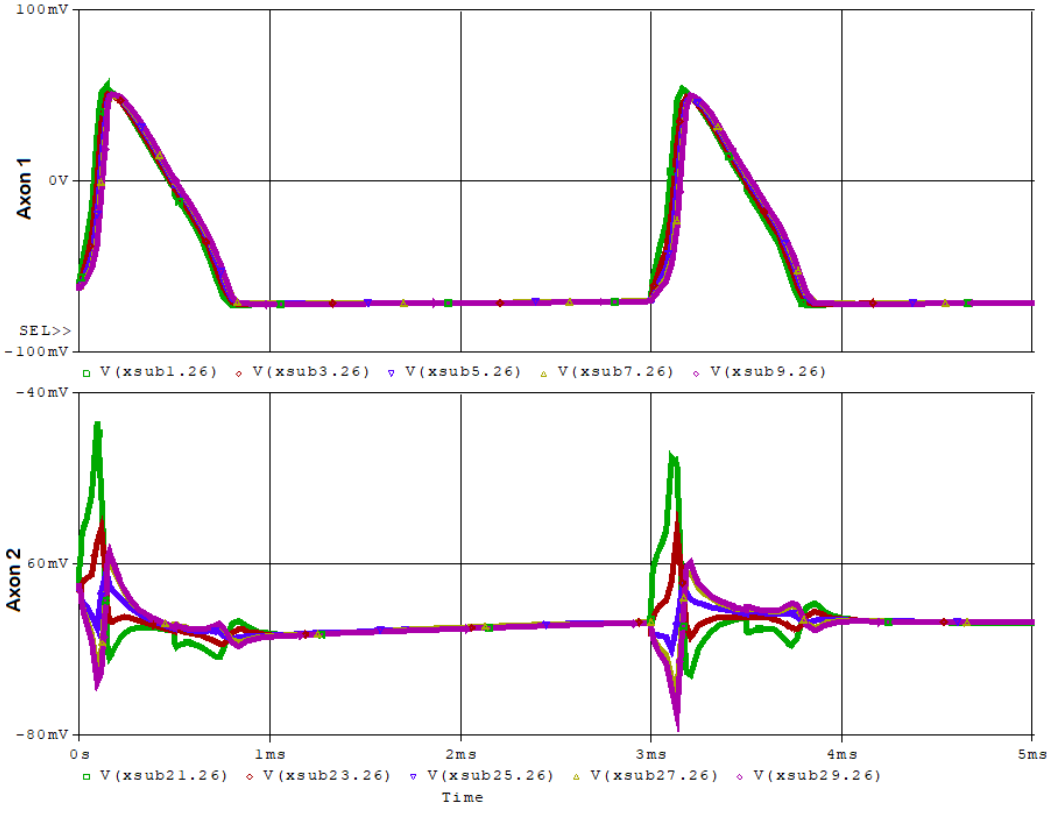

(b) No excitation of passive axon by ephatic coupling. Axon 1 is active and firing; Axon 2 is passive but didn't get induced by Axon 2; The lines are representing the membrane voltages at five consecutive nodes

FIGURE 5.3: Effects of coupling on passive axon

Axon Types	d_{NR} (μm)	d_{IN} (μm)	L_{Min} (μm)	R_{Min} (Ω)
$A\alpha$	20	28	8	8.4E+6
$A\alpha$	13	18.2	5.2	13E+6
$A\beta$	12	16.8	4.8	14E+6
$A\beta$	6	8.4	2.4	28E+6
$A\delta$	5	7	2	33.6E+6
$A\delta$	1	1.4	0.4	168E+6

Table 5.1: Minimum value of transverse extracellular resistance R_{Min} for maximum coupling effect for all Group A PNS axons where d_{NR} diameter of node, d_{IN} diameter of internode, L_{Min} minimum distance between two nodes of two parallel axons

5.3.1 Excitation of passive axon and range of inter-axon distance

We have seen from our calculation that in a perfectly aligned two myelinated axons, in HH cell representation of the Axon 2 dependent voltage source and distance between two NRs is of the order of micrometre, the current generated by AP of $O(10^{-7})$ should be sufficient to excite AP in the 2nd axon. Figure 5.3(a), shows AP generated at axon 2 induced by the AP generated at axon 1 while satisfying mentioned conditions. Next, we found out for what range of $R(L)$ such AP could be induced in the 2nd axon. We considered that the minimum range of current needed to initiate AP is $O(nA)$. Therefore, $R(L)$ must be at least of $O(10^6)\Omega$. Then, $L = \frac{A*R(L)}{\rho} = \frac{O(10^{-12})*O(10^6)}{O(10^{-2})} = O(10^{-4})m = O(100\mu m)$. So ephaptically induced AP may happen until the interaxonal distance with perfect alignment is of the order of 100 μm. Beyond this, there will not be sufficient excitation current to induce AP in the 2nd axon. Figure 5.3(b) shows that at $L = 104\mu m$ the AP has not generated at axon 2. The variation of transversal and longitudinal resistances as inter-axonal length increases for Group-A type axons of all diameters are shown in Figure 5.4. The transversal extracellular resistance increases with the increase of inter-axon distance whereas longitudinal extracellular resistance decreases with increases of inter-axon distance. In Figure 5.5, we showed an approximate maximum inter-axon distance to induce AP in axon 2 for all Group-A types axons. The maximum effect of coupling will happen when two axons are at their closest possible arrangement. In that case, the distance between two NRs will be double of their myelin thickness. So, $L_{Min} = (d_{IN} - d_{NR})$ where d_{IN} is diameter of internode and d_{NR} is diameter of Nodes of Ranvier and $R_{Min} = \rho\frac{L_{Min}}{A}$. Table 5.1 shows the table of R_{Min} for all Group-A-types axons. So, that's the results of the exploration of the effects of ephaptic coupling of active axon on the axon which is passive in the case of perfectly aligned two myelinated axons. In a real neural system, in a bundle of myelinated axons, there are always more than two axons laying in different alignments; so their conjugate effects may generate different outcomes than our exploration results.

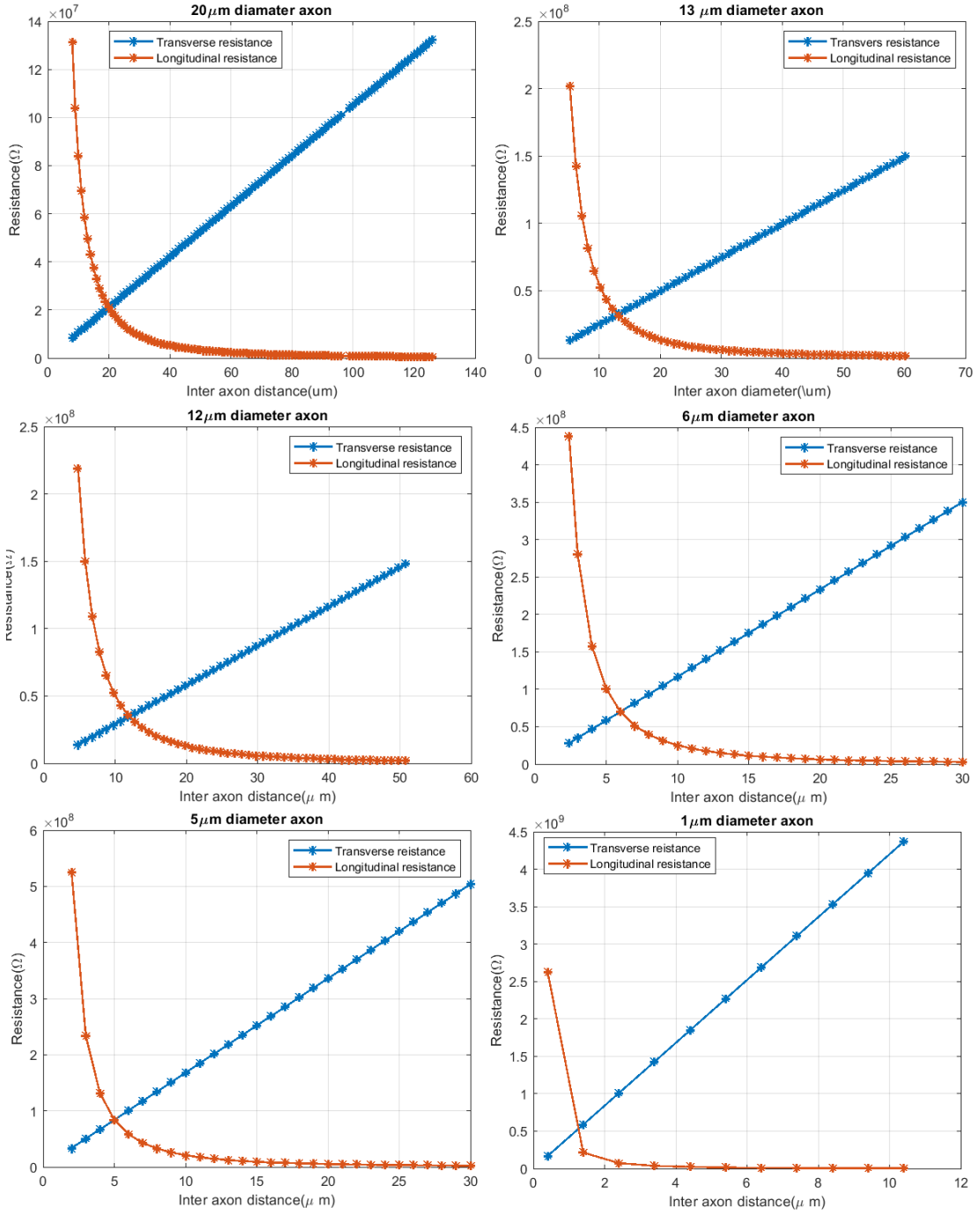

FIGURE 5.4: Extracellular resistance varies with inter-axon distance

5.3.2 Inhibition of spikes due to coupling

So far, we found that ephaptic coupling can induce AP from simulated axon to passive axon and excite that in some ideal conditions. Here, we explored under what condition, the ephaptic coupling can inhibit AP in other axons. We know that AP is generated in NR when membrane potential V_m reaches the threshold voltage V_{TH}. Now, membrane

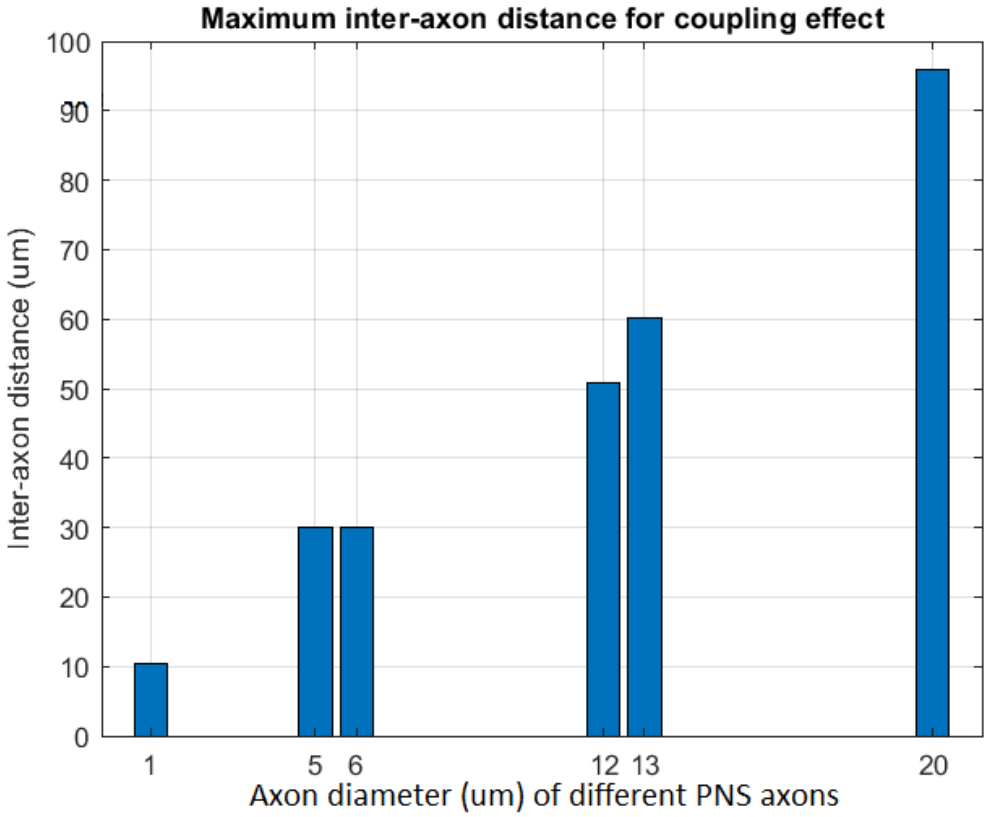

FIGURE 5.5: Maximum inter-axon distance for coupling effects of active axon on passive axon for all Group-A PNS axons

potential is equal to intra-cellular potential minus extra-cellular potential [$V_m = V_{x11} - V_{12}$, as shown in Figure 5.1]. When two axons are firing at the same time, that means the impulses at NRs at two axons are generated at the same, the current flowing through the extracellular longitudinal resistance decreases the membrane voltage V_m across the next NRs. In that case, if the current which will flow through the axon, is not to be able to bring the V_m above V_{TH} the AP will not be generated; in other words, AP will be inhibited. Figure 5.6(a), shows 5 NRs at a single small diameter axon generating synchronous AP, but Figure 5.6(b), shows that when two small-diameter axons are coupled in 2nd NRs onwards the alternate APs in the spike trail is inhibited. This is, due to the coupling effect that happened after the generation of AP at the first node. The current flowing through extracellular resistance decreases membrane voltages across the next NRs. Now, being a small diameter axon, the current flowing through the axon is not strong enough to bring the V_m above threshold voltage V_{TH}, hence the spike is inhibited.

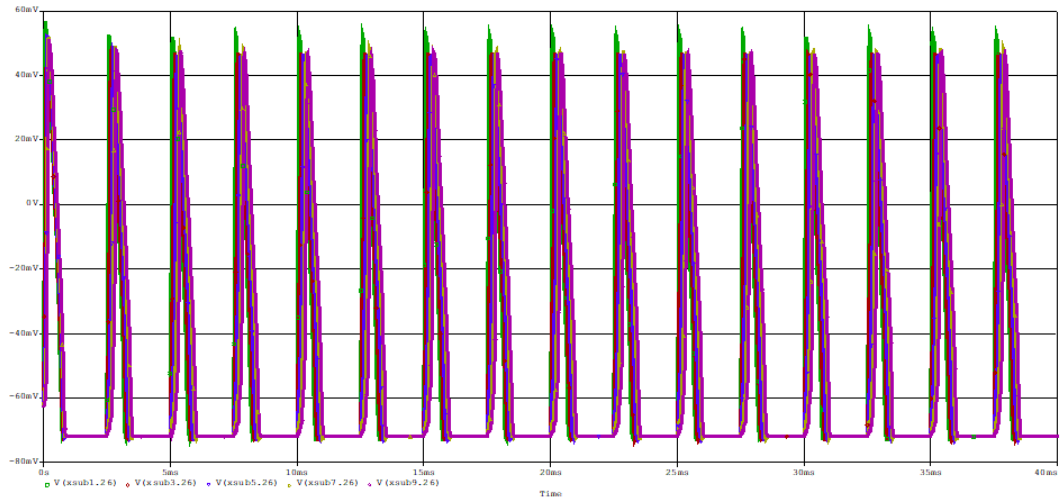

(a) Spikes are generated at all 5 NRs in $1\mu m$ diameter $A\delta$ axon

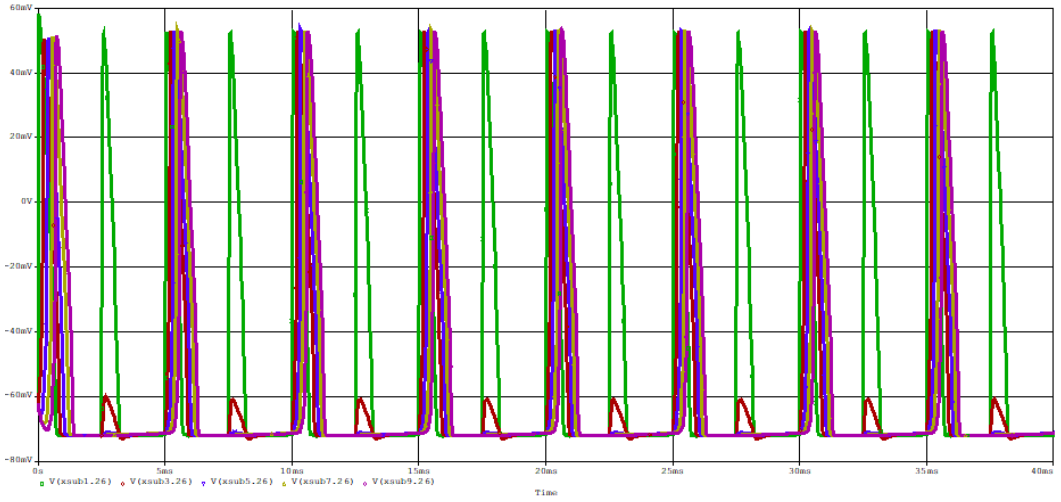

(b) Alternate spikes are inhibited from 2nd NR onwards in two axons bundle of $1\mu m$ diameter $A\delta$ axon

FIGURE 5.6: Inhibition of AP due to ephaptic coupling

5.3.3 Reduction of conduction velocity:

When both the axons in the bundle are firing at the same time, the current flow through the longitudinal resistance will decrease the membrane voltage V_M across the next NRs in axons. This will increase the time taken by the next NRs to reach threshold voltage V_{TH}, which implies that the Conduction Velocity (CV) of the axons will be decreased. When we simulated both the axons in the bundle with input current at the same time we found the propagation of spikes through the NRs as shown in Figure 5.7(b). Figure 5.7(a) shows the propagation of spikes with the same input current in a single axon. So, in the case of a single axon, spikes propagate from 1st NR, showing in the Figure 5.7(a) with the green line, to 10th NR showing in the Figure 5.7(a) with the pink line in 2ms time. But, at double axons bundle spike propagates from 1st NR (the green one) to 10th NR (the pink one) in approx. 4.5ms time. So in coupled axons spike took a little longer

time to propagate from 1st NR to 10th; which means CV is reduced at coupled axons bundle.

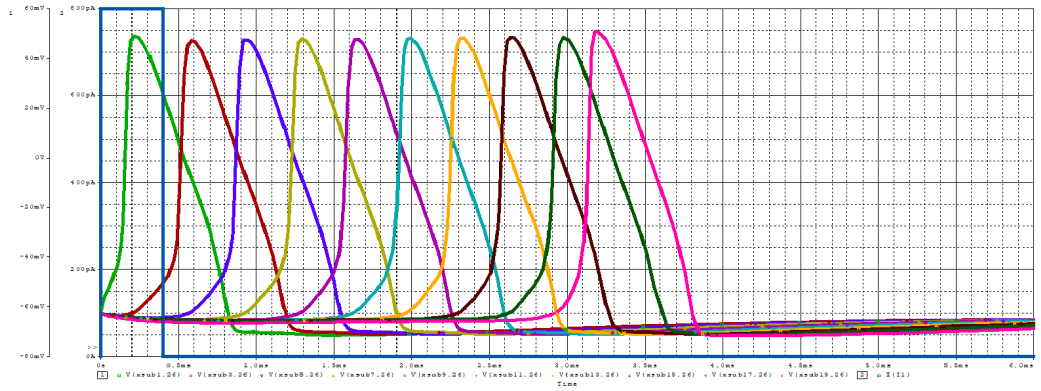

(a) Single Axon

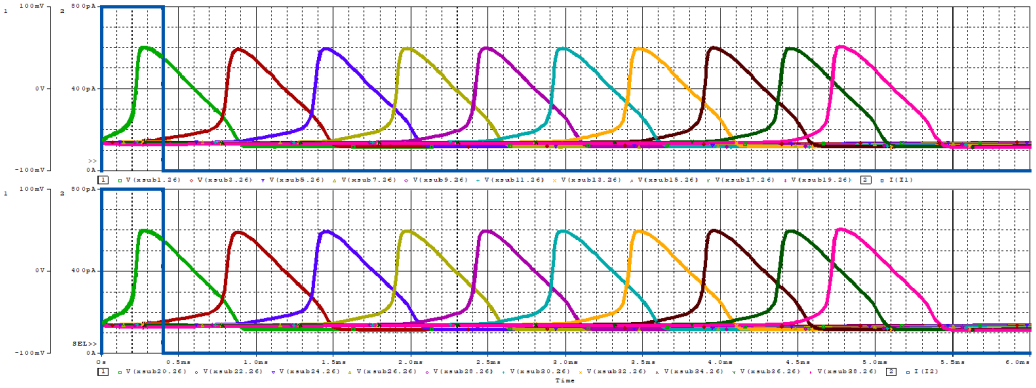

(b) Double Axons

FIGURE 5.7: (a) At single axon spikes propagates from first NR (the green one) to tenth NR (the pink one) in 2.3ms time, and the amplitude of the spike at tenth NR is a little larger than the rest of the NRs; (b) At double axon spikes propagates from first NR (the green one) to tenth NR (the pink one) in 4.8ms time; so in double axon spikes take longer time to propagate from 1st NR to 10th; hence CV is reduced at the double axon, and the shape of the APs at all NRs are same

5.3.4 Synchronization of phases of two active axons

When in two axons, the NR of the axon-1 is fired a little later than the NR of the axon-2, the spike in axon-2 will lead to the spike generated at axon-1. In that case, the current flowing through the extracellular resistance from axon-1 is larger when the next NR in axon-2 is ready to fire because the current generated from NR of axon-1 gets less time to relax. This effect will make the 2nd NR in axon-2 take longer to fire which in effect reduce the CV of axon-2. In a similar way, when 1st NR in axon-1 is fired a little later in 1st NR of axon-2, the current in extracellular resistance from 1st NR of axon-2 will be lesser when 2nd NR of axon-1 is ready to fire; because the current from 1st NR of

axon-2 had more time to relax. This will in effect decrease the firing time of the 2nd NR of axon-1, which means the CV of axon-1 will be increased. These effects of coupling will lead to closing the gap of firing times between NRs of two axons and eventually synchronizing the spikes of two axons. We observed this effect of ephaptic coupling in synchronizing out of phase spikes of parallel axons in Figure 5.8. In that figure, in two parallel axons, axon 2 is fired first and axon 2 fires 0.1ms later. We observed that after propagation of the spikes through some NRs, they started firing synchronously at the last NR.

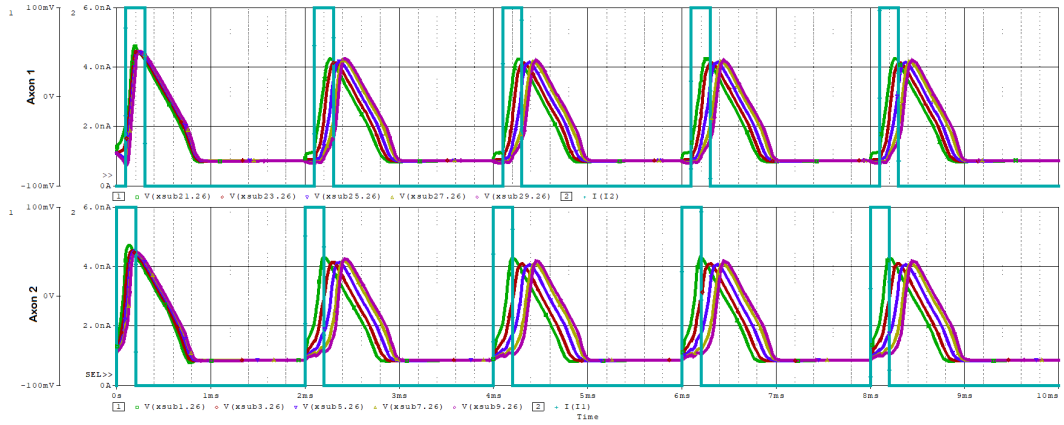

FIGURE 5.8: Effects of coupling on spike synchronization; The spikes fired in different times get synchronized in later nodes

5.3.5 Effect of misalignment between two axons

So far, we have explored the effects of ephaptic coupling when two axons are aligned. Next, we investigated what happens when two axons are not aligned two each other. As shown in Figure 5.9, as the axons are being staggered the cylindrical resistive coupling path between NRs of two axons will be shrinkage. In Figure 5.9, L_R is the replacement variable denoting the replacement of the NR in axon 2 from NR of axon 1. Then the diameter of the cylinder for calculating resistive path is $= (L_{NR} - LR)$ and the value of $R(L) = \rho \frac{4*L}{\pi*(L_{NR}-LR)^2}$. The variable can vary between 0 and L_{NR}; after that myelin of one axon overlaps the NR of the other axon, giving no coupling effect of exciting NR at the other axon. We modelled our circuit in this way and simulated it with the input current. The simulation result showed that no AP was generated from axon 1 to axon 2 when they are staggered as shown in Figure 5.10. The current flowing through the longitudinal extracellular resistance is less than the $O(10^{-9})$ as the length of myelin IN is of $O(10^{-3})$, hence no AP was generated from axon 1 to axon 2 when the axons are staggered, but, we found the other effects of coupling were there; such as in small diameter axons the spikes were inhibited in later NRs in axons in small diameter axons as shown in Figure 5.11, and CV was reduced compared to the single axon.

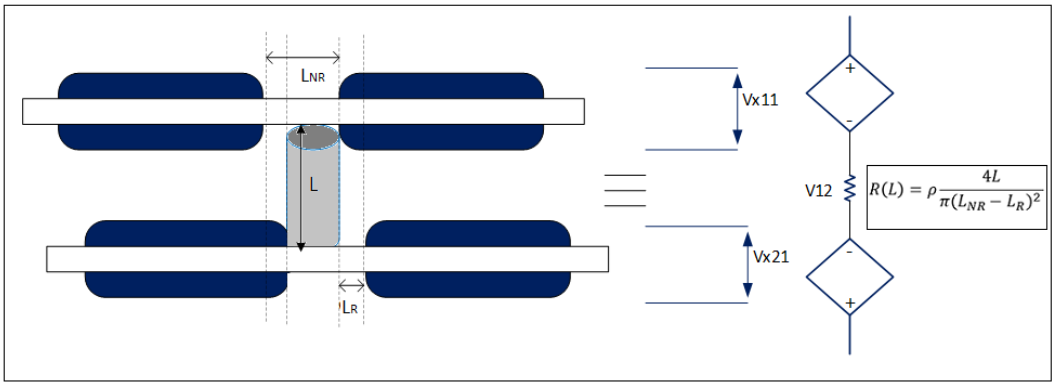

FIGURE 5.9: When two axons are not aligned then effects of resistive coupling started receding based on the overlapping areas of two nodes

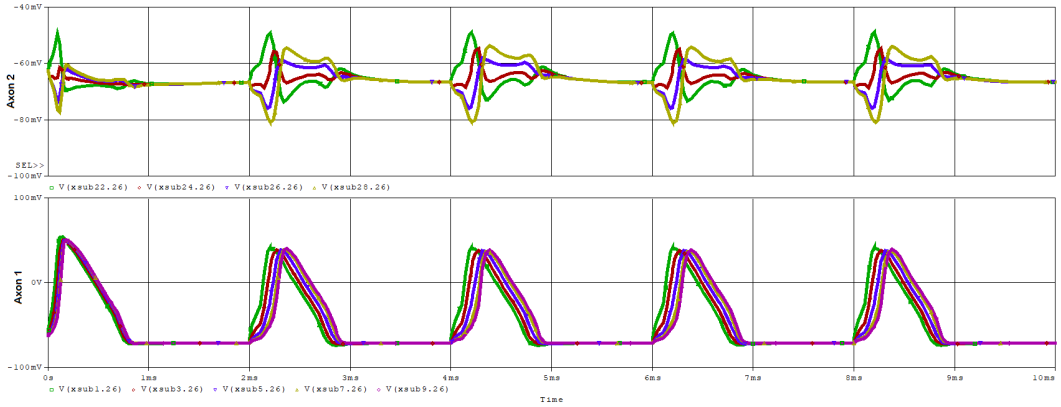

FIGURE 5.10: When two axons are staggered the AP are not generated from axon-1 to axon-2

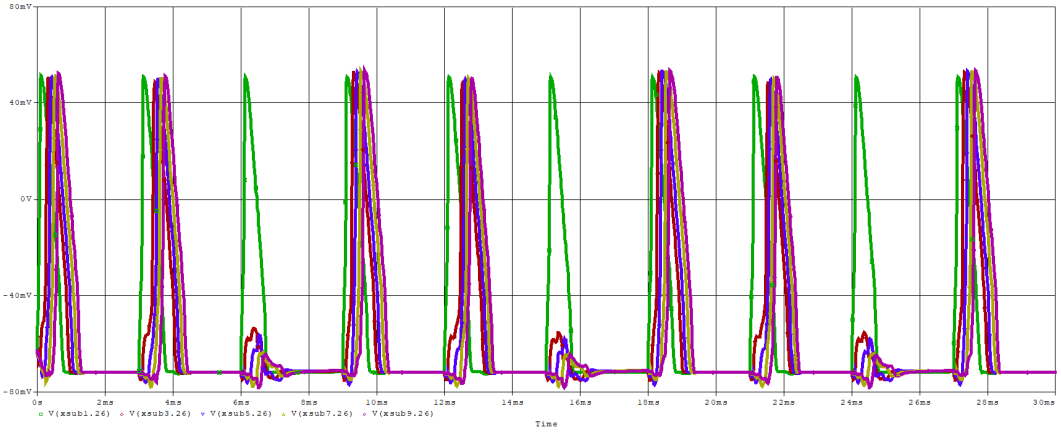

FIGURE 5.11: When two axons are staggered then APs are still inhibited in later NRs in case of small diameter axons

5.4 Results and Discussion

In this work, we modelled ephaptic coupling between two parallel axons arranged in a bundle using circuit theory. We modelled both aligned and staggered axons in a bundle and simulated coupling effects. From the results generated from our model, we found that (1) in an ideal condition when both axons are aligned and close to each other, if one axon is simulated and fired, then active axon can excite AP in the passive axon, (2) there is a range of inter-axon distance within which the coupling effects occur,(3) in smaller diameter axons the external current generated at earlier nodes during AP generation can inhibit the spike in later nodes, (4) the CV of coupled axons decreases due to coupling effect, (5) coupling effects will lead to synchronization of spikes in axons fired in different times, (6) in case of staggered axons the intensity of the external current is lesser, hence AP are not generated in passive axon but other effects such as inhibition of spikes in smaller diameter axons still occurs.

5.5 Conclusions

Here, we develop a computational model which generated the effects of ephaptic coupling between two parallel myelinated axons, based on the circuit theory approach. The results generated from the model shows that ephaptic coupling plays a significant role in information processing through axonal pathways. For instance, based on a situation ephaptic coupling can both excite or inhibit APs in Nodes of Ranvier in white matter tracts. Also, our results show that the effects of ephaptic coupling can lower the speed of spike transmission in myelinated axons if all the axons are firing synchronously at the same time. If the myelinated axons are firing at different times then due to effects of coupling, eventually the nodes of Ranvier will get synchronize and will start firing at the same time, by increasing the speed of transmission of spikes in the axon which was firing later and lowering the speed of transmission of spikes which was firing earlier than the other. This shows the transmission of spikes in a single axon is different from the signal transmission through a bundle of axons and coupling plays a role in the propagation of signals through axonal pathways. In the next chapter, we used this model of the coupled axon to build our multi axon model and explore signal propagation characteristics of an axon bundle.

Chapter 6

Circuit Model for analysing Signal Propagation Dynamics in Myelinated Axon Bundle

6.1 Introduction

Structural brain connectivity refers to the axonal fibre bundles and pathways that form the brain's physical communication network, and functional connectivity refers to the synchronisation of neural activity between different neuronal populations. Our hypothesis is that, as the functional connectivity is calculated by the phase correlation between the signals at two brain regions; the absence of it despite having structural connectivity implies disruption of signal propagation between these two regions. In the previous chapters, we have designed and developed computational circuit models for single myelinated axon [in Chapter 4] and ephatically coupled double myelinated axons [in Chapter 5] and examined their signal propagation dynamics by determining CV, cut-off frequency for them. Here, our objective is to design a computational circuit model for exploring signal propagation disruption behaviour in a myelinated axon bundle. To do so, in this chapter, we have designed and developed a computational circuit model for a bunch of myelinated axons by extending the circuit models that we have designed in Chapter 4 and Chapter 5. We simulated our electrical circuit model by passing signals both from stimulated current and voltage sources. By simulating the circuit with the current signal we calculated CV and observed that CV varies with the Fibre Density (FD) of the bundle. We have used the terminology 'fibre density' interchangeably with 'fibre pack density'. We determined the relation between CV and FD for the axon bundle. By simulating the circuit with sinusoidal voltage signals of low to high frequency, we wanted to experiment with 'rate code' (the average number of APs per unit time) propagation

through the axon bundle. But, with the input of high-frequency sinusoidal voltage signal, we found a surprising effect that firing pattern at Nodes of Ranvier (NR) changes from Action Potential (AP) generation to sub-threshold oscillation of low voltage spikes, which eventually becomes unable to generate APs at next NR after passing through the internode (IN). This effect occurs at a very high frequency, which we termed as the 'Limiting Frequency' (LF), because beyond this frequency signals can not propagate down the axon bundle. We also observed that this LF varies inversely with the FD of the axon bundle. Then, we performed another experiment to explore how the signal propagates when axons in the bundle are getting input in a random manner. We found that when the ephaptic coupling is strong it can induce the passive axons and excite them to fire synchronously with simulated axons and propagates signals through the bundle. Then we performed a stochastic analysis of the circuit model to investigate how the bundle performs to stochastic behaviour. We fired each of the axons in the bundle with random noise and observed the signal propagation characteristics through it. At the end of this chapter, we defined the system definition for our circuit model of a bunch of axons and found that the behaviour of the system exhibits the characteristics of a low pass filter. We also calculated cut-off frequency beyond which axon bundle can no longer convey information from one region to another. In Section 6.2 we designed, developed and simulated the computational circuit model for the myelinated axon bundle. In Section 6.3 we defined system function for the same. For design and simulation of the circuit, we have used the circuit simulation tool PSpice and for system identification of the model, we have used MATLAB as done in previous chapters.

6.2 Signal propagation modelling in myelinated axon bundle

Here, we have designed the computational model for the myelinated axon bundle using the circuit theory approach. In our modelling, we use the data of FMN, PNS axons and CNS axons and generated results accordingly. Within bundle (CNS or PNS), axons are packed densely and (in general) aligned in parallel. As shown in Figure 6.1(a) and (c), in the ultrastructure of CNS and PNS axons, the CNS myelinated axons are densely packed within white matter and the myelin sheaths of neighbouring fibres often directly touch, whereas the PNS axons are separated by connective tissue and are covered with a basal lamina (Stassart et al., 2018). We adhered to the concept of densely pack fibre bundle in our modelling by implementing the theory of circle packing into a circle which is a two-dimensional packing problem with the objective of packing unit circles into the smallest possible larger circle (Friedman, 2014). The smallest possible larger circle defines the virtual confined area around the densely packed fibres which are used for calculating the cross-sectional area of the fibre bundle. As shown in Figure 6.1.(b), we modelled the bundle for 12 axons following the Figure 6.1.(a) of CNS axon bundle. For

the time being for the PNS axon also implemented the same theory of circle packing into a circle for modelling the outer area of the fibre bundle, where we know that the PNS axons are not circular like CNS axons and don't always touch each other. All the axons in the bundle connected with each other in the form of a chain. In our experiment, we varied the number of axons in the bundle from 2 to up to 12 and in each case, we followed the theory of circle packing into a circle given by Friedman (2014) to define the cross-sectional area of the bundle. In our model, we defined fibre density (FD) as AF/AT and total intracellular to extracellular areas ratio, as Aax/AE, where AF is the sum of the cross-sectional areas of the fibres, including their myelin sheaths, Aax is the sum of their cross-sectional intracellular areas, AE is the total cross-sectional extracellular area of the model, and AT is its total cross-sectional area. To model these variables we followed the work of Capllonch-Juan and Sepulveda (2020). In a densely packed bundle, the fibre density of the bundle is $>= 0.5$.

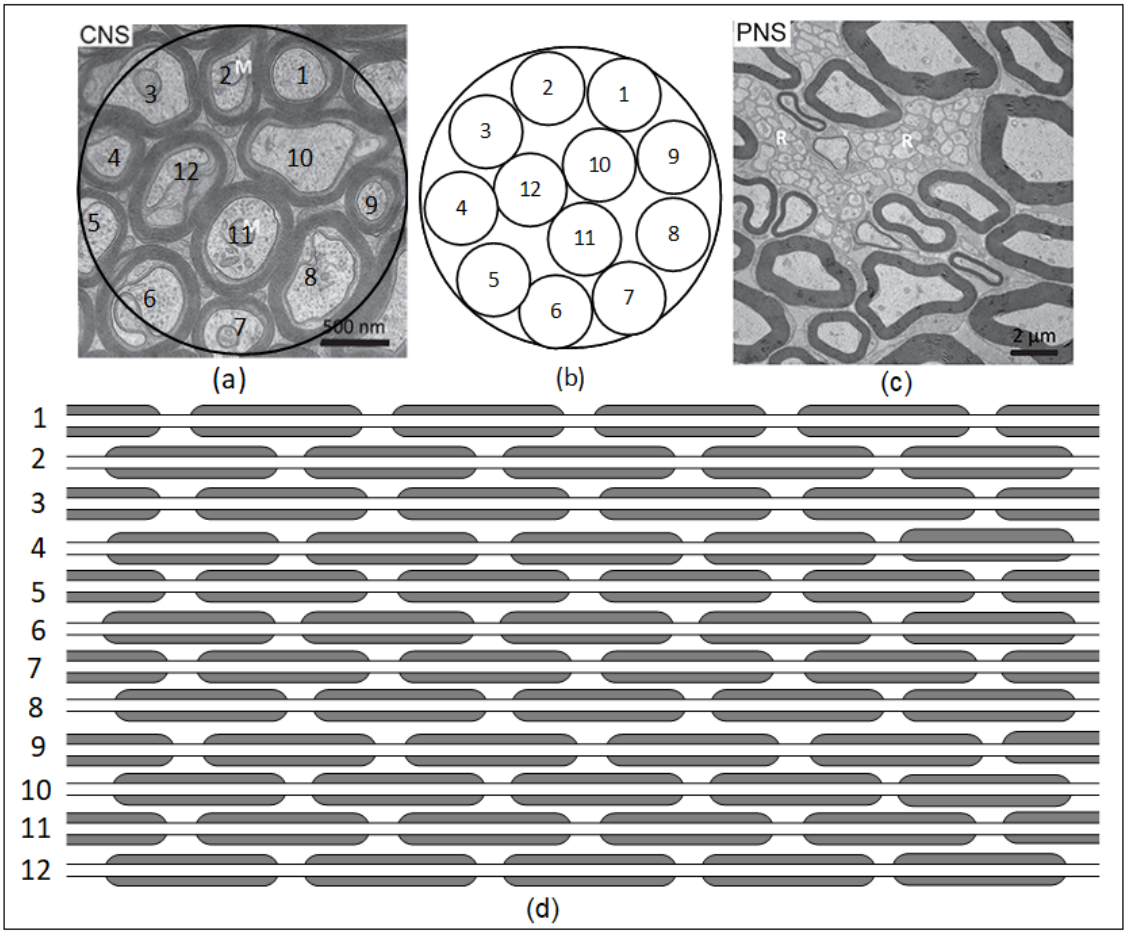

FIGURE 6.1: (a) and (c) Ultrastructure of myelinated axons in the CNS and PNS; (b) cross-sectional view of the adhered model design of fibre bundle from Fig. (a) for CNS axon bundle of 12 axons, for PNS axon bundle we adhered the same design but leave 20% extra space in extracellular space to model the gap between axons in the bundle; because in the PNS, the Schwann cell plasma membrane is covered with a basal lamina and the myelinated fibres are separated by connective tissue (Stassart et al., 2018). (d) Schematic view of fibre bundle consists of 12 axons

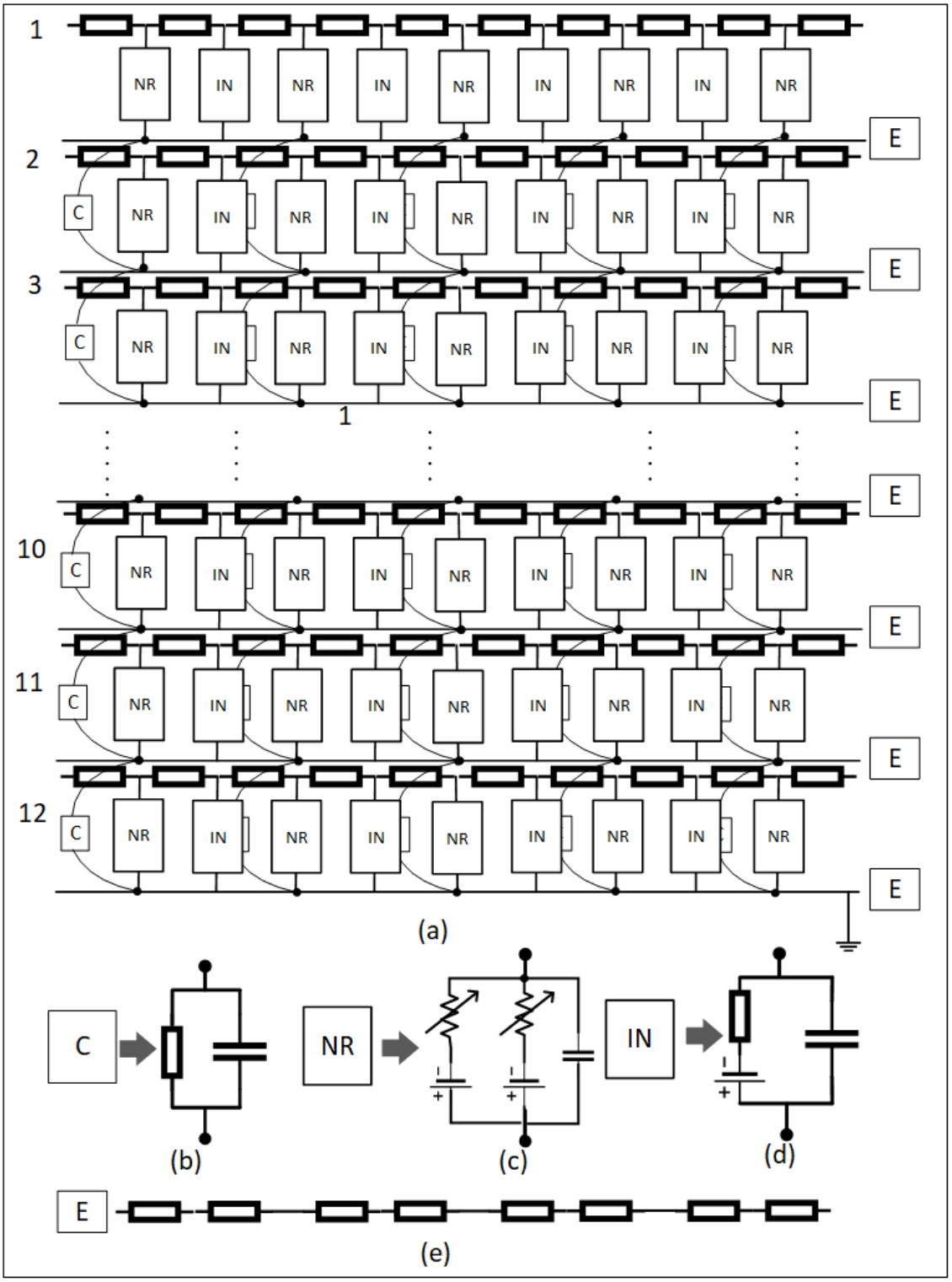

FIGURE 6.2: Schematic diagram of 12 myelinated axons parallel to each other and ephapticaly connected

6.2.1 Circuit design and simulation of axon bundle using PSpice

The circuit details of the basic units representing NR and IN in PSpice have been given in Chapter 4. For the present experiments, we modelled the axon bundle consists of 12 chains in parallel, each chain being 5 NR cells and 4 IN cells in length (12 X 9 model) as shown in Fig. 6.2 using a circuit simulation tool PSpice. The whole extracellular volume of the nerve is modelled with a resistor network which uses Barr and Plonsey (1992) as the basic model of the extracellular medium between two cables. Ours is an adaptation from such a model that suits any number of myelinated axons. The longitudinal extracellular resistance R_{eL} value is calculated using cross-sectional area AE and IN length L_{IN} and extracellular resistivity value R_e as $330\Omega cm$ taken from Goldwyn and Rinzel (2016) using ($R_{eL} = R_e * L/AE$). Thus based on the length of the axon the R_L resistance is added up in series to model the extracellular resistance. The transverse extracellular resistance R_T value between two NR is calculated using the same formula and length of NR and distance between two myelinated axons. We showed in Chapter 4 that we modelled our circuit based on two ways of modelling the intracellular axonal fluid in an axon (1) pure resistive and (2) resistive-capacitive. The results obtained from the resistive model was accurate only for FMN, but for PNS and CNS axons the resistive-capacitive model gives accurate results. So we selected the resistive model for the FMN axon and the resistive-capacitive model for PNS and CNS axons and followed the same here. Based on the calculation we showed in Chapter 5, Section 5.2, that resistance offered by capacitive path is at least 12 orders higher than the resistive path we ignored the dielectric behaviour of extracellular fluid represented by capacitive circuit. All different axon type that we have used in our model are given in Table 2.3 in Chapter 2. All electrical parameters are of the standard values and given in Table 4.2 in Chapter 4; the values of the variables related to the experiments performed in this chapter are given in Table A.5. Twelve identical electrical current sources were placed on the left end of the model so that all 12 chains could be stimulated simultaneously. The rectangular current pulses were all identical, i.e. 0.6 nA in amplitude and 0.25 ms in duration, and stimulation was applied intra-cellularly. Voltage recordings were made from the NR cells 1, 3, 5, 7 and 9 of each chain in order to measure AP propagation through the coupled axon bundle. The longitudinal propagation velocity CV was calculated from the measured total propagation time, IN length of each different axon.

Model	Bundle diameter (μm)	Axons in bundle	Outer diameter of axon(μm)	Inner diameter of axon(μm)	L_{NR} (μm)	L_{IN} mm	A_T $(\mu m)^2$	A_F $(\mu m)^2$	A_{ax} $(\mu m)^2$	A_E $(\mu m)^2$	R_{eL} $M\Omega$	R_{eT} $M\Omega$
FMN	28	2	14	10	2	2	616	308	157.14	308	21.4	4.2
FMN	56.41	12	14	10	2	2	2499.86	1848	942.86	651.86	10	4.2
$A\alpha-20$	56	2	28	20	2	2	2464	1232	628.57	1232	5.3	8.4
$A\alpha-20$	112.81	12	28	20	2	2	9999.43	7392	3771.43	2607.43	2.5	8.4
$A\alpha-13$	36.4	2	18.2	13	1.3	1.3	1041.04	520.52	265.57	520.52	8.2	12.9
$A\alpha-13$	73.33	12	18.2	13	1.3	1.3	4224.76	3123.12	1593.43	1101.64	3.9	12.9
$A\alpha-12$	33.6	2	16.8	12	1.2	1.2	887.04	443.52	226.29	443.52	8.9	14
$A\alpha-12$	67.69	12	16.8	12	1.2	1.2	3599.79	2661.12	1357.71	938.67	4.2	14
$A\alpha-6$	16.8	2	8.4	6	0.6	0.6	221.76	110.88	56.57	110.88	17.8	28
$A\alpha-6$	33.84	12	8.4	6	0.6	0.6	899.95	665.28	339.43	234.67	8.4	28
$A\alpha-5$	14	2	7	5	0.5	0.5	154	77	39.29	77	21	33.6
$A\alpha-5$	28.2	12	7	5	0.5	0.5	624.96	462	235.71	162.96	10	33.6
$A\alpha-1$	2.8	2	1.4	1	0.1	0.1	6.16	3.08	1.57	3.08	107	168
$A\alpha-1$	5.64	12	1.4	1	0.1	0.1	25	18.48	9.43	6.52	50.62	168
SBC	3.54	2	1.77	1.35	1	0.16	9.85	4.92	2.86	4.92	109.8	65.7
SBC	7.13	12	1.77	1.35	1	0.16	39.99	29.54	17.18	10.42	51.9	65.7
GBCMed	6.4	2	3.2	2.41	1	0.24	32.18	16.09	9.13	16.09	48.9	58.2
GBCMed	12.89	12	3.2	2.41	1	0.24	130.60	96.55	54.76	34.06	23.1	58.2
GBCLat	8.02	2	4.01	3.06	1	0.18	50.54	26.27	14.71	25.26	25.8	102
GBCLat	16.16	12	4.01	3.06	1	0.18	205.09	151.61	88.29	53.48	12.2	102

Table 6.1: Data for axon bundles for different types of axon; Here we showed data for axon bundle of 2 axons and 12 axons; in Chapter A we gave all the data

6.2.2 Conduction Velocity and Fibre Density

Conduction velocity (CV)which is the speed at which an impulse propagates down an axonal pathway, is an important aspect of nerve conduction studies. Conduction velocities are specific to each individual axon and depend on an axon's diameter and myelin length, we have seen in Chapter 4 CV of a single axon varies. There, we have shown the CV of different PNS and CNS axons, FMN and validated the results with the published data. Here, in this work, we have calculated the CV of coupled axons bundle for different types of axons and for a different number of axons in the bundle and plotted them against the bundle's fibre density. Our simulation results obtained from the circuit model revealed that the CV of coupled axon gets influenced by the coupling effects from other axons. As the bundle density increases in the bundle, the CV of coupled axons decreases. In Figure 6.3 we plotted the CV with FD for all axon types obtained from our models. We performed a curve-fitting on the plotted data which resulted in a second-order polynomial equation as given below by Equation 6.1:

$$f(x) = p1 * x^2 + p2 * x + p3 \tag{6.1}$$

where x denotes FD and $f(x)$ denotes CV. This is a new mathematical relationship between the conduction velocity of an axon in a bundle with the fibre density of the bundle; which describes how the conduction velocity of an axon will change based on the fibre packing density of the bundle. The values of the parameters with (95% confidence intervals) for different types of axons are placed in Table 6.2. Thus, we quantified the relationship of conduction velocity of an axon bundle with its fibre density. Our finding is valid as Binczak et al. (2001) also mentioned in his work that due to ephaptic coupling the speed of the AP will reduce.

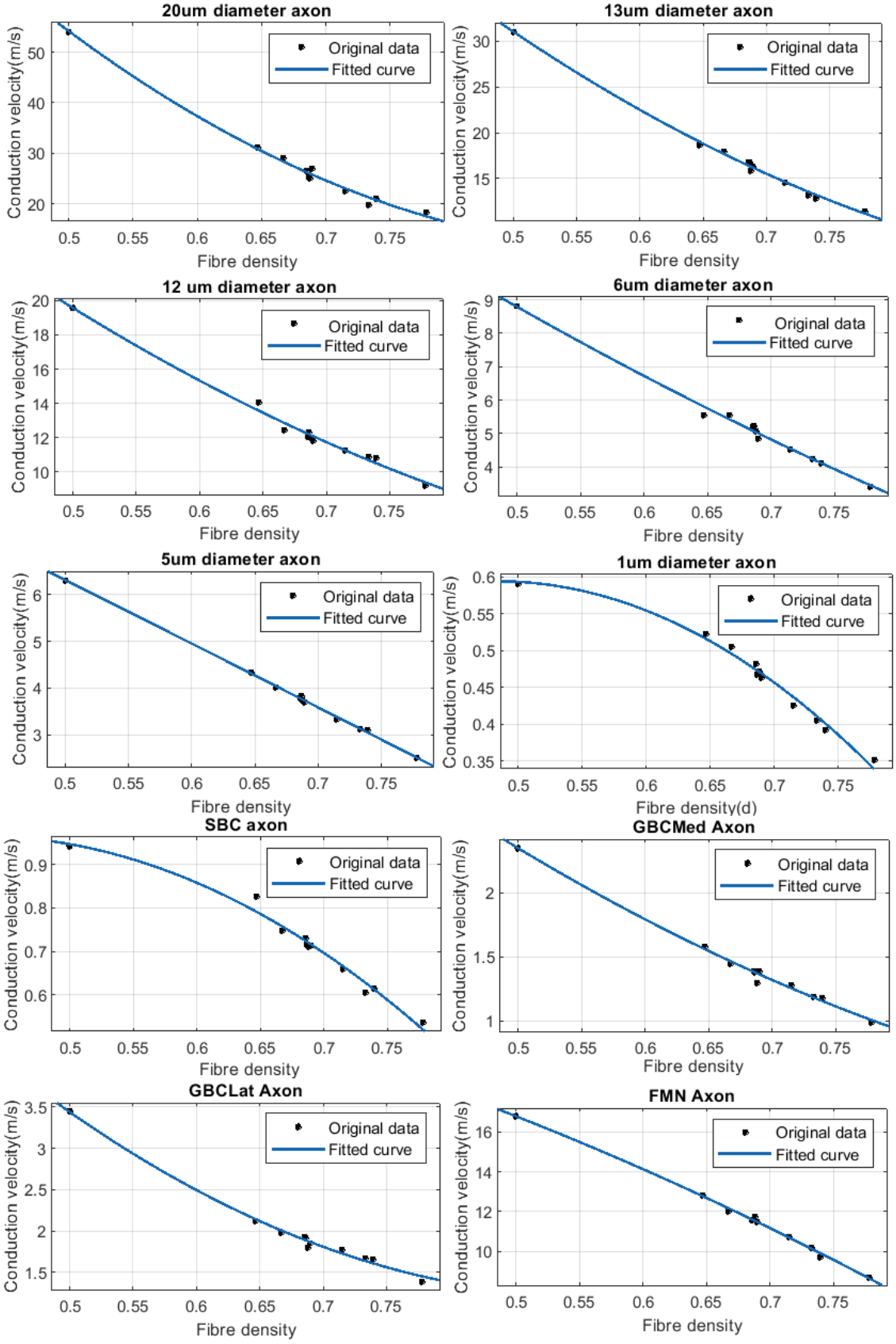

FIGURE 6.3: CV Vs FD; For all axon types it is observed that CV varies inversely with FD and the relation between CV and FD is best described by polynomial equation; Here, the data are not equally sampled across density due to the characteristics of fibre packing density of tightly packed bundle

Axon Types	**Diameter**	**Model**	**Coefficient p1**	**Coefficient p2**	**Coefficient p3**	**SSE**	**Adjusted R-square**	**RMSE**
FMN	$10\mu m$	Resistive	-0.077 (-0.15, -0.005)	-2.19 (-2.33, -2.05)	11.65 (11.53, 11.76)	0.1447	0.99	0.13
$A\alpha$	$20\mu m$	Resistive-capacitive	1.043 (0.54, 1.55)	-8.06 (-9.05, -7.07)	26.35 (25.55,27.15)	7.09	0.99	0.94
$A\alpha$	$13\mu m$	Resistive-capacitive	0.0397 (0.198, 0.597)	-4.59 (-4.99, -4.197)	16.51 (16.19,16.83)	1.123	0.99	0.37
$A\beta$	$12\mu m$	Resistive-capacitive	0.165 (0.004, 0.33)	-2.4 (-2.7, -2.08)	12.27 (12.01,12.52)	0.73	0.99	0.3
$A\beta$	$6\mu m$	Resistive-capacitive	0.042 (-0.03, 0.11)	-1.31 (-1.48, -1.17)	5.11 (4.99,5.22)	0.14	0.99	0.13
$A\delta$	$5\mu m$	Resistive-capacitive	-0.002 (-0.02, -0.017)	-0.98 (-1.02, -0.94)	3.8 (3.77,3.83)	0.012	0.998	38E-3
$A\delta$	$1\mu m$	Resistive-capacitive	-0.015 (-0.02, -0.01)	-0.084 (-0.09, -0.08)	0.476 (0.47, 0.48)	0.64E-3	0.98	8.95E-3
SBC	$1.35\mu m$	Resistive-capacitive	-0.02 (-0.03, -0.01)	-0.133 (-0.15, -0.12)	0.73 (0.71, 0.74)	2.27E-3	0.98	1.68E-2
$GBCM$	$2.41\mu m$	Resistive-capacitive	0.02 (0.003, 0.04)	-0.32 (-0.35, -0.28)	1.39 (1.34, 1.42)	9.51E-3	0.99	3.45E-2
$GBCL$	$3.06\mu m$	Resistive-capacitive	0.07 (0.039, 0.092)	-0.43 (-0.48, -0.37)	1.9 (1.86, 1.94)	0.02	0.99	5E-2

Table 6.2: Curve fitting statistics parameters for different axons

6.2.3 Maximum Myelin Length and Fibre Density

In Chapter 4, we performed an experiment and analysis on the myelin length of the single axon to investigate how the length of the myelin segment plays role in signal propagation through the axon. In that study, we found that there is an upper limit on the length of IN segment beyond which signal propagation does not occur. Here, we wanted to extend that study to investigate if the upper limit of myelin length value remains the same for the axon bundle or varies with the bundle. So, we designed a circuit of axon bundles of various myelin lengths and the various number of axons and simulated them with the input current. We performed these experiments on PNS axons for a number of axons in bundles up to 10. Our simulation results showed that the upper limit of myelin length that we obtained from a single axon model, changes in the axon bundle. We also found that with a number of axons in the axon bundle this upper limit of myelin length varies. We put our simulation results obtained from our models in Figure 6.4; where we displayed the simulation results for different diameters of PNS axons. The results show that with the number of axons in the bundle, the upper limit of myelin length for propagating signal without disruption shortens. This is a new relationship that we obtained on MML and FD of a bundle of myelinated axons.

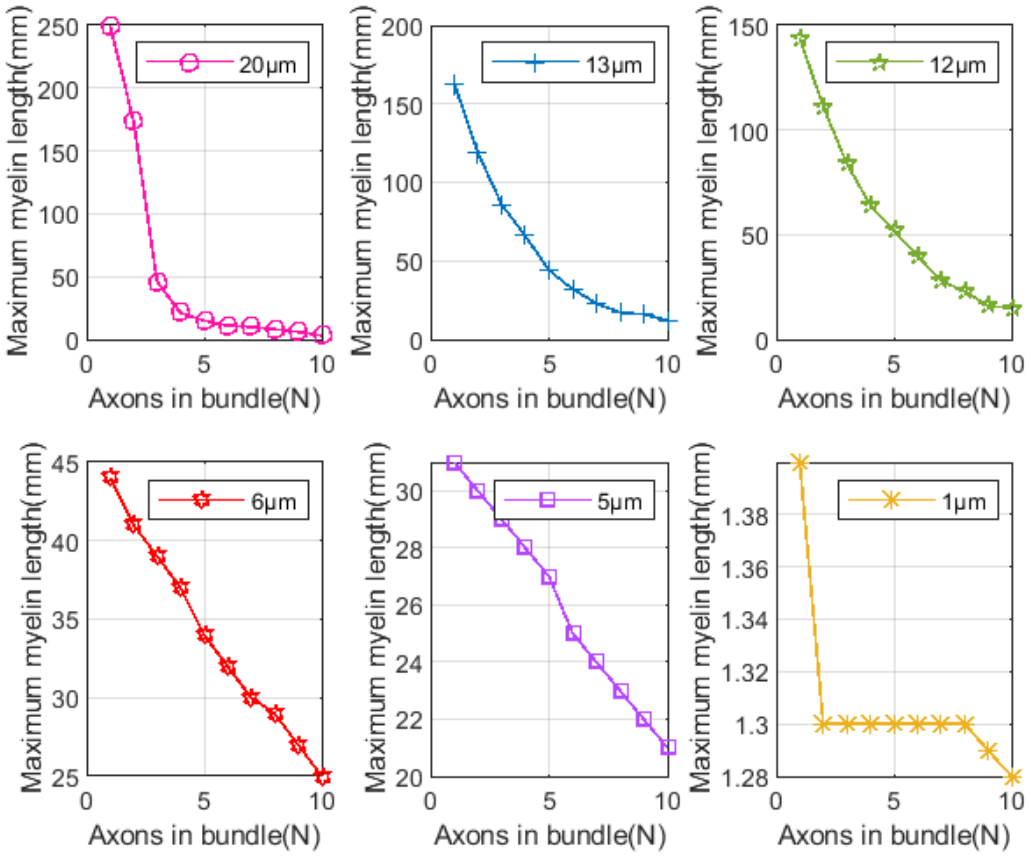

FIGURE 6.4: MML varies with number of axons in bundle; the result is consistent for different types of PNS axons: the plot with pink line shows PNS axon $A\alpha - 20\mu m$ diameter, the plot with blue line shows PNS axon $A\alpha - 13\mu m$ diameter, the plot with green line shows PNS axon $A\alpha - 12\mu m$ diameter, the plot with red line shows PNS axon $A\alpha - 6\mu m$ diameter, the plot with purple line shows PNS axon $A\alpha - 5\mu m$ diameter, the plot with yellow line shows PNS axon $A\alpha - 1\mu m$ diameter

6.2.4 Limiting Frequency and Fibre Density

High frequency brain activity have been reported in literature (Moffett et al., 2017; Fedele et al., 2015; Scheer et al., 2011). We simulated the axons in the bundle with a sinusoidal voltage pulse of low to the very high-frequency range. We observed that at a high-frequency sinusoidal voltage input the NR switches from firing AP to generating sub-threshold spikes. This frequency beyond which the NR cell stops emanating APs and starts generating sub-threshold spikes; we termed it as LF because it limits the signal propagation through bundle as the sub-threshold spikes can not generate AP at next NR. Further increase of input frequency shows that the amplitude of sub-threshold oscillation is decreasing. Eventually, this leads to disruption of the signal propagating through the axon. We further noticed that this LF varies with the density of the bundle. As we examined the LF with the number of axons in the bundle we found that LF decreases

with the increase of fibre density. In Figure 6.5 we showed in FMN, A$\alpha - 20\mu m$ and GBCLat axon, how membrane voltage drops from 50mv to nearly -60mv with an increase of input frequency of the signal. The red star shows the point where the transition from 50mv to -60mv happened.

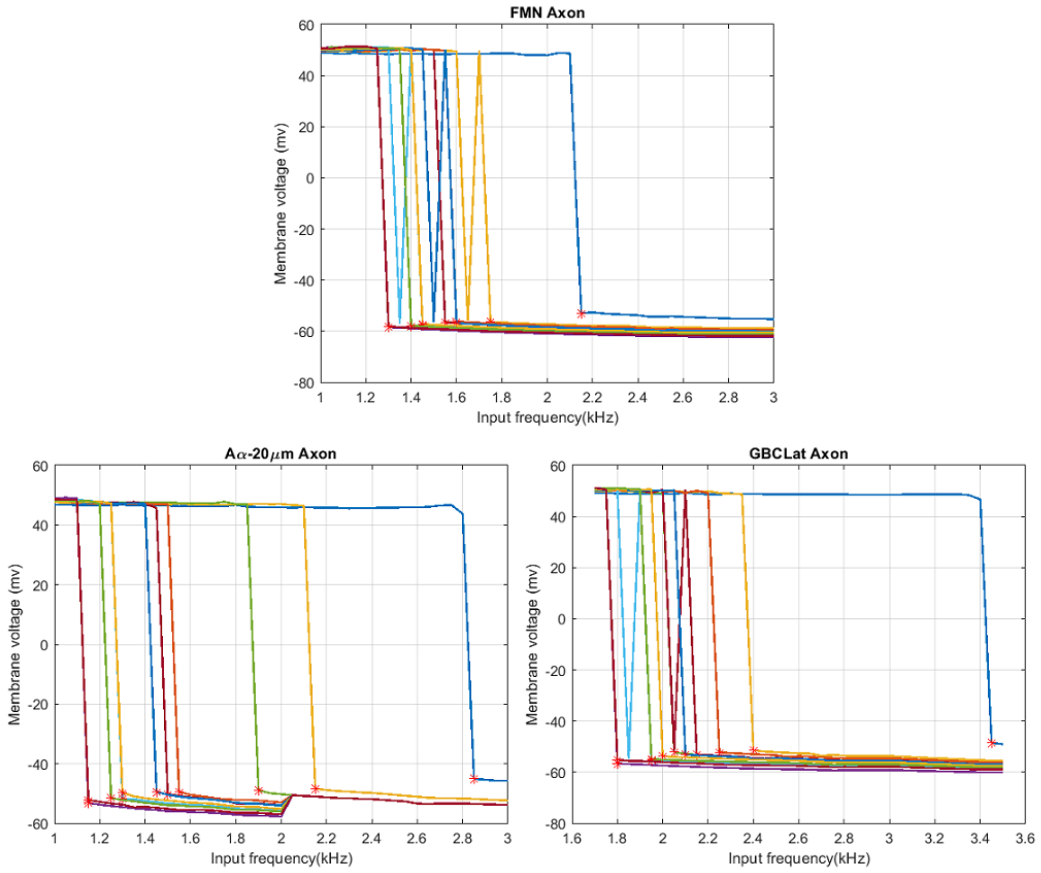

FIGURE 6.5: In FMN axon (a) membrane voltage drops with increase of input frequency (b) LF decreases with increases of FD

In Figure 6.6 we showed in FMN, A$\alpha - 20\mu m$ and GBCLat axons bundle how LF value changes with FD of the bundle. As seen in Figure 6.6, in all the three plots the LF value is decreasing for an increase of FD value except in three cases number of axons in the bundle are 8, 9, 10. But in the rest of the cases with an increase of FD value, the LF value is decreasing. So, that shows the LF value of an axon gets influenced by the coupling effects and as the number of fibre varies the LF value also gets change. This is an important finding from our model that shows that any high-frequency sub-threshold oscillation occurs in any part of the brain that will not be propagated to other parts via the myelinated axon bundle.

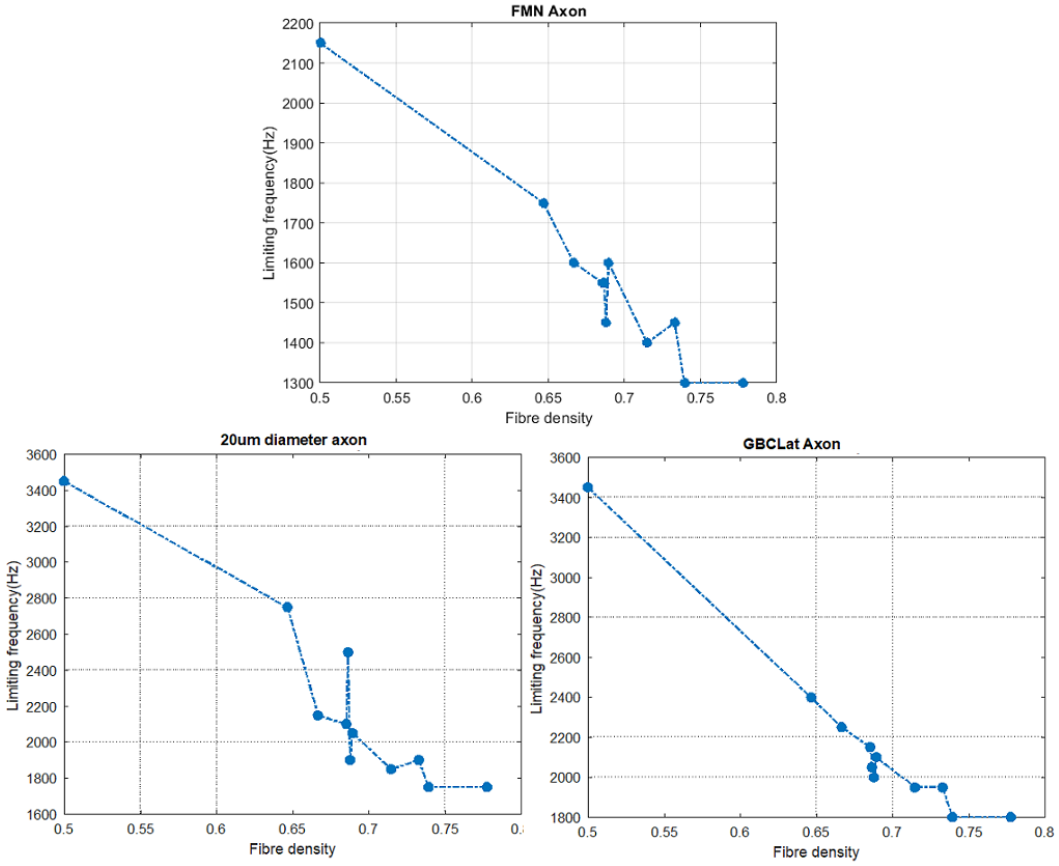

FIGURE 6.6: LF varying with FD for larger diameter and smaller diameter axons in resistive (FMN) and resistive-capacitive model (PNS and CNS)

6.2.5 Stochastic firing of axons in bundle

So far in our experiments in axon bundle, we were firing all the axons simultaneously and generating results. In this section, we performed an experiment where we wanted to see how the axon will be propagating signals when they are fired stochastically. We performed this experiment in two steps. In the first step, we took the 12 axons bundle of FMN and started firing the axons in a gradual manner starting from 1 axon to 12 axons simultaneously and examined how the signal propagates at the end of the bundle. In a second step, we fired each of the axons in a bundle with a random noise source and observed how the signal propagates at the end of the bundle.

One axon is simulated: When only the 1st axon is simulated among 12 axons in the bundle we found that at the end of the bundle only the 1st axon has sent the signal and all the other axons are dormant and have not generated any signal. The same thing happens if any single axon in the bundle is fired among the 12 axons. As shown in the bottom part of Figure 6.7, xsub1 is the NR of the 1st axon that is fired with input current and generated AP shown by the green line and denoted by V(xsub1.26), whereas

xsub21 to xsub121 are the NRs of 2nd axon to 12th axon which was not simulated but got induced by 1st axon's AP and each generated a low sub-threshold spike denoted by V(xsub1.26) to V(xsub121.26), which are put together and shown by the purple line, which is the colour of the V(xsub121.26) the 12th axon. The dynamics at the end of the bundle are shown in the top part of the Figure 6.7. In Figure 6.7, xsub9 is the last NR of the 1st axon that has fired; shown by V(xsub9.26) by the green line, whereas xsub29 to xsub129 are last NRs of 2nd axon to 12th axon which has not generated any spikes and remained passive shown together by purple line where dots of other colours are basically lines of other axon's membrane potential.

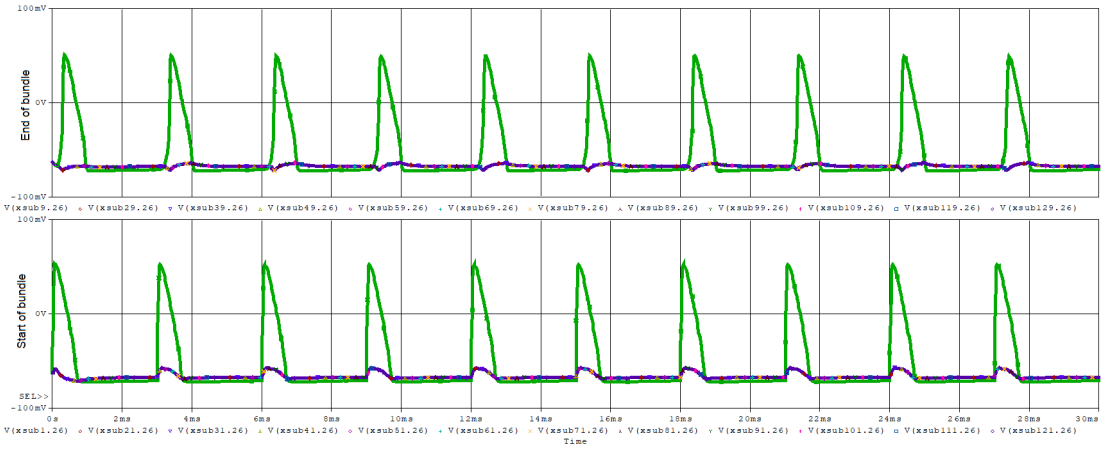

FIGURE 6.7: When one axon is simulated in the bundle the firing at the beginning and end of the bundle

Two axons are simulated: When two axons are simulated among the 12 axons in the bundle the dynamics of AP generation is shown in Figure 6.8. We simulated 1st and 2nd axons, so the NR of 1st and 2nd axons generated AP, but they induced ephaptically the other axons in the bundle and they also started firing but not as the same way as 1st and 2nd axon as shown in Figure 6.8. Every alternate spike was off from the spike trail in AP generated by the 3rd axon to the 12th axon. The red line shows the AP generated by the 1st and 2nd axon and the purple line shows the AP generated by the 3rd to 12th axon as shown in the bottom part of Figure 6.8. The dynamics at the end of the bundle is shown at the top part in Figure 6.8. The last NR of the 1st axon and 2nd axon is fired the same way as they were firing at the beginning of the bundle; shown together by the red line. The last NR of the 3rd axon to 12th axon are firing alternate spikes in the same way they fired at the beginning of the bundle with some phase lag, shown by the purple line.

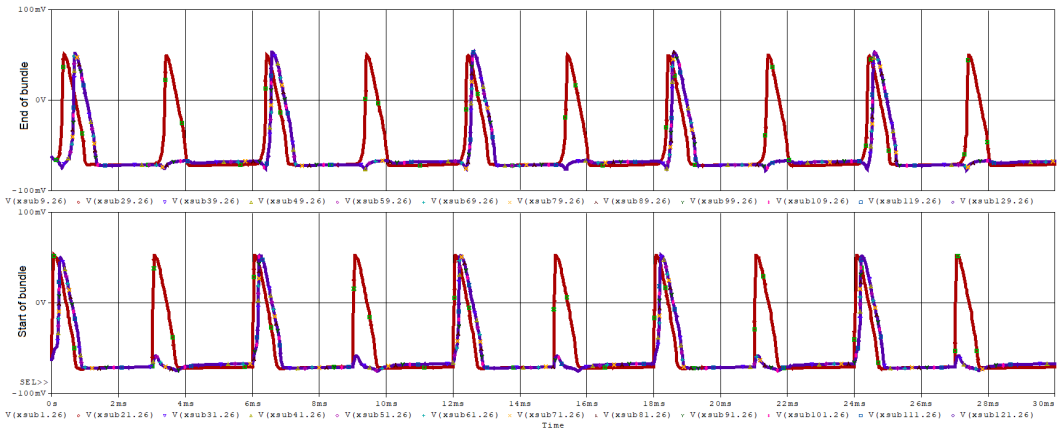

FIGURE 6.8: When two axons are simulated in the bundle the firing at the beginning and end of the bundle

Three axons are simulated: When three axons are simulated in the bundle, what happens in the axon bundle is shown in Figure 6.9. When the 1st, 2nd and 3rd axons are stimulated, they are fired simultaneously as shown by the dark purple line (the line of 3rd axon) in the bottom part in Figure 6.9. We found that the rest of the axons also got simulated by the ephaptic coupling and fired simultaneously but with different patterns; as shown by the light purple colour line (the line of 12th axon) in the bottom part of Figure 6.9. We observed some interesting coupling effects in the spike trail generated by induced axons (4th to 12th axon) at the beginning of the bundle; the first induced spike was generated at the same time as the spike generated by simulated axons (1st, 2nd 3rd axon); the second induced spike was generated at some phase lag with the second simulated spike; the third induced spike was not generated; the fourth induced spike was generated at the same time with a fourth simulated spike; the fifth induced spike was again not generated, and this whole pattern was repeated in subsequent spikes; as shown in bottom section Figure 6.9. At the end of the bundle, we observed the same firing pattern as the beginning of the bundle; as shown in Figure 6.9.

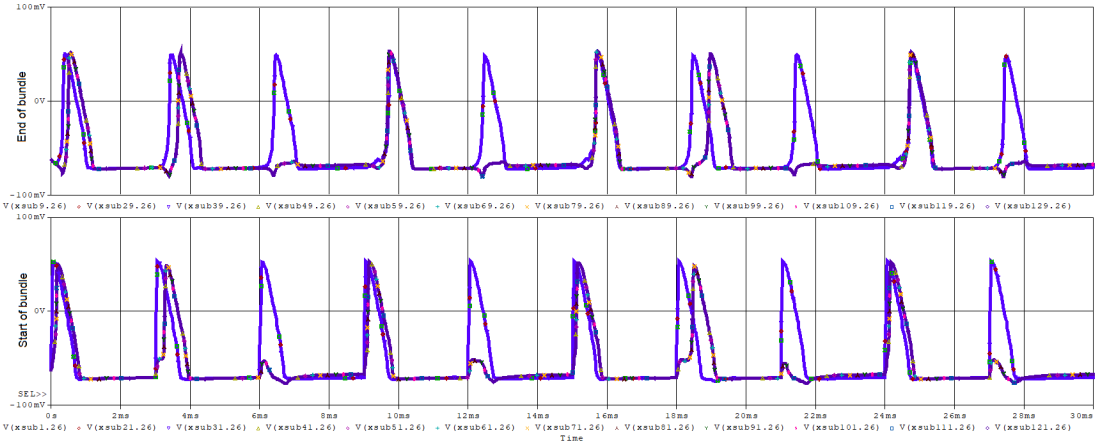

FIGURE 6.9: When three axons are simulated in the bundle the firing at the beginning and end of the bundle

Four or more axons are simulated: From simulations of four axons and onward in the bundle, we observed similar patterns in firing in the bundle as described by Figure 6.10. We found that when four axons or more are simulated in the bundle it induced the rest of the axons in the bundle by strong ephaptic coupling and the induced axons fired in the same pattern as simulated axons. The bottom part in Figure 6.10 shows the firing pattern at the beginning of the axon bundle and the top part of the Figure 6.10 shows the firing pattern at the end of the bundle. Both the beginning and end of the bundle were firing in the same pattern.

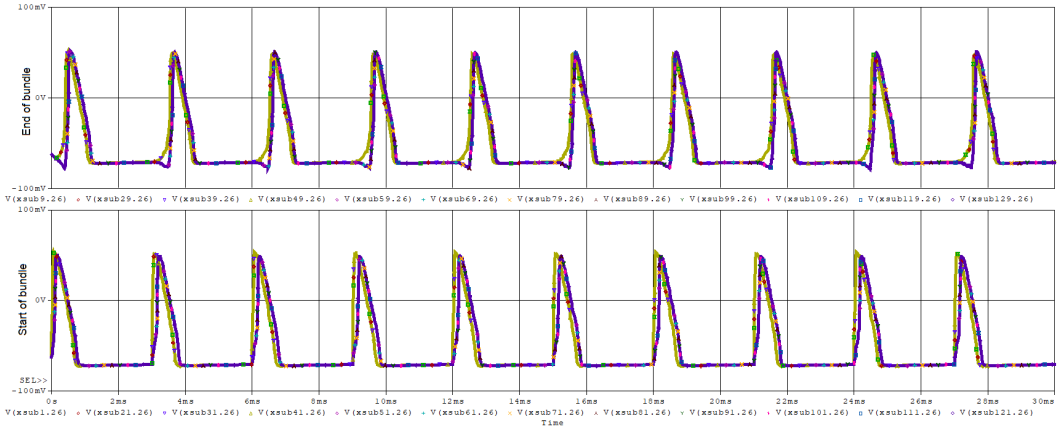

FIGURE 6.10: When four or more axons are simulated the firing at beginning and end of the bundle

So here we conclude that in a bundle of 12 axons if more than 3 axons are simulated in a random way then all the rest of the axons will be induced strongly by ephaptic coupling. When we compared the firing pattern in larger and very small diameter axons, we found that the effects of strong ephaptic coupling occur differently in them. In the medium to larger diameter axons ($2\mu m$ to $20\mu m$) we observed that when 4 or more axons are simulated then all induced axons are firing in phase with simulated axons and the signal propagates to the end of the bundle without any loss; as shown in Figure 6.10. But for very small diameter ($< 2\mu m$) axons we observed some loss of AP at the end of the bundle. So, when 4 or more axons are simulated, at the beginning of the bundle, both simulated NR and induced NR were excited and generated all APs with respect to input current, but at the end of the bundle both simulated and induced NRs are firing in phase but some APs were not generated as shown in Figure 6.11. As we can see in Figure 6.11, at the end of the bundle the NRs are firing in a 2:1 ratio with the APs generated at the beginning of the bundle. So, here some of the APs were inhibited by the coupling effect which leads to some information loss in passing the signal through the bundle.

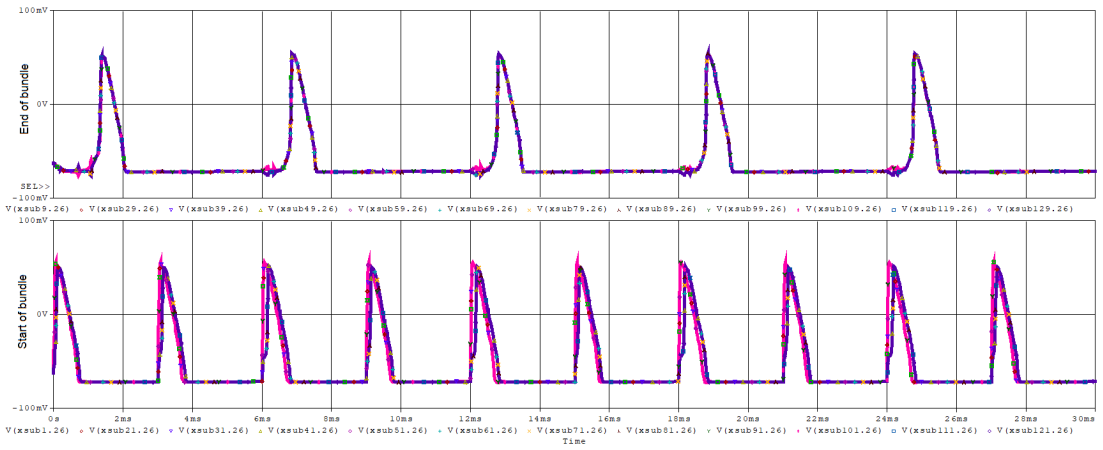

FIGURE 6.11: When four or more axons are simulated for smaller diameter axons few AP are not generated at the end of the bundle

We quantified the signal propagation through the bundle of axons when they are randomly fired for different types of axons. We calculated the population average value of all the signals generated at the beginning and end of the bundle and then calculated their mean firing rate respectively. Thus we got the population average mean firing rate of the axons for the beginning and end of the bundle, shown in Table 6.3. We compare them to find if the signal has propagated fully or there was some information loss. We found that for small diameter axons mean firing rate is changing when four or more axons are fired in a bundle of twelve axons. So here we showed that due to coupling effects signals propagation can be disputed in densely packed high fibre density small diameter axon bundle.

Axon type	**Mean firing rate at the beginning**	**Mean firing rate at the end**
$A\alpha - 20\mu m$ diameter	0.0101	0.0101
$A\alpha - 13\mu m$ diameter	0.0092	0.0092
$A\beta - 12\mu m$ diameter	0.0092	0.0092
$A\beta - 6\mu m$ diameter	0.0092	0.0092
$A\delta - 5\mu m$ diameter	0.0092	0.0092
$A\delta - 1\mu m$ diameter	0.0086	0.0043
GBCLat-3.06μm diameter	0.0086	0.0086
GBCMed-2.41μmdiameter	0.0079	0.0063
SBC-1.35μm diameter	0.0086	0.0043

Table 6.3: Population average mean firing rate at the beginning and end of the bundle for different types of axons

Axons are simulated with random noise source: Here, we extended our experiment to study the behaviour of the circuit when simulated with random noise source. We generated a random noise source by using the RND function in PSpice and offset it by -0.5V to center the random values at 0V with a +/- of 0.5V.

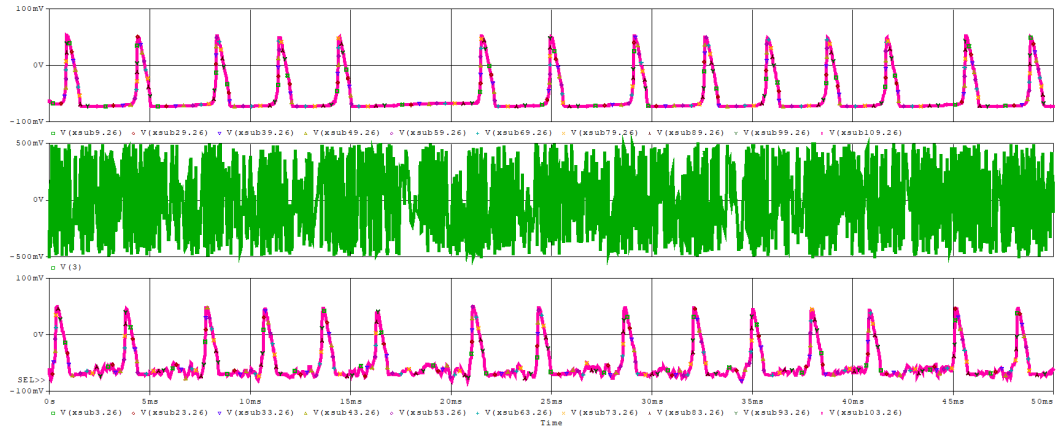

FIGURE 6.12: FMN axons are simulated with random noise source at the beginning of the bundle

We simulated each of the axons with this noise source and checked how the NR are firing at the beginning and at the end of the bundle. We performed this experiment on the FMN axon, a larger diameter PNS axon and a smaller diameter CNS axon. In Figure 6.12 we showed the results we obtained by firing FMN axons in a bundle with a random noise source. We found the NRs are simulated in a non-periodic manner at the beginning of the bundle and the beginning and end of the bundle are not firing in the same pattern and some of the APs are not generated as shown in Figure 6.12. In Figure 6.13 we showed the results seen in larger diameter PNS axon. We found that the NR of the axons at the beginning of the bundle got simulated by the random noise source and firing but not in a periodic manner. We also found that the signal is propagated at the end of the bundle but NRs are not firing in the same pattern as the beginning of the bundle and some APs are inhibited, as shown Figure 6.13

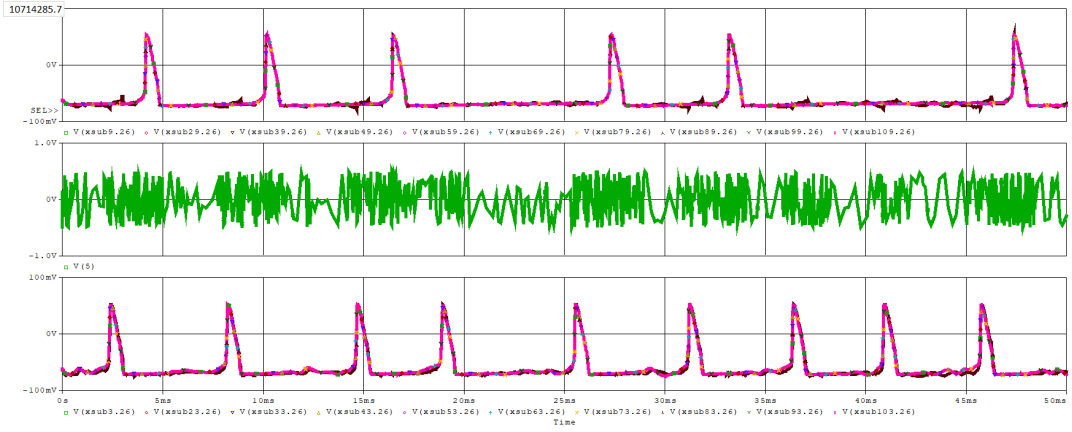

FIGURE 6.13: PNS axons are simulated with random noise source at the beginning of the bundle

When checked with a bundle of smaller diameter SBC axons we found similar results as shown in Figure 6.14. We simulated the bundle of SBC axons of diameter 1.35μm with

a random noise source. Here also we found the NRs at the beginning of the bundle were firing but not in any periodic manner. When we checked the end of the bundle we found that some of the firings of AP were inhibited and the NRs are not firing in a similar way as the beginning of the bundle, as shown in Figure 6.14.

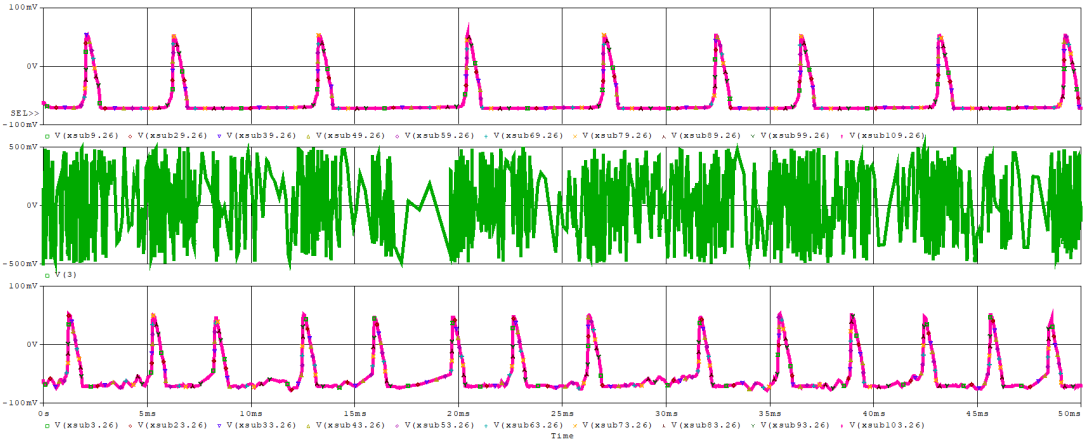

FIGURE 6.14: CNS axons are simulated with random noise source at the beginning of the bundle

6.3 Frequency response modelling in an axon bundle

6.3.1 Transfer Function modelling for Multi-Axon bundle

In Chapter 4 we have created the transfer function model for IN section of an axon and analysed its system behaviour and signal propagation characteristics in the frequency domain using MATLAB software. In this section, we created a transfer function model for the axon bundle. We used the model of IN section that we created in Chapter 4, in transfer function modelling of axon bundle here, but we took the transfer function model of lower poles and zeroes to reduce the computational complexity of the model. But before that, we created a transfer function model of the NR section. To create the transfer function model of the NR section, we first converted the subcircuit model of NR created in PSPice modelling into a Simscape block and imported it into MATLAB platform as shown in Figure 6.15.(a). We simulated the circuit with current pulse 0.6nA and generated the AP from the model as shown in Figure 6.15.(b). We got the same results as we validated the output with PSpice tool. Then we modelled a parallel circuit axon bundle with the NR and IN subcircuits as shown in Figure 6.16. We simulated the circuit with impulse input and generated impulse response. With this input and output, we linearised the circuit with MATLAB's 'Linear Analysis' control design analysis tool and generated the gain plot and phase plot.

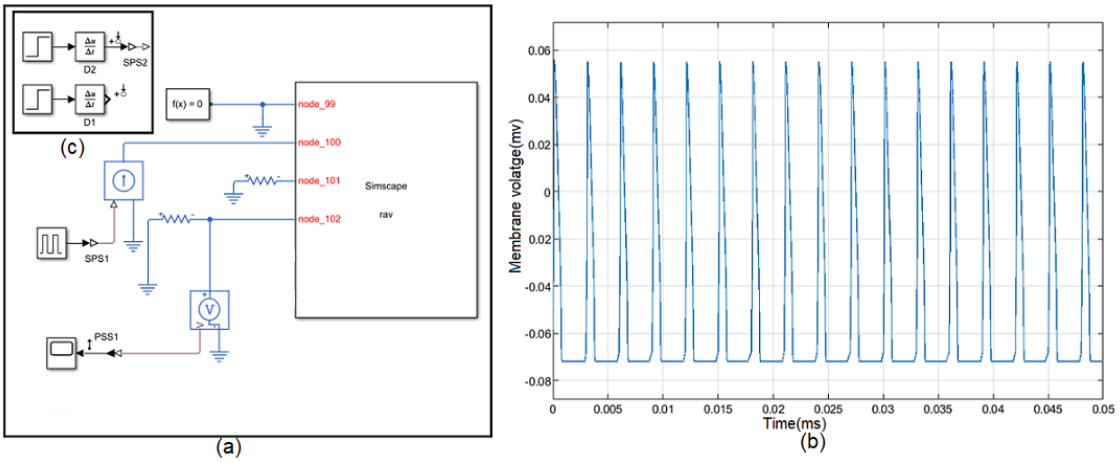

FIGURE 6.15: Simscape model of NR and its output same as PSPice model

6.3.2 Gain and Phase analysis of NR

Figure 6.17.(a) shows the bode plot that was generated from the system model formed after linearization of the NR block when placed into a parallel circuit of two axons. The gain and phase plot shows that the behaviour of the linearised NR block exhibits the characteristics of a low pass filter. The gain plot started at 150 dB due to the behaviour of system input and output which is $O(10^{-9})$ in input and $O(10^{-3})$ in output. The phase plot started at 0 dB and shows that the phase will change towards a higher frequency. In

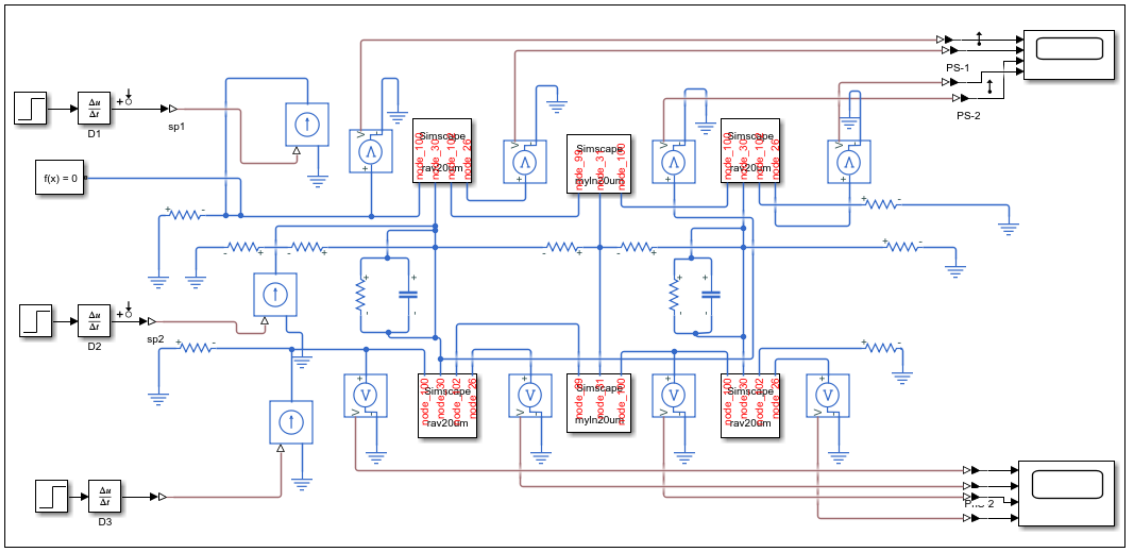

FIGURE 6.16: Simscape model of parallel circuit build using NR and IN PSpice sub-circuits

Figure 6.17.(b) we placed the output of the linearise system and output of the original NR block. The figure of colour red is the original NR system output and the figure of the colour blue is the linearised system output. As we can see from the graph the

output of the system model is in the same phase as the output of the circuit model; their peak amplitude also matches; but the magnitude of the system output is smaller than the circuit output and system output is not starting its waveform from -0.07v but from -0.03v.

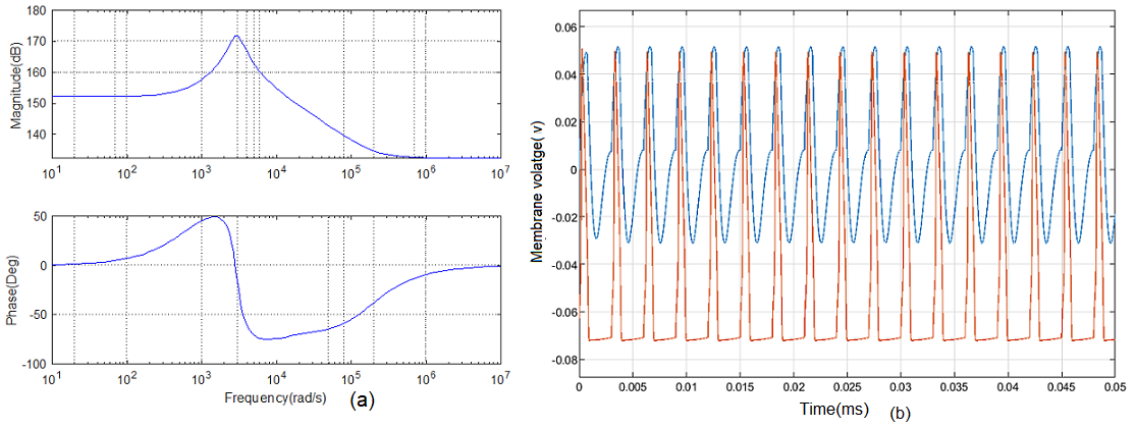

FIGURE 6.17: (a) Bode plot of system function NR (b) Output of system function of NR with it original model output

6.3.3 Model interconnection

Then, we connected the system function of NR and IN together and build the models for the axon bundle using MATLAB function 'append', 'connect'. In Figure 6.18(a), we show the interconnection of the bundle of three axons generated by using the system function of NR and IN and in Figure 6.18(b) we show the single system function developed by interconnecting NR, IN models of three axons.

6.3.4 Gain and Phase analysis of interconnected model

We generated the phase and gain plot and compared the output of the three axons model with the original model as shown in Figure 6.19. As shown in Figure 6.19.(b) the waveform of the red line is the original system's output and the waveform of the blue line is the system model's output. As seen in the figure the system model's output is in phase with the original system's output but the magnitude of the system model's output is smaller than the original circuit model's output. The output waveform generated by the system model started at -0.02V and went up to 0.042V whereas the output of the circuit model starts at -0.067V and goes up to 0.045V. The gain and phase plot in Figure 6.19.(b) shows that the bundle system behaviour is like a low pass filter. In the gain plot in Figure 6.19.(b) we can see that it has started at 150 dB which is due to the behaviour of system input and output which is $O(10^{-9})$ in input and $O(10^{-3})$ in output.

The phase plot started at 0 db and shows that the phase will change up to 30 degrees towards a higher frequency before the system reaches the cross-over frequency of the system. The crossover frequency is the frequency point at which the gain and phase plot after that will be greatly reduced. Figure 6.20 shows the gain and phase plot of all the inputs and outputs of three axon system function sysT3ax. The inputs of the system function sysT3ax are e(1), e(2) and e(3) and outputs are u(1), u(2) and u(3). The gain phase plot of e(1) to u(1), e(2) to u(2) and e(3) to u(3) are of three axons coupled in the bundle, as shown in Figure 6.20. Figure 6.20 shows the dynamic of phase-frequency characteristics of three axons in the bundle are the same. So, the phase plot shows that the signal propagates through the bundle of 3 axons will not change its phase when reaches the end of the bundle and input and output of the bundle will be in phase up to the cross-over frequency of the system. Similar way, we interconnected the NR and

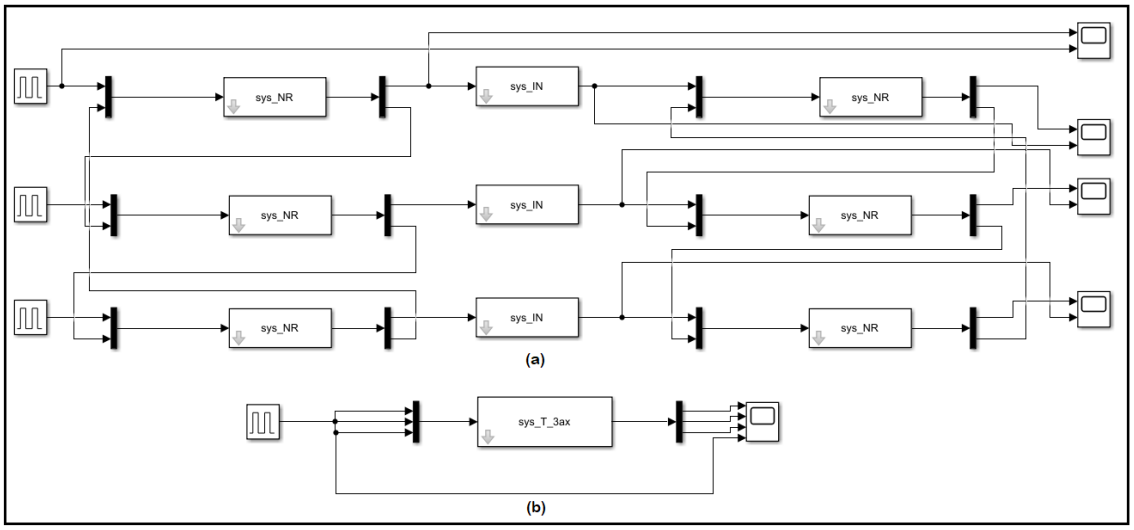

FIGURE 6.18: (a)The system function model of three axons bundle build with system function of NR and IN (b) The single system function model developed after interconnecting three models

IN models and built the system function model for 12 axons. The process of generating 12 axons model took much longer time than 3 axons. Figure 6.21 shows the gain and phase plots of 12 axons in the bundle. The phase plots of the Figure 6.21 give the phase-frequency characteristics of signal propagation through the axons in the bundle. Our objective was to find out the phase-frequency characteristic of signal propagation through white matter tracts i.e. a bundle of myelinated axons. This Figure 6.21 describes the phase-frequency characteristics of a myelinated axon bundle which are ephaptically coupled. The phase-frequency plot shows that the behaviour of the system definition of a bunch of axons is similar to a low pass filter; that it will pass the signal of a certain frequency and dampen out signal beyond that frequency. We determine the cut-off frequency (-3db) of 319.42Hz of the system.

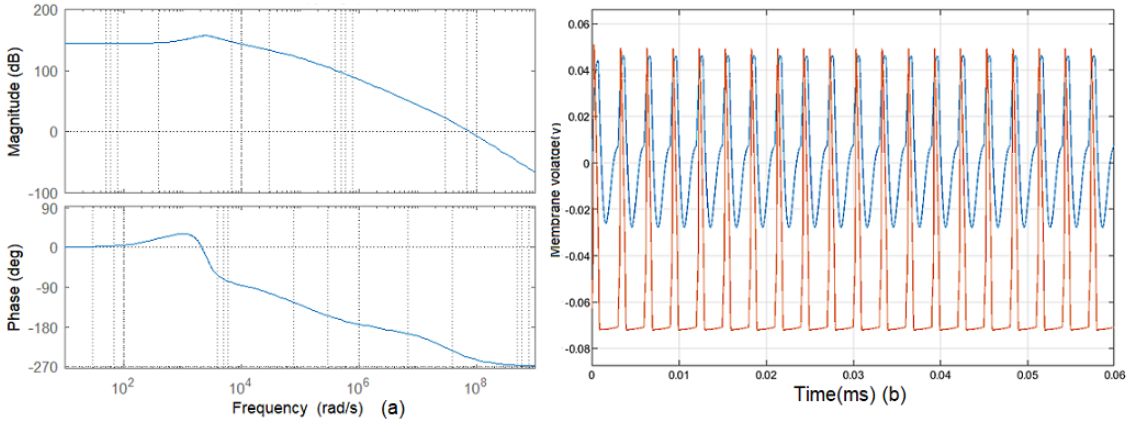

FIGURE 6.19: (a) Gain and phase plot, ((b) Output waveform of system function model of three axons bundle build with system function of NR and IN

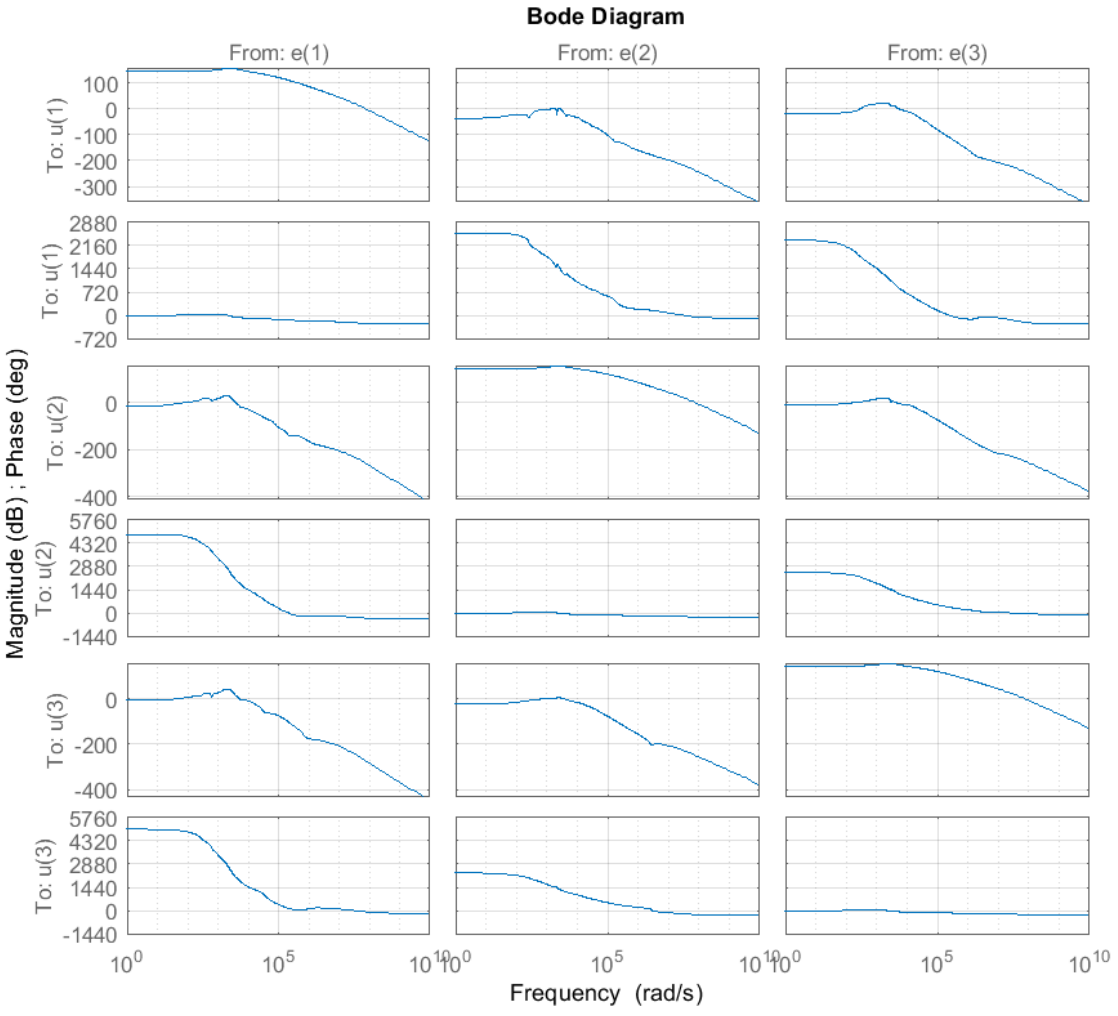

FIGURE 6.20: Gain and phase plot of all the inputs and outputs of three axon model

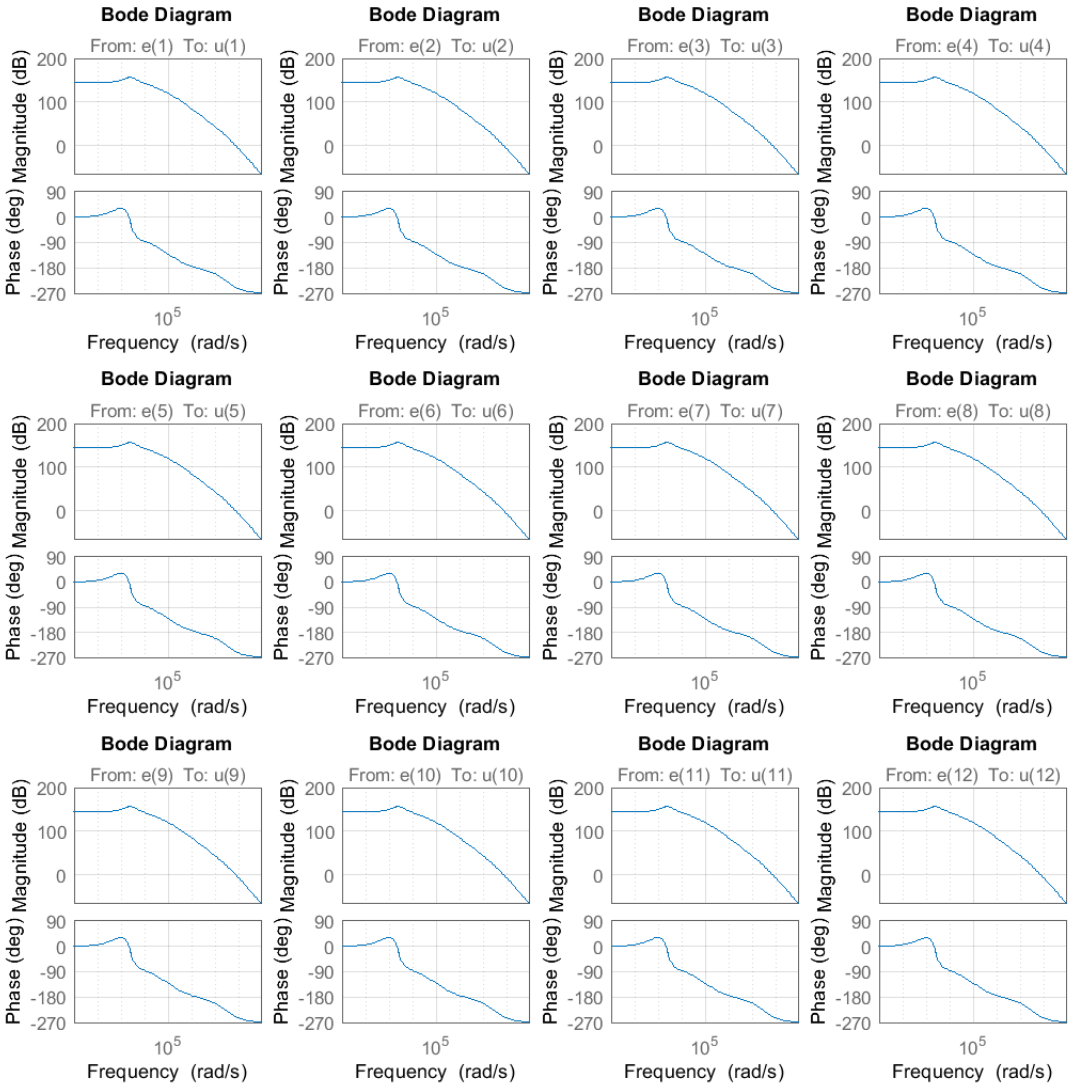

FIGURE 6.21: Gain and phase plot of all the inputs and outputs of 12 axon model

6.4 Results and Discussion

Here, we developed a computational circuit model for a bundle of axons and explore the propagation of the signal through them. From our simulation results, we found that CV varies with the density of the fibre bundle. We defined the relation between CV and FD by forming an equation and found that CV varies inversely with FD. So this implies that as the density of fibre bundle will increase in the case of myelinated axon the transmission speed of spike will slow down. From our experiments, we derived a new frequency for the axon bundle which we termed as LF. The LF defines the frequency beyond which the nodes of Ranvier will stop transmitting the signal through the bundle. This is an important finding from our model that shows that any high-frequency sub-threshold oscillation occurs in any part of the brain will not be propagated to other parts via the myelinated axon bundle. We calculated this LF for different FD values of densely

pack fibre bundle for larger and smaller diameter axons. We found that the value of LF is lowering for higher FD values. Then, we found that the upper limit of myelin length for non-disruptive signal propagation varies with the FD of the axon bundle. As the FD value increasing the maximal length of myelin for non-disruptive signal propagation is decreasing. Our exploration of the circuit model also shows that in the case of densely packed bundles, for small diameter axons the signal may get lost due to coupling effects while propagating through the bundle. We also defined a system function for the axon bundle which shows the behaviour of the bundle is similar to the low pass filter. We analysed the gain and phase plot of the bundle and found that the output signal at the end of the bundle will be in phase with the input signal of the bundle up to the cross-over frequency of the system. This system model can be extended and used in future for the study of system behaviour of myelinated axon bundle for any number of axons.

6.5 Conclusions

Based on our simulation results we conclude that signal transmission in a bundle of myelinated axons is influenced by the coupling effects of the number of fibres in the bundle. If the density of the fibres is higher then the transmission speed of the impulses will slow down. We also conclude from our simulation model that very high-frequency stimulus input will disrupt signal propagation through the bundle of axons and the threshold of this frequency changes inversely with the density of the fibre bundle. We also conclude from our computational model that due to the influence of ephaptic coupling in the bundle the signal propagation through myelin will be altered. The maximal myelin length where impulse can propagate without dying out will shorten with the increase of FD. The identification of the system model of the myelinated axon bundle exhibits the behaviour of a low pass filter. The analysis of gain and phase plot of axon bundle implies that after the cross-over frequency the firing between two consecutive nodes of Ranvier may get out of phase. Our model of simulation can serve as the basis for a more detailed theory of signal transmission through a myelinated axon bundle in various experimental conditions.

Chapter 7

Conclusions

This project aims to model the phase and frequency characteristics of white matter tracts with a circuit modelling approach so that signal propagation through white matter tracts can be characterized in both temporal and frequency domains, and correspondence between structural and functional connectivity can be established.

The steps to accomplish that goal are, model the structural connectivity of the brain from MRI data and extract parameter values for tracts, design a circuit based computational model of the structural connectivity using parameter values obtain from MRI data analysis, generate a system definition for the model, then finally analysis its phase and frequency characteristics.

We started working with MRI data processing where we have designed an algorithm to parcellate cortical surface. With the exiting methods of parcellation of the cortical surface, we can only parcellate cortical surface into defined anatomical brain ROIs. Using our algorithms we can demonstrate that cortical surface can also be parcellated into any number of equal size areas. We have presented a framework for a toolchain that process structural and diffusional MRI data and calculate graph theory measures for quantifying the structural connectivity based on equal area parcellation to define brain ROIs. The framework is of the fully automated toolchain that does not need separate intervention at its different processing stages. Being based on equal parcellation, the construction of structural connectomes can be customized based on user need making it available for structural connection analysis for neonates as well as brain injury cases. The entire toolchain processes have been validated with HCP data which showed correct working and its ease of use.

From our single axon model, we have observed that the model exhibits low pass filter behaviour. That means the model passes the signal of specific frequencies and dampens signals of other frequencies. The cut-off frequency of the model varies with the geometry of the axon. We have formulated a mathematical relation between the cut-off frequency

and myelin length. We have also noted that the conduction velocity of signal propagation through a single axon varies with the axon's geometry. We have also found that there is an upper limit of myelin length beyond which signal propagation will be disrupted. From these, we can conclude that signal propagation disruption will occur in a single myelinated axon if the axon's myelin length is beyond its upper limit or the signal's frequency is above the cut-off frequency of the myelin. Overall we can conclude that the experiment results we obtained here imply that depending on the myelin geometry a rate coded nerve signal propagation through structural connection could be disrupted resulting in functional disconnection between two brain areas.

We have observed that an axon's conduction velocity is inversely proportional to the axon bundle density from our axon bundle modelling. We have derived a mathematical relationship between the conduction velocity and the fibre density of the axon bundle. From this observation of the mathematical model, we can conclude that in densely packed bundles in which the axons are ephaptically coupled with each other, an impulse's transmission speed will reduce with higher density of axons. In other words, in a tightly coupled axon bundle signal propagation will face resistance. We have also found a new phenomenon where we see the high-frequency signal changes the firing of the AP to sub-threshold impulses in nodes of Ranvier which leads to disruption of signal propagation to the next NR. This is an important finding from our model that shows that any high-frequency sub-threshold oscillation occurs in any part of the brain will not be propagated to other parts via the myelinated axon bundle. We have also found that the axon bundle's behaviour is similar to a low pass filter that passes selective signals below the cut off frequency. Our simulation output implies that ephaptic coupling plays a significant role in signal transmission through the myelinated axon bundle, either by altering the transmission speed of impulses or changing the timing of AP firing. Based on the geometrical structure of the myelinated axon, their alignment in the bundle and their distance between each other, ephaptic coupling can either excite or inhibit the firing in nearby axons, which can lead to amplification or pacification of mass neuron firings.

In the below section, we have summarised the tasks that have been accomplished and the scope of future works:

7.1 Current work

- A new parcellating cortical surface method has been developed to generate equal-sized brain areas (ROIs) of the cortical surface. The existing method of cortical surface parcellation is based on anatomical definitions of different brain areas. This method is not useful for neonates or adults' brains with neuroplasticity anomalies. We propose a new methodology to parcellate the cortical surface into equal-sized

areas from the structural MRI image for extracting white matter tracts' geometrical properties.

- We have designed a computational circuit model to analyse temporal and phase-frequency characteristics of signal propagation in a single myelinated axon. We have implemented the circuit model using the PSPice tool along with Matlab. Using the model, we have derived CV, MML for a single axon. Then we have defined a transfer function for the myelin segment of a single myelinated axon. Using this transfer function, we have derived cut-off frequency for a single axon. Using these data, we defined a mathematical relationship between cut-off frequency and myelin length.

- We have modelled the effects of ephaptic coupling between two myelinated axons using circuit theory.

- We have designed a computational circuit model to determine phase-frequency signal propagation characteristics through a myelinated axon bundle. For the design of this model, we have used the PSPice circuit simulation tool along with Matlab. We further determined the CV, MML, and LF characteristics for the axon bundle from the simulation model. We determined the mathematical relationship between the CV and the density of the fibre bundle. Then we defined a transfer function of the axon bundle and derived the phase-frequency characteristics of signal propagation through the axon bundle.

7.2 Future plan

- Our models are based on simulated data. As a scope for future work, we need to experimentally validate all the results.

- We have theoretically proved using the 12 axons model that temporal and phase-frequency characteristics of signal propagation through a bundle of myelinated axons exists. But we have not verified the scalability of this model yet. To extend the scope of our work, we need to prove that the same theory holds for a large number of axons. Also, as future work, we would experiment with signal propagation in the model by scaling the length of axons, for example, 15cm between hemispheres and 1m for the spinal cord.

- In this work, we have developed a framework for an automated toolchain. The different parts of the model can be further integrated and enhanced so that all aspects of structural and functional connectivity can be measured in further detail.

Appendix A

Appendix

1. Matlab code for Equal Area Parcellation.

```
function equal_parcellation(N)
%
% equal_parcellation -Automated parcellation of cortical surface based on
    equal area sphere partitioning.
%% Usage: equal_parcellation(fname,N)

% Author:   Sarbani.Das@soton.ac.uk
% Created:  20 March 2017
%
%%%%%%%%%%%%%%%%%%%%%%%%%%%%%%%%%%%%%%%%%%%%%%%%%%%%%%%%%%%%%%%%%%%%%%%%%%%%%%%
for run=1:2
    if run==1
        fname = '../surf/rh.sphere.reg';
        hem= 'r';
        dir='right';
    elseif run ==2
        fname = '../surf/lh.sphere.reg';
        hem= 'l';
        dir='left'
    end
    if (fopen(fname, 'rb', 'b') < 0)
      str = sprintf('could not open surface file %s.', fname) ;
      error(str) ;
    end
    if ischar(N)
      N=str2num(N);
    end
    [vertex_cor,~]=read_surf(fname);
    points_x =100*eq_point_set(2,N);
    points_x=points_x';
    point_x1=points_x;
    if(hem=='r')
    points_x=[-points_x(:,1) points_x(:,2) points_x(:,3)];
    end
    N=size(points_x,1);
%     [vertex_cor,~]=read_surf(fname);
    V=size(vertex_cor,1);
    atlas_point=zeros(1,5);
```

```
    f=1;
    for v=1:V
        [nearestIndex,~] = mesh_vertex_nearest(points_x,vertex_cor(v,:));
        if f==1
            f=0;
            atlas_point=[v-1,nearestIndex,vertex_cor(v,:)];
        else
        atlas_point=[atlas_point;[v-1,nearestIndex,vertex_cor(v,:)]];
        end
    end
    for n=1:N
        lxyz_n=zeros(1,3);
        lindex=zeros(1,1);
        lvals=zeros(1,1);
        f=1;
        for v=1:V
         if n==atlas_point(v,2)
             if f==1
                 lxyz_n=atlas_point(v,3:5);
                 lindex=atlas_point(v,1);
                 lvals=0.1000000;
                 f=0;
             else
             lxyz_n=[lxyz_n;atlas_point(v,3:5)];
             lindex=[lindex;atlas_point(v,1)];
             lvals=[lvals;0.1000000];
             end
         end
        end
        subjid='117122';
        labelfile=string(dir)+'/'+string(hem)+'h.node'+string(n)+'.label';
        write_label(lindex,lxyz_n,lvals,labelfile,subjid);

    end
end
```

2. Python code for creating strucurtal connectome for a set of subjects.

```
#!/usr/bin/env python

import math, os, sys
import math, os, sys
MRTRIX_LIB_PATH='~/mrtrix3/scripts/'
sys.path.append(os.path.expanduser(MRTRIX_LIB_PATH))
import lib.app, lib.cmdlineParser
from datetime import date

def abspath(*arg):
  return os.path.abspath(os.path.join(*arg))

def relpath(*arg):
  return os.path.relpath(os.path.join(*arg),lib.app.workingDir)

from lib.printMessage  import printMessage
from lib.errorMessage  import errorMessage
from lib.runCommand    import runCommand


lib.app.author = 'SD'
```

```
lib.cmdlineParser.initialise('Generate Structural Connectome for Human
    Connectome Project')
lib.app.parser.add_argument('input_dir', help='The input directory
    containing Diffusional and Structural preprocessed files')
lib.app.parser.add_argument('output_dir', help='The output directory will
    have 5TT.mif, vis.mif,nodes.mif,nodes_fixsgm.mif,DWI.mif,meanb0.mif
    ,.....,connectome.csv')

lib.app.initialise()

lib.app.args.input_dir = relpath(lib.app.args.input_dir)
indir = lib.app.args.input_dir
if not os.path.exists(indir):
  errorMessage('input directory not found');
outdir = lib.app.args.output_dir
outdir = str(date.today())+'_'+outdir
#lib.app.checkOutputFile (outdir)
#lib.app.make_dir(outdir)

inFiles = os.listdir(indir)
for inputdir in inFiles:
 if len(inputdir) < 6:
   printMessage('not enough files found in input directory.')
 else:
   printMessage('Generating Structural connectome for '+str(inputdir))


 outputdir = outdir+'/'+str(inputdir)
 inputdir = indir+'/'+inputdir
 lib.app.checkOutputFile (outputdir)
 lib.app.make_dir(outputdir)

 runCommand('cp -R '+abspath(inputdir)+' '+abspath(outputdir))

 printMessage('Generate a tissue-segmented image appropriate for
    Anatomically-Constrained Tractography:')
 #5ttgen fsl T1w_acpc_dc_restore_brain.nii.gz 5TT.mif -premasked
 runCommand('5ttgen  fsl '+abspath(inputdir,'T1w_acpc_dc_restore_brain.nii.
    gz')+' '+abspath(outputdir,'5TT.mif')+' -premasked')


 printMessage('Collapse the multi-tissue image into a 3D greyscale image for
     visualisation: Check in mrview')
 #5tt2vis 5TT.mif vis.mif; mrview vis.mif
 runCommand('5tt2vis '+abspath(outputdir,'5TT.mif')+' '+abspath(outputdir,'
    vis.mif'))
 #runCommand('mrview '+abspath(outputdir,'vis.mif'))

 printMessage('Modify the integer values in the parcellated image')
 #labelconvert aparc+aseg.nii.gz FreeSurferColorLUT.txt fs_default.txt nodes
    .mif
 runCommand('labelconvert '+abspath(inputdir,'aparc+aseg.nii.gz')+' /home/
    koushik/mrtrix3/FreeSurferColorLUT.txt /home/koushik/mrtrix3/src/
    connectome/tables/fs_default.txt '+abspath(outputdir,'nodes.mif'))

 printMessage('Replace FreeSurfers estimates of sub-cortical grey matter')
```

```
runCommand('labelsgmfix '+abspath(outputdir,'nodes.mif')+' '+abspath(
   inputdir,'T1w_acpc_dc_restore_brain.nii.gz')+' /home/koushik/mrtrix3/src
   /connectome/tables/fs_default.txt '+abspath(outputdir,'nodes_fixSGM.mif'
   )+' -premasked')

printMessage('Convert the diffusion images into a non-compressed format')
runCommand('mrconvert '+abspath(inputdir,'data.nii.gz')+' '+abspath(
   outputdir,'DWI.mif')+' -fslgrad '+abspath(inputdir,'bvecs')+'  '+abspath
   (inputdir,'bvals')+' -datatype float32 -stride 0,0,0,1')

printMessage('Generate a mean b=0 image (useful for visualisation):')
runCommand('dwiextract '+abspath(outputdir,'DWI.mif')+' - -bzero | mrmath -
    mean '+abspath(outputdir,'meanb0.mif')+' -axis 3')

printMessage('Estimate the response function; note that here we are
   estimating multi-shell, multi-tissue response functions:')
runCommand('dwi2response msmt_5tt '+abspath(outputdir,'DWI.mif')+' '+
   abspath(outputdir,'5TT.mif')+' '+abspath(outputdir,'RF_WM.txt')+' '+
   abspath(outputdir,'RF_GM.txt')+' '+abspath(outputdir,'RF_CSF.txt')+' -
   voxels '+abspath(outputdir,'RF_voxels.mif'))

printMessage('check appropriateness of response function voxel selections')
#runCommand('mrview '+abspath(outputdir,'meanb0.mif')+' -overlay.load '+
   abspath(outputdir,'RF_voxels.mif')+' -overlay.opacity 0.5')

printMessage('Perform Multi-Shell, Multi-Tissue Constrained Spherical
   Deconvolution:')
runCommand('dwi2fod msmt_csd '+abspath(outputdir,'DWI.mif')+' '+abspath(
   outputdir,'RF_WM.txt')+' '+abspath(outputdir,'WM_FODs.mif')+' '+abspath(
   outputdir,'RF_GM.txt')+' '+abspath(outputdir,'GM.mif')+' '+abspath(
   outputdir,'RF_CSF.txt')+' '+abspath(outputdir,'CSF.mif')+' -mask '+
   abspath(inputdir,'nodif_brain_mask.nii.gz'))

runCommand('mrconvert '+abspath(outputdir,'WM_FODs.mif')+' - -coord 3 0 |
   mrcat '+abspath(outputdir,'CSF.mif')+' '+abspath(outputdir,'GM.mif')+' -
    '+abspath(outputdir,'tissueRGB.mif')+' -axis 3')

printMessage('Visually make sure that both the tissue segmentations and the
    white matter FODs are sensible')
#runCommand('mrview '+' '+abspath(outputdir,'tissueRGB.mif')+' -odf.load_sh
    '+' '+abspath(outputdir,'WM_FODs.mif'))

printMessage('Generate the initial tractogram:')
runCommand('tckgen '+abspath(outputdir,'WM_FODs.mif')+' '+abspath(outputdir
   ,'10M.tck')+' -act '+abspath(outputdir,'5TT.mif')+' -backtrack -
   crop_at_gmwmi -seed_dynamic '+abspath(outputdir,'WM_FODs.mif')+' -
   maxlength 250 -number 10M -cutoff 0.06')


#mrresize WM_FODs.mif FOD_downsampled.mif -scale 0.5 -interp sinc
runCommand('mrresize '+abspath(outputdir,'WM_FODs.mif')+' '+abspath(
   outputdir,'FOD_downsampled.mif')+' -scale 0.5 -interp sinc')

#Apply the Spherical-deconvolution Informed Filtering of Tractograms (SIFT)
    algorithm.This method reduces the overall streamline count, but
   provides more biologically meaningful estimates of structural connection
    density
printMessage('Apply the Spherical-deconvolution Informed Filtering of
   Tractograms (SIFT) algorithm.')
```

```
runCommand('tcksift '+abspath(outputdir,'10M.tck')+' '+abspath(outputdir,'
   FOD_downsampled.mif')+' '+abspath(outputdir,'1M_SIFT.tck')+' -act '+
   abspath(outputdir,'5TT.mif')+' -term_number 1M')


#Map streamlines to the parcellated image to produce a connectome:
printMessage('Map streamlines to the parcellated image to produce a
   connectome:')
runCommand('tck2connectome '+abspath(outputdir,'1M_SIFT.tck')+' '+abspath(
   outputdir,'nodes_fixSGM.mif')+' '+abspath(outputdir,'connectome.csv'))

lib.app.complete()
```

3. PSPICE code of circuit modeling for Axon

```
.SUBCKT RAV 100 99 101 102
**********************************************************************
*
*
* coNa = 491.0E-3 Extracellular sodium concentration (mol/L)
* ciNa = 50.0E-3 Intracellular sodium concentration (mol/L)
* coK = 20.11E-3 Extracellular potassium concentration (mol/L)
* ciK = 400.0E-3 Intracellular potassium concentration (mol/L)
* GNaMax=120.0E-3
* GKMax =36.0E-3
* V_r = -62.5E-3 Resting Membrane Potential (V)
* Temp = 6.3 Temperature (Degrees Celsius)
* b = 0.02 Relative permeability of sodium to potassium
* R = 8.314 Reiberg gas constant (joules/(mole*kelvin))
* Z = 1.0 Sodium and potassium ionicvalence
* F = 9.648E4 Faraday's constant (coulombs/mole)
*
**********************************************************************
*
Rax1 99 31 4E6
Rax 31 102 4E6
Ri1 100 103 1E-22
Ri 103 101 1E-22
Rnode 103 30 30E-6
FNA 31 27 VINA 1
FK 31 28 VIK 1
VNk 28 30 -72.0E-3
VNNa 27 30 55.0E-3
ENAK 26 0 31 30 1
CE 31 30 {1E-12} IC=-62.5E-3
*Sodium current current pathway
*M variable
CM 2 0 0.26E-3 IC=0.0393
RM 2 0 1E10
GAM 0 2 POLY(2) 2 0 5 0 0 0 1 0 -1
GBM 0 2 POLY(2) 2 0 6 0 0 0 0 0 -1
EAM 5 0 value={-0.1*(v(26)*1E3+35)/(exp(-0.1*(v(26)*1E3+35))-1)}
RAM 5 0 1E10
EBM 6 0 value={4*exp(-(v(26)*1E3+60)/18)}
RBM 6 0 1E10
* Sodium current current pathway
* H Variable
CH 3 0 0.26E-3 IC=0.6798
RH 3 0 1E10
```

```
GAH 0 3 POLY(2) 3 0 7 0 0 0 1 0 -1
GBH 0 3 POLY(2) 3 0 8 0 0 0 0 0 -1
EAH 7 0 value={0.07*exp(-0.05*(v(26)*1E3+60))}
RAH 7 0 1E10
EBH 8 0 value={1/(1+exp(-0.1*(v(26)*1E3+30)))}
RBH 8 0 1E10
*Potassium current current pathway
* K parameters
CN 4 0 0.26E-3 IC=0.2803
RN 4 0 1E10
GAN 0 4 POLY(2) 4 0 9 0 0 0 1 0 -1
GBN 0 4 POLY(2) 4 0 10 0 0 0 0 0 -1
EAN 9 0 value={-0.01*(v(26)*1E3+50)/(exp(-0.1*(v(26)*1E3+50))-1)}
RAN 9 0 1E10
EBN 10 0 value={0.125*exp(-0.0125*(v(26)*1E3+60))}
RBN 10 0 1E10
EMNA 15 0 26 11 1
RMNA 15 0 1E10
EM3 53 0 POLY(1) 2 0 0 0 0 1
EM3H 16 0 POLY(2) 53 0 3 0 0 0 0 0 1
RM3H 16 0 1E10
GNA 0 20 POLY(2) 15 0 16 0 0 0 0 0 6.7858E-006
VINA 20 0 0
VNA 11 0 55.0E-3
RNA 11 0 1E10
VK 12 0 -72.0E-3
RK 12 0 1E10
EMK 17 0 26 12 1
RMK 17 0 1E10
EN4 18 0 poly(1) 4 0 0 0 0 0 1
RN4 18 0 1E10
GK 0 21 POLY(2) 17 0 18 0 0 0 0 0 2.0358E-006
VIK 21 0 0
.ENDS
.SUBCKT MYLN 99 101 100 102
Rax 99 103 4E-6
Rax2 103 100 4E-6
RMY 103 30 250E6
CMY 103 31 1.5E-12
R 101 31 4E6
R2 31 102 4E6
VNAK 31 30 -63E-3
.ENDS
 .SUBCKT MYLNSHEATH 3 4 15 16
xsub2 3 4 5 6 MYLN
xsub3 5 6 7 8 MYLN
xsub4 7 8 9 10 MYLN
xsub5 9 10 11 12 MYLN
xsub6 11 12 13 14 MYLN
xsub7 13 14 15 16 MYLN
xsub8 15 16 17 18 MYLN
.ENDS



I 0 2 pulse(0 6E-9 10E-6 100.0E-9 100.0E-9 0.1E-3 0.2E-3)
R2 1 0 1E100
*node1
xsub1 1 2 3 4 RAV
```

```
xsub2 3 4 5 6 MYLNSHEATH
*node2
xsub3 5 6 7 8 RAV
xsub4 7 8 9 10 MYLNSHEATH
*node3
xsub5 9 10 11 12 RAV
R3 11 0 1E100
R4 12 0 1E100
.TRAN 0.1ms 5ms 0
.PROBE
.END
```

4. Color look up table for newly parcellated regions.

No.	Area	R	G	B
0	node1	25	5	25
1	node2	220	20	100
2	node3	125	100	160
3	node4	100	25	0
4	node5	120	70	50
5	node6	220	20	100
6	node7	20	20	60
7	node8	180	220	140
8	node9	220	60	220
9	node10	180	40	120
10	node11	140	20	140
11	node12	20	30	140
12	node13	35	75	50
13	node14	225	140	140
14	node15	200	35	75
15	node16	160	100	50
16	node17	80	160	20
17	node18	20	220	60
18	node19	60	220	60
19	node20	220	180	140
20	node21	20	100	50
21	node22	220	60	20
22	node23	120	100	60
23	node24	220	20	20
24	node25	220	180	220
25	node26	60	20	220
26	node27	160	140	180
27	node28	80	20	140
28	node29	75	50	125
29	node30	20	220	160
30	node31	20	180	140
31	node32	140	220	220
32	node33	100	0	100
33	node34	70	20	170
34	node35	150	150	200
35	node36	255	192	32
36	node37	158	21	36
37	node38	120	32	70
38	node39	30	25	200
39	node40	240	10	100

FIGURE A.1: The Color Look Up Table.

5. Matlab code for estimating transfer function models by specifying number of poles.

```
%% Estimate Transfer Function Models by Specifying Number of Poles
%

%%
% Load time-domain system response data and use it to estimate a transfer
% function for the system.
%load iddata1 z1;
fitpercent = [];
pol = [];
i= 1;
previous = 0;
present = 10;
flag =0;
for np = 2:15
 sys = tfest(z1,np);

%%
% |z1| is an |iddata| object that contains time-domain, input-output data.

%%
% |np| specifies the number of poles in the estimated transfer function.
simlog
%%
% |sys| is an |idtf| model containing the estimated transfer function.

%%
% To see the numerator and denominator coefficients of the resulting
    estimated
% model |sys|, enter:
sys.Numerator;
sys.Denominator;

%%
% To view the uncertainty in the estimates of the numerator and denominator
% and other information, use |tfdata|.
v = sys.Report.Fit.FitPercent;
fitpercent(1,i) = v;
present = v;
pol(1,i)= np;
zeros = 0;
%if Test(i-1)==0||Test(i-2)==0 && Test(i+1)==0||Test(i+2)==0
%if v < 100 && v> 90 && (previous == present || abs(previous-present) < 1)
    && flag == 0
if v>99 && flag == 0

        fte = bandwidth(sys);
        poles = np;
        %%%%%%%%%%%%%%%%%%%5
        [mag,phase,wout] = bode(sys);                    % Get Plot Data
        mag = squeeze(mag);                                          %
    Reduce (1x1xN) Matrix To (1xN)
        phase= squeeze(phase);
        magr2 = (mag/max(mag)).^2;                                   %
    Calculate Power Of Ratio Of   m a g /max(mag)
        dB3 = interp1(magr2, [wout phase mag], 0.5, 'spline');       %
    Find Frequency & Phase & Amplitude of Half-Power (-3 dB) Point
        %dB3 = interp1(magr2, wout, 0.5, 'spline');
```

```
        figure(1)
        subplot(2,1,1)
        semilogx(wout, 20*log10(mag), '-b',  dB3(1), 20*log10(dB3(3)), '+r',
    'MarkerSize',10)
        ylabel('Magnitude(dB)')
        text(dB3(1),20*log10(dB3(3)),'\leftarrow cutoff frequency')
        grid
        subplot(2,1,2)
        semilogx(wout, phase, '-b',  dB3(1), dB3(2), '+r', 'MarkerSize',10)
        ylabel('Phase(Deg)')
        xlabel('Frequency(rad/s)')
        grid
        flag = 1;
end
        i= i+1;



previous = v;

end
figure(2);
 plot(pol, fitpercent);
 grid;
 axis([2 15 90 104]);
 xlabel('Poles');
 ylabel('Fit Percent');
```

---

6. Pspice modeling of two myelinated axon propagating signal.

```
.SUBCKT RAV 103 99 102
**********************************************************************
*
*
* coNa = 491.0E-3 Extracellular sodium concentration (mol/L)
* ciNa = 50.0E-3 Intracellular sodium concentration (mol/L)
* coK = 20.11E-3 Extracellular potassium concentration (mol/L)
* ciK = 400.0E-3 Intracellular potassium concentration (mol/L)
* GNaMax=120.0E-3
* GKMax =36.0E-3
* V_r = -62.5E-3 Resting Membrane Potential (V)
* Temp = 6.3 Temperature (Degrees Celsius)
* b = 0.02 Relative permeability of sodium to potassium
* R = 8.314 Reiberg gas constant (joules/(mole*kelvin))
* Z = 1.0 Sodium and potassium ionicvalence
* F = 9.648E4 Faraday's constant (coulombs/mole)
*
**********************************************************************
*
Rax1 99 31 4
Rax 31 102 4
*Ri1 100 103 1E-22
*Ri 103 101 1E-22
```

```
FNA 31 27 VINA 1
FK 31 28 VIK 1


VNk 28 30 -72.0E-3
VNNa 27 30 55.0E-3
ENAK 26 0 31 30 1
CE 31 30 {1E-12} IC=-62.5E-3
Rnode 103 30 30E6

*Sodium current current pathway
*M variable
CM 2 0 0.26E-3 IC=0.0393
RM 2 0 1E10
GAM 0 2 POLY(2) 2 0 5 0 0 0 1 0 -1
GBM 0 2 POLY(2) 2 0 6 0 0 0 0 0 -1
EAM 5 0 value={-0.1*(v(26)*1E3+35)/(exp(-0.1*(v(26)*1E3+35))-1)}
RAM 5 0 1E10
EBM 6 0 value={4*exp(-(v(26)*1E3+60)/18)}
RBM 6 0 1E10


* Sodium current current pathway
* H Variable
CH 3 0 0.26E-3 IC=0.6798
RH 3 0 1E10
GAH 0 3 POLY(2) 3 0 7 0 0 0 1 0 -1
GBH 0 3 POLY(2) 3 0 8 0 0 0 0 0 -1
EAH 7 0 value={0.07*exp(-0.05*(v(26)*1E3+60))}
RAH 7 0 1E10
EBH 8 0 value={1/(1+exp(-0.1*(v(26)*1E3+30)))}
RBH 8 0 1E10


*Potassium current current pathway
* K parameters
CN 4 0 0.26E-3 IC=0.2803
RN 4 0 1E10
GAN 0 4 POLY(2) 4 0 9 0 0 0 1 0 -1
GBN 0 4 POLY(2) 4 0 10 0 0 0 0 0 -1
EAN 9 0 value={-0.01*(v(26)*1E3+50)/(exp(-0.1*(v(26)*1E3+50))-1)}
RAN 9 0 1E10
EBN 10 0 value={0.125*exp(-0.0125*(v(26)*1E3+60))}
RBN 10 0 1E10
EMNA 15 0 26 11 1
RMNA 15 0 1E10
EM3 53 0 POLY(1) 2 0 0 0 0 1
EM3H 16 0 POLY(2) 53 0 3 0 0 0 0 0 1
RM3H 16 0 1E10
GNA 0 20 POLY(2) 15 0 16 0 0 0 0 0 6.7858E-006
VINA 20 0 0
VNA 11 0 55.0E-3
RNA 11 0 1E10
VK 12 0 -72.0E-3
RK 12 0 1E10
EMK 17 0 26 12 1
RMK 17 0 1E10
EN4 18 0 poly(1) 4 0 0 0 0 0 1
```

```
RN4 18 0 1E10
GK 0 21 POLY(2) 17 0 18 0 0 0 0 0 2.0358E-006
VIK 21 0 0
.ENDS

.SUBCKT MYLN 103 101 102
*Rax 99 103 4E-6
*Rax2 103 100 4E-6
RMY 103 30 250E6
CMY 103 31 1.5E-12
Rout 101 31 3E6
Rout2 31 102 3E6
VNAK 31 30 -63E-3
.ENDS


* Current at single axon I1 0 2 pulse(0 6E-9 0 1E-6 1E-6 0.2E-3 2E-3)
*I1 0 2 pulse(0 6E-9 5E-3 100.0E-9 100.0E-9 0.1E-3 0)
I1 0 22 pulse(0 6E-9 1.5E-3 100.0E-9 100.0E-9 0.1E-3 2E-3)
I2 0 33 pulse(0 6E-9 1E-3 100.0E-9 100.0E-9 0.1E-3 2E-3)
*I1 0 22 pulse(0 6E-9 0.2E-3 1E-9 1E-9 0.1E-3 0.2E-3)
*I2 0 33 pulse(0 6E-9 1E-3 1E-9 1E-9 0.6E-3 0)
Ro0 33 0 1E100
Ro1 1 2 1E-22
xsub1 2 22 23 RAV
xsub11 2 33 34 RAV
Ro2 2 3 0.1E-22
Ro3 3 4 1E-22
xsub2 4 23 24 MYLN
xsub12 4 34 35 MYLN
Ro4 4 5 1E-22
Ro5 5 6 1E-22
xsub3 6 24 25 MYLN
xsub13 6 35 36 MYLN
Ro6 6 7 1E-22
Ro7 7 8 1E-22
xsub4 8 25 26 MYLN
xsub14 8 36 37 MYLN
Ro8 8 9 1E-22
Ro9 9 10 1E-22
xsub5 10 26 27 MYLN
xsub15 10 37 38 MYLN
Ro10 10 11 1E-22
Ro11 11 12 1E-22
xsub6 12 27 28 MYLN
xsub16 12 38 39 MYLN
Ro12 12 13 1E-22
Ro13 13 14 1E-22
xsub7 14 28 29 MYLN
xsub17 14 39 40 MYLN
Ro14 14 15 1E-22
Ro15 15 16 1E-22
xsub8 16 29 30 MYLN
xsub18 16 40 41 MYLN
Ro16 16 17 1E-22
Ro17 17 18 1E-22
xsub9 18 30 31 MYLN
xsub19 18 41 42 MYLN
Ro18 18 19 1E-22
```

```
Ro19 19 20 1E-22
xsub10 20 31 32 RAV
xsub20 20 42 43 RAV
Ro20 20 21 1E-22
**

xsub72 21 32 83 MYLN
xsub712 21 43 135 MYLN
Ro74 21 52 1E-22
Ro75 52 56 1E-22
xsub73 56 83 84 MYLN
xsub713 56 135 136 MYLN
Ro76 56 57 1E-22
Ro77 57 58 1E-22
xsub74 58 84 85 MYLN
xsub714 58 136 137 MYLN
Ro78 58 59 1E-22
Ro79 59 60 1E-22
xsub75 60 85 86 MYLN
xsub715 60 137 138 MYLN
Ro710 60 61 1E-22
Ro711 61 62 1E-22
xsub76 62 86 87 MYLN
xsub716 62 138 139 MYLN
Ro712 62 63 1E-22
Ro713 63 64 1E-22
xsub77 64 87 88 MYLN
xsub717 64 139 140 MYLN
Ro714 64 65 1E-22
Ro715 65 66 1E-22
xsub78 66 88 89 MYLN
xsub718 66 140 141 MYLN
Ro716 66 67 1E-22
Ro717 67 68 1E-22
xsub79 68 89 90 MYLN
xsub719 68 141 142 MYLN
Ro718 68 69 1E-22
Ro719 69 70 1E-22
xsub710 70 90 91 RAV
xsub720 70 142 143 RAV
Ro720 70 71 1E-22

R1 1 0 1E100
*R3 43 0 1E100
R4 91 0 1E100
R5 143 0 1E100
*R6 22 0 1E100
R7 71 0 1E100
*.tran 0.5ms 5ms 0
.tran 0.5ms 15ms 0
.options LIMIT 9999
.probe
.END
```

7. Pspice modeling of myelinated axon bundle consisting of 12 axons propagating signal.

```
.SUBCKT RAV 100 30 102
**************************************************************************
*
*
* coNa = 491.0E-3 Extracellular sodium concentration (mol/L)
* ciNa = 50.0E-3 Intracellular sodium concentration (mol/L)
* coK = 20.11E-3 Extracellular potassium concentration (mol/L)
* ciK = 400.0E-3 Intracellular potassium concentration (mol/L)
* GNaMax=120.0E-3
* GKMax =36.0E-3
* V_r = -62.5E-3 Resting Membrane Potential (V)
* Temp = 6.3 Temperature (Degrees Celsius)
* b = 0.02 Relative permeability of sodium to potassium
* R = 8.304 Reiberg gas constant (joules/(mole*kelvin))
* Z = 1.0 Sodium and potassium ionicvalence
* F = 9.648E4 Faraday's constant (coulombs/mole)
*
**************************************************************************
*
*Length of node of Ranvier = 2  m
**RI=3,500MOhm/m; Ri=3,500*2/1000000=7KOhm
Ri1 100 31 3.5E4
Ri2 31 102 3.5E4
*Ro1 100 30 32.3E6
*Ro2 30 101 32.3E6
*Rnode 103 30 30E-6

FNA 31 27 VINA 1
FK 31 28 VIK 1


VNk 28 30 -72.0E-3
VNNa 27 30 55.0E-3
ENAK 26 0 31 30 1
CE 31 30 {1.5E-12} IC=-62.5E-3


*Sodium current current pathway
*M variable
CM 2 0 0.26E-3 IC=0.0393
RM 2 0 1E10
GAM 0 2 POLY(2) 2 0 5 0 0 0 1 0 -1
GBM 0 2 POLY(2) 2 0 6 0 0 0 0 0 -1
EAM 5 0 value={-0.1*(v(26)*1E3+35)/(exp(-0.1*(v(26)*1E3+35))-1)}
RAM 5 0 1E10
EBM 6 0 value={4*exp(-(v(26)*1E3+60)/18)}
RBM 6 0 1E10


* Sodium current current pathway
* H Variable
CH 3 0 0.26E-3 IC=0.6798
RH 3 0 1E10
GAH 0 3 POLY(2) 3 0 7 0 0 0 1 0 -1
GBH 0 3 POLY(2) 3 0 8 0 0 0 0 0 -1
EAH 7 0 value={0.07*exp(-0.05*(v(26)*1E3+60))}
RAH 7 0 1E10
EBH 8 0 value={1/(1+exp(-0.1*(v(26)*1E3+30)))}
RBH 8 0 1E10
```

```
*Potassium current current pathway
* K parameters
CN 4 0 0.26E-3 IC=0.2803
RN 4 0 1E10
GAN 0 4 POLY(2) 4 0 9 0 0 0 1 0 -1
GBN 0 4 POLY(2) 4 0 10 0 0 0 0 0 -1
EAN 9 0 value={-0.01*(v(26)*1E3+50)/(exp(-0.1*(v(26)*1E3+50))-1)}
RAN 9 0 1E10
EBN 10 0 value={0.125*exp(-0.0125*(v(26)*1E3+60))}
RBN 10 0 1E10
EMNA 15 0 26 11 1
RMNA 15 0 1E10
EM3 53 0 POLY(1) 2 0 0 0 0 1
EM3H 16 0 POLY(2) 53 0 3 0 0 0 0 0 1
RM3H 16 0 1E10
GNA 0 20 POLY(2) 15 0 16 0 0 0 0 0 6.7858E-006
VINA 20 0 0
VNA 11 0 55.0E-3
RNA 11 0 1E10
VK 12 0 -72.0E-3
RK 12 0 1E10
EMK 17 0 26 12 1
RMK 17 0 1E10
EN4 18 0 poly(1) 4 0 0 0 0 0 1
RN4 18 0 1E10
GK 0 21 POLY(2) 17 0 18 0 0 0 0 0 2.0358E-006
VIK 21 0 0
.ENDS


*Myelin of 20micrometer axon of 2mm myelin length
*Diameter = 20micrometer
*Myelin thickness= 4micrometer
*Myelin length= 2mm
*RI=3,500MOhm/m; Rin=3,500*2/1000=7MOhm
*RM=0.32MOhm.m;  RMY= 0.32*1000/2=160MOhm
*CM=1300pF/m; CMY=1300*2/1000=2.6pF
*CI=7.409E-14 F m; CIN= (0.07409*1000)/2=37.045pF
.SUBCKT MYLN 99 31 100
Rin1 99 103 3.5E6
Rin2 103 100 3.5E6
Cin 99 100 37.045E-12
RMY 103 30 160E6
CMY 103 31 2.6E-12
VNAK 30 31 -63E-3
.ENDS


I1 0 1          pulse(0 6E-9 0 1E-9 1E-9 0.5E-3 3E-3  )
I2 0 21        pulse(0 6E-9 0 1E-9 1E-9 0.5E-3 3E-3  )
I3 0 41        pulse(0 6E-9 0 1E-9 1E-9 0.5E-3 3E-3  )
I4 0 61        pulse(0 6E-9 0 1E-9 1E-9 0.5E-3 3E-3  )
I5 0 81        pulse(0 6E-9 0 1E-9 1E-9 0.5E-3 3E-3  )
I6 0 151      pulse(0 6E-9 0 1E-9 1E-9 0.5E-3 3E-3  )
I7 0 171      pulse(0 6E-9 0 1E-9 1E-9 0.5E-3 3E-3  )
I8 0 191      pulse(0 6E-9 0 1E-9 1E-9 0.5E-3 3E-3  )
```

```
I9 0 211     pulse(0 6E-9 0 1E-9 1E-9 0.5E-3 3E-3  )
I10 0 231   pulse(0 6E-9 0 1E-9 1E-9 0.5E-3 3E-3  )
I11 0 251   pulse(0 6E-9 0 1E-9 1E-9 0.5E-3 3E-3  )
I12 0 271   pulse(0 6E-9 0 1E-9 1E-9 0.5E-3 3E-3  )



RL0 100 0 1
RL1 100 101 716252.1416
RL2 101 102 716252.1416
RL3 102 103 716252.1416
RL4 103 104 716252.1416
RL5 104 105 716252.1416
RL6 105 106 716252.1416
RL7 106 107 716252.1416
RL8 107 108 716252.1416
RL9 108 109 716252.1416
RL10 109 0 1E100


*First Axon
R1 1 0 1E100
xsub1 1 2 3  RAV
REX1 2 100 1
xsub2 3 4 5  MYLN
REX2 4 101 1
xsub3 5 6 7  RAV
REX3 6 102 1
xsub4 7 8 9  MYLN
REX4 8 103 1
xsub5 9 10 11  RAV
REX5 10 104 1
xsub6 11 12 13  MYLN
REX6 12 105 1
xsub7 13 14 15  RAV
REX7 14 106 1
xsub8 15 16 17  MYLN
REX8 16 107 1
xsub9 17 18 19  RAV
REX9 18 108 1
R4 19 0 1E100

*Second Axon
R21 21 0 1E100
xsub21 21 22 23  RAV
REX21 22 100 1
xsub22 23 24 25  MYLN
REX22 24 101 1
xsub23 25 26 27  RAV
REX23 26 102 1
xsub24 27 28 29  MYLN
REX24 28 103 1
xsub25 29 30 31  RAV
REX25 30 104 1
xsub26 31 32 33  MYLN
REX26 32 105 1
xsub27 33 34 35  RAV
REX27 34 106 1
```

```
xsub28 35 36 37  MYLN
REX28 36 107 1
xsub29 37 38 39  RAV
REX29 38 108 1
R14 39 0 1E100

*Third Axon
R31 41 0 1E100
xsub31 41 42 43  RAV
REX31 42 100 1
xsub32 43 44 45  MYLN
REX32 44 101 1
xsub33 45 46 47  RAV
REX33 46 102 1
xsub34 47 48 49  MYLN
REX34 48 103 1
xsub35 49 50 51  RAV
REX35 50 104 1
xsub36 51 52 53  MYLN
REX36 52 105 1
xsub37 53 54 55  RAV
REX37 54 106 1
xsub38 55 56 57  MYLN
REX38 56 107 1
xsub39 57 58 59  RAV
REX39 58 108 1
R24 59 0 1E100

*FouCTh Axon
R41 61 0 1E100
xsub41 61 62 63  RAV
REX41 62 100 1
xsub42 63 64 65  MYLN
REX42 64 101 1
xsub43 65 66 67  RAV
REX43 66 102 1
xsub44 67 68 69  MYLN
REX44 68 103 1
xsub45 69 70 71  RAV
REX45 70 104 1
xsub46 71 72 73  MYLN
REX46 72 105 1
xsub47 73 74 75  RAV
REX47 74 106 1
xsub48 75 76 77  MYLN
REX48 76 107 1
xsub49 77 78 79  RAV
REX49 78 108 1
R34 79 0 1E100

*Fifts Axon
R51 81 0 1E100
xsub51 81 82 83  RAV
REX51 82 100 1
xsub52 83 84 85  MYLN
REX52 84 101 1
xsub53 85 86 87  RAV
REX53 86 102 1
xsub54 87 88 89  MYLN
```

```
REX54 88 103 1
xsub55 89 90 91  RAV
REX55 90 104 1
xsub56 91 92 93  MYLN
REX56 92 105 1
xsub57 93 94 95  RAV
REX57 94 106 1
xsub58 95 96 97  MYLN
REX58 96 107 1
xsub59 97 98 99  RAV
REX59 98 108 1
R44 99 0 1E100

*Sixth Axon
R61 151 0 1E100
xsub61 151 152 153  RAV
REX61 152 100 1
xsub62 153 154 155  MYLN
REX62 154 101 1
xsub63 155 156 157  RAV
REX63 156 102 1
xsub64 157 158 159  MYLN
REX64 158 103 1
xsub65 159 160 161  RAV
REX65 160 104 1
xsub66 161 162 163  MYLN
REX66 162 105 1
xsub67 163 164 165  RAV
REX67 164 106 1
xsub68 165 166 167  MYLN
REX68 166 107 1
xsub69 167 168 169  RAV
REX69 168 108 1
R54 169 0 1E100

*Seventh Axon
R71 171 0 1E100
xsub71 171 172 173  RAV
REX71 172 100 1
xsub72 173 174 175  MYLN
REX72 174 101 1
xsub73 175 176 177  RAV
REX73 176 102 1
xsub74 177 178 179  MYLN
REX74 178 103 1
xsub75 179 180 181  RAV
REX75 180 104 1
xsub76 181 182 183  MYLN
REX76 182 105 1
xsub77 183 184 185  RAV
REX77 184 106 1
xsub78 185 186 187  MYLN
REX78 186 107 1
xsub79 187 188 189  RAV
REX79 188 108 1
R64 189 0 1E100

*Eighth Axon
R81 191 0 1E100
```

```
xsub81 191 192 193  RAV
REX81 192 100 1
xsub82 193 194 195  MYLN
REX82 194 101 1
xsub83 195 196 197  RAV
REX83 196 102 1
xsub84 197 198 199  MYLN
REX84 198 103 1
xsub85 199 200 201  RAV
REX85 200 104 1
xsub86 201 202 203  MYLN
REX86 202 105 1
xsub87 203 204 205  RAV
REX87 204 106 1
xsub88 205 206 207  MYLN
REX88 206 107 1
xsub89 207 208 209  RAV
REX89 208 108 1
R74 209 0 1E100

*Nine Axon
R91 211 0 1E100
xsub91 211 212 213  RAV
REX91 212 100 1
xsub92 213 214 215  MYLN
REX92 214 101 1
xsub93 215 216 217  RAV
REX93 216 102 1
xsub94 217 218 219  MYLN
REX94 218 103 1
xsub95 219 220 221  RAV
REX95 220 104 1
xsub96 221 222 223  MYLN
REX96 222 105 1
xsub97 223 224 225  RAV
REX97 224 106 1
xsub98 225 226 227  MYLN
REX98 226 107 1
xsub99 227 228 229  RAV
REX99 228 108 1
R84 229 0 1E100

*Ten Axon
R101 231 0 1E100
xsub101 231 232 233  RAV
REX101 232 100 1
xsub102 233 234 235  MYLN
REX102 234 101 1
xsub103 235 236 237  RAV
REX103 236 102 1
xsub104 237 238 239  MYLN
REX104 238 103 1
xsub105 239 240 241  RAV
REX105 240 104 1
xsub106 241 242 243  MYLN
REX106 242 105 1
xsub107 243 244 245  RAV
REX107 244 106 1
xsub108 245 246 247  MYLN
```

```
REX108 246 107 1
xsub109 247 248 249  RAV
REX109 248 108 1
R94 249 0 1E100

*Eleven Axon
R111 251 0 1E100
xsub111 251 252 253  RAV
REX111 252 100 1
xsub112 253 254 255  MYLN
REX112 254 101 1
xsub113 255 256 257  RAV
REX113 256 102 1
xsub114 257 258 259  MYLN
REX114 258 103 1
xsub115 259 260 261  RAV
REX115 260 104 1
xsub116 261 262 263  MYLN
REX116 262 105 1
xsub117 263 264 265  RAV
REX117 264 106 1
xsub118 265 266 267  MYLN
REX118 266 107 1
xsub119 267 268 269  RAV
REX119 268 108 1
R104 269 0 1E100

*Twelve Axon
R121 271 0 1E100
xsub121 271 272 273  RAV
REX121 272 100 1
xsub122 273 274 275  MYLN
REX122 274 101 1
xsub123 275 276 277  RAV
REX123 276 102 1
xsub124 277 278 279  MYLN
REX124 278 103 1
xsub125 279 280 281  RAV
REX125 280 104 1
xsub126 281 282 283  MYLN
REX126 282 105 1
xsub127 283 284 285  RAV
REX127 284 106 1
xsub128 285 286 287  MYLN
REX128 286 107 1
xsub129 287 288 289  RAV
REX129 288 108 1
R114 289 0 1E100

*Transverse resistance
RT1 2 22 8E6
RT2 6 26 8E6
RT3 10 30 8E6
RT4 14 34 8E6
RT5 18 38 8E6

RT11 22 42 8E6
RT12 26 46 8E6
RT13 30 50 8E6
```

```
RT14 34 54 8E6
RT15 38 58 8E6

RT21 42 62 8E6
RT22 46 66 8E6
RT23 50 70 8E6
RT24 54 74 8E6
RT25 58 78 8E6

RT31 62 82 8E6
RT32 66 86 8E6
RT33 70 90 8E6
RT34 74 94 8E6
RT35 78 98 8E6

RT41 82 152 8E6
RT42 86 156 8E6
RT43 90 160 8E6
RT44 94 164 8E6
RT45 98 168 8E6

RT51 152 172 8E6
RT52 156 176 8E6
RT53 160 180 8E6
RT54 164 184 8E6
RT55 168 188 8E6

RT61 172 192 8E6
RT62 176 196 8E6
RT63 180 200 8E6
RT64 184 204 8E6
RT65 188 208 8E6

RT71 192 212 8E6
RT72 196 216 8E6
RT73 200 220 8E6
RT74 204 224 8E6
RT75 208 228 8E6

RT81 212 232 8E6
RT82 216 236 8E6
RT83 220 240 8E6
RT84 224 244 8E6
RT85 228 248 8E6

RT91 232 252 8E6
RT92 236 256 8E6
RT93 240 260 8E6
RT94 244 264 8E6
RT95 248 268 8E6

RT101 252 272 8E6
RT102 256 276 8E6
RT103 260 280 8E6
RT104 264 284 8E6
RT105 268 288 8E6


.tran .5ms 20ms
```

```
.probe
.options LIMIT 99999
.END
```

Table A.1: Data table for $A\alpha - 20\mu m$ and $A\alpha - 13\mu m$ bundle

Model	**Bundle diameter (μm)**	**Axons in bundle**	**Outer diameter of axon(μm)**	**Inner diameter of axon(μm)**	L_{NR} (μm)	L_{IN} mm	A_T $(\mu m)^2$	A_F $(\mu m)^2$	A_{ax} $(\mu m)^2$	A_E $(\mu m)^2$	R_{eL} $M\Omega$	R_{eT} $M\Omega$
$A\alpha - 20\mu m$-Bundle- 2	56	2	28	20	2	2	2464.00	1232.00	628.57	1232.00	5.35	8.4
$A\alpha - 20\mu m$-Bundle- 3	60.31	3	28	20	2	2	2858.07	1848.00	942.86	1010.07	6.53	8.4
$A\alpha - 20\mu m$-Bundle-4	67.59	4	28	20	2	2	3589.68	2464.00	1257.14	1125.68	5.86	8.4
$A\alpha - 20\mu m$-Bundle-5	75.62	5	28	20	2	2	4493.97	3080.00	1571.43	1413.97	4.66	8.4
$A\alpha - 20\mu m$-Bundle-6	84	6	28	20	2	2	5544.00	3696.00	1885.71	1848.00	3.57	8.4
$A\alpha - 20\mu m$-Bundle-7	84	7	28	20	2	2	5544.00	4312.00	2200.00	1232.00	5.35	8.4
$A\alpha - 20\mu m$-Bundle-8	92.51	8	28	20	2	2	6724.51	4928.00	2514.29	1796.51	3.67	8.4
$A\alpha - 20\mu m$-Bundle-9	101.16	9	28	20	2	2	8041.12	5544.00	2828.57	2497.12	2.64	8.4
$A\alpha - 20\mu m$-Bundle-10	106.76	10	28	20	2	2	8956.00	6160.00	3142.86	2796.00	2.36	8.4
$A\alpha - 20\mu m$-Bundle-11	109.84	11	28	20	2	2	9480.20	6776.00	3457.14	2704.20	2.44	8.4
$A\alpha - 20\mu m$-Bundle-12	112.81	12	28	20	2	2	9999.43	7392.00	3771.43	2607.43	2.53	8.4
$A\alpha - 13\mu m$-Bundle-2	36.4	2	18.2	13	1.3	1.3	1041.04	520.52	265.57	520.52	8.24	12.9
$A\alpha - 13\mu m$-Bundle-3	39.20	3	18.2	13	1.3	1.3	1207.53	780.78	398.36	426.75	10.0	12.9
$A\alpha - 13\mu m$-Bundle-4	43.93	4	18.2	13	1.3	1.3	1516.64	1041.04	531.14	475.60	9.02	12.9
$A\alpha - 13\mu m$-Bundle-5	49.15	5	18.2	13	1.3	1.3	1898.70	1301.30	663.93	597.40	7.18	12.9
$A\alpha - 13\mu m$-Bundle-6	54.6	6	18.2	13	1.3	1.3	2342.34	1561.56	796.71	780.78	5.49	12.9
$A\alpha - 13\mu m$-Bundle-7	54.6	7	18.2	13	1.3	1.3	2342.34	1821.82	929.50	520.52	8.24	12.9
$A\alpha - 13\mu m$-Bundle-8	60.13	8	18.2	13	1.3	1.3	2841.11	2082.08	1062.29	759.03	5.65	12.9
$A\alpha - 13\mu m$-Bundle-9	65.75	9	18.2	13	1.3	1.3	3397.37	2342.34	1195.07	1055.03	4.06	12.9
$A\alpha - 13\mu m$-Bundle-10	69.39	10	18.2	13	1.3	1.3	3783.91	2602.60	1327.86	1181.31	3.63	12.9
$A\alpha - 13\mu m$-Bundle-11	71.39	11	18.2	13	1.3	1.3	4005.38	2862.86	1460.64	1142.52	3.75	12.9
$A\alpha - 13\mu m$-Bundle-12	73.32	12	18.2	13	1.3	1.3	4224.76	3123.12	1593.43	1101.64	3.89	12.9

8.

Model	$A\delta - 6\mu m$**-Bundle diameter** (μm)	**Axons in bundle**	**Outer diameter of axon**(μm)	**Inner diameter of axon**(μm)	L_{NR} (μm)	L_{IN} mm	A_T $(\mu m)^2$	A_F $(\mu m)^2$	A_{ax} $(\mu m)^2$	A_E $(\mu m)^2$	R_{eL} $M\Omega$	R_{eT} $M\Omega$
$A\delta - 12\mu m$-Bundle2	33.6	2	16.8	12	1.2	1.2	887.04	443.52	226.29	443.52	8.9	14
$A\delta - 12\mu m$-Bundle3	36.18	3	16.8	12	1.2	1.2	1028.90	665.28	339.43	363.62	10.8	14
$A\delta - 12\mu m$-Bundle4	40.55	4	16.8	12	1.2	1.2	1292.28	887.04	452.57	405.24	9.7	14
$A\delta - 12\mu m$-Bundle5	45.37	5	16.8	12	1.2	1.2	1617.83	1108.80	565.71	509.03	7.7	14
$A\delta - 12\mu m$-Bundle6	50.4	6	16.8	12	1.2	1.2	1995.84	1330.56	678.86	665.28	5.9	14
$A\delta - 12\mu m$-Bundle7	50.4	7	16.8	12	1.2	1.2	1995.84	1552.32	792.00	443.52	8.9	14
$A\delta - 12\mu m$-Bundle8	55.50	8	16.8	12	1.2	1.2	2420.82	1774.08	905.14	646.74	6.1	14
$A\delta - 12\mu m$-Bundle9	60.69	9	16.8	12	1.2	1.2	2894.80	1995.84	1018.29	898.96	4.4	14
$A\delta - 12\mu m$-Bundle10	64.05	10	16.8	12	1.2	1.2	3224.16	2217.60	1131.43	1006.56	3.9	14
$A\delta - 12\mu m$-Bundle11	65.90	11	16.8	12	1.2	1.2	3412.87	2439.36	1244.57	973.51	4.0	14
$A\delta - 12\mu m$-Bundle12	67.68	12	16.8	12	1.2	1.2	3599.79	2661.12	1357.71	938.67	4.2	14
$A\delta - 6\mu m$-Bundle2	16.8	2	8.4	6	0.6	0.6	221.76	110.88	56.57	110.88	17.8	28
$A\delta - 6\mu m$-Bundle3	18.09	3	8.4	6	0.6	0.6	257.23	166.32	84.86	90.91	21.7	28
$A\delta - 6\mu m$-Bundle4	20.27	4	8.4	6	0.6	0.6	323.07	221.76	113.14	101.31	19.5	28
$A\delta - 6\mu m$-Bundle5	22.68	5	8.4	6	0.6	0.6	404.46	277.20	141.43	127.26	15.5	28
$A\delta - 6\mu m$-Bundle6	25.2	6	8.4	6	0.6	0.6	498.96	332.64	169.71	166.32	11.9	28
$A\delta - 6\mu m$-Bundle7	25.2	7	8.4	6	0.6	0.6	498.96	388.08	198.00	110.88	17.8	28
$A\delta - 6\mu m$-Bundle8	27.7536	8	8.4	6	0.6	0.6	605.21	443.52	226.29	161.69	12.2	28
$A\delta - 6\mu m$-Bundle9	30.3492	9	8.4	6	0.6	0.6	723.70	498.96	254.57	224.74	8.8	28
$A\delta - 6\mu m$-Bundle10	32.0292	10	8.4	6	0.6	0.6	806.04	554.40	282.86	251.64	7.8	28
$A\delta - 6\mu m$-Bundle11	32.9532	11	8.4	6	0.6	0.6	853.22	609.84	311.14	243.38	8.1	28
$A\delta - 6\mu m$-Bundle12	33.8436	12	8.4	6	0.6	0.6	899.95	665.28	339.43	234.67	8.4	28

9.

Model	**Bundle diameter** (μm)	**Axons in bundle**	**Outer diameter of axon**(μm)	**Inner diameter of axon**(μm)	L_{NR} (μm)	L_{IN} mm	A_T $(\mu m)^2$	A_F $(\mu m)^2$	A_{ax} $(\mu m)^2$	A_E $(\mu m)^2$	R_{eL} $M\Omega$	R_{eT} $M\Omega$
$A\delta - 5\mu m$-Bundle2	14	2	7	5	0.5	0.5	154.00	77.00	39.29	77.00	21.42	33.6
$A\delta - 5\mu m$-Bundle3	15.0	3	7	5	0.5	0.5	178.63	115.50	58.93	63.13	26.13	33.6
$A\delta - 5\mu m$-Bundle4	16.8	4	7	5	0.5	0.5	224.35	154.00	78.57	70.35	23.45	33.6
$A\delta - 5\mu m$-Bundle5	18.9	5	7	5	0.5	0.5	280.87	192.50	98.21	88.37	18.67	33.6
$A\delta - 5\mu m$-Bundle6	21	6	7	5	0.5	0.5	346.50	231.00	117.86	115.50	14.28	33.6
$A\delta - 5\mu m$-Bundle7	21	7	7	5	0.5	0.5	346.50	269.50	137.50	77.00	21.42	33.6
$A\delta - 5\mu m$-Bundle8	23.12	8	7	5	0.5	0.5	420.28	308.00	157.14	112.28	14.69	33.6
$A\delta - 5\mu m$-Bundle9	25.29	9	7	5	0.5	0.5	502.57	346.50	176.79	156.07	10.57	33.6
$A\delta - 5\mu m$-Bundle10	26.69	10	7	5	0.5	0.5	559.75	385.00	196.43	174.75	9.44	33.6
$A\delta - 5\mu m$-Bundle11	27.46	11	7	5	0.5	0.5	592.51	423.50	216.07	169.01	9.76	33.6
$A\delta - 5\mu m$-Bundle12	28.20	12	7	5	0.5	0.5	624.96	462.00	235.71	162.96	1012	33.6
$A\delta - 1\mu m$-Bundle2	2.8	2	1.4	1	0.1	0.1	6.16	3.08	1.57	3.08	107.14	168.0
$A\delta - 1\mu m$-Bundle3	3.01	3	1.4	1	0.1	0.1	7.15	4.62	2.36	2.53	130.68	168.0
$A\delta - 1\mu m$-Bundle4	3.37	4	1.4	1	0.1	0.1	8.97	6.16	3.14	2.81	117.26	168.0
$A\delta - 1\mu m$-Bundle5	3.78	5	1.4	1	0.1	0.1	11.23	7.70	3.93	3.53	93.35	168.0
$A\delta - 1\mu m$-Bundle6	4.2	6	1.4	1	0.1	0.1	13.86	9.24	4.71	4.62	71.42	168.0
$A\delta - 1\mu m$-Bundle7	4.2	7	1.4	1	0.1	0.1	13.86	10.78	5.50	3.08	107.14	168.0
$A\delta - 1\mu m$-Bundle8	4.62	8	1.4	1	0.1	0.1	16.81	12.32	6.29	4.49	73.47	168.0
$A\delta - 1\mu m$-Bundle9	5.05	9	1.4	1	0.1	0.1	20.10	13.86	7.07	6.24	52.86	168.0
$A\delta - 1\mu m$-Bundle10	5.33	10	1.4	1	0.1	0.1	22.39	15.40	7.86	6.99	47.21	168.0
$A\delta - 1\mu m$-Bundle11	5.49	11	1.4	1	0.1	0.1	23.70	16.94	8.64	6.76	48.81	168.0
$A\delta - 1\mu m$-Bundle12	5.64	12	1.4	1	0.1	0.1	25.00	18.48	9.43	6.52	50.62	168.0

Table A.3: Data table for $A\alpha - 5\mu m$ and $A\alpha - 1\mu m$ bundle

10.

Table A.4: Data for SBC and GBCMed axon bundles

Model	$A\delta - 5\mu m$**-Bundle diameter** (μm)	**Axons in bundle**	**Outer diameter of axon**(μm)	**Inner diameter of axon**(μm)	L_{NR} (μm)	L_{IN} mm	A_T $(\mu m)^2$	A_F $(\mu m)^2$	A_{ax} $(\mu m)^2$	A_E $(\mu m)^2$	R_{eL} $M\Omega$	R_{eT} $M\Omega$
SBC-Bundle2	3.54	2	1.77	1.35	1.35	0.1638	9.85	4.92	2.86	4.92	109.7	65.7
SBC-Bundle3	3.81	3	1.77	1.35	1.35	0.1638	11.42	7.38	4.30	4.04	133.9	65.7
SBC-Bundle4	4.27	4	1.77	1.35	1.35	0.1638	14.34	9.85	5.73	4.50	120.1	65.7
SBC-Bundle5	4.78	5	1.77	1.35	1.35	0.1638	17.96	12.31	7.16	5.65	95.6	65.7
SBC-Bundle6	5.31	6	1.77	1.35	1.35	0.1638	22.15	14.77	8.59	7.38	73.1	65.7
SBC-Bundle7	5.31	7	1.77	1.35	1.35	0.1638	22.15	17.23	10.02	4.92	109.7	65.7
SBC-Bundle8	5.84	8	1.77	1.35	1.35	0.1638	26.87	19.69	11.46	7.18	75.2	65.7
SBC-Bundle9	6.39	9	1.77	1.35	1.35	0.1638	32.13	22.15	12.89	9.98	54.1	65.7
SBC-Bundle10	6.74	10	1.77	1.35	1.35	0.1638	35.79	24.62	14.32	11.17	48.3	65.7
SBC-Bundle11	6.94	11	1.77	1.35	1.35	0.1638	37.88	27.08	15.75	10.81	50.0	65.7
SBC-Bundle12	7.13	12	1.77	1.35	1.35	0.1638	39.96	29.54	17.18	10.42	51.8	65.7
GBCM-Bundle2	6.4	2	3.2	2.41	2.41	0.2386	32.18	16.09	9.13	16.09	48.9	58.3
GBCM-Bundle3	6.89	3	3.2	2.41	2.41	0.2386	37.33	24.14	13.69	13.19	59.6	58.3
GBCM-Bundle4	7.72	4	3.2	2.41	2.41	0.2386	46.89	32.18	18.25	14.70	53.5	58.3
GBCM-Bundle5	8.64	5	3.2	2.41	2.41	0.2386	58.70	40.23	22.82	18.47	42.6	58.3
GBCM-Bundle6	9.6	6	3.2	2.41	2.41	0.2386	72.41	48.27	27.38	24.14	32.6	58.3
GBCM-Bundle7	9.6	7	3.2	2.41	2.41	0.2386	72.41	56.32	31.94	16.09	48.9	58.3
GBCM-Bundle8	10.57	8	3.2	2.41	2.41	0.2386	87.83	64.37	36.51	23.46	33.5	58.3
GBCM-Bundle9	11.56	9	3.2	2.41	2.41	0.2386	105.03	72.41	41.07	32.62	24.1	58.3
GBCM-Bundle10	12.20	10	3.2	2.41	2.41	0.2386	116.98	80.46	45.64	36.52	21.5	58.3
GBCM-Bundle11	12.55	11	3.2	2.41	2.41	0.2386	123.82	88.50	50.20	35.32	22.2	58.3
GBCM-Bundle12	12.89	12	3.2	2.41	2.41	0.2386	130.60	96.55	54.76	34.06	23.1	58.3

11.

Model	$A\delta - 5\mu m$**-Bundle diameter** (μm)	**Axons in bundle**	**Outer diameter of axon**(μm)	**Inner diameter of axon**(μm)	L_{NR} (μm)	L_{IN} mm	A_T $(\mu m)^2$	A_F $(\mu m)^2$	A_{ax} $(\mu m)^2$	A_E $(\mu m)^2$	R_{eL} $M\Omega$	R_{eT} $M\Omega$
GBCL-Bundle2	8.02	2	4.01	3.06	3.06	0.18	50.54	25.27	14.71	25.27	25.8	102
GBCL-Bundle3	8.63	3	4.01	3.06	3.06	0.18	58.62	37.90	22.07	20.72	31.4	102
GBCL-Bundle4	9.68	4	4.01	3.06	3.06	0.18	73.63	50.54	29.43	23.09	28.2	102
GBCL-Bundle5	10.81	5	4.01	3.06	3.06	0.18	92.17	63.17	36.79	29.00	22.4	102
GBCL-Bundle6	12.03	6	4.01	3.06	3.06	0.18	113.71	75.81	44.14	37.90	17.2	102
GBCL-Bundle7	12.03	7	4.01	3.06	3.06	0.18	113.71	88.44	51.50	25.27	25.8	102
GBCL-Bundle8	13.24	8	4.01	3.06	3.06	0.18	137.92	101.07	58.86	36.85	17.7	102
GBCL-Bundle9	14.48	9	4.01	3.06	3.06	0.18	164.93	113.71	66.21	51.22	12.7	102
GBCL-Bundle10	15.29	10	4.01	3.06	3.06	0.18	183.69	126.34	73.57	57.35	11.3	102
GBCL-Bundle11	15.73	11	4.01	3.06	3.06	0.18	194.44	138.98	80.93	55.46	11.7	102
GBCL-Bundle12	16.15	12	4.01	3.06	3.06	0.18	205.09	151.61	88.29	53.48	12.1	102
FMN-Bundle2	28	2	14	10	2	2	616.00	308.00	157.14	308.00	21.4	4.2
FMN-Bundle3	30.1	3	14	10	2	2	714.52	462.00	235.71	252.52	26.1	4.2
FMN-Bundle4	33.7	4	14	10	2	2	897.42	616.00	314.29	281.42	23.4	4.2
FMN-Bundle5	37.8	5	14	10	2	2	1123.49	770.00	392.86	353.49	18.6	4.2
FMN-Bundle6	42	6	14	10	2	2	1386.00	924.00	471.43	462.00	14.2	4.2
FMN-Bundle7	42	7	14	10	2	2	1386.00	1078.00	550.00	308.00	21.4	4.2
FMN-Bundle8	46.2	8	14	10	2	2	1681.13	1232.00	628.57	449.13	14.6	4.2
FMN-Bundle9	50.5	9	14	10	2	2	2010.28	1386.00	707.14	624.28	10.5	4.2
FMN-Bundle10	53.3	10	14	10	2	2	2239.00	1540.00	785.71	699.00	9.4	4.2
FMN-Bundle11	54.9	11	14	10	2	2	2370.05	1694.00	864.29	676.05	9.7	4.2
FMN-Bundle12	56.4	12	14	10	2	2	2499.86	1848.00	942.86	651.86	10.1	4.2

Table A.5: Data table for GBCLat and FMN axons

12.

Bibliography

AHMJ Aertsen. Dynamics of activity and connectivity in physiological neuronal networks. *Nonlinear dynamics and neuronal networks*, 1991.

Costas A Anastassiou, Rodrigo Perin, Henry Markram, and Christof Koch. Ephaptic coupling of cortical neurons. *Nature neuroscience*, 14(2):217, 2011.

Alex M Andrew. Spiking neuron models: Single neurons, populations, plasticity. *Kybernetes*, 32(7/8), 2003.

A Arvanitaki. Effects evoked in an axon by the activity of a contiguous one. *Journal of neurophysiology*, 5(2):89–108, 1942.

Yaniv Assaf, Tamar Blumenfeld-Katzir, Yossi Yovel, and Peter J Basser. Axcaliber: a method for measuring axon diameter distribution from diffusion mri. *Magnetic resonance in medicine*, 59(6):1347–1354, 2008.

Roger C Barr and Robert Plonsey. Electrophysiological interaction through the interstitial space between adjacent unmyelinated parallel fibers. *Biophysical journal*, 61(5): 1164–1175, 1992.

Karla Batista-García-Ramó and Caridad Ivette Fernández-Verdecia. What we know about the brain structure–function relationship. *Behavioral Sciences*, 8(4):39, 2018.

Christian Beaulieu. The basis of anisotropic water diffusion in the nervous system–a technical review. *NMR in Biomedicine*, 15(7-8):435–455, 2002.

Christian Beaulieu. The biological basis of diffusion anisotropy. In *Diffusion MRI*, pages 155–183. Elsevier, 2014.

Sara L Bengtsson, Zoltán Nagy, Stefan Skare, Lea Forsman, Hans Forssberg, and Fredrik Ullén. Extensive piano practicing has regionally specific effects on white matter development. *Nature neuroscience*, 8(9):1148–1150, 2005.

S Binczak, JC Eilbeck, and Alwyn C Scott. Ephaptic coupling of myelinated nerve fibers. *Physica D: Nonlinear Phenomena*, 148(1-2):159–174, 2001.

Urs Braun, Sarah F Muldoon, and Danielle S Bassett. On human brain networks in health and disease. *eLS*, 2015.

MH Brill, SG Waxman, JW Moore, and RW Joyner. Conduction velocity and spike configuration in myelinated fibres: computed dependence on internode distance. *Journal of Neurology, Neurosurgery & Psychiatry*, 40(8):769–774, 1977.

B Bunow, I Segev, and JW Fleshman. Modeling the electrical behavior of anatomically complex neurons using a network analysis program: excitable membrane. *Biological cybernetics*, 53(1):41–56, 1985.

M Capllonch-Juan and F Sepulveda. Conduction velocity effects due to ephaptic interactions between myelinated axons. In *EMBEC & NBC 2017*, pages 659–662. Springer, 2017.

Miguel Capllonch-Juan and Francisco Sepulveda. Modelling the effects of ephaptic coupling on selectivity and response patterns during artificial stimulation of peripheral nerves. *PLOS Computational Biology*, 16(6):e1007826, 2020.

Ana Carpio and Ireneo Peral. Propagation failure along myelinated nerves. *Journal of nonlinear science*, 21(4):499–520, 2011.

Charles CH Cohen, Marko A Popovic, Jan Klooster, Marie-Theres Weil, Wiebke Möbius, Klaus-Armin Nave, and Maarten HP Kole. Saltatory conduction along myelinated axons involves a periaxonal nanocircuit. *Cell*, 180(2):311–322, 2020.

Anders M Dale, Bruce Fischl, and Martin I Sereno. Cortical surface-based analysis: I. segmentation and surface reconstruction. *Neuroimage*, 9(2):179–194, 1999.

HK Das, D Das, R Doley, and PP Sahu. Quantifying demyelination in nk venom treated nerve using its electric circuit model. *Scientific reports*, 6(1):1–8, 2016.

Dominique Debanne, Emilie Campanac, Andrzej Bialowas, Edmond Carlier, and Gisèle Alcaraz. Axon physiology. *Physiological reviews*, 91(2):555–602, 2011.

Gustavo Deco, Viktor K Jirsa, Peter A Robinson, Michael Breakspear, and Karl Friston. The dynamic brain: from spiking neurons to neural masses and cortical fields. *PLoS computational biology*, 4(8):e1000092, 2008.

Antonio Díaz-Parra, Zachary Osborn, Santiago Canals, David Moratal, and Olaf Sporns. Structural and functional, empirical and modeled connectivity in the cerebral cortex of the rat. *NeuroImage*, 159:170–184, 2017.

Benjamin M Ellingson, Noriko Salamon, and Langston T Holly. Advances in mr imaging for cervical spondylotic myelopathy. *European Spine Journal*, 24(2):197–208, 2015.

T Fedele, HJ Scheer, M Burghoff, G Curio, and R Körber. Ultra-low-noise eeg/meg systems enable bimodal non-invasive detection of spike-like human somatosensory evoked responses at 1 khz. *Physiological measurement*, 36(2):357, 2015.

Daniel J Felleman and David C Van Essen. Distributed hierarchical processing in the primate cerebral cortex. *Cerebral cortex (New York, NY: 1991)*, 1(1):1–47, 1991.

Bruce Fischl. Freesurfer. *Neuroimage*, 62(2):774–781, 2012.

Bruce Fischl, Martin I Sereno, and Anders M Dale. Cortical surface-based analysis: Ii: inflation, flattening, and a surface-based coordinate system. *Neuroimage*, 9(2): 195–207, 1999.

Bruce Fischl, André Van Der Kouwe, Christophe Destrieux, Eric Halgren, Florent Ségonne, David H Salat, Evelina Busa, Larry J Seidman, Jill Goldstein, David Kennedy, et al. Automatically parcellating the human cerebral cortex. *Cerebral cortex*, 14(1):11–22, 2004.

Richard Fitzhugh. Computation of impulse initiation and saltatory conduction in a myelinated nerve fiber. *Biophysical journal*, 2(1):11–21, 1962.

Vinzenz Fleischer, Angela Radetz, Dumitru Ciolac, Muthuraman Muthuraman, Gabriel Gonzalez-Escamilla, Frauke Zipp, and Sergiu Groppa. Graph theoretical framework of brain networks in multiple sclerosis: A review of concepts. *Neuroscience*, 2017.

Marc C Ford, Olga Alexandrova, Lee Cossell, Annette Stange-Marten, James Sinclair, Conny Kopp-Scheinpflug, Michael Pecka, David Attwell, and Benedikt Grothe. Tuning of ranvier node and internode properties in myelinated axons to adjust action potential timing. *Nature communications*, 6(1):1–14, 2015.

Erich Friedman. Circles in circles, 2014.

Karl J Friston. Functional and effective connectivity: a review. *Brain connectivity*, 1 (1):13–36, 2011.

Karl J Friston, Lee Harrison, and Will Penny. Dynamic causal modelling. *Neuroimage*, 19(4):1273–1302, 2003.

Katharine Gammon. Neurodegenerative disease: brain windfall. *Nature*, 515(7526): 299–300, 2014.

Wulfram Gerstner, Werner M Kistler, Richard Naud, and Liam Paninski. *Neuronal dynamics: From single neurons to networks and models of cognition*. Cambridge University Press, 2014.

Erin M Gibson, David Purger, Christopher W Mount, Andrea K Goldstein, Grant L Lin, Lauren S Wood, Ingrid Inema, Sarah E Miller, Gregor Bieri, J Bradley Zuchero, et al. Neuronal activity promotes oligodendrogenesis and adaptive myelination in the mammalian brain. *Science*, 344(6183), 2014.

L Goldman and James S Albus. Computation of impulse conduction in myelinated fibers; theoretical basis of the velocity-diameter relation. *Biophysical journal*, 8(5): 596–607, 1968.

Joshua H Goldwyn and John Rinzel. Neuronal coupling by endogenous electric fields: cable theory and applications to coincidence detector neurons in the auditory brain stem. *Journal of neurophysiology*, 115(4):2033–2051, 2016.

Patric Hagmann, Leila Cammoun, Xavier Gigandet, Reto Meuli, Christopher J Honey, Van J Wedeen, and Olaf Sporns. Mapping the structural core of human cerebral cortex. *PLoS biology*, 6(7):e159, 2008.

Patric Hagmann, Maciej Kurant, Xavier Gigandet, Patrick Thiran, Van J Wedeen, Reto Meuli, and Jean-Philippe Thiran. Mapping human whole-brain structural networks with diffusion mri. *PloS one*, 2(7):e597, 2007.

Xiao Han, Dzung L Pham, Duygu Tosun, Maryam E Rettmann, Chenyang Xu, and Jerry L Prince. Cruise: cortical reconstruction using implicit surface evolution. *NeuroImage*, 23(3):997–1012, 2004.

Julia J Harris and David Attwell. The energetics of cns white matter. *Journal of Neuroscience*, 32(1):356–371, 2012.

Evan S Hill and Jonathan M Blagburn. Presynaptic effects of biogenic amines modulating synaptic transmission between identified sensory neurons and giant interneurons in the first instar cockroach. *Journal of Comparative Physiology A: Neuroethology, Sensory, Neural, and Behavioral Physiology*, 187(8):633–645, 2001.

Alan L Hodgkin and Andrew F Huxley. A quantitative description of membrane current and its application to conduction and excitation in nerve. *The Journal of physiology*, 117(4):500–544, 1952.

Christopher J Honey, Rolf Kötter, Michael Breakspear, and Olaf Sporns. Network structure of cerebral cortex shapes functional connectivity on multiple time scales. *Proceedings of the National Academy of Sciences*, 104(24):10240–10245, 2007.

Christopher J Honey, Jean-Philippe Thivierge, and Olaf Sporns. Can structure predict function in the human brain? *Neuroimage*, 52(3):766–776, 2010.

CJ Honey, O Sporns, Leila Cammoun, Xavier Gigandet, Jean-Philippe Thiran, Reto Meuli, and Patric Hagmann. Predicting human resting-state functional connectivity from structural connectivity. *Proceedings of the National Academy of Sciences*, 106 (6):2035–2040, 2009.

Andreas Horn, Dirk Ostwald, Marco Reisert, and Felix Blankenburg. The structural–functional connectome and the default mode network of the human brain. *Neuroimage*, 102:142–151, 2014.

Chihiro Hosoda, Kanji Tanaka, Tadashi Nariai, Manabu Honda, and Takashi Hanakawa. Dynamic neural network reorganization associated with second language vocabulary acquisition: A multimodal imaging study. *Journal of Neuroscience*, 33(34):13663–13672, 2013.

Marc-Thorsten Hütt, Marcus Kaiser, and Claus C Hilgetag. Perspective: network-guided pattern formation of neural dynamics. *Phil. Trans. R. Soc. B*, 369(1653):20130522, 2014.

AF Huxley and R Stämpeli. Evidence for saltatory conduction in peripheral myelinated nerve fibres. *The Journal of physiology*, 108(3):315–339, 1949.

Eugene M Izhikevich. *Dynamical systems in neuroscience*. MIT press, 2007.

Ileana O Jelescu and Matthew D Budde. Design and validation of diffusion mri models of white matter. *Frontiers in Physics*, 5:61, 2017.

Daniel Johnston and Samuel Miao-Sin Wu. *Foundations of cellular neurophysiology*. MIT press, 1994.

Derek K Jones. *Diffusion mri*. Oxford University Press, 2010.

Marcus Kaiser. *Changing Connectomes: Evolution, Development, and Dynamics in Network Neuroscience*. MIT Press, 2020.

Eric R Kandel, James H Schwartz, Thomas M Jessell, Steven A Siegelbaum, A James Hudspeth, et al. *Principles of neural science*, volume 4. McGraw-hill New York, 2000.

Bernhard Katz and Otto H Schmitt. Electric interaction between two adjacent nerve fibres. *The Journal of physiology*, 97(4):471–488, 1940.

Paul Leopardi. A partition of the unit sphere into regions of equal area and small diameter. *Electronic Transactions on Numerical Analysis*, 25(12):309–327, 2006.

Nikos K Logothetis, Jon Pauls, Mark Augath, Torsten Trinath, and Axel Oeltermann. Neurophysiological investigation of the basis of the fmri signal. *nature*, 412(6843): 150–157, 2001.

Peter Manza, Sheng Zhang, Chiang-Shan R Li, and Hoi-Chung Leung. Resting-state functional connectivity of the striatum in early-stage parkinson's disease: Cognitive decline and motor symptomatology. *Human brain mapping*, 37(2):648–662, 2016.

D Masanotti, P Langlois, and J Taylor. A method to model neuron activity. In *Engineering in Medicine and Biology Society, 2006. EMBS'06. 28th Annual International Conference of the IEEE*, pages 4192–4195. IEEE, 2006.

Arnaud Messé, Marc-Thorsten Hütt, Peter König, and Claus C Hilgetag. A closer look at the apparent correlation of structural and functional connectivity in excitable neural networks. *Scientific reports*, 5:7870, 2015.

Bratislav Mišić, Richard F Betzel, Marcel A De Reus, Martijn P Van Den Heuvel, Marc G Berman, Anthony R McIntosh, and Olaf Sporns. Network-level structure-function relationships in human neocortex. *Cerebral Cortex*, 26(7):3285–3296, 2016.

Steven X Moffett, Sean M OMalley, Shushuang Man, Dawei Hong, and Joseph V Martin. Dynamics of high frequency brain activity. *Scientific reports*, 7(1):1–5, 2017.

Seyede Ghazal Mohades, Esli Struys, Peter Van Schuerbeek, Katrien Mondt, Piet Van De Craen, and Robert Luypaert. Dti reveals structural differences in white matter tracts between bilingual and monolingual children. *Brain Research*, 1435:72–80, 2012.

John W Moore, Ronald W Joyner, Micheal H Brill, Stephen D Waxman, and Manuel Najar-Joa. Simulations of conduction in uniform myelinated fibers. relative sensitivity to changes in nodal and internodal parameters. *Biophysical journal*, 21(2):147–160, 1978.

W Nonner, E Rojas, and R Stämpfli. Asymmetrical displacement currents in the membrane of frog myelinated nerve: early time course and effects of membrane potential. *Pflügers Archiv*, 375(1):75–85, 1978.

D Raffelt, JD Tournier, S Rose, GR Ridgway, R Henderson, S Crozier, O Salvado, and A Connelly. Apparent fibre density: A novel measure for the analysis of diffusion-weighted magnetic resonance images. *NeuroImage*, 59(4):3976–3994, 2012.

David A Raffelt, J-Donald Tournier, Robert E Smith, David N Vaughan, Graeme Jackson, Gerard R Ridgway, and Alan Connelly. Investigating white matter fibre density and morphology using fixel-based analysis. *Neuroimage*, 144:58–73, 2017.

Wilfrid Rall. Core conductor theory and cable properties of neurons. *Comprehensive physiology*, 2011.

F Ramon and JOHN W Moore. Ephaptic transmission in squid giant axons. *American Journal of Physiology-Cell Physiology*, 234(5):C162–C169, 1978.

Mikail Rubinov and Olaf Sporns. Complex network measures of brain connectivity: uses and interpretations. *Neuroimage*, 52(3):1059–1069, 2010.

Mikail Rubinov, Olaf Sporns, Cees van Leeuwen, and Michael Breakspear. Symbiotic relationship between brain structure and dynamics. *BMC neuroscience*, 10(1):55, 2009.

HJ Scheer, T Fedele, G Curio, and M Burghoff. Extension of non-invasive eeg into the khz range for evoked thalamocortical activity by means of very low noise amplifiers. *Physiological measurement*, 32(12):N73, 2011.

Alexander A Schlegel, Justin J Rudelson, and Peter U Tse. White matter structure changes as adults learn a second language. *Journal of cognitive neuroscience*, 24(8): 1664–1670, 2012.

Jan Scholz, Miriam C Klein, Timothy EJ Behrens, and Heidi Johansen-Berg. Training induces changes in white-matter architecture. *Nature neuroscience*, 12(11):1370–1371, 2009.

H Schumann, E Koppenhofer, and H Wiese. Compensation of the low-pass filter properties of the current measuring internode in potential-clamped myelinated nerve fibres. *Gen. Physiol. Biophys*, 2:287–295, 1983.

Alwyn C Scott. The electrophysics of a nerve fiber. *Reviews of Modern Physics*, 47(2): 487, 1975.

Judith M Segall, Elena A Allen, Rex E Jung, Erik B Erhardt, Sunil K Arja, Kent Kiehl, and Vince D Calhoun. Correspondence between structure and function in the human brain at rest. *Frontiers in neuroinformatics*, 6, 2012.

Armin H Seidl. Regulation of conduction time along axons. *Neuroscience*, 276:126–134, 2014.

Sarab S Sethi, Valerio Zerbi, Nicole Wenderoth, Alex Fornito, and Ben D Fulcher. Structural connectome topology relates to regional bold signal dynamics in the mouse brain. *Chaos: An Interdisciplinary Journal of Nonlinear Science*, 27(4):047405, 2017.

MN Shneider and M Pekker. Correlation of action potentials in adjacent neurons. *Physical biology*, 12(6):066009, 2015.

Robert E Smith, Jacques-Donald Tournier, Fernando Calamante, and Alan Connelly. Anatomically-constrained tractography: improved diffusion mri streamlines tractography through effective use of anatomical information. *Neuroimage*, 62(3):1924–1938, 2012.

Robert E Smith, Jacques-Donald Tournier, Fernando Calamante, and Alan Connelly. Sift: spherical-deconvolution informed filtering of tractograms. *Neuroimage*, 67:298–312, 2013.

Seong-Jin Son, Jonghoon Kim, and Hyunjin Park. Structural and functional connectional fingerprints in mild cognitive impairment and alzheimers disease patients. *PloS one*, 12(3):e0173426, 2017.

Olaf Sporns, Giulio Tononi, and Rolf Kötter. The human connectome: a structural description of the human brain. *PLoS computational biology*, 1(4):e42, 2005.

Ruth M Stassart, Wiebke Möbius, Klaus-Armin Nave, and Julia M Edgar. The axon-myelin unit in development and degenerative disease. *Frontiers in neuroscience*, 12: 467, 2018.

DI Stephanova and H Bostock. A distributed-parameter model of the myelinated human motor nerve fibre: temporal and spatial distributions of action potentials and ionic currents. *Biological cybernetics*, 73(3):275–280, 1995.

DI Stephanova and H Bostock. A distributed-parameter model of the myelinated human motor nerve fibre: temporal and spatial distributions of electrotonic potentials and ionic currents. *Biological cybernetics*, 74(6):543–547, 1996.

Daumante Suminaite, David A Lyons, and Matthew R Livesey. Myelinated axon physiology and regulation of neural circuit function. *Glia*, 67(11):2050–2062, 2019.

Keiichiro Susuki. Myelin: a specialized membrane for cell communication. *Nature Education*, 3(9):59, 2010.

M Symms, HR Jäger, K Schmierer, and TA Yousry. A review of structural magnetic resonance neuroimaging. *Journal of Neurology, Neurosurgery & Psychiatry*, 75(9): 1235–1244, 2004.

Robert B Szlavik, Abuhanif K Bhuiyan, Anthony Carver, and Frank Jenkins. Neural-electronic inhibition simulated with a neuron model implemented in spice. *IEEE Transactions on neural systems and rehabilitation engineering*, 14(1):109–115, 2006.

I Tasaki and K Frank. Measurement of the action potential of myelinated nerve fiber. *American Journal of Physiology-Legacy Content*, 182(3):572–578, 1955.

Ichiji Tasaki and Minoru Fujita. Action currents of single nerve fibers as modified by temperature changes. *Journal of neurophysiology*, 11(4):311–315, 1948.

J-Donald Tournier, Fernando Calamante, and Alan Connelly. Robust determination of the fibre orientation distribution in diffusion mri: non-negativity constrained super-resolved spherical deconvolution. *Neuroimage*, 35(4):1459–1472, 2007.

J-Donald Tournier, Fernando Calamante, David G Gadian, and Alan Connelly. Direct estimation of the fiber orientation density function from diffusion-weighted mri data using spherical deconvolution. *NeuroImage*, 23(3):1176–1185, 2004.

Jacques-Donald Tournier, Susumu Mori, and Alexander Leemans. Diffusion tensor imaging and beyond. *Magnetic resonance in medicine*, 65(6):1532–1556, 2011.

Takayoshi Tsubo and Makoto Kurokawa. Verification of the effect of the axon fluid as a highly dielectric medium in the high-speed conduction of action potentials using a novel axon equivalent circuit. *Biophysics and physicobiology*, 15:214–228, 2018.

Olga Tymofiyeva, Christopher P Hess, Etay Ziv, Nan Tian, Sonia L Bonifacio, Patrick S McQuillen, Donna M Ferriero, A James Barkovich, and Duan Xu. Towards the baby connectome: mapping the structural connectivity of the newborn brain. *PloS one*, 7 (2):e31029, 2012.

Jelle Veraart, Els Fieremans, and Dmitry S Novikov. Diffusion mri noise mapping using random matrix theory. *Magnetic resonance in medicine*, 76(5):1582–1593, 2016.

Jinhui Wang, Liang Wang, Yufeng Zang, Hong Yang, Hehan Tang, Qiyong Gong, Zhang Chen, Chaozhe Zhu, and Yong He. Parcellation-dependent small-world brain functional networks: a resting-state fmri study. *Human brain mapping*, 30(5):1511–1523, 2009.

Franz Waxman. *The axon: structure, function, and pathophysiology*. Oxford University Press, USA, 1995.

Thomas Fischer Weiss. *Cellular biophysics*, volume 1. MIT press Cambridge, Mass:, 1996.

Thomas Fisher Weiss. *Cellular biophysics: electrical properties*. Number 576.32/. 36 WEI. 1994.

Susan Whitfield-Gabrieli and Alfonso Nieto-Castanon. Conn: a functional connectivity toolbox for correlated and anticorrelated brain networks. *Brain connectivity*, 2(3): 125–141, 2012.

William S Yamamoto and Theodore B Achacoso. Scaling up the nervous system of caenorhabditis elegans: Is one ape equal to 33 million worms? *Computers and biomedical research*, 25(3):279–291, 1992.

Gorka Zamora-López, Yuhan Chen, Gustavo Deco, Morten L Kringelbach, and Changsong Zhou. Functional complexity emerging from anatomical constraints in the brain: the significance of network modularity and rich-clubs. *Scientific reports*, 6:38424, 2016.